

Large-area Coating and Patterning of Functional Nanocomposites:  
Design, Synthesis and Characterization

BY

THOMAS M. SCHUTZIUS  
B.S., University of Illinois at Chicago, 2008

THESIS

Submitted in partial fulfillment of the requirements  
for the degree of Doctor of Philosophy in Mechanical Engineering  
in the Graduate College of the  
University of Illinois at Chicago, 2013

Chicago, Illinois

Defense Committee:

Constantine M. Megaridis, Chair and Advisor  
Alan Feinerman, Electrical & Computer Engineering  
Michael Cho, Bioengineering  
Gregory M. Jursich, Bioengineering  
Ilker S. Bayer, Istituto Italiano di Tecnologia

Copyright by  
Thomas M. Schutzius  
2013

To my parents.

## ACKNOWLEDGMENTS

A PhD thesis is truly the effort of a collective, not an individual, and I was fortunate to have been surrounded by a great supporting cast. First and foremost, I would like to sincerely thank my advisor, and mentor, Prof. Constantine M. Megaridis. He advised me to seek more than a masters degree; he advised a mechanical engineer (read: *chemistry-phobic!*) to pursue a PhD in coatings and materials research. He supported me through the tough times, the long nights, and the many iterations to manuscripts. It was with his unwavering support that I am now in the unique position of beginning an ETH postdoctoral fellowship at the Swiss Federal Institute of Technology this fall (2013). He took a personal interest in me, and made my PhD experience an extremely positive one. Thank you Prof.

If Prof. Megaridis was my primary advisor, then Ilker S. Bayer and Manish K. Tiwari would have to be classified as researcher advisors. The sheer ambition of this thesis was made possible by their passion and ideas. Some of the most enjoyable times of my PhD were spent with them. They were both responsible for introducing me to research in superhydrophobic coatings, and they have been extremely supportive of the research topics that evolved from there (*i.e.*, wettability patterning). They truly are first rate collaborators. I would also like to thank ISB for serving on my thesis committee. MKT, and his wife Niru, also deserve special mention for their hospitality when I visited them at Switzerland. They have, and continue to make, my transition to ETH a smooth one.



## ACKNOWLEDGMENTS (Continued)

I would like to thank Prof. Jursich, Prof. Feinerman, and Prof. Cho for serving on my thesis committee. To Prof. Jursich and Prof. Feinerman, I would also like to express my sincere thanks for their collaboration on many aspects of the nanocomposite coating work and access to their laboratory resources. Prof. Feinerman’s researchers, Prateek and Tatjana, also deserve to be mentioned for their assistance.

To Prof. Ranjan Ganguly, I would sincerely like to thank him for taking the time to proofread this thesis. It was also a pleasure to have him in our laboratory during his sabbatical.

I would also like to acknowledge all of the hard work and dedication from my labmates Srikar, Arindam, Joseph, Shreyas, Aritra, and Ramsey. Special thanks to Arindam and Joseph for their collaboration on the nanocomposite coatings work. I believe that this group was a close one, and everyone contributed to make the research environment an exceptional one. To the undergraduate students that I advised closely, Mohamed, Gustav, Jim, Jared, Zach, and Alex, it has been a real pleasure to work with you. Mohamed deserves special note as he was the recipient of the 2013 National Science Foundation (NSF) Graduate Research Fellowship. That achievement represents one of the proudest moments of my PhD. The visiting research scholars to our laboratory also deserve to be acknowledged: Muhammad Raffi and Anjana Jain. Their experience and insight was a great resource for our laboratory. I also participated in a high school outreach program with Benito Juarez—which was run through our laboratory—and had the opportunity to “teach” some very bright students who deserve mention: Miguel Torres, Clemencia Garnica, Daisy Torres, Gabby Gonzalez, and Ray Hruby. Miguel deserves special

## ACKNOWLEDGMENTS (Continued)

mention for advancing to the IL state science fair competition. Interacting with them was a real joy.

Thomas, Alex, Joshua, Kevin, Tim, Joe, Tom, Sam, Bob, Dan, Sean, Altaf, and Jim, I am grateful to call you friends. You have all acted in one way or another to distract me from my PhD, and I sincerely thank you for it. To Tom, Altaf, and Jim, I am glad to see the establishment of a PTS alumni association and that what we started as undergraduates continues to grow today. I have also had some notable mentors—prior to the PhD—who deserve special mention: Sandy Dirker (teacher), Robbie Field (teacher), Jim Hansen (engineer), and Jim Knoedel (coach).

To my family (and the future in-laws), I am profoundly grateful for their love and support. It goes without saying, but as with anything I have achieved, they deserve a portion of the credit. Last, but not least, I would like to thank my fiancée Lauren. She provides great support and perspective, and I am very much looking forward to our future adventures.

TMS

## TABLE OF CONTENTS

<u>CHAPTER</u>		<u>PAGE</u>
<b>1</b>	<b>INTRODUCTION . . . . .</b>	<b>1</b>
1.1	Nanotechnology: Historical Perspective . . . . .	1
1.2	Approaches to Nanotechnology . . . . .	6
1.3	Nanocomposites: Background and Motivation . . . . .	7
1.3.1	Anisotropic . . . . .	8
1.3.2	Surface Patterned . . . . .	9
1.3.3	Volumetrically Patterned . . . . .	10
1.3.4	Wettability: Considerations of Super-hydrophobic/-hydrophilic Surfaces . . . . .	11
1.4	Thesis Objective . . . . .	21
1.4.1	Environmentally Benign Superhydrophobic Coatings . . . . .	21
1.4.2	Stretchable Superhydrophobic Composite Coatings . . . . .	21
1.4.3	Fluoropolymer Blends: Multifunctional Liquid Repellent Nanocomposites . . . . .	22
1.4.4	Wettability Engineering: Handling Low Surface Tension Liquids . . . . .	22
1.4.5	Wettability Engineering: Thermal Stability and Scalability . . . . .	23
1.4.6	Wettability Engineering: Shaping and Mobilizing Liquid $\mu$ -Volumes . . . . .	24
1.5	Scope of the Work . . . . .	25
<b>2</b>	<b>ENVIRONMENTALLY BENIGN SUPERHYDROPHOBIC COATINGS . . . . .</b>	<b>27</b>
2.1	Introduction . . . . .	27
2.2	Experimental . . . . .	31
2.2.1	Materials . . . . .	31
2.2.2	Procedure . . . . .	32
2.2.3	Characterization . . . . .	33
2.3	Results and Discussion . . . . .	34
<b>3</b>	<b>STRETCHABLE SUPERHYDROPHOBIC COMPOSITE COATINGS . . . . .</b>	<b>43</b>
3.1	Introduction . . . . .	43
3.2	Experimental . . . . .	47
3.2.1	Materials . . . . .	47
3.2.2	Procedure . . . . .	48
3.2.3	Characterization . . . . .	49
3.3	Results and Discussion . . . . .	52

## TABLE OF CONTENTS (Continued)

<u>CHAPTER</u>		<u>PAGE</u>
<b>4</b>	<b>FLUOROPOLYMER BLENDS: MULTIFUNCTIONAL LIQUID REPELLENT NANOCOMPOSITES</b> . . . . .	64
4.1	Introduction . . . . .	64
4.2	Experimental . . . . .	68
4.2.1	Materials . . . . .	68
4.2.2	Procedure . . . . .	70
4.2.3	Characterization . . . . .	76
4.3	Results and Discussion . . . . .	77
<b>5</b>	<b>WETTABILITY ENGINEERED SURFACES: HANDLING LOW SURFACE TENSION LIQUIDS</b> . . . . .	88
5.1	Introduction . . . . .	88
5.2	Experimental . . . . .	91
5.2.1	Materials and Procedure . . . . .	91
5.2.2	Characterization . . . . .	92
5.3	Results and Discussion . . . . .	93
<b>6</b>	<b>WETTABILITY ENGINEERED SURFACES: THERMAL STABILITY AND SCALABILITY</b> . . . . .	107
6.1	Introduction . . . . .	107
6.2	Experimental . . . . .	111
6.2.1	Materials . . . . .	111
6.2.2	Procedure . . . . .	111
6.2.3	Characterization . . . . .	112
6.3	Results and Discussion . . . . .	113
<b>7</b>	<b>WETTABILITY ENGINEERED SURFACES: SHAPING AND MOBILIZING LIQUID <math>\mu</math>-VOLUMES</b> . . . . .	130
7.1	Introduction . . . . .	130
7.2	Experimental . . . . .	132
7.2.1	Materials . . . . .	132
7.2.2	Procedure . . . . .	132
7.2.3	Characterization . . . . .	135
7.3	Results and Discussion . . . . .	136
<b>8</b>	<b>CONCLUSIONS AND RESEARCH OUTLOOK</b> . . . . .	162
8.1	Thesis conclusion . . . . .	162
8.1.1	Environmentally Benign Superhydrophobic Coatings . . . . .	162
8.1.2	Stretchable Superhydrophobic Composite Coatings . . . . .	163
8.1.3	Fluoropolymer Blends: Multifunctional Liquid Repellent Nanocomposites . . . . .	163
8.1.4	Wettability Engineering: Handling Low Surface Tension Liquids . . . . .	164

## TABLE OF CONTENTS (Continued)

<u>CHAPTER</u>		<u>PAGE</u>
8.1.5	Wettability Engineering: Thermal Stability and Scalability . .	165
8.1.6	Wettability Engineering: Shaping and Mobilizing Liquid $\mu$ - Volumes . . . . .	166
8.2	Expected research contribution . . . . .	166
8.2.1	Environmentally Benign Superhydrophobic Coatings . . . . .	166
8.2.2	Stretchable Superhydrophobic Composite Coatings . . . . .	167
8.2.3	Fluoropolymer Blends: Multifunctional Liquid Repellent Nanocom- posites . . . . .	168
8.2.4	Wettability Engineering: Handling Low Surface Tension Liquids	168
8.2.5	Wettability Engineering: Thermal Stability and Scalability . .	169
8.2.6	Wettability Engineering: Shaping and Mobilizing Liquid $\mu$ - Volumes . . . . .	169
8.3	Recommendations for future research . . . . .	170
8.3.1	Environmentally Benign Superhydrophobic Coatings . . . . .	170
8.3.2	Stretchable Superhydrophobic Composite Coatings . . . . .	170
8.3.3	Fluoropolymer Blends: Multifunctional Liquid Repellent Nanocom- posites . . . . .	171
8.3.4	Wettability Engineering: Handling Low Surface Tension Liquids	171
8.3.5	Wettability Engineering: Thermal Stability and Scalability . .	171
8.3.6	Wettability Engineering: Shaping and Mobilizing Liquid $\mu$ - Volumes . . . . .	171
<b>APPENDICES . . . . .</b>		<b>173</b>
<b>Appendix A . . . . .</b>		<b>174</b>
<b>Appendix B . . . . .</b>		<b>182</b>
<b>Appendix C . . . . .</b>		<b>197</b>
<b>CITED LITERATURE . . . . .</b>		<b>208</b>
<b>VITA . . . . .</b>		<b>231</b>

## LIST OF TABLES

<u>TABLE</u>		<u>PAGE</u>
I	EXAMPLE OF DISPERSIONS USED FOR CREATING PE-XGNP COMPOSITE COATINGS. . . . .	33
II	COMPOSITION RANGE OF NBR/PARTICLE DISPERSIONS . .	48
III	DISPERSION COMPOSITIONS FOR ELASTOMERIC SUPER-HYDROPHOBIC COATINGS WITH MINIMAL PARTICLE CONTENT . . . . .	51
IV	COMPOSITION OF ORGANIC SOLVENT-BASED DISPERSIONS USED TO MAKE PVDF-CLAY COMPOSITE COATINGS. . . . .	69
V	COMPOSITION OF ORGANIC SOLVENT-BASED DISPERSIONS USED TO MAKE PVDF-PECA-CLAY COMPOSITE COATINGS.	71
VI	COMPOSITION (IN WT.% OF DISPERSION) AND CORRESPONDING NAMES OF ACETONE/WATER-BASED DISPERSIONS USED TO MAKE PVDF-PMC-CLAY COMPOSITE COATINGS. . . . .	73
VII	COMPOSITION OF ACETONE/WATER-BASED DISPERSION USED TO MAKE PVDF-PMC-CNW COMPOSITE COATING REPELLENT TO BOTH WATER AND WATER+IPA (0.17 CNW MASS FRACTION). . . . .	74
VIII	APPARENT ADVANCING CONTACT ANGLE AND RECEDING CONTACT ANGLE VALUES FOR LIQUIDS OF DIFFERENT SURFACE TENSIONS ON A SUPEROLEOPHOBIC PMC-CNF COATING (60 WT.% CNF); VALUES OBTAINED FROM HANDBOOK. <sup>10</sup> . . . . .	93
IX	MEASURED AND PREDICTED AVERAGE SPEEDS FOR FLUIDS OF DIFFERENT DYNAMIC VISCOSITY (VISCOSITY VALUES OBTAINED FROM HANDBOOK <sup>11</sup> ) TO TRAVERSE A LENGTH IN 1 MILLIMETER-WIDE STC TRACKS. . . . .	100
X	COMPOSITION OF DISPERSIONS USED TO MAKE MSQ-HFS COATINGS. . . . .	111

## LIST OF TABLES (Continued)

<u>TABLE</u>		<u>PAGE</u>
XI	CONCENTRATIONS OF ALL INGREDIENTS USED IN THE DISPERSION FOR GENERATING SUPERHYDROPHOBIC COATINGS BY DROP CASTING METHODS. . . . .	134
XII	WATER CONTACT ANGLE VALUES ON MICRO-TEXTURED SILICON-CARBIDE SURFACES (SANDPAPER) FOR THREE CASES: 1) UNCOATED; 2) PMC-HFS COMPOSITE COATING; 3) INK COATED ON PMC-HFS COMPOSITE. . . . .	138

## LIST OF FIGURES

<u>FIGURE</u>		<u>PAGE</u>
1	(a) <i>Mollusk shell</i> ; <sup>2</sup> (b) <i>abalone shell</i> ; <sup>3</sup> (c) <i>Namib desert beetle</i> , bumps indicate hydrophilic chemical patterns (photograph); <sup>4</sup> (d) <i>cylindrical silica diatom</i> (ceramic composite); <sup>5</sup> (e) <i>polypropylene-CaCO<sub>3</sub> nanocomposite</i> ; <sup>6</sup> (f) <i>poly(vinylidene fluoride)-graphite nanocomposite</i> ; <sup>7</sup> (g) <i>hydrophobic-hydrophilic patterned nanocomposite</i> , with hydrophilic areas containing red, green, and blue dye solutions (photograph); <sup>8</sup> (h) profilometer image of a three-dimensional patterned <i>poly(vinyl alcohol)-CdTe nanocomposite</i> . <sup>9</sup> All images are micrographs unless otherwise stated. All images reproduced with permission from the respective publishers (citations included in text). . . . .	5
2	Schematic of the equilibrium contact angle ( $\theta_e$ ) determined via forces. .	12
3	Liquid droplet edge undergoing a small displacement ( $dx$ ) on a (a) textured but homogeneous, and (b) chemically heterogeneous surface. . . .	13
4	Ideal solid surfaces with sinusoidal texture profiles. (a)-(b) Hydrophobic surface ( $\theta_e > 90^\circ$ ), (c)-(d) hydrophilic surface ( $\theta_e < 90^\circ$ ). (a) & (c) and (b) & (d) are in Wenzel and Cassie wetting states, respectively. . . . .	15
5	Schematic depicting a liquid drop in a superhydrophobic state ( $\theta^* > 150^\circ$ ) on a re-entrant, fibrous, wettable ( $\theta_e < 90^\circ$ ) substrate. Fibers have a radius $r_f$ and an interspacing value of $2d_f$ . . . . .	17
6	(a) Schematic of a lubricant impregnated surface with a liquid droplet partially wetting it. (b) Such surfaces display extremely low values for $\Delta\theta$ , enabling them to have low droplet sliding angles $\alpha$ without high $\theta_a^*$ values. (c)-(d) Show the sliding dynamics of a water droplet on a tilted lubricant-impregnated surface which is comprised of a carbon nanofiber-fluoroacrylic copolymer composite suffused with Krytox lubricant (unpublished). . . . .	20
7	High magnification TEM image of an xGnP platelet demonstrating a platelet thickness below 5 nm. Scale bar is 5 nm. . . . .	35



## LIST OF FIGURES (Continued)

<u>FIGURE</u>		<u>PAGE</u>
8	15 mL vials all containing 0.12 g of polyethylene copolymer in 10 g of water. Vial 2 also contains ~1 g of ammonium hydroxide, while vial 3 also contains 1.6 g of acetic acid. Note the phase separation in vial 3 as a result of acidification. . . . .	36
9	Suspensions of 0.1 wt.% xGnP in water with (a) no electrolyte, and (b) electrolyte (0.1 wt.% NaCl). (c) Scattering effect demonstrated on a diluted (0.002 wt.%) xGnP-water suspension. . . . .	37
10	(a) xGnP-water suspensions in 20 mL glass vials with varying concentration of $\text{NH}_3(\text{aq})$ (left vial 0 wt.%, middle vial 1.0 wt.%, right vial 7.7 wt.% $\text{NH}_3(\text{aq})$ ). (b) The vials from <b>a</b> with 1 g of a 42 wt.% PE dispersion in water added to each. (c) The vials from <b>b</b> after 60 min of bath sonication. Note the apparent stability of the dispersion in the rightmost vial. . . . .	39
11	(a) $\theta_a^*$ ( $\text{---}\square\text{---}$ ) and $\theta_r^*$ ( $\text{---}\circ\text{---}$ ) vs. $w_p$ (xGnP mass fraction in the dry composite coating); (b) Coating add-on level ( $\tau$ ) vs. $w_p$ for coatings characterized in <b>a</b> . . . . .	39
12	SEM images of the spray deposited coating ( $w_p = 0.54$ ) (a) low magnification (50 $\mu\text{m}$ scale bar); (b) high magnification (5 $\mu\text{m}$ scale bar). . .	41
13	The electrical conductivity of the PE-xGnP composite coating ( $\gamma$ ) as a function of filler concentration ( $w_p$ ). . . . .	42
14	ESEM images of composite coating SC1, deposited on indium foil, unstrained, demonstrating hierarchical roughness by dual filler particle addition for (a) low magnification (50 $\mu\text{m}$ scale bar) and (b) higher magnification (2 $\mu\text{m}$ scale bar). . . . .	44
15	Sessile water droplet contact angle ( $\theta^*$ ) variation as a function of filler particle concentration ( $w_p$ ) for coatings with different fillers: PTFE ( $\text{---}\square\text{---}$ ), CB ( $\text{---}\circ\text{---}$ ), and PTFE+CB ( $\text{---}\triangle\text{---}$ ). The PTFE+CB case maintains a filler particle wt. ratio of 9:1 PTFE:CB. The coatings were deposited on glass slides. Each data point represents 10 water contact angle measurements. . . . .	46

## LIST OF FIGURES (Continued)

<u>FIGURE</u>		<u>PAGE</u>
16	Water droplet sliding angle ( $\alpha$ ) as a function of filler particle concentration ( $w_p$ ) for coatings with different fillers. The coatings were deposited on glass slides. 40 measurements were averaged for each data point. For $w_p$ less than 72 wt.% PTFE+CB and 80 wt.% PTFE, water droplets remained pinned to the coating's surface even when inverted. PTFE+CB (--- $\Delta$ ---); PTFE (— $\square$ —) . . . . .	47
17	TEM image showing the morphology of the CB filler particles used in this work. Image analysis showed that the mean diameter of the CB primary units is 21 nm (standard deviation 3 nm). . . . .	50
18	Water droplet sliding angles as a function of strain ( $\epsilon$ ) for coatings deposited on silicone rubber and polyester fabric. 10 sliding angle measurements were averaged for each data point. Uncoated silicone rubber did not allow droplet sliding even when inverted. The uncoated fabric showed inconsistent sliding angles in the range of 30° to 90° . SC1 on silicone rubber (--- $\Delta$ ---); SC1 on fabric (— $\diamond$ —); SC2 on silicone rubber (— $\square$ —); SC2 on fabric (— $\circ$ —). . . . .	53
19	Water droplet sliding angles ( $\alpha$ ) for coatings deposited on silicone rubber and polyester fabric at both stretched (S) and contracted (C) conditions. Coated silicone rubber substrates were cyclically stretched to 30% strain, while coated fabric substrates were cyclically stretched to 70% strain. 10 measurements were averaged to obtain each data point. SC1 on silicone rubber (--- $\Delta$ ---); SC1 on fabric (— $\diamond$ —); SC2 on silicone rubber (— $\square$ —); SC2 on fabric (— $\circ$ —). . . . .	54
20	ESEM images of the uncoated polyester fabric at (a) low-magnification (50 $\mu$ m scale bar), and (b) higher magnification (5 $\mu$ m scale bar). ESEM images of composite coating SC1, deposited on polyester fabric, unstrained, demonstrating conformal coating of the fabric fibers at (c) low magnification (200 $\mu$ m scale bar), and (d) higher magnification (50 $\mu$ m scale bar). . . . .	59
21	(a)-(c) ESEM images of composite coating SC1 (deposited on indium foil, strained to 18%) at different magnifications increasing from left to right showing crazing. (d)-(f) ESEM images of composite coating SC1 deposited on silicone rubber relaxed after stretching to 30% strain. The inset in (f) displays a magnified image of broken fibrils. Scale bars ( $\mu$ m): (a) 200; (b) 50; (c) 2; (d) 200; (e) 50; (f) 5. . . . .	62

## LIST OF FIGURES (Continued)

<u>FIGURE</u>		<u>PAGE</u>
22	ESEM image of nanoclay platelets demonstrating partial exfoliation. A small amount of ethyl 2-cyanoacrylate monomer was added to facilitate adhesion of the clay to the substrate for imaging purposes (10:1 clay:polymer wt. ratio). The inset shows a magnified image of the area marked by the dotted box. Scale bar is 1 $\mu\text{m}$ . . . . .	70
23	Quaternary and sexternary phase diagrams of the solutions utilized for spray without any clay fillers. Filled symbols indicate PVDF phase separation from liquid to a solid state. The insets display images of vials containing solutions with the specified compositions; scale bar is 10 mm. The magnetic stir bar can be seen at the bottom of each vial. (a) PVDF, solvent (acetone, NMP), water phase diagram; (b) PVDF, solvent (acetone, NMP, TFA), 20 wt.% PMC in water. For both (a) and (b), NMP was kept at a constant 9:1 wt. ratio with respect to PVDF. The concentration of TFA in the total solution was < 0.2 wt.% TFA. Gray areas indicate unstable or phase inverted regimes. . . . .	78
24	ESEM images of PVDF-PMC-clay composite coatings. (a) 2:3 wt. ratio PVDF:PMC and $w_p = 0.29$ (100 $\mu\text{m}$ scale bar); (b) 1:1 wt. ratio PVDF:PMC and $w_p = 0.29$ (2 $\mu\text{m}$ scale bar). . . . .	80
25	Sessile contact angle ( $\theta^*$ ) vs. nanoclay mass fraction ( $w_p$ ) for PVDF-clay, PVDF-PECA-clay, and PVDF-PMC-clay nanocomposites spray deposited on plain paper. Varying concentrations of polymers were used and are defined as: PVDF ( $\text{---}\diamond\text{---}$ ), PVDF:PECA 3:2 ( $\text{---}\triangleleft\text{---}$ ), PVDF:PMC 1:1 ( $\text{---}\circ\text{---}$ ), PVDF:PMC 2:3 ( $\text{---}\square\text{---}$ ), and PVDF:PMC 2:1 ( $\text{---}\triangle\text{---}$ ). Increases in contact angle values were not appreciable beyond the mass fractions investigated here and are therefore not shown. . . . .	82
26	Water contact angle hysteresis ( $\Delta\theta^*$ ) for (a) PVDF-clay and (b) PVDF-PMC-clay nanocomposite coatings spray cast on plain paper. Each bar represents a measurement at a single location on a large-area sample. For (a) $w_p = 0.75$ with a corresponding water sessile contact angle of $143 \pm 4$ deg. For (b) the PVDF:PMC wt. ratio is 1:1, and $w_p = 0.375$ . The corresponding water sessile contact angle is $164 \pm 4$ deg. . . . .	83
27	Water-IPA (9:1 wt. ratio) droplet hysteresis ( $\Delta\theta^*$ ) measurements for PVDF-PMC-clay nanocomposite coating spray cast on aluminum foil. For this particular coating, the polymer is a mixture of 1:1 wt. ratio PVDF:PMC, and $w_p = 0.375$ . The water-IPA sessile contact angle for this coating is $154 \pm 4$ deg. . . . .	84

## LIST OF FIGURES (Continued)

<u>FIGURE</u>		<u>PAGE</u>
28	(a) ESEM micrograph of surface morphology of a PVDF-PMC-CNW composite coating with $w_p = 0.09$ (20 $\mu\text{m}$ scale bar). (b) Higher magnification image showing composite surface morphology made up of randomly assembled CNWs, some of which form needle-like features protruding from the hydrophobic polymer matrix (5 $\mu\text{m}$ scale bar). . . . .	86
29	$\theta^*$ , $\gamma$ , and $\Delta\theta^*$ as a function of CNW mass fraction, $w_p$ . The polymer is a blend of PVDF and PMC (1:1 wt. ratio). For $\theta^*$ and $\Delta\theta^*$ , the unfilled squares correspond to water, while filled circles correspond to a water-IPA mixture (9:1 wt. ratio) with surface tension of 40.42 mN $\text{m}^{-1}$ . Each point marks the average of five measurements. . . . .	87
30	Continuous fountain-pen printing setup: 1) Syringe containing wax-hexane solution (dispensed by an automated syringe pump, not pictured); 2) linearly translating substrate (attained by a computer controlled linear actuator, not pictured); 3) detail showing polypropylene nozzle dispensing wax-hexane solution onto the coated (oleophobicized) glass slide, substrate moving right-to-left, nozzle held at a fixed position. . . . .	90
31	SEM micrographs of a superoleophobic, spray-deposited, fluoroacrylic/CNF composite coating with $w_p = 0.60$ CNF at (a) low-magnification and (25 $\mu\text{m}$ scale bar) (b) high-magnification (5 $\mu\text{m}$ scale bar). . . . .	94
32	SEM micrographs of a wax-coated, fluoroacrylic/CNF ( $w_p = 0.60$ CNF) composite coating at (a) low-magnification (50 $\mu\text{m}$ scale bar) and (b) high-magnification (25 $\mu\text{m}$ scale bar). Arrows in (b) demonstrate example measurements of the interspacing values between micro-texture features that remain exposed after wax-patterning. . . . .	99
33	Measured data for liquid wetting meniscus position ( $x$ ) as a function of time ( $t$ ) for acetone (—□—; average of 10 trials), ethanol (—○—; average of 14 trials) and hexadecane (—△—; average of 14 trials) flowing in wax-patterned STC tracks. Washburn theory prediction of $x$ vs. $t$ for acetone (solid line), ethanol (dashed line) and hexadecane (dot dashed line) for liquid flow in wettable 18 $\mu\text{m}$ pores (from Equation 5.3). Inset is a top-view image of horizontally-placed patterned tracks with ethanol advancing by capillary action. . . . .	102

## LIST OF FIGURES (Continued)

<u>FIGURE</u>		<u>PAGE</u>
34	STC line tracks printed with wax on a superoleophobic fluoroacrylic/CNF composite coating. Two identical hexadecane droplets are placed, one outside the wax-coated area (left), and the other (top middle) on the wax line at (a) $t=0$ s, (b) $t=1$ s and (c) $t=3$ s. Note how the fluid advances along the straight track via capillary action. Scale bar is 1.0 mm. . . . .	103
35	(a) Schematic of anisotropic wetting of water droplets placed in line STC tracks. $\alpha$ and $\beta$ define tilting angles with respect to axes parallel and normal to the track, respectively; droplets remain pinned for $\alpha > 0^\circ$ and slide for adequate values of $\beta > 0^\circ$ ; (b)-(c) demonstrate the confinement of a water droplet ( <i>i.e.</i> , no mobility) even for $\alpha = 90^\circ$ ; (d)-(f) demonstrate droplet sliding action for $\beta = 45^\circ$ in the time period $t = 0$ to 14 s. Inset scale bars are all 1 mm and the droplet volume is 10 $\mu\text{L}$ . . . . .	105
36	ESEM images of superhydrophobic MSQ-HFS coating ( $w_p = 0.5$ ) with increasing magnification from (a) to (b). (a) 50 $\mu\text{m}$ scale bar (b) 2 $\mu\text{m}$ scale bar. . . . .	115
37	(a) Apparent advancing ( $\theta_a^*$ ; —□—) and receding ( $\theta_r^*$ ; — — —○— — —) contact angles vs. filler particle concentration ( $w_p$ ). (b) Sessile ( $\theta^*$ ) contact angle vs. $w_p$ for untreated (—□—) and flame treated (— — —○— — —) coatings. . . . .	115
38	Apparent advancing contact angle $\theta_a^*$ for spray cast, HFS filler-containing coatings vs. $\theta_a$ for spin-coated MSQ (plotted in terms of their cosines). Coatings contain different concentrations of HFS, as indicated in the legend. Unfilled data points indicate flame-treated coatings. Plotted lines are for the two wetting theories; the dashed line is for Wenzel (Equation 5 with $R = 1.48$ ), while the solid line is for Cassie-Baxter (Equation 4 with $\Phi_{sl} = 0.04$ ). . . . .	116
39	Sessile contact angle ( $\theta^*$ ) vs. laser fluence ( $\phi$ ) of the coating (bottom axis) and laser translation speed ( $u_t$ top axis; laser irradiance was held constant at $I = 0.2 \text{ MW cm}^{-2}$ ). The filler concentration was $w_p = 0.5$ (—□—) and $w_p = 0.0$ (— — —○— — —). All further laser processing was done with $u_t = 2 \text{ cm s}^{-1}$ . . . . .	119

## LIST OF FIGURES (Continued)

<u>FIGURE</u>		<u>PAGE</u>
40	A sequence of images showing an advancing water contact angle measurement at the transition between a superhydrophilic (laser patterned) and the surrounding superhydrophobic area. Inset in (a) shows the laser patterned, hydrophilic, circular spot on the superhydrophobic coating ( $w_p = 0.6$ ) prior to water droplet deposition (scale bar is 500 $\mu\text{m}$ ). The scale bars in (b)-(d) are 500 $\mu\text{m}$ . Arrows in (b)-(d) mark the outer extent of the patterned area. Part of the needle in (d) is obscured by the liquid. (e) is a SEM micrograph depicting the transition area with a vertical dashed line separating the hydrophobic (left) from the hydrophilic area (right). The scale bar in (e) is 20 $\mu\text{m}$ . . . . .	121
41	(a) Photographic and (b) optical microscope images of superhydrophilic patterns (dark) on a superhydrophobic MSQ-HFS coating; (c) hydrophilic, laser patterned lines (dark), and (d) surface-tension-confined channel showing wetting of the lines in (c) by water through capillary action. (e)-(f) SEM images of a STC channel with increasing magnification; (g) SEM image of a laser patterned area revealing porosity. For 0.18 mm-wide STC channels, the water propagation velocity was measured to be 2.5 mm s <sup>-1</sup> . Scale bars: (a) 2 mm; (b) 500 $\mu\text{m}$ ; (c)-(d) 1 mm; (e) 200 $\mu\text{m}$ ; (f) 10 $\mu\text{m}$ ; (g) 2 $\mu\text{m}$ . . . . .	123
42	Superhydrophobic MSQ-HFS coating deposited onto copper substrates and laser-processed to create hydrophilic patterns. (a) Superhydrophobic spots on superhydrophobic background; (b) Superhydrophobic spots on superhydrophilic background; (c) pattern from (b) placed in a water bath and subjected to heating; the hydrophobic islands act as preferred gas nucleation sites—arrows indicate vapor bubbles that grow gradually and detach before this cycle repeats itself over and over. Both scale bars are 400 $\mu\text{m}$ . . . . .	125
43	Water droplet sliding angle ( $\alpha$ ) vs. treatment temperature (T) of a superhydrophobic coating ( $w_p = 0.6$ ). Coatings were treated for 1 hr on a hot plate in open air. At 500 °C treatment temperature, the water droplet ceased to slide, indicating full-loss of the superhydrophobic property of the coating. . . . .	126

## LIST OF FIGURES (Continued)

<u>FIGURE</u>		<u>PAGE</u>
44	TGA plot (mass vs. $T$ ) for (a) HFS, and (b) MSQ under different gas atmospheres (nitrogen $- - -$ , air $---$ ). The inset in (a) shows three 15 mL glass vials containing 10 g of water and 0.07 g HFS. The HFS contained in vial 1 was not subjected to prior TGA treatment, while the HFS in vials 2 and 3 was. For the HFS in vial 2, TGA was performed under nitrogen conditions. For vial 3 it was run under artificial air conditions. In (b), the dotted (...) drop-down line denotes the thermal treatment temperature (1 hr, open air, hot plate) for a superhydrophobic coating ( $w_p = 0.6$ ) above which total loss of droplet sliding behavior was observed (see Figure 43). This temperature marked the beginning of the wettability transition. . . . .	129
45	Schematic outlining the procedure for synthesizing the wettability patterned coatings. (a) Begins with a micro-textured SiC substrate; (b) a PMC-HFS composite coating is dropcast onto the SiC substrate forming a superhydrophobic surface; (c) hydrophilic inkjet patterns are successively applied until the desired level of hydrophilicity is achieved. $r_i$ and $r_o$ represent the inner and outer radii of the hydrophilic annular patterns, respectively. $w_i$ and $w_o$ represent the inner and outer widths of the hydrophilic annular patterns, respectively. . . . .	133
46	Drop impact at $We=80$ on superhydrophobic-paper (a), entirely wettability patterned paper (b), hydrophilic ring pattern on hydrophobic background with $r_o =$ (c) 0.5 mm, (d) 1 mm, (e) 1.5 mm, (f) 2 mm and (g) 2.5 mm, and $w_o = 0.20$ mm. The inset scale bar is 2.0 mm. . . . .	139
47	Schematic illustrating hole formation in a thin liquid lens formed through droplet impact on a wettability patterned surface. $V_h$ , $h_h$ , $U_h$ , $r_h$ , and $r_o$ represent the approximate volume of the hole, the approximate height of the hole, the velocity of the hole expansion, the radius of the hole, and the outer radius of the wettability patterned annulus, respectively. . . . .	143
48	Plot of $\Delta E$ vs. $r_h$ for a liquid lenses of varying initial droplet diameter ( $D_0$ ) and constant annular pattern conditions, $r_o = 2.5$ mm. The liquid displaced by generating a hollow cylinder of volume $V_h$ in the center of the lens was accounted for in this model. The following values of $D_0$ were used: 2.1 mm ( $---$ ), 1.9 mm ( $- - -$ ), and 1.7 mm ( $- - -$ ). . . . .	144
49	Impact on a hydrophilic annulus with $r_o = 2.5$ mm and $w_o = 0.50$ mm width for $We = 80$ . The dotted line indicates an axis of symmetry as well as the propulsion direction of the eventual droplet. . . . .	145

## LIST OF FIGURES (Continued)

<u>FIGURE</u>		<u>PAGE</u>
50	Droplet impact ( $We = 80$ ) on concentric hydrophilic annular patterns with the following properties: $r_o = 2.5$ mm, $w_o = 0.50$ mm, $r_i = 1.35$ mm, and $w_i = 0.20$ mm. . . . .	147
51	Droplet impact ( $We = 60$ ) on a hydrophilic annulus with $r_o = 2.34$ mm and $w_o = 1.3$ mm width. Both top (TV) and side (SV) views are shown and is noted on the left of the image. Scale bars: top view is 2.0 mm; side view is 1.0 mm. The time (in ms) for top and side views are synchronized unless otherwise stated in the side view images. . . . .	149
52	Plots of displacement ( $h$ ) vs. spatial coordinates ( $x$ and $y$ ) for a vibrating circular membrane with $m = 0$ and $n = 2$ ; this is the so-called (0,2) mode. The parameters used were $c = 1.45$ m s <sup>-1</sup> , $r_o = 2.34$ mm, and $h_{max} = 3.0$ mm. The time $t$ is (a) 0 ms and (b) 4.4 ms. Inset images are from Figure 51 at (a) $t = 7.00$ ms and (b) $t = 15.33$ ms. . . . .	150
53	$\Delta r_h = r_o - r_{o,i}$ ( $r_{o,i}$ is the initial hole radius) vs. $\Delta t$ ; the hole formed after droplet impact ( $We = 60$ ) on a hydrophilic annuli with the following properties: $r_o = 2.34$ mm and $w_o$ varies between 0.8-1.3 mm. 6 trials total. Equation 7.3 is plotted (—) for $D_0 = 2.1$ mm and $r_{h,0} = 0.373$ mm, which was the average value initial hole radius for the experimentally measured cases. . . . .	152
54	Droplet impact ( $We=100$ ) on a wettability patterned square with sides of 4.5 mm and a 2.7 mm by 0.866 mm hydrophobic cross. Scale bar shown is 2.0 mm. . . . .	154
55	The process used to create a silver cross outline from a wettability pattern: (a) Hydrophilic cross outline pattern on the superhydrophobic surface. The hydrophilic square has sides of 4.5 mm and the centered inner hydrophobic cross is of dimensions 2.7 mm by 0.866 mm; (b) drop impact onto the hydrophobic cross ( $We = 100$ ) leaves a water template of the desired pattern; (c) silver nanoparticle ink is dispersed throughout the water template; (d) silver film after low-temperature sintering; (e) microscopic view of (d) shows the silver formed on the hydrophilic patterned section and did not extend onto the hydrophobic area. . . . .	155
56	Droplet impact on a superhydrophobic line with a width of 0.5 mm at $We=60$ . Scale bar is 2.0 mm. . . . .	156



## LIST OF FIGURES (Continued)

<u>FIGURE</u>		<u>PAGE</u>
57	Droplet impact ( $We = 14$ ) on a half-annulus wettability pattern (indicated by a dashed white line) with $r_o = 1.95$ mm and $w_o = 0.2$ mm. The droplet is propelled towards a circular wettability pattern (indicated by white filled circular region) with radius 2.0 mm. The distance between the edge of the half annulus and the closest edge of the circular wettability pattern is 4.0 mm. Inset scale bar is 2.0 mm. . . . .	159
A1	(a) Photograph of beaded water droplets on a MSQ-HFS film applied on an aluminum plate. (b) Flame treatment of the coating shown in (a) using a propane torch for a few seconds from a distance of 5-10 cm. (c) Photograph of the flame-treated coating just before depositing a water droplet ( $> 10$ $\mu$ L). (d) Completely wetting droplet spreading on the flame-treated coating. (e) Completely wetting droplet at its final fully-spread state. . . . .	176
A2	Superhydrophobic MSQ-HFS coatings patterned with a single pass of a $CO_2$ laser beam at a fixed power (1.0 W) and speed ( $2.0$ cm $s^{-1}$ ) with a constant focal length and variable distance between the lens and the substrate. The inset scale bars are 100 $\mu$ m. The distance between the laser (lens) and the substrate is decreasing from (a) to (k). The optimum range is between (e)-(h) with the minimum line width in (g) being $109 \pm 6$ $\mu$ m. Inset scale bars in the images are all 100 $\mu$ m. . . . .	177
A3	Superhydrophobic MSQ-HFS film deposited onto two quartz substrates (2.54 cm dia.) before (right) and after (left) laser processing, which induces hydrophilicity and increases transparency. A water droplet has been deposited on each surface, but is visible as a bead only on the superhydrophobic disk (right). The droplet on the superhydrophilic disk (left) has fully spread, thus becoming indistinguishable. . . . .	178
A4	XPS data of untreated (superhydrophobic) and heat-treated (superhydrophilic) MSQ-HFS coatings. (a)-(c) Si 2p region; (d)-(f) O 1s region; (g)-(i) C 1s region. Figures in the left column represent untreated state, while figures in the middle and right columns are the corresponding thermally treated states. Thermal treatment was performed by either a flame ((b), (e) and (h)) or $CO_2$ laser ((c), (f) and (i)). For a given region, each peak is designated by a number. . . . .	179

## LIST OF FIGURES (Continued)

<u>FIGURE</u>		<u>PAGE</u>
A5	A sequence of images demonstrating the super-wetting behavior of water on laser patterned areas of the MSQ-HFS coating for (a)-(b) room temperature conditions ( $T = 25^\circ\text{C}$ ), and (c)-(d) $T = 138^\circ\text{C}$ . The time difference from (a) to (b) is 1.0 s, and (c) to (d) is 0.4 s. Images were captured with a high speed camera mounted overhead at a frame rate of $250\text{ s}^{-1}$ . The size of the laser patterned areas is $6.4\text{ cm}^2$ ; water droplet volumes are $< 10\text{ }\mu\text{L}$ . . . . .	180
A6	(a)-(b) SEM micrographs of spray deposited MSQ-HFS coatings ( $w_p = 0.5$ ) with increasing magnification left-to-right after flame treatment ( <i>i.e.</i> , superhydrophilic coating). Scale bars: (a) $50\text{ }\mu\text{m}$ ; (b) $10\text{ }\mu\text{m}$ . . . .	181
B1	Schematic of the experimental setup. 1) drop generation; 2) high speed camera; 3) cold light source; 4) floating table; 5) sample; 6) platform. $L$ represents the distance from tip of needle to surface of sample. . . . .	190
B2	(a-d) Schematic demonstrating the wettability patterned coating synthesis process; SEM micrographs of the wettability patterned coating before and after each processing step at (e-h) low- and (i-l) high-magnifications. Scale bar in (e-h) equals $50\text{ }\mu\text{m}$ ; Scale bar in (i-l) equals $10\text{ }\mu\text{m}$ . . . . .	191
B3	Plot of hole height ( $h_h$ ) vs. hole radius ( $r_h$ ) for two cases: 1) Accounting for the change in lens shape due to volume displacement as a result of hole formation (—); 2) no change in lens shape (— — — —). The following parameters were used: $D_0 = 2.1\text{ mm}$ , $r_0 = 2.5\text{ mm}$ . . . . .	192
B4	Plot of $\Delta E$ vs. $r_h$ for two cases: 1) Accounting for the change in lens shape due to volume displacement as a result of hole formation (—); 2) no change in lens shape (— — — —). The following parameters were used: $D_0 = 2.1\text{ mm}$ , $r_0 = 2.5\text{ mm}$ . . . . .	193
B5	Plot of $V_h V_0^{-1}$ vs. $r_h$ accounting for the change in lens shape due to volume displacement as a result of hole formation (—). The following parameters were used: $D_0 = 2.1\text{ mm}$ , $r_0 = 2.5\text{ mm}$ . $V_h V_0^{-1}$ is 9.3% at $r_h = 0.52\text{ mm}$ which is the critical hole radius. . . . .	193
B6	Schematic depicting a non-axisymmetric penetrating hole in a liquid lens on a single annulus wettability pattern with outer radius $r_o$ and width $w_o$ . The hole has a height $h_h$ and a radius $r_h$ , and its centerline is positioned at $r = r_o - w_o - r_h$ . . . . .	194

## LIST OF FIGURES (Continued)

<u>FIGURE</u>		<u>PAGE</u>
B7	Plot of $\Delta E$ (calculated from Equation B11) vs. $w_o$ for the following conditions: $D_0 = 2.1$ mm, $r_o = 2.5$ mm, $r_h = 0.05$ mm; no inner annulus is considered in this analysis. . . . .	195
B8	Drop impact ( $We = 30$ ) on a superhydrophobic line of width 0.5 mm. .	195
B9	Drop impact ( $We = 60$ ) on a superhydrophobic line of width 3.0 mm. .	196
B10	Droplet impact ( $We = 100$ ) on a wettability patterned surface designed to rapidly sample numerous small volumes of liquid. . . . .	196
B11	Copy of the license allowing republication of copyright material for Chapter 3. . . . .	199
B12	Copy of the license allowing republication of copyright material for Chapter 4. . . . .	200
B13	Copy of the license allowing republication of copyright material for Chapter 5. . . . .	201
B14	Copy of the license allowing republication of copyright material for Chapter 6. . . . .	202
B15	Copy of the declaration of co-authorship allowing republication of co-authored material for Chapter 3. . . . .	203
B16	Copy of the declaration of co-authorship allowing republication of co-authored material for Chapter 4. . . . .	204
B17	Copy of the declaration of co-authorship allowing republication of co-authored material for Chapter 5. . . . .	205
B18	Copy of the declaration of co-authorship allowing republication of co-authored material for Chapter 6. . . . .	206
B19	Copy of the declaration of co-authorship allowing republication of co-authored material for Chapter 7. . . . .	207

## SUMMARY

Fabrication of polymer nanocomposites from wet-phase processing of nanoparticle/polymer dispersions remains a very active area of research today due to its ability to create nano-functional materials by low-cost, large-area techniques in out-of-cleanroom settings. The benefits of such nano-materials are widely documented; however, many of their applications remain limited due to their *durability* and *scalability*. Durability refers to the tendency of a nano-material to retain its desirable properties (*e.g.*, superhydrophobicity). Scalability refers to the ability of a given nano-material synthesis procedure to be “scaled-up” to manufacturing-level processing. This encompasses many different areas including the following: cost and availability of raw materials; processing time and area; etc. With this in mind, the following topics have been pursued in this thesis.

One area of nanotechnology research that has made great strides towards low-cost, large-area fabrication of functional nanocomposites is liquid repellent coatings. By combining solution processed hydrophobic polymers and nanoparticle suspensions, one can form a dispersion for spray (*i.e.*, wet processing) that results in a water (superhydrophobic) and even oil (superoleophobic) repellent coating with good substrate adhesion and flexibility. So while it appears that large-area processing of superhydrophobic coatings has been realized, in reality most established processes require the use of organic solvents and fluorinated polymers, which raises issues of cost, safety, and environmental impact, and therefore limits industrial implementation. To the former problem, the obvious solution is to replace the organic solvents with water, which

## SUMMARY (Continued)

gives rise to an oxymoron: *A superhydrophobic coating from a water-based dispersion.* To the latter problem, the solution is to supplement hydrophobic fluorine containing chemicals (*e.g.*,  $-\text{CF}_3$ ) with hydrocarbons (*e.g.*,  $-\text{CH}_3$ ). Each problem on its own is difficult; together they are especially hard. The first portion of the thesis addresses these problems with several approaches, culminating in the first ever water-based, non-fluorinated polymer-particle dispersion for synthesis of superhydrophobic coatings from spray.

Durability of nano-materials, especially as it relates to superhydrophobicity, is a major problem and in some instances is the reason why commercial and industrial applications have not been realized. Surfaces typically become compromised through fouling (*e.g.*, oils) or mechanical failure (*e.g.*, strain). Nano-materials also, due to their relatively small size, tend to be brittle. For superhydrophobic applications, substrate adhesion may be low due to the widespread use of fluoropolymers. The second portion of this thesis investigates the final composition of nanocomposites (*e.g.*, filler concentration and types; polymer types, etc.) on mechanical durability, wettability, and electrical conductivity. This thesis reports the first wettability study of a classic, extremely durable nanocomposite: poly(vinylidene fluoride) and nanoclay. It is also the first to study to investigate failure modes of elastomeric superhydrophobic nanocomposites undergoing mechanical strain and the associated effects on coating wettability.

While many applications require spatially uniform wettability, as was the focus of the first and second portion of the thesis, the third part of this thesis focuses on processing nanocomposites with patterns of hydrophobicity and hydrophilicity by large-area techniques—so called wettability patterned (engineered) surfaces. *Patterned wettability (PW)* finds important appli-

cations in the areas of fog capture, pool boiling, and lab-on-a-chip (LOC), where major property enhancement is achieved when hydrophobic/hydrophilic spatial features are  $\sim 100\mu\text{m}$ —a non-trivial result considering the emphasis placed on nanotechnology in modern research. However, *PW* surfaces rely on fabrication methods that are too costly, non-scalable, and inflexible; property enhancement is also not persistent. In this thesis, one of the first superoleophobic/superoleophilic patterned surfaces is presented, which has potential application in combinatorial chemistry, and in *health care applications* for surface microfluidic devices capable of *pumpless* transport of low-surface tension liquids. Other WP surfaces—developed and presented in this thesis—were also shown to play an important role in fluid dynamic events such as droplet impact; their role was to shape the final conformation of a drop (*i.e.*, liquid volume shaping). Finally, as was stated previously, PW surfaces demonstrated significant property enhancement of pool boiling processes (*i.e.*, *energy applications*); however, coating synthesis remains costly and non-scalable for current technology. This work aims to bridge this gap by developing low-cost, large-area PW surfaces for high temperature heat transfer applications.

This thesis demonstrates the potential of low-cost, large-area wet processing of functional nano-structured composites for advancement—and industrial implementation—of many technologies.

## LIST OF SYMBOLS, NOMENCLATURE, OR ABBREVIATIONS

### Acronym

CA	contact angle
CB	Cassie-Baxter
CB	carbon black
CNF	carbon nanofiber
CNW	carbon nanowhisker
DLVO	Derjaguin-Landau-Verwey-Overbeek
DMAc	N,N-dimethylacetamide
DMF	dimethylformamide
ECA	ethyl 2-cyanoacrylate
EMI	electromagnetic interference
ESEM	environmental scanning electron microscope
FLG	few layer graphene
HFS	hydrophobic fumed silica
HSQ	hydrogen silsesquioxane
IPA	isopropanol
MSQ	methylsilsesquioxane

NBR poly(acrylonitrile-co-butadiene) rubber

NMP N-methyl-2-pyrrolidone

NSP nanoscale silicate platelets

PE polyolefin; can also refer to polyethylene.

PECA poly(ethyl 2-cyanoacrylate)

PFA perfluorinated acids

PFEMA perfluoroalkyl ethyl methacrylate copolymers

PFOA perfluorooctanoic acid

PMC fluoroacrylic copolymer

POSS polysilsesquioxanes

PTFE poly(tetrafluoroethylene)

PVDF poly(vinylidene fluoride)

SEM scanning electron microscope

STC surface tension confined

TEM transmission electron microscope

TEP triethyl phosphate

TFA trifluoroacetic acid

TGA thermogravimetric analysis



VOCs volatile organic compounds

WP wettability patterned

xGnP exfoliated graphite nanoplatelet

XPS X-ray photoelectron spectroscopy

### **Dimensionless Groups**

$\text{Bo} = \frac{\rho g r_d^2}{\sigma_{lv}}$  Bond number

$\text{Re} = \frac{D_0 U_0}{\nu}$  Reynolds number

$\text{We} = \frac{\rho D_0 U_0^2}{\sigma_{lv}}$  Weber number

### **Subscript**

0 initial

a advancing

a air (Appendix B.2)

c critical

C16H34 hexadecane

cap capillary

CB Cassie-Baxter

curv curvature

d liquid droplet

drag drag

dry dry substrate

e equilibrium

f fiber

film liquid film

focal focal length

g gravity

h hole

i inner

L laser

l liquid

m meniscus

max maximum

n nozzle

o outer

p particle

PE polyethylene-acrylic acid copolymer.

pore pore

$\rho$	density (inertia)
r	receding
$\sigma$	surface tension
s	solid
t	translation (linear)
tor	torus
track	wettability track
v	vapor
wax	paraffin wax
wet	wet substrate
x	x-direction

### **Greek Variables**

$\alpha$	absorption coefficient (Appendix A).	$\text{cm}^{-1}$
$\alpha$	droplet sliding angle	$^{\circ}$
$\beta$	droplet launch angle (Chapter 7)	$^{\circ}$
$\beta$	tilting angle	$^{\circ}$
$\gamma$	effective acceleration (Chapter 7)	$\text{m s}^{-2}$
$\gamma$	electrical conductivity	$\text{S m}^{-1}$

$\Delta\sigma$	change in surface energy for an advancing liquid column	$\text{J m}^{-2}$
$\Delta\theta^*$	contact angle hysteresis	$^\circ$
$\Delta E$	change in energy	$\text{J}$
$\Delta r$	change in radius	$\text{m}$
$\Delta t$	change in time	$\text{s}$
$\delta$	diffusion length	$\text{cm}$
$\epsilon$	coefficient of restitution (Chapter 7)	
$\epsilon$	strain (Chapter 3)	
$\eta$	efficiency	
$\theta$	contact angle (untextured, chemically homogeneous surface)	$^\circ$
$\theta^*$	apparent contact angle	$^\circ$
$\kappa$	thermal diffusivity	$\text{cm}^2 \text{s}^{-1}$
$\lambda$	wavelength	$\text{cm}$
$\mu$	dynamic viscosity	$\text{Pa s}$
$\nu$	kinematic viscosity	$\text{m}^2 \text{s}^{-1}$
$\rho$	density	$\text{g cm}^{-3}$
$\sigma$	interfacial tension	$\text{N m}^{-1}$
$\tau$	coating add-on thickness	$\text{g m}^{-2}$

$\Phi$	fractional surface area	$\text{m}^2 \text{ m}^{-2}$
$\phi$	azimuthal angle (Appendix B)	$^\circ$
$\phi$	fluence	$\text{J cm}^{-2}$

### Variables

$A$	area	$\text{m}^2$
$C$	coefficient	
$c$	volumetric concentration	$\text{cm}^3 \text{ cm}^{-3}$
$c$	wave speed (Chapter 7; Appendix B)	$\text{m s}^{-1}$
$D$	diameter	$\text{mm}$
$d$	diameter	$\text{mm}$
$E$	energy	$\text{J}$
$F$	force	$\text{N}$
$f$	fractional surface area	$\text{cm}^2 \text{ cm}^{-2}$
$f$	frequency (Chapter 7)	$\text{s}^{-1}$
$f$	general function (Appendix B)	
$g$	acceleration due to gravity	$\text{m s}^{-2}$
$\bar{h}$	nominal liquid film thickness	$\text{mm}$
$h$	circular membrane displacement (Appendix B)	

$h$	height	m
$I$	irradiance	MW cm <sup>-2</sup>
$J_m$	Bessel function of order $m$	
$K$	thermal conductivity	W cm <sup>-1</sup> K <sup>-1</sup>
$L$	length	m
$l$	length	mm
$m$	mass	g
$n$	index (Appendix B)	
$p$	pressure	Pa
$Q$	volumetric flow rate	μL min <sup>-1</sup>
$R$	radius (Appendix B).	m
$R$	roughness ratio	cm <sup>2</sup> cm <sup>-2</sup>
$R$	surface reflection coefficient (Appendix A).	
$r$	radial coordinate (Appendix B)	
$r$	radius	mm
$S$	spreading parameter	J
$T$	temperature	°C
$t$	time	s

$U$	velocity	$\text{m s}^{-1}$
$u$	velocity	$\text{m s}^{-1}$
$V$	volume	$\text{mL}$
$w$	mass fraction	$\text{g g}^{-1}$
$w$	width (Chapter 7; Appendix B)	$\text{mm}$
$x$	represents a position variable	$\text{cm}$
$z_{mn}$	$n$ th zero of $J_m$	

## CHAPTER 1

### INTRODUCTION

#### 1.1 Nanotechnology: Historical Perspective

Since this thesis is primarily focused on modern-day nanotechnology research—which at the moment encompasses a wide-range of research areas—it is instructive to consider its origins briefly; this acts to give context and meaning to the enclosed work. From a materials perspective, nano-scale particles, or so-called nanoparticles, are nothing new. As an example, consider colloidal gold. It likely first appeared in Egypt and China around the 5th or 4th century B.C. (1); however, its original use was of an aesthetic or curative nature. By 1718, a treatise on colloidal gold was written (2), and its first proper scientific treatment was given by Faraday in 1857. He showed that the color of the gold colloidal suspension was not due to the color of the particles themselves but rather to their small size (*i.e.*, structure) (3). Measurements of nanoparticle sizes were then made in the early 20th century by Richard Adolf Zsigmondy (1925 Chemistry Nobel Prize) down to 4 nm (gold(III) oxide particles in glass; so-called cranberry glass) with use of an ultramicroscope (4). He was also the first person to use the term “nano-meter” explicitly for expressing particle size. By 1914, structural characterization (of table salt) with atomic resolution was achieved with X-ray crystallography; this led to the discovery of ionic bonds. This was made possible by the pioneering work of Wilhelm Röntgen (5) (1901 Physics Nobel Prize; the first physics Nobel) and Max von Laue (6) (1914 Physics Nobel



Prize). The same year the length of the C–C bond in an allotrope of carbon (*i.e.*, diamond) was determined: 0.152 nm (7). By 1916, another allotrope of carbon (graphite) had its structure solved by the method of powder diffraction (8); that technique was developed by Peter Debye (9) (1936 Chemistry Nobel Prize) and Paul Scherrer.

Nano-scale films or coatings are also nothing new. Thin films (nano-scale thick; commonly referred to as Langmuir-Blodgett (LB) films) consisting of oils were already being experimented with by the polymath Benjamin Franklin in 1773 (10). In fact, the use of oil to “calm waters” was well known to the ancients Aristotle and Pliny (11). Lord Rayleigh (1904 Physics Nobel Prize) quantified the effect seen by Franklin and showed the film thickness to be 1.6 nm (12). The study of LB films by Irving Langmuir (1932 Chemistry Nobel Prize) led to the concept of the monolayer which is now ubiquitous in nanotechnology research (13). From these examples it is obvious that advances in interface and colloid science and X-ray crystallography existed well before they became associated with nanotechnology (~100 years).

Richard Feynman is the first to set the stage for what becomes modern-day nanotechnology research. In 1959, he gave a lecture at an American Physical Society (APS) meeting entitled, “There’s Plenty of Room at the Bottom,” which is generally regarded as the first impetus or inspiration for the field of nanotechnology (14); for a modern researcher in nanotechnology, it reads as extremely prescient. If nothing else, this lecture serves to give broad vision and justification to a single field devoted to studying all-things “small”. He classifies the field as a type of solid-state physics whose aim is to understand strange (important) phenomena occurring in complex situations. His bold proposal to scientists can be stated succinctly as: *manipulate*,

*control, and characterize things at atomic scales.* Drexler (15) addressed the feasibility of manipulation at the atomic scale two decades later. He proposed utilizing molecular engineering of protein molecules to act as molecular machinery. He drew analogies between common macroscopic technologies and their molecular examples. Cables are collagen; motors are flagella; clamps are enzymatic binding sites; numerical control systems are genetic systems (15).

Nanotechnology and nanoscience in general got a jump-start in the 1980s with the invention of the scanning tunneling microscope by Gerd Binnig and Heinrich Rohrer (1986 Physics Nobel Prize) (16) and the birth of cluster physics, whose aim was to bridge the gap between gas and condensed phases (17). Clusters can be defined as an aggregate of  $10^{3-4}$  atoms or molecules with a diameter  $\leq 1$  nm and represent an interesting research area due to their dramatic size-dependent properties (17). However, for electronic size effects in metallic clusters, the cluster may contain several hundred to many millions of atoms (1-10 nm) (18). This research led to the development of fullerenes by Harold Kroto, Robert Curl, and Richard Smalley (19) (1996 Chemistry Nobel Prize), the “rediscovery”<sup>1</sup> of the multi-walled carbon nanotube by Sumio Iijima (21), and the discovery of the single-walled carbon nanotubes by Sumio Iijima (22) and Bethune (23; 24), which ultimately bolstered the developing field of nanotechnology.

In general, nanotechnology deals in the investigation of materials and phenomena at length scales  $< 100$  nm. The subject continues to receive greater interest owing to the exciting results reported over a wide range of fields. One particular reason for the interesting observed

---

<sup>1</sup>Multi-walled carbon nanotubes were discovered several decades before (20).

behavior is the high surface area to volume ratio, which scales as  $\sim d^{-1}$ , where  $d$  is the characteristic length scale. At such scales, the particles—or so-called nanoparticles—have a relatively large proportion of molecules residing on their surface. For a given material, this fact can lead its nanoparticle form to have significantly different material behavior (*e.g.*, melting point, reactivity) as compared with its bulk state; this is the so-called *size effect*. *Quantum effects* also become more important for nanoparticles, affecting their optical, magnetic, and electrical properties (1).

The main advantage of nanomaterials is that manipulation of such properties can take place without the need for chemical modification. By properly designing and implementing nanomaterials, one can achieve extremely tunable, highly optimized materials for novel technologies and applications. By combining nanoparticles with bulk materials, such as polymers, one can achieve outstanding property enhancement. For example, by dispersing carbon nanotubes (CNT) in a non-conductive polymer (epoxy) matrix, one can generate a percolating structure that is electrically conductive at extremely low concentrations of CNT ( $\sim 0.003$  wt.%) (25).

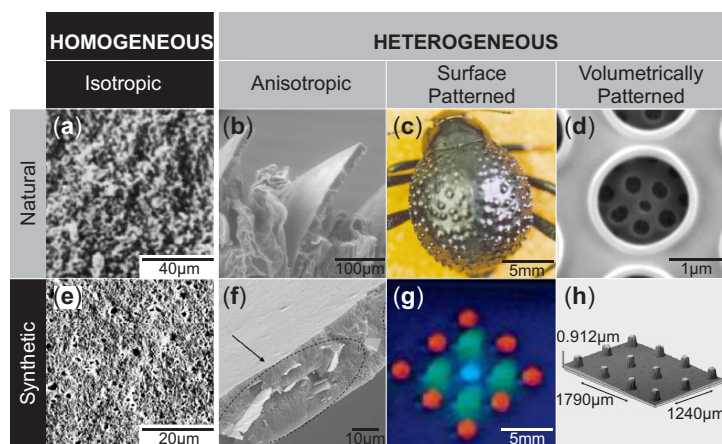


Figure 1. (a) *Mollusk shell*;<sup>2</sup> (b) *abalone shell*;<sup>3</sup> (c) *Namib desert beetle*, bumps indicate hydrophilic chemical patterns (photograph);<sup>4</sup> (d) *cylindrical silica diatom* (ceramic composite);<sup>5</sup> (e) *polypropylene-CaCO<sub>3</sub> nanocomposite*;<sup>6</sup> (f) *poly(vinylidene fluoride)-graphite nanocomposite*;<sup>7</sup> (g) *hydrophobic-hydrophilic patterned nanocomposite*, with hydrophilic areas containing red, green, and blue dye solutions (photograph);<sup>8</sup> (h) profilometer image of a three-dimensional patterned *poly(vinyl alcohol)-CdTe nanocomposite*.<sup>9</sup> All images are micrographs unless otherwise stated. All images reproduced with permission from the respective publishers (citations included in text).

## 1.2 Approaches to Nanotechnology

Approaches to synthesizing nanomaterials on an individual basis are as diverse as the field itself; however, from a high-level perspective the approaches can generally be classified as follows: top-down, bottom-up, or mixed. Top-down refers to a progressive reduction (*e.g.*, milling) of dimensions—without atomic-level control—through externally controlled tools (*e.g.*,

---

<sup>2</sup>Reproduced with kind permission from Springer Science and Business Media, *Experimental Mechanics*, 42, 2002, 395–403, Rigid biological composite materials: Structural examples for biomimetic design, G. Mayer and M. Sarikaya, Figure 2e, Copyright 2002.

<sup>3</sup>Reprinted from *Materials Science & Engineering A: Structural Materials: Properties, Microstructure and Processing*, 390, A. Lin and M. A. Meyers, Growth and structure in abalone shell, 27–41, Copyright 2005, with permission from Elsevier.

<sup>4</sup>Reprinted by permission from Macmillan Publishers Ltd: *Nature*, A. R. Parker and C. R. Lawrence, Water capture by a desert beetle, 414, 33–34, Copyright 2001.

<sup>5</sup>Reprinted from *Progress In Materials Science*, 53, M. A. Meyers, P.-Y. Chen, A. Y.-M. Lin, and Y. Seki, Biological materials: Structure and mechanical properties, 1–206, Copyright 2008, with permission from Elsevier.

<sup>6</sup>Reprinted from *Polymer*, 43, C. M. Chan, J. S. Wu, J. X. Li, and Y. K. Cheung, Polypropylene/calcium carbonate nanocomposites, 2981–2992, Copyright 2002, with permission from Elsevier.

<sup>7</sup>Reprinted from *Advanced Materials*, 21, F. He, S. Lau, H. L. Chan, and J. Fan, High dielectric permittivity and low percolation threshold in nanocomposites based on poly(vinylidene fluoride) and exfoliated graphite nanoplates, 710–715, Copyright 2009, with permission from John Wiley and Sons.

<sup>8</sup>Reprinted (adapted) with permission from *Nano Letters*, 6, L. Zhai, M. C. Berg, F. C. Cebeci, Y. Kim, J. M. Milwid, M. F. Rubner, and R. E. Cohen, Patterned superhydrophobic surfaces: Toward a synthetic mimic of the Namib Desert beetle, 1213–1217. Copyright 2006 American Chemical Society.

<sup>9</sup>Reprinted from *Advanced Functional Materials*, 17, E. Tekin, P. J. Smith, S. Hoeppener, A. M. J. van den Berg, A. S. Susha, A. L. Rogach, J. Feldmann, and U. S. Schubert, Inkjet printing of luminescent CdTe nanocrystal-polymer composites, 23–28, Copyright 2007, with permission from John Wiley and Sons.

photolithography, inkjet printing) while bottom-up refers to a molecule by molecule building process and relies on chemical assembly by the principles of molecular recognition (*i.e.*, self-assembly) (26; 27; 28). The mixed approach involves elements of both top-down and bottom-up (*i.e.*, soft lithography) (29; 30). All three are suitable approaches to generation of nanomaterials, with each approach having its own advantages and disadvantages. In general, all three approaches are utilized to create a very important class of nanomaterials: the *nanocomposite*.

### 1.3 Nanocomposites: Background and Motivation

Nanocomposites can be generally defined as a multiphase material where at least one constituent phase has one, two, or three dimensions  $< 100$  nm (31). In its broadest sense, this definition can be taken to include colloids and copolymers; however, it is generally taken to mean a solid bulk matrix phase that contains a nanoscale dimensional phase, which causes the properties to differ markedly from that of the bulk due to dissimilarities in structure and chemistry. Even with this restriction of scope, the diversity of nanocomposites is wide, and for the purpose of clarity, we restrict our discussion to *polymer-based* and *polymer-filled nanocomposites*. These classes of nanocomposites can be subdivided to either *homogeneous* or *heterogeneous*; heterogeneous nanocomposites generally have an added degree of complexity as compared with their homogeneous counterparts.

Figure 1 presents examples of homogeneous and heterogeneous nanocomposites in natural and synthetic form. In general, homogeneous nanocomposites are isotropic, meaning that their material properties are independent of orientation. Natural and synthetic examples of isotropic nanocomposites are the homogeneous mollusk shell, based upon calcium carbonate (Figure 1a,

(32)), and the polypropylene- $\text{CaCO}_3$  nanocomposite (Figure 1e, (33)), respectively. Heterogeneous polymer-based and polymer filled nanocomposites can be further subdivided into many categories, but we restrict our discussion to only three for clarity: *anisotropic*, *surface patterned*, and *volumetrically patterned*.

### 1.3.1 Anisotropic

*Anisotropic* nanocomposites have material properties which are directionally dependent, usually arising from the highly oriented nanoscale (geometric) features within the nanocomposite. As a natural example, Figure 1b presents the image of an abalone shell, which contains crumbled nano-layers (organic material) “sandwiched” in-between oriented mesolayers (rigid) (34). Such orientation provides the shell with rigidity and strength. Figure 1f presents a micrograph of a poly(vinylidene fluoride)-exfoliated graphite nanocomposite cross-section, clearly showing the oriented nature of the exfoliated graphite (35). In both the cases, oriented nano-platelets give rise to advantageous anisotropic material behavior. For synthetic nanocomposites, this concept has led to the development of electrically percolating polymer nanocomposites based upon highly oriented, high-aspect ratio, conductive nanoparticles at ultra-low particle concentrations (25). Low-concentrations of nanoparticles in nanocomposites allow the nanocomposite to maintain more of the advantageous properties associated with its bulk polymer matrix (*i.e.*, durability, transparency, etc.) while introducing additional functionality. Highly oriented, high aspect ratio nanoparticles may also produce nanocomposites where electrical percolation is directionally dependent, allowing one to produce highly sophisticated, next generation terahertz (THz) devices (36).

### 1.3.2 Surface Patterned

*Surface patterned* nanocomposites utilize chemical patterning to either: 1) alter their final formation (*e.g.*, pattern); or 2) to impart site-selective self-assembly behavior. Originally, chemical patterning was used to deposit resists which acted to protect underlying precious metal nanomaterials during wet etching. In the case of soft lithography, resists were comprised of self-assembled monolayers (SAMs; ~2-3 nm thick) (37). For gold patterning, hexadecanethiol SAMs were deposited by a poly(dimethylsiloxane) (PMDS) stamp onto gold foils; subsequently, hexadecanethiol was chemically converted to hexadecanethiolate and played the role of resist during wet etching (30). Then, surface patterned nanocomposites were used to generate sophisticated wettability patterned surfaces which performed phase management of liquids (*e.g.*, water, methanol) for important heat transfer processes (pool boiling, condensation) (38; 39). More recently, such wettability patterning—hydrophilic spots on a hydrophobic background—has even been shown to be useful for improving the behavior of golf balls (*i.e.*, Surlyn<sup>®</sup> resins; a well studied matrix for nanocomposites (40)) under wet playing conditions; moisture is attracted to the hydrophilic domains while leaving the hydrophobic region dry so that the friction between the golf club head and the golf ball surface (a desirable feature) is not reduced (41)! Figure 1c presents a natural example of a surface patterned composite, the Namib desert beetle, which has regular domains of hydrophilicity patterned on a hydrophobic composite wing (*i.e.*, wettability patterned), enabling it to perform so-called fog capture—a site-selective process—and survive in an extremely arid, desert environment (42). A synthetic example of the surface patterned nanocomposite is presented in Figure 1g, which bears the same wetting properties



as the Namib desert beetle (*i.e.*, wettability patterned), and represents an excellent example of biomimicry (43). Chemical patterning of the synthetic hydrophobic nanocomposite is achieved by selectively depositing solution processed polyelectrolytes directly onto its surface (43). What results is regular surface domains of hydrophilicity—as a result of polyelectrolyte deposition—on a hydrophobic background, mimicking the fog capture behavior of the Namib desert beetle (43). Beyond fog capture, such surface patterned nanocomposites have found promising applications in diverse fields, such as surface microfluidics (*i.e.*, lab-on-a-chip, lab-on-paper; (44; 45; 46)), multiphase heat transfer (*i.e.*, pool boiling, condensation, (47; 38; 48)), and droplet impact (*i.e.*, printing, bio-chips; (49; 50)). In some areas—like soft-lithography—this research area can be considered mature; however, in areas such as multiphase heat transfer, it can be considered young and rapidly evolving.

### 1.3.3 Volumetrically Patterned

*Volumetrically patterned* nanocomposites have geometric order/structure in one, two, or three dimensions extending beyond crystal or chemical structure. Figure 1d presents a natural example of such nanocomposites, the cylindrical silica diatom (51), where biological self-assembly processes are responsible for the formation of regular cylindrical features based upon silica. Figure 1h presents a synthetic example of a volumetrically patterned nanocomposite—based upon poly(vinyl alcohol) and CdTe—which was formed by three-dimensional inkjet patterning (52). From a biological standpoint, extremely complex structures can be achieved due to Nature’s well developed self-assembly processes. From a synthetic standpoint, self-assembly techniques (bottom-up) can be developed and implemented in order to achieve nanocomposites

of comparable complexity; however, top-down techniques such as three-dimensional printing (53) have also demonstrated excellent resolution and capabilities. Examples of volumetrically patterned nanocomposites—not considering those found in Nature—are quite numerous, and many represent the most advanced technologies afforded by nanotechnology today. One example is three dimensional printing of micro-, submicro-, and nano-wires for applications as high performance micro-solenoids (inductors) and plasmonic nanoantennas (54; 53; 55). Nanoimprint lithography has demonstrated the ability to print color images at the highest physical resolution possible—~100,000 dots per inch (DPI)—for applications in security, steganography, nanoscale optical filters, and high-density spectrally encoded optical data storage (56). Electrospinning has demonstrated the ability to form polymer-DNA composites capable of allowing individual strains of DNA to be analyzed, opening up possibilities for novel sequencing techniques and mechanical characterization of DNA molecules (57).

#### **1.3.4 Wettability: Considerations of Super-hygrophobic/-hygrophilic Surfaces**

While nanocomposites have facilitated many new areas of research, they have also reinvigorated several long-existing ones, owing to the degree of sophistication (*e.g.*, patterns, structures) with which nanocomposites can presently be generated, making possible studies which were previously thought unrealizable. One research area in particular which has seen a type of resurgence as a result of nanotechnological developments is the study of wettability, especially on surfaces with extreme wettability properties (*i.e.*, liquid repellency). The study of wettability is a classical field which is mainly concerned with the behavior of solid-liquid-vapor interactions (58). It finds its roots in the pioneering work of Thomas Young (59), yet it still has great practical

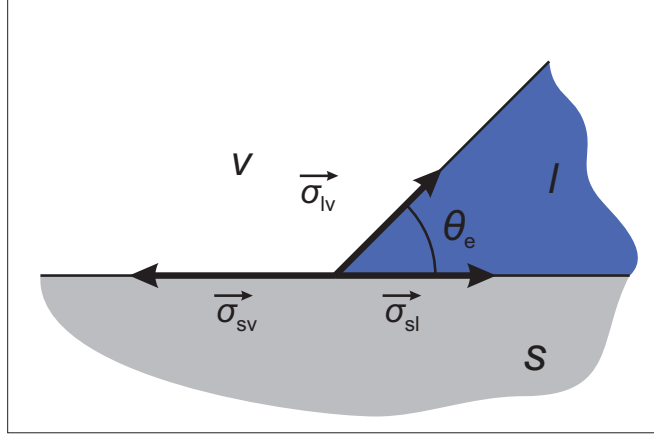


Figure 2. Schematic of the equilibrium contact angle ( $\theta_e$ ) determined via forces.

importance today in the fields of ink-jet printing (60; 61; 62), microscale printing (63), coatings (64), textiles (65), and the study of self-assembly (*i.e.*, dissipative structures) (66; 67).

When a liquid drop is placed on a smooth, untextured surface, one of two things can occur: 1) The drop can spread completely (total wetting) or 2) the drop can form a spherical cap and the contact line remains static (partial wetting). The parameter that distinguishes the two wetting states is referred to as the *spreading parameter*,  $S$ , and is defined as

$$S = [E_s]_{\text{dry}} - [E_s]_{\text{wet}} = \sigma_{sv} - (\sigma_{sl} + \sigma_{lv}), \quad (1.1)$$

where the coefficients  $\sigma$  represent the surface tensions at the solid/vapor ( $\sigma_{sv}$ ), solid/liquid ( $\sigma_{sl}$ ), and liquid/vapor ( $\sigma_{lv}$ ) interfaces, respectively (68). In fact, it is the sign of  $S$  that predicts the

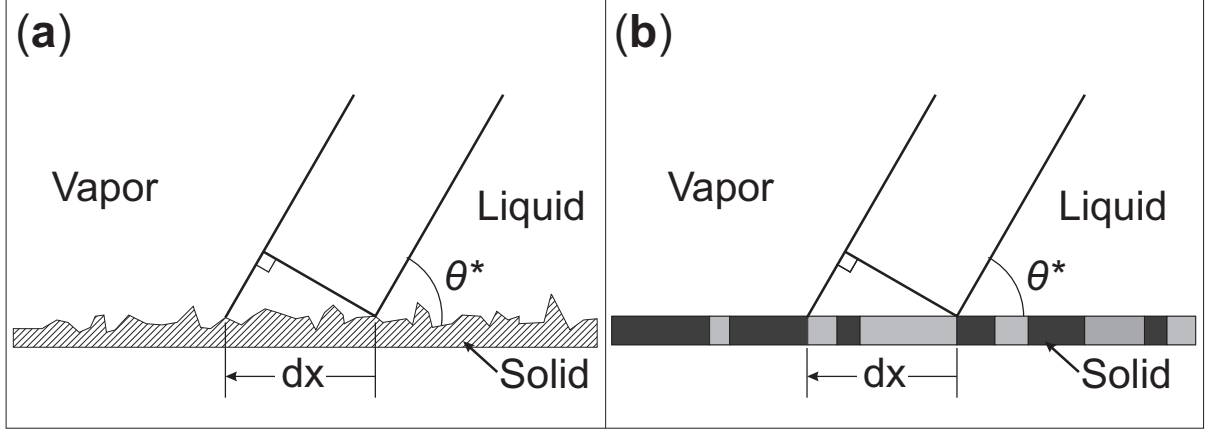


Figure 3. Liquid droplet edge undergoing a small displacement ( $dx$ ) on a (a) textured but homogeneous, and (b) chemically heterogeneous surface.

wetting behavior;  $S > 0$  predicts total wetting and  $S < 0$  predicts partial wetting (68). For the case of  $S < 0$ , the liquid drop will form a dome-like shape on the substrate with a finite equilibrium contact angle,  $\theta_e$ . By summing the forces acting on the line of contact (triple line) and setting them equal to zero and projecting the equilibrium forces onto the solid plane, one obtains Young's relation (59) and the definition of  $\theta_e$

$$\sigma_{lv} \cos \theta_e = \sigma_{sv} - \sigma_{sl}. \quad (1.2)$$

This previous analysis applies for atomically smooth and chemically homogeneous surfaces; however, many of the surfaces of practical importance have surface roughness or are chemically heterogeneous, making analysis more complicated.

Two standard models exist to describe the wetting behavior of a partially wetting drop on a textured or chemically heterogeneous surface. The former case received treatment by Wenzel (69) and is depicted in Figure 3a. The basic assumption is that the local contact angle is given by Equation 1.2, and the goal is to find the apparent contact angle  $\theta^*$  on a rough, chemically homogeneous surface.  $\theta^*$  can be found from an energy consideration. By taking a small displacement  $dx$  of the contact line parallel to the surface, the surface energies change by  $dE$  as,  $dE = R(\sigma_{sl} - \sigma_{sv}) dx + \sigma_{lv} dx \cos \theta^*$ , where  $R$  ( $R > 1$ ) is the ratio of true surface area to apparent surface area, and substituting into Equation 1.2 leads to Wenzel's equation

$$\cos \theta^* = R \cos \theta_e. \quad (1.3)$$

Equation 1.3 states that surface roughness always magnifies the wetting properties of the surface, *e.g.*, hydrophobic surfaces become more hydrophobic. The theory for the wetting behavior of a partially wetting droplet on a planar chemically heterogeneous surfaces was first treated by Cassie and Baxter (70) and is depicted in Figure 3b. The assumptions are: 1) the surface is made of two species, each with their own intrinsic contact angle  $\theta_1$  and  $\theta_2$  and fractional surface area  $f_1$  and  $f_2$  ( $f_1 + f_2 = 1$ ), respectively. The goal is to find  $\theta^*$ . The energy change associated with a small displacement of the contact line can be defined as,  $dE = f_1(\sigma_{sl} - \sigma_{sv})_1 dx + f_2(\sigma_{sl} - \sigma_{sv})_2 dx + \sigma_{lv} dx \cos \theta^*$ , where the indices 1 and 2 represent the species wet during the displacement of the contact line, and solving for the minimum energy state of this differential and substituting Equation 1.2 leads to the Cassie-Baxter equation

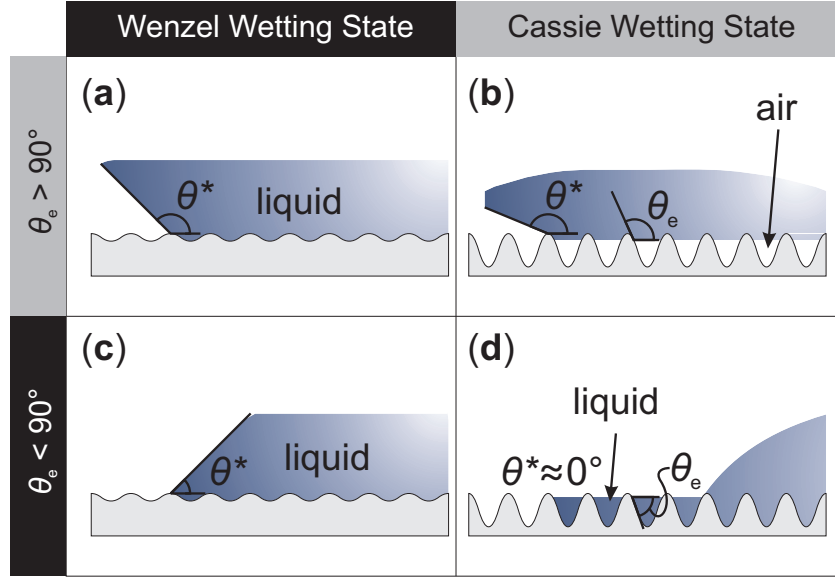


Figure 4. Ideal solid surfaces with sinusoidal texture profiles. (a)-(b) Hydrophobic surface ( $\theta_e > 90^\circ$ ), (c)-(d) hydrophilic surface ( $\theta_e < 90^\circ$ ). (a) & (c) and (b) & (d) are in Wenzel and Cassie wetting states, respectively.

$$\cos \theta^* = f_1 \cos \theta_1 + f_2 \cos \theta_2. \quad (1.4)$$

Equation 1.4 states that the cosine of the apparent contact angle,  $\theta^*$ , is given by a weighted average of the cosines of the constituent equilibrium contact angle values.

From Equation 1.3, it is valid to suppose that for a hydrophobic surface ( $\theta_e > 90^\circ$ ), increasing  $R$  should lead to  $\theta^* = 180^\circ$ ; however, the situation is more complicated than that for highly

textured surfaces, and Equation 1.3 is only valid for mildly textured surfaces. In fact, with the proper amount and type of surface texture entrainment of air between a liquid droplet and the solid hydrophobic surface can become thermodynamically favorable resulting in  $\theta^* \rightarrow 180^\circ$  (71; 72). This case is depicted schematically by Figure 4, where increasing the amplitude and holding the frequency constant of the sinusoidal surface texture from **a** to **b** results in the entrapment of air in **b**, and results in the so-called *fakir droplet* (73). The droplet is also said to be in a Cassie wetting state (chemically heterogeneous)—even though the solid surface is chemically homogeneous—because it is resting on a composite surface of solid and air. In this special case, Equation 1.4 can be rewritten as,

$$\cos \theta^* = -1 + \Phi_{sl} (\cos \theta_e + 1), \quad (1.5)$$

where  $\Phi_{sl}$  is the solid/liquid fractional area ( $\Phi_{sl} < 1$ ). When a liquid droplet resides on a textured surface in a Cassie wetting state, it is possible for  $\theta^* > 150^\circ$ , and when it does, the surface is deemed superhydrophobic. For the case of water, the surface is called *superhydrophobic*. From thermodynamic arguments, one can show that such a situation is energetically favorable if  $\theta_e$  satisfies the following inequality,

$$\theta_e > \theta_c \text{ with } \cos \theta_c = -\frac{1 - \Phi_{sl}}{R - \Phi_{sl}}, \quad (1.6)$$

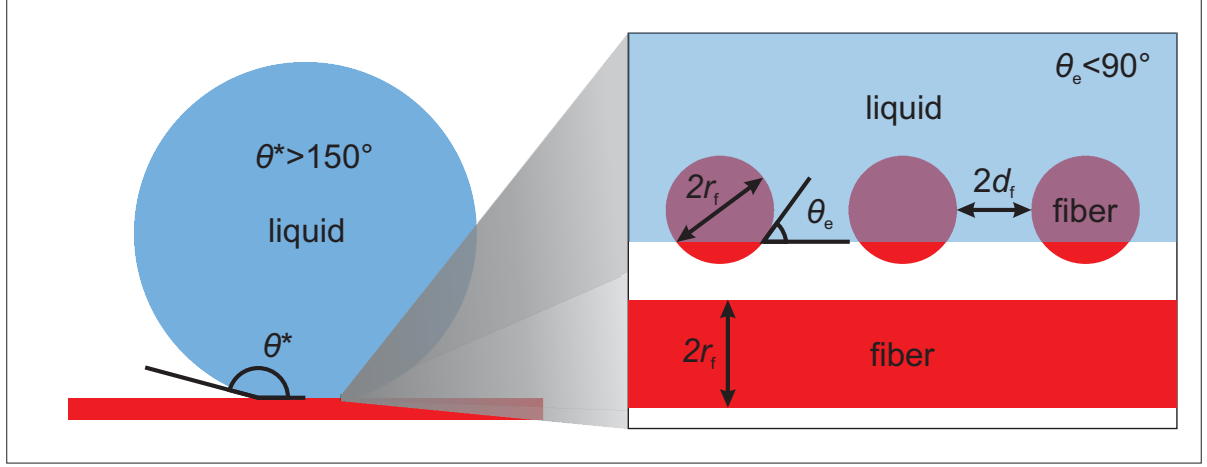


Figure 5. Schematic depicting a liquid drop in a superhydrophobic state ( $\theta^* > 150^\circ$ ) on a re-entrant, fibrous, wettable ( $\theta_e < 90^\circ$ ) substrate. Fibers have a radius  $r_f$  and an interspacing value of  $2d_f$ .

where  $\theta_c$  is the critical contact angle and  $\Phi_{sl}$  is the relative area fraction of solid surface underneath the liquid drop.

In the reverse case, we see from Equation 1.3 that if  $\theta_e < 90^\circ$ , as  $R$  increases, then  $\theta^* \rightarrow 0^\circ$ ; however, as with the prior case, the validity of Wenzel's equation is restricted. Increasing  $R$  for specific types of surface texture can lead to this super-wetting state ( $\theta^* = 0^\circ$ ; superhydrophilic). One such process is depicted in Figure 4, where increasing the amplitude of the sinusoidal surface texture (constant frequency) for a hydrophilic surface ( $\theta_e < 90^\circ$ ) results in a wetting transition from **c** (Wenzel) to **d** (Cassie), and such a situation is referred to as a penetrating film, since “islands” of the coating still rise above the absorbed liquid (58). It is a Cassie wetting



state because the droplet is resting on a composite solid/liquid surface. From thermodynamic arguments, one can show that such a situation is energetically favorable if  $\theta_e$  satisfies the following inequality

$$\theta_e < \theta_c \text{ with } \cos \theta_c = \frac{1 - \Phi_{sl}}{R - \Phi_{sl}}, \quad (1.7)$$

where  $\Phi_{sl}$  is the relative area fraction of solid surface underneath the liquid drop. In the case of water, a surface that has  $\theta^* = 0^\circ$  is referred to as superhydrophilic.

Superhydrophobic surfaces are usually (not always, see *rose petal effect*, (74)) characterized by low-solid/liquid adhesion and low droplet *sliding angles* ( $\alpha$ )—the tilt angle required by the substrate to induce droplet sliding—due to the relatively small value for  $\Phi_{sl}$  (for superhydrophobic surfaces,  $\Phi_{sl} \approx 0.05$ ). For a given liquid, if  $\alpha < 10^\circ$ , the surface is said to be *self-cleaning* to that liquid, provided that gravitational effects are negligible. The importance of the force of gravity can be quantified by the Bond number (dimensionless), which is the ratio of body (*e.g.*, gravity) to surface tension forces, and is defined as

$$\text{Bo} = \frac{\rho g r_d^2}{\sigma_{lv}}, \quad (1.8)$$

where  $\rho$  is the density of the fluid (or density difference between fluids),  $g$  is the acceleration due to gravity, and  $r_d$  is the radius of the liquid droplet.  $\text{Bo} < 1$  is a sufficient requirement for surface tension to be the dominate force. The sliding angle ( $\alpha$ ) can be estimated from (75; 76)

$$\sin \alpha = \frac{2r_d \sigma_{lv} (\cos \theta_r^* - \cos \theta_a^*)}{\rho V g}, \quad (1.9)$$

where  $\theta_a^*$  and  $\theta_r^*$  are the apparent advancing and receding contact angle values,  $\rho$  is the density of the liquid droplet, and  $V$  is the volume of the liquid droplet (see (58) for an overview of  $\theta_a^*$  and  $\theta_r^*$ ). From this analysis we see that droplet mobility is dependent not on a high  $\theta^*$  (statistical apparent contact angle) or  $\theta_a^*$ , but rather it depends on the difference between the cosines of  $\theta_r^*$  and  $\theta_a^*$ ; in order to increase droplet mobility, the difference should be minimized (*i.e.*,  $\theta_r^* \approx \theta_a^*$ ). The difference between the two apparent contact angles is defined as ,  $\Delta\theta^* = \theta_a^* - \theta_r^*$ , and the quantity  $\Delta\theta^*$  is called *contact angle hysteresis*.

The above discussion primarily applies to situations at thermodynamic equilibrium; however, many liquid repellent surfaces (*e.g.*, superoleophobic) rely on metastable thermodynamic wetting conditions to repel liquids (*e.g.*, oil). The reason is that no known surface has  $\theta_e > 90^\circ$  for oil, meaning that all untextured surfaces are inherently oleophilic; however, *reentrant surface texture* is capable of rendering an oleophilic surface superoleophobic (metastable) (77; 78). Figure 5 presents an image of a liquid droplet in a metastable superhydrophobic wetting state. It also shows the contact line behavior and how  $\theta_e < 90^\circ$  is satisfied locally while still being able to have  $\theta^* > 150^\circ$ .

It should also be mentioned that for drops to be in low-adhesion Cassie states—like the one depicted in Figure 4b—the surfaces need not promote the entrainment of air. In fact, if instead of air, the surface is impregnated with a non-miscible lubricant, then drops placed on the surface can display a high degree of droplet mobility even under extreme pressures (68

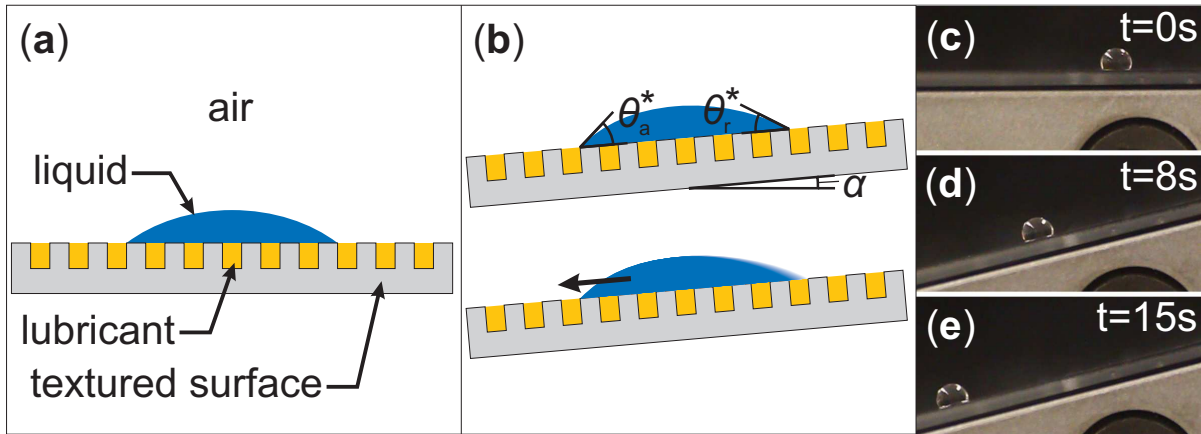


Figure 6. (a) Schematic of a lubricant impregnated surface with a liquid droplet partially wetting it. (b) Such surfaces display extremely low values for  $\Delta\theta$ , enabling them to have low droplet sliding angles  $\alpha$  without high  $\theta_a^*$  values. (c)-(d) Show the sliding dynamics of a water droplet on a tilted lubricant-impregnated surface which is comprised of a carbon nanofiber-fluoroacrylic copolymer composite suffused with Krytox lubricant (unpublished).

MPa) and condensation conditions (79; 80; 81). Figure 6a shows a schematic of a lubricant impregnated surface. Even though the  $\theta_a^*$  for a liquid droplet on a lubricated surface is much less than that on a traditional superhydrophobic surface, its contact angle hysteresis is still quite small ( $\Delta\theta \approx 2^\circ$  for  $\sigma_{lv} = 18 - 72 \text{ mN m}^{-1}$ , (80)), enabling a high degree of droplet mobility. This wetting behavior is depicted schematically in Figure 6b and experimentally in Figure 6c-e.

## 1.4 Thesis Objective

The primary objective of this thesis is to present fundamental investigations into design, synthesis, and characterization of large-area, technologically relevant nano-structured composites with a bias towards application in advanced fluid management technologies. With this objective, the following research topics were considered:

### 1.4.1 Environmentally Benign Superhydrophobic Coatings

- Design and generate a water-based dispersion consisting of hydrophobic polymer(s) and particle(s) in order to eliminate the use of volatile organic compounds in synthesis of superhydrophobic nanocomposites;
- optimize the polymer and particle type as well as concentrations so that when they are deposited by spray processing they form a superhydrophobic coating;
- demonstrate multi-functionality (*e.g.*, electrical conductivity) so that said water-based dispersion may find broader applications;
- highlight the nuances of spray processing of water-based dispersions and how it compares with spraying organic solvent-based dispersions.

### 1.4.2 Stretchable Superhydrophobic Composite Coatings

- Design elastomeric superhydrophobic nanocomposites capable of maintaining their liquid repellent property through flexing and uniaxial straining to directly address issues of nanocomposite durability and highlight them for future nanocomposite design;

- identify failure modes of superhydrophobic elastomeric coatings in order to give insight into suitable operating conditions (*e.g.*, strain, substrate) and to aid in future design.

#### 1.4.3 Fluoropolymer Blends: Multifunctional Liquid Repellent Nanocomposites

- Identify two polymers that when blended have the following properties: high adhesion, cohesion, and a high-degree of hydrophobicity;
- develop a rational scheme for blending the said polymers and ensure that the final polymer concentration in solution is high enough to facilitate spray processing (*e.g.*,  $> 1$  wt.%);
- identify the “optimum” nanoparticle type and concentration so that when incorporated into the said polymer blend, the resulting nanocomposite demonstrates liquid repellency to water and lower surface tension liquids, the goal is to minimize nanoparticle concentration to enhance nanocomposite strength and reduce costs associated with synthesis;
- demonstrate the versatility of the dispersion by showing tunable multi-functional properties (*e.g.*, electrical conductivity) of the resulting nanocomposite.

#### 1.4.4 Wettability Engineering: Handling Low Surface Tension Liquids

- Identify a coating system capable of repelling a variety of organic, low-surface tension liquids;
- identify a hydrophilic polymer with well studied wetting behavior to organic solvents (having well-known wetting values will aid in modelling the fluid dynamic behavior) that is capable of being solution-processed and patterned onto said coating in a facile manner;

- identify a suitable patterning technique and polymer concentration to optimize pattern size and behavior;
- demonstrate rapid transport of said liquids in a pumpless manner (meniscus velocities  $\sim 10 \text{ cm s}^{-1}$ );
- demonstrate site-selective wetting behavior of liquids with a wide-range of surface tension values ( $20\text{--}72 \text{ mN m}^{-1}$ );
- identify a suitable model in order to predict fluid dynamic behavior (hemiwicking) and to aid in future design of low-surface tension surface microfluidic systems (such a model will identify theoretical limits to miniaturization);
- show directional sliding behavior of high surface tension liquids, such as water.

#### 1.4.5 Wettability Engineering: Thermal Stability and Scalability

- Identify a polymer/nanoparticle system that is not based upon traditional organic polymers but rather upon silicon chemistry; such a system—if chosen correctly—should have enhanced temperature stability;
- identify suitable concentrations of polymer and nanoparticles in a dispersion for forming a superhydrophobic coating from spray processing;
- identify a suitable technique for transforming said superhydrophobic coating to superhydrophilic in a rapid manner;
- identify a large-area, flexible patterning technique capable of transforming said superhydrophobic coating to superhydrophilic in a well-defined spatial manner;

- identify optimum patterning conditions including maximum patterning speeds;
- identify the physical mechanism responsible for the wettability transition with both wettability transformation techniques;
- demonstrate pumpless transport of water in superhydrophilic channels and measure maximum meniscus velocities.
- demonstrate the temperature stability of the wetting property in unpatterned and patterned regions for potential multi-phase mass transfer applications;
- under boiling conditions, demonstrate site-selective nucleation behavior of water on a superhydrophobic/superhydrophilic patterned coating for potential application in multi-phase mass transfer applications.

#### 1.4.6 Wettability Engineering: Shaping and Mobilizing Liquid $\mu$ -Volumes

- Design and synthesize a nanocomposite capable of repelling liquid droplets impinging at velocities greater than  $3 \text{ m s}^{-1}$ ;
- identify and implement suitable wettability patterning system capable of transforming said nanocomposite to hydrophilic—without altering surface texture—in a spatial manner with a patterning accuracy of  $\sim 100 \text{ }\mu\text{m}$ ;
- characterize droplet impact on superhydrophobic/hydrophilic annular wettability patterns for droplet lens formation applications and complex shaping;
- identify optimum patterning and droplet impact conditions for annular droplet formation—without loss of liquid—for lab-on-a-chip style applications;

- utilize suitable drop impact and thin film rupture models to guide design;
- utilize complex droplet  $\mu$ -volume shapes as a soft (water) template for forming conductive silver patterns for potential applications in terahertz devices;
- develop thermodynamic and fluid mechanical models to aid in rational design of wettability engineered surfaces.

### 1.5 Scope of the Work

As stated previously, approaches to synthesizing nanocomposites can be top-down, bottom-up, or mixed. In all cases, the first step involves a “bulk” additive process (top-down) to form a liquid-repellent coating; however, there may be elements of self-organization due to “slack” interactions (*e.g.*, van der Waals interactions) in polymers, copolymers, or surfactant functionalized nanoparticles. There is no doubt that it is a complicated picture, but we take the coating process to be a top-down process. For wettability patterned coatings, a post processing step is required. In this case, we employ top-down techniques due to their flexibility, accuracy, and ease of use. Therefore, this thesis generally is concerned with the study of dispersions and the fluid-based top-down approaches to synthesize nanocomposites from them. All the nanocomposites studied herein are polymer-based; the choice of nanoparticles was application specific. For instance, the non-fluorinated, water-based dispersion utilized high-aspect ratio, hydrophobic nanoparticles which could be dispersed in water by modifying the pH. The primary concern was water dispersibility. The chosen wettability patterning techniques are nanocomposite specific; therefore, they are also application specific. Chapter 2 focuses on design considerations of



dispersions for producing a superhydrophobic coating from a water-based, non-fluorinated dispersion. Chapters 3 and 4 are primarily concerned with optimizing polymer blends, nanoparticle types, and nanoparticle concentrations for synthesizing highly-durable multi-functional superhydrophobic coatings. Chapters 5, 6, and 7 are primarily concerned with synthesizing and characterizing wettability patterned (engineered) nanocomposites for a variety of applications. Chapter 5 focuses on pumpless transport and handling of low-surface tension liquids. Chapter 6 is concerned with producing a high-temperature stable, wettability patterned surface (superbiphilic) for application in multi-phase mass transfer. Chapter 7 focuses less on nanocomposite synthesis, and more on manipulating droplet impact behavior with wettability patterning for complex droplet formation and lab-on-a-chip style applications. Finally, some conclusions and expected research contributions, as well as recommendations for future research, are given.

## CHAPTER 2

### ENVIRONMENTALLY BENIGN SUPERHYDROPHOBIC COATINGS

This chapter has been submitted for publication in (82). This chapter has a non-provisional patent application in (83).

#### 2.1 Introduction

Spray deposition of polymer composite coatings that contain high-aspect ratio filler particles has been demonstrated as a low-cost, large-area process for modifying the wettability (*e.g.*, superhydrophobicity (84; 85; 86; 87), superoleophobicity (88)), electrical conductivity (87; 88; 89; 90), and EMI shielding (89; 90) properties of a variety of surfaces. The purpose of the filler particles is dual, namely to impart surface texture—a requisite for water repellency—and introduce additional functionality. With regards to liquid repellency, a low-surface energy polymer ( $\sim 20$  mJ/m<sup>2</sup>) must be incorporated into the coating—a general requirement of any liquid repellency treatment—which is conveniently achieved by utilizing fluoropolymers (*e.g.*, fluoroacrylic copolymers, poly(tetrafluoroethylene), etc.). However, concerns over the byproducts of fluoropolymer degradation, *e.g.*, long-chain perfluorinated acids (PFAs), which have a documented ability to bioaccumulate (91; 92), as well as the potential adverse effects that PFA maternal concentrations can have on human offspring (93; 94), have led to a shift in the manufacture and usage of fluoropolymers. One common PFA of particular concern is perfluorooctanoic acid (PFOA). In 2006, the EPA introduced its PFOA (perfluorooctanoic acid) Stewardship

Program and invited eight major fluoropolymer and telomer manufacturers to commit to eliminating precursor chemicals that can break down into PFOA; in one case, DuPont introduced so-called short-chain chemistry, whereby the length of perfluorinated chains within polymers are kept below a threshold in order to avoid degradation into PFOA. In other applications, usage of fluoropolymers in products that come in sustained contact with the human body or in disposable items intended for landfilling after consumption must be minimized. For these applications, polymers such as polyolefins (PE) are far more preferable. Where the environment is concerned, hydrophobic polymers intended for application by spray should ideally be water-borne, so as to minimize the usage of harmful volatile organic compounds (VOCs)—a common, non-trivial problem with coatings aiming to achieve superhydrophobicity upon deposition. Water dispersion of hydrophobic polymers could be facilitated by introducing pendant carboxylic acid functional groups that can be charge-stabilized by increasing the pH of the dispersing medium (water) (95; 96); in short, acid functional groups form negative carboxylate ions, thus creating charge repulsion, and ultimately stabilization. Carboxylic acid groups also act to promote adhesion with polar surfaces.

The choice of filler particles is quite restrictive, as the particles should possess a high-aspect ratio, re-entrant characteristics (*i.e.*, high curvatures), low-surface energy, and still be dispersible in water. One such filler is fatty amine salt modified nanoclay (97) (*i.e.*, organoclay), which is highly hydrophobic in its native state, but can be dispersed in water by reducing the pH due to its cationic surfactant functionalization (98). However, for the case of water-based PE dispersions with carboxylic acid functionality or anionic surfactants (emulsifiers), the dis-

persions are of a basic character rendering cationic surfactant modified fillers (*i.e.*, organoclay) not feasible. Another common filler—exfoliated graphite (*e.g.*, graphene, few layer graphene (FLG), or exfoliated graphite nanoplatelet (xGnP))—might be useful due to its ability to form said carboxylic acid groups at the periphery of its basal planes without forming oxygen groups normal to the plane (*i.e.*, not becoming graphene/graphite oxide) by large-area processing (99). Maintaining limited oxygen functionality allows the filler to stay relatively hydrophobic, while still being water-dispersible under proper (high) pH conditions. This is an important point, meaning that no ionic surfactant functionality is required to play the role of dispersant (when in the dispersion) or surface energy reducer (when cast in the coating), as is the case with nanoclays—potentially reducing the fabrication cost. There is also a myriad of other non-high-aspect ratio, hydrophobic fillers that might benefit from a similar approach (*e.g.*, hydrophobic fumed silica); however this is out of the scope of the present study.

Approaches to utilizing graphene/graphite in superhydrophobic applications are reported in the literature and a few will be briefly discussed here to demonstrate applicability. In a recent report (100), a dispersion consisting of colloidal graphite and polytetrafluoroethylene was spray cast and sintered to form the basis for a conductive, thermally stable, water-repellent coating. Other approaches to utilizing graphite—or its exfoliated form, graphene—to form superhydrophobic films have included aerogels (101), poly(vinylidene fluoride) composites (102), and Nafion blends (103). Graphene oxide films can also be superhydrophobic when modified by octadecylamine; however, this is not suitable for our application for the same reason organoclays cannot being used (104). Work regarding wettability tuning for graphene films to water has been

done, but it relies on chemisorption of acetone to defects in graphene reduced from graphene-oxide as its mechanism (105). In all of these studies, none of the systems were water-based, and some contained some type of fluoropolymer, which makes them not environmentally friendly or benign.

Approaches to non-fluorinated superhydrophobic coating treatments are numerous; however, from a water repellency standpoint they are not ideal. The surface tensions of typical end bonds in organic hydrophobic coating treatments are ranked from highest to lowest as  $-\text{CH}_2 > -\text{CH}_3 > -\text{CF}_2 > -\text{CF}_2\text{H} > -\text{CF}_3$ , with fluorine-containing bonds having the lowest surface tension (106). Replacing  $-\text{CF}_3$  with  $-\text{CH}_3$  chemistries introduces more stringent requirements (*e.g.*, more roughness) when designing coating surface texture, if superhydrophobicity is the goal. Holtzinger et al. provided a description of available methods of fluorine-free superhydrophobic coating treatments as well as their intricacies (107). Achieving a superhydrophobic coating with non-fluorine chemistry is relatively simple though when compared with developing water-based superhydrophobic coating treatments.

Very few works have been reported on water-based superhydrophobic coating treatments from spray, and even fewer have been fluorine-free. Reports on hydrophobic coatings from water-based dispersions have been around for some time (108); however, interest in superhydrophobic coating treatments from all-aqueous dispersions is a relatively recent research endeavor. As one example, a recent patent application claims a superhydrophobic coating realized by spray deposition of an all-aqueous dispersion consisting of a fluoroacrylic copolymer, bentonite nanoclay, and water (98). So while water-based superhydrophobic coating systems

are few, fluorine-free versions are even more scarce. Researchers have looked into the use of rare earth metals—of which some are known to be hydrophobic—in an all-aqueous sol-gel process to achieve hydrophobic coatings (*e.g.*, lanthanum) (109); however, these coatings were not superhydrophobic and their use—as their name implies—may be cost prohibitive and therefore limited in terms of industrial scalability.

We report herein—for the first time—an approach to produce an all-water-based, non-fluorinated superhydrophobic surface treatment from a sprayable PE-xGnP dispersion. Hydrophobic components are stabilized in water by their acid functional groups via increased pH. Such an approach to water-repellent coatings is expected to find wide application within consumer products aiming to achieve simple, low-cost, large-area, environmentally benign superhydrophobic treatments. It is emphasized that xGnP is employed due to its ability to be simply modified by carboxylic acid chemistry, but that any hydrophobic, high-aspect ratio filler with similar chemistry can also be used. As one possibility, one can modify nanoclay by an anionic surfactant and follow the same procedures listed here for processing of xGnP to achieve similar results.

## **2.2 Experimental**

### **2.2.1 Materials**

Exfoliated graphite nano-platelets (xGnP<sup>®</sup> Brand Nanoplatelets; Grade C 300) were obtained from XG Sciences (average particle thickness  $\sim 2$  nm, average particle diameter  $< 2$   $\mu\text{m}$ , surface area  $300\text{ m}^2\text{ g}^{-1}$ ). Polyethylene-acrylic acid copolymer (PE) dispersion in water (42

wt.%) was obtained from DOW Chemical (96). Ammonium hydroxide (29%) was obtained from Fisher Scientific and formic acid (97%) was obtained from Alfa-Aesar.

### **2.2.2 Procedure**

The procedure began by first combining the ammonium hydroxide and xGnP in a 20 mL vial (refer to Table I for specific concentrations). The mixture was placed in a sonication bath (output power 70 W; frequency 42 kHz; Cole-Parmer, Model# 08895-04) for several minutes until a paste was formed. Next, water was added to the mixture and probe sonication (750 W, 13 mm probe dia., 20 % amplitude, 20 kHz frequency, Sonics & Materials, Inc.) was performed for several minutes. Once stabilized, the PE dispersion (42 wt.% in water) was added to the xGnP-NH<sub>3</sub>(aq)-H<sub>2</sub>O mixture and was bath sonicated for 60 min or until stable. It should be noted that a high quality dispersion can also be achieved by adding the PE dispersion to the xGnP-NH<sub>3</sub>(aq)-H<sub>2</sub>O suspension while under intense mechanical mixing with a stir bar (> 1200 RPM; StableTemp<sup>®</sup> Ceramic Hot Plate). In this approach, for a 20 mL vial, it is important to keep the mass of the dispersion ~10 g so as to maximize the intensity of mixing. Once a stable dispersion is produced, it is spray deposited (Paasche VLS, siphon feed, 0.73 mm nozzle) onto either glass slides, paper, or aluminum foil and dried at 80 °C in an oven for 1 hr. In order to form high quality coatings, it is necessary to heat the substrates while they are being coated in order to avoid excess water from collecting on the surface—a problem not typically encountered for VOCs, such as acetone. In our application, we utilized a heat gun (Proheat<sup>®</sup> Varitemp<sup>®</sup> PH-1200, 1300 W max) to heat the substrate from a distance of ~10-20 cm.

TABLE I

EXAMPLE OF DISPERSIONS USED FOR CREATING PE-XGNP COMPOSITE  
COATINGS.

ingredient	concentration (wt.%)
PE	2.8
xGnP	0.8-10.0
NH <sub>3</sub> (aq) (29%)	6.7
water	89.7–80.5

### 2.2.3 Characterization

Wettability characterization of the spray deposited coating was done by measuring advancing and receding contact angle values by the sessile drop method, whereby 5-10  $\mu\text{L}$  volumes of water were dispensed (advancing measurement) and removed (receding measurement) through a flat tipped needle. Contact angle measurements were made with images captured with a high-speed, backlit image acquisition setup (Redlake MotionPro). A new spot was used on the substrate for each individual measurement. Morphological characterization of the spray deposited coatings was done with a Hitachi S-3000N Scanning Electron Microscope (SEM) after the samples were coated with a 4 nm layer of Pt/Pd. Characterization of the particle filler xGnP was done with a JEOL JEM-3010 Transmission Electron Microscope (TEM) to deter-



mine the degree of xGnP exfoliation. According to the manufacturer, xGnP is in granular form and requires mechanical agitation to become exfoliated. For TEM preparation, xGnP (0.013 g) was added to formic acid (10.0 g) in a 20 mL vial. The suspension was probe sonicated (13 mm probe; 20% amplitude; 1.0 kJ energy delivered to probe), mechanically mixed at room temperature for 10 min, and bath sonicated for 30 min; the suspension was then added dropwise onto a holey carbon grid for subsequent TEM analysis. Figure 7 presents a side-view image of a typical xGnP platelet demonstrating adequate exfoliation (~10 layers of graphene). The xGnP filler comes with a variety of oxygen containing functional groups at the edges of the platelet as a result of the exfoliation process—according to the manufacturer—which include carboxyl, lactone, pyrone, hydroxyl, and carbonyl. The weight concentration of oxygen generally increases with the degree of platelet exfoliation—and for the type of xGnP used in this study—the concentration is around 2 wt.% as stated by the manufacturer.

### **2.3 Results and Discussion**

In general, for commercial applications of paint or coating treatments, the stability of the dispersion is an extremely important property, and in the case of this study, the pH of the overall dispersion is most critical. Figure 8 presents images of three side-by-side 15 mL vials, all containing water and PE. The difference between the contents of the three vials is in their pH values. The dispersion in vial 1 is slightly basic, vial 2 basic, and vial 3 acidic; note how vial 3 is phase separated. The PE utilized in this study has acrylic acid functionality—a so-called acid functional group—which allows it to become water dispersible under basic conditions, and stay dispersed even at elevated pH values. In the case of vial 3, the addition of acetic acid

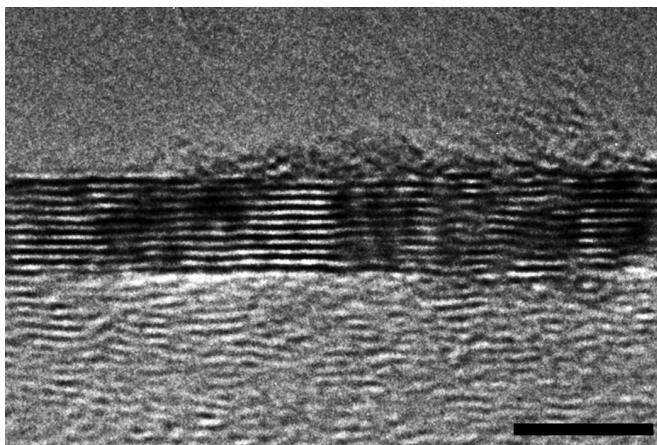


Figure 7. High magnification TEM image of an xGnP platelet demonstrating a platelet thickness below 5 nm. Scale bar is 5 nm.

no longer allows the acrylic acid groups to retain their charge, in turn phase separating the solution.

Figure 9(a) presents an image of a suspension formed by xGnP (hydrophobic) in water. Since these particles are inherently hydrophobic, their apparent stabilization in water without the aid of dispersants is likely due to electrostatic repulsion (*i.e.*, ionization of acid functional groups). Figure 9(b) presents an image of an xGnP-water suspension containing an electrolyte, which acts to suppress the electrical double layer over the particles and destabilize the suspension; this is a characteristic property of lyophobic colloids stabilized by electrostatic repulsion, in accordance with Derjaguin-Landau-Verwey-Overbeek (DLVO) theory (110). Figure 9(c) presents an image of the suspension undergoing laser irradiation (simple laser pointer) perpendicular to the point-



Figure 8. 15 mL vials all containing 0.12 g of polyethylene copolymer in 10 g of water. Vial 2 also contains  $\sim 1$  g of ammonium hydroxide, while vial 3 also contains 1.6 g of acetic acid.

Note the phase separation in vial 3 as a result of acidification.

of-view; note the light scattering, which is characteristic trait of a fine, well dispersed suspension supporting the colloidal nature of the xGnP-water suspension. In fine suspensions, such a scattering effect is observed for shorter wavelengths of light (*i.e.*, blue) and is commonly referred to as the Tyndall effect—another indicator of a fine suspension—whereby longer wavelengths are scattered less strongly while passing through the suspension while shorter wavelengths of light are scattered more intensely, giving the appearance of a blue color.

Figure 10 presents a sequence of images of the PE-xGnP dispersion after each major processing step (*i.e.*, probe sonication of xGnP-water suspension, addition of PE, bath sonication of the final dispersion); *ceteris paribus*, the pH of the individual dispersions increases from vial-

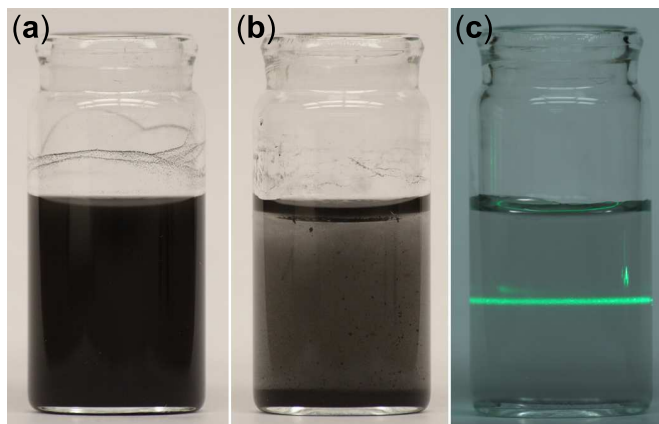


Figure 9. Suspensions of 0.1 wt.% xGnP in water with (a) no electrolyte, and (b) electrolyte (0.1 wt.% NaCl). (c) Scattering effect demonstrated on a diluted (0.002 wt.%) xGnP-water suspension.

to-vial, according to their location from left to right (*i.e.*, the left vial has the lowest pH, the right vial has the highest pH). Figure 10a presents three xGnP-water suspensions after probe sonication (first processing step). Based on visual observation, the stability of the dispersions did not appear to vary significantly from neutral to basic conditions. According to a previous report of water suspensions containing carboxylic-acid functionalized graphene (110), increasing the pH of the suspension only acts to increase the stability of the suspension, with the zeta potential increasing from -30 mV for pH  $\sim$ 6.1 to -43 mV for pH  $\sim$ 10. Since the xGnP-water suspension is to be stabilized by a similar mechanism, the outcome that no change in colloidal behavior is observed for increased pH is thus expected. Figure 10b shows the same three vials after the addition of the PE solution. In all cases, the xGnP aggregates to produce an unstable

dispersion that requires the third processing step: bath sonication. The dispersions (in vials) after that final processing step are depicted in Figure 10c; the left vial (dispersion pH  $\sim 7$ ) is unstable, while the middle and right vials (pH  $> 7$ ) are stable. It appears that in the case of vial 1, the xGnP undergoes irreversible aggregation due to the addition of PE. Aggregation of exfoliated graphite in water is a frequent problem encountered when reducing graphene oxide to graphene in water with hydrazine, due to the hydrophobicity of graphene (110; 111). This problem can be addressed by controlling the pH of the suspension in order to utilize non-reactive edge functional groups (*e.g.*, carboxylic acid) to charge stabilize the suspensions (110). The energy required to exfoliate—or in this case re-disperse—graphite can become quite high owing to the extremely large surface area required to separate as well as the strong Van der Waals interactions between adjacent platelets (110). Regarding the stability of xGnP in aqueous solutions, previous work (described above) has shown that aqueous suspensions of graphene oxide and chemically converted graphene have zeta potentials  $< -30$  mV (stable) for pH values ranging from 7 to 11—decreasing pH results in a lower magnitude of zeta potential and hence the dispersion is less stable (110). We hypothesize that the increased pH allows for charging of edge functional groups on xGnP (higher magnitude of zeta potential) and enables it to be re-dispersed much easier than for neutral conditions (pH=7).

Figure 11a presents a plot of advancing and receding water contact angle values on spray deposited PE-xGnP coatings as a function of filler particle concentration in the dry composite coating. We define the filler particle concentration as a mass fraction,  $w_p = m_{\text{xGnP}} / (m_{\text{xGnP}} + m_{\text{PE}})$ , where  $m_{\text{xGnP}}$  and  $m_{\text{PE}}$  are the respective masses of xGnP and PE in the composite coating. As



Figure 10. (a) xGnP-water suspensions in 20 mL glass vials with varying concentration of  $\text{NH}_3(\text{aq})$  (left vial 0 wt.%, middle vial 1.0 wt.%, right vial 7.7 wt.%  $\text{NH}_3(\text{aq})$ ). (b) The vials from **a** with 1 g of a 42 wt.% PE dispersion in water added to each. (c) The vials from **b** after 60 min of bath sonication. Note the apparent stability of the dispersion in the rightmost vial.

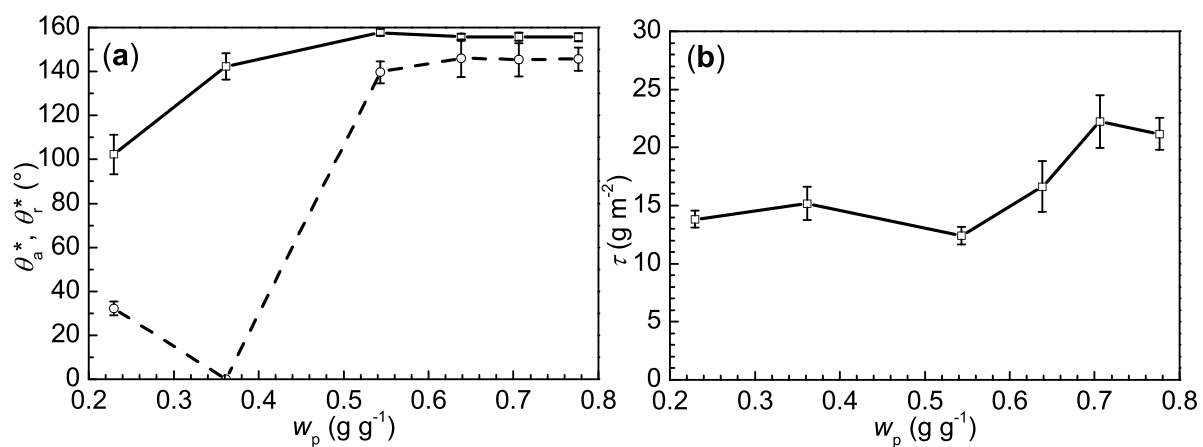


Figure 11. (a)  $\theta_a^*$  (—□—) and  $\theta_r^*$  (---○---) vs.  $w_p$  (xGnP mass fraction in the dry composite coating); (b) Coating add-on level ( $\tau$ ) vs.  $w_p$  for coatings characterized in **a**.

observed in previous spray coating studies (112; 48) —as in the classic Johnson and Dettre (113) experiment—initially advancing contact angle values increase while receding contact angles decrease, leading to a widening contact angle hysteresis ( $\Delta\theta^* = \theta_a^* - \theta_r^*$ ). After sufficient filler loading, the receding contact angle value abruptly jumps and becomes comparable with the advancing contact angle value (*i.e.*, low-contact angle hysteresis), indicating water droplet mobility and ultimately liquid repellency; at  $w_p = 0.64$ ,  $\Delta\theta^* = 9^\circ$ . The wettability transition from low  $\theta_a^*$  and high  $\Delta\theta^*$  values to high  $\theta_a^*$  and low  $\Delta\theta^*$  values is commonly referred to as the Wenzel (69)-to-Cassie Baxter (70) transition, and is usually associated with a large increase in liquid droplet mobility. As is widely reported in other spray coating literature, coating morphology as a result of spray processing and filler inclusion can—under proper circumstances—produce highly textured surfaces (114; 115; 116; 117); when coupled with low-surface energy polymers, such coatings are capable of becoming superhydrophobic, and in some cases superoleophobic (88; 112; 116). Figure 11b shows the individual add-on levels of coating in order to achieve the desired wetting properties presented in Figure 11a. All of the coating add-on levels are in the range of 10-25 g m<sup>-2</sup>, which is a typical level required to achieve superhydrophobicity from spray coating when coating untextured substrates.

Figure 12 presents a sequence of SEM micrographs (increasing magnification a-to-b) of a superhydrophobic coating ( $w_p = 0.54$ ) demonstrating its high surface texture. While the surface is highly textured, it also has certain roughness features that contribute to liquid repellency better than other surfaces would (*e.g.*, hierarchical, re-entrant, porous) (72; 77). Figure 13 presents a plot of coating electrical conductivity ( $\gamma$ ) vs.  $w_p$ ; increasing concentrations of xGnP result

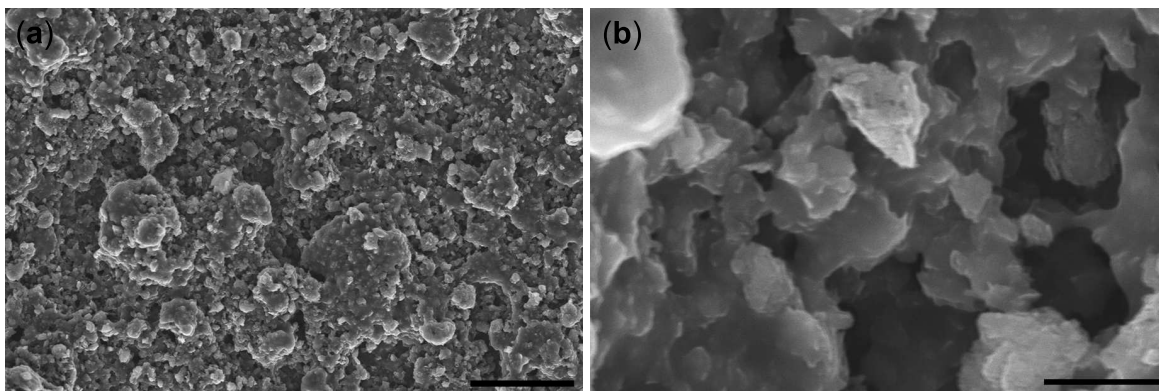


Figure 12. SEM images of the spray deposited coating ( $w_p = 0.54$ ) (a) low magnification (50  $\mu\text{m}$  scale bar); (b) high magnification (5  $\mu\text{m}$  scale bar).

in an increase in conductivity of the composite coating (measured by the two probe method). While the conductivity levels are relatively low (88; 90)—likely owing to non-alignment of graphite platelets as well as the porosity of the coating—such formulations may still be useful for anti-static coatings for packaging applications.



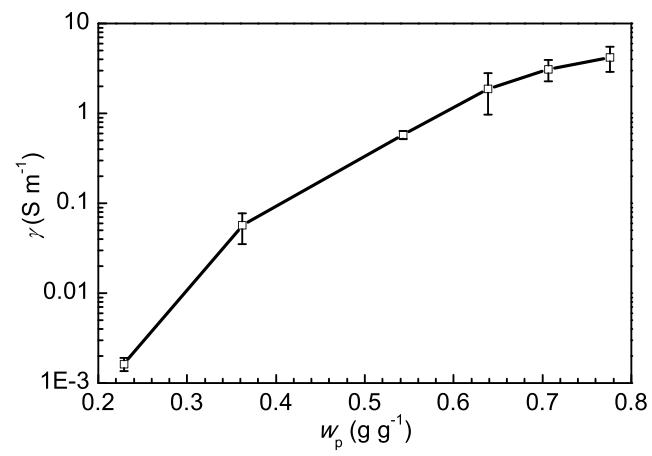


Figure 13. The electrical conductivity of the PE-xGnP composite coating ( $\gamma$ ) as a function of filler concentration ( $w_p$ ).

## CHAPTER 3

### STRETCHABLE SUPERHYDROPHOBIC COMPOSITE COATINGS

This chapter is reprinted from Composites Part A: Applied Science and Manufacturing, 42, Thomas M. Schutzius, Manish K. Tiwari, Ilker S. Bayer, and Constantine M. Megaridis, High Strain Sustaining, Nitrile Rubber Based, Large-Area, Superhydrophobic, Nanostructured Composite Coatings, 979–985, Copyright 2011, with permission from Elsevier (118).

#### 3.1 Introduction

Nitrile rubber, NBR, is a hydrophobic, solution-processable rubber used extensively in the automotive industry (seals, fuel lines, oil hoses, etc.) for its excellent oil, fuel, and heat resistance (119; 120; 121). Introducing fillers, such as carbon black (CB) and clay, to NBR is well established, with previous works emphasizing mechanical property improvement (119; 120; 121; 122; 123; 124; 125; 126). Manipulation of the surface texture with added filler particles is a relatively unexplored feature, which can be used to tune the wettability of the resulting flexible composite coatings. In fact, carefully designed polymer composite coatings with filler particles can even demonstrate superhydrophobicity (static water sessile droplet contact angle over  $150^\circ$ ) and self-cleaning capabilities (low water droplet sliding angle or low contact angle hysteresis) (115; 117). A hierarchical surface morphology in particular (with micron-to-nanoscale roughness) is known to facilitate such high water repellency (lotus effect) (127; 128; 129). The well-known elastomeric properties of intrinsically hydrophobic nitrile rubber could thus be uti-

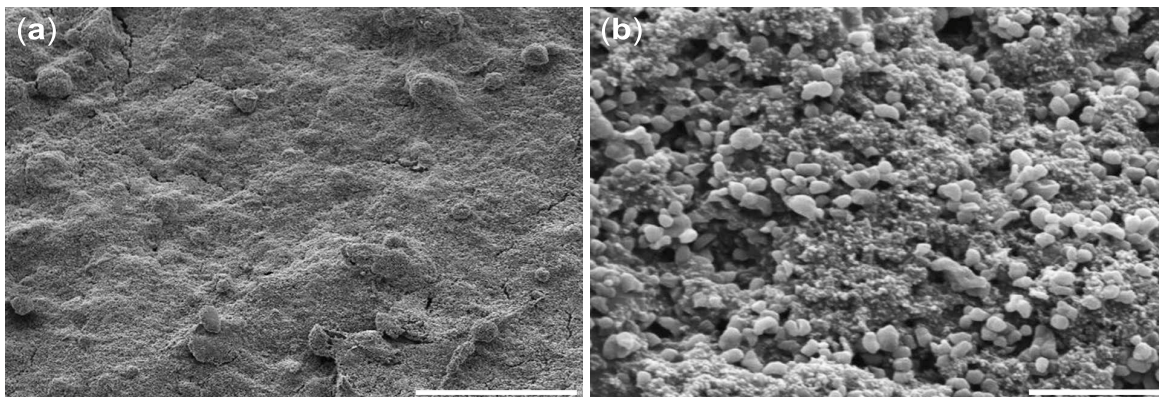


Figure 14. ESEM images of composite coating SC1, deposited on indium foil, unstrained, demonstrating hierarchical roughness by dual filler particle addition for (a) low magnification (50  $\mu\text{m}$  scale bar) and (b) higher magnification (2  $\mu\text{m}$  scale bar).

lized for the fabrication of flexible, or even stretchable, water repellent composite coatings. Such materials can be considered for stretchable substrates (*e.g.*, rubber, textiles) undergoing moderate to intense strain when super-water repellency is required. This approach is expected to work for any elastomeric, hydrophobic, solution processable polymer (*e.g.*, fluoroelastomers).

While there have been abundant previous studies on synthetic superhydrophobic surfaces (115; 117; 127; 128; 129; 130; 86; 131; 132; 133; 78), work related to *stretchable* polymer-based (elastomeric) surfaces is scarce. Zhang et al. (134), produced a polyamide film with a triangular net-like structure that was stretchable and switched between superhydrophobicity and superhydrophilicity (*i.e.*, reversible wetting) depending on its state of strain. Choi et al. (135) presented a method of dip coating fabrics to attach fluorodecyl polyhedral oligomeric silsesquiox-

ane molecules and impart tunable oleophobicity to fabrics subjected to strain; increasing strain resulted in a decrease in oleophobicity. Recently, another group (136) demonstrated the ability to make recycled-rubber-based water repellent surfaces by stamped texture. The literature on simple-to-apply water-repellent coatings for hydrophobizing textiles is quite extensive; see the reviews by Bahners et al. (137) and Gowri et al. (138) for an introduction to currently available methods. For the sake of brevity, we mention only a few relevant techniques. Gao and McCarthy (132) demonstrated a simple dip coating technique for hydrophobizing polyester and microfiber polyester fabrics. Coulson et al. (139; 140) utilized a plasma technique to achieve ultra-low surface energy well-adhered polymeric films for creating both hydrophobic and oleophobic surfaces applied on cotton substrates without any solvents (which are required for spray or dip coating applications). Several other authors have also demonstrated relatively simple textile coatings that are repellent to both water and low-surface tension liquids (*e.g.*, hexane, hexadecane) (141; 142; 143). While reversible wetting, rubber-based hydrophobic surfaces, and simple hydrophobic coating application methods for textiles have been demonstrated, works showing the ability to maintain superhydrophobicity (high contact angle) and self-cleaning ability (low sliding angle) at increasing strains are lacking. In previous studies, the property of liquid repellency was both substrate and strain dependent. In the present work, coatings applied on a variety of flexible substrates maintain superhydrophobicity through a range of strains. We describe a simple, true one-step, spray process based on commodity chemicals applied, either upon manufacture or in a post-processing step, to an existing flexible substrate to impart superhydrophobicity to its surface.

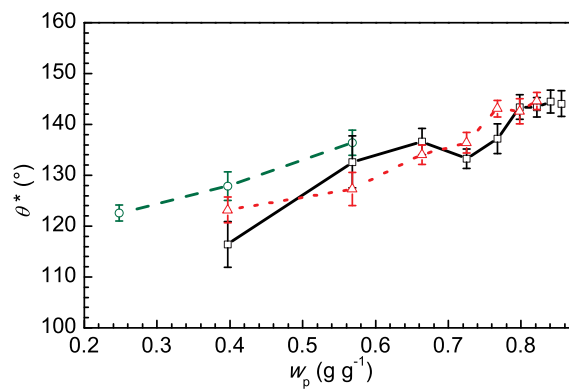


Figure 15. Sessile water droplet contact angle ( $\theta^*$ ) variation as a function of filler particle concentration ( $w_p$ ) for coatings with different fillers: PTFE (—□—), CB (—○—), and PTFE+CB (—△—). The PTFE+CB case maintains a filler particle wt. ratio of 9:1 PTFE:CB. The coatings were deposited on glass slides. Each data point represents 10 water contact angle measurements.

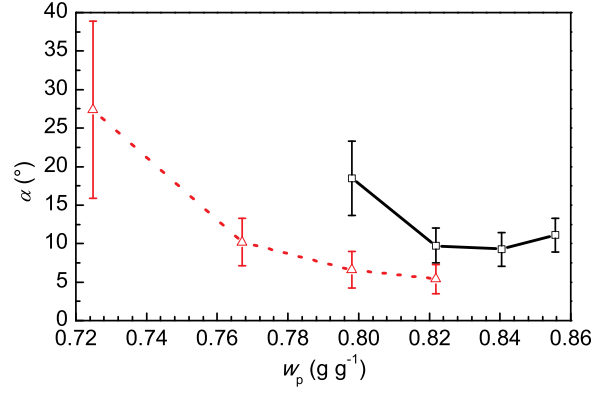


Figure 16. Water droplet sliding angle ( $\alpha$ ) as a function of filler particle concentration ( $w_p$ ) for coatings with different fillers. The coatings were deposited on glass slides. 40 measurements were averaged for each data point. For  $w_p$  less than 72 wt.% PTFE+CB and 80 wt.% PTFE, water droplets remained pinned to the coating's surface even when inverted.

PTFE+CB (--- $\triangle$ ---); PTFE (— $\square$ —)

## 3.2 Experimental

### 3.2.1 Materials

The materials used were: PTFE (Sigma Aldrich,  $2.15 \text{ g cm}^{-3}$  density), CB (Cabot, BP2000,  $1.9 \text{ g cm}^{-3}$  density), acetone (99.5%, Sigma Aldrich), poly(acrylonitrile-co-butadiene) rubber (37-39% acrylonitrile, Sigma Aldrich,  $1 \text{ g cm}^{-3}$  density), polyester fabric (local fabric store), microscope glass slides, indium foil (Sigma Aldrich, 0.25 mm thick, 99.99% metals basis), and silicone rubber ( $1/2'' \times 1/16'' \times 36''$ , McMaster-Carr).

TABLE II

## COMPOSITION RANGE OF NBR/PARTICLE DISPERSIONS

ingredient	concentration (wt.%)
NBR	1.5
filler particles	1.0-9.0
acetone	97.5-89.5 (balance)

**3.2.2 Procedure**

Pieces of NBR were dissolved in acetone at 40 °C under constant mechanical stirring to obtain a 10 wt.% solution. PTFE and PTFE-CB suspensions were prepared by dispersing the particles in acetone under bath sonication for 30 minutes. Upon maintaining a good degree of particle dispersion in acetone, the NBR solution and the suspensions were blended for subsequent spray deposition. Table II describes the composition ranges for the blends used to produce the coatings. Clean microscope glass slides, silicone rubber, and polyester fabric were used as substrates for the coatings. Coatings were spray deposited onto the substrates with a single spray application at a fixed distance of 19 cm using an airbrush atomizer (Paasche VL siphon feed, 0.55 mm spray nozzle) mounted on an automated industrial dispensing robot (EFD, Ultra TT Series). The airbrush was operated by passing pressurized air through the nozzle to move the particle slurry via siphon feeding; this air stream also acted to augment

atomization at the nozzle exit. The pressure drop across the sprayer varied from 2.7-4.1 bar depending on conditions. Each type of filler, and their combination, was incorporated into the dispersion at increasing levels until the dispersion could no longer be sprayed consistently. The coated substrates were dried for 30 minutes at 80°C in an oven. The dispersion compositions which yielded superhydrophobic coatings with an optimally low amount of filler particle loading are listed in Table III. Coatings deposited on flexible substrates were mounted between two linear clamps and stretched using a programmable linear actuator (Velmex). For uniaxial straining, coated polyester fabrics were placed on a stretchable supporting substrate (silicone rubber) in order to facilitate water droplet sliding angle measurements. The stretching limits used for silicone rubber and polyester fabric were 30% and 70% strain, respectively. These limits were chosen based on apparent coating and substrate degradation and not based on loss of superhydrophobicity. Since acetone was the only liquid component of the slurry, the surface tension of the sprayed fluid should be close to that of acetone ( $22.72 \text{ mN m}^{-1}$  at 25°C). No viscosity measurements were performed for these slurries.

### **3.2.3 Characterization**

A backlit optical image acquisition setup was used to record water droplet images for sessile contact angle ( $\theta^*$ ) measurements. Water droplet sliding angle ( $\alpha$ ) measurements were performed on a tilting stage (accuracy of 1 degree); the stage was gradually inclined until the droplets rolled off. The water droplet volume used for both  $\theta^*$  and  $\alpha$  measurements was 11.6  $\mu\text{L}$ . Environmental scanning electron microscope (ESEM) images were obtained using a Philips XL30 ESEM-FEG after all samples were sputter coated with a 5 nm-thick layer of gold-palladium. For high-



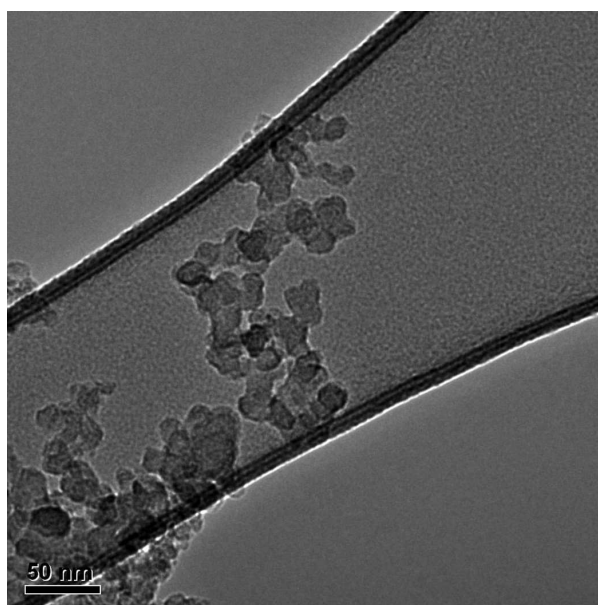


Figure 17. TEM image showing the morphology of the CB filler particles used in this work.

Image analysis showed that the mean diameter of the CB primary units is 21 nm (standard deviation 3 nm).

TABLE III

DISPERSION COMPOSITIONS FOR ELASTOMERIC SUPERHYDROPHOBIC

COATINGS WITH MINIMAL PARTICLE CONTENT

ingredient	SC1 (wt.%)	SC2 (wt.%)
NBR	1.5	1.5
CB	0.5	0.0
PTFE	4.5	7.0
acetone	93.5	91.5

resolution observation of how the composite coating behaves under strain, flexible indium foil substrate was used. Once coated, the indium foil was first stretched to  $\epsilon = 18\%$  strain, the upper-limit the indium foil could bear before failing, and was subsequently sputter-coated with 5 nm gold-palladium before imaging on the ESEM. Transmission electron microscope (TEM) images of the CB filler particles were obtained using a JEOL JEM-2010F. Scanning electron microscope (SEM) images of the PTFE filler particles were obtained in a previous study; the mean diameter of the PTFE particles was measured to be 260 nm (standard deviation 54.2 nm) (117).

### 3.3 Results and Discussion

Composite coatings containing filler particles allow control of surface roughness. Composite coatings containing both nanometer-scale particles (*e.g.*, CB, size < 100 nm) and submicrometer-scale particles (*e.g.*, PTFE, sizes in the range 100–500 nm) generate hierarchical surface roughness, thus facilitating water repellency. Previous work (117) suggests that while it is possible to achieve self-cleaning surfaces by utilizing a single type of filler particle in a composite coating, adding two fillers of different length scales may allow the coating to become self-cleaning at even lower levels of particle loading. Ultimately, utilizing the minimum required amount of filler to attain a self-cleaning surface is of utmost importance for the coatings investigated here, as maximizing the amount of NBR in the final composite coating is essential to its mechanical integrity. Figure 14 shows ESEM images that demonstrate hierarchical micro to nanoscale roughness by utilizing dual-scale fillers. Figure 14(a) shows the presence of micro-scale roughness which is attributed to the early dynamic interactions of the fillers, PTFE and CB, with NBR during the spray impact process. Figure 14(b) demonstrates the submicrometer-scale roughness due to the PTFE particles, as well as the nanoscale roughness introduced by the CB particles.

Filler particle addition to a composite coating can affect surface wettability in two different ways. The first is by increasing the surface roughness, and the second is by changing the surface energy, which depends on the wettability of the filler particles themselves (hydrophobic or hydrophilic). Both mechanisms play an important role in affecting  $\theta^*$  on coated surfaces.  $\theta^*$  can be described by either the Wenzel (69) or Cassie-Baxter (70) equations, depending on the state the droplet is in. For heterogeneous surfaces, utilization of these equations requires that

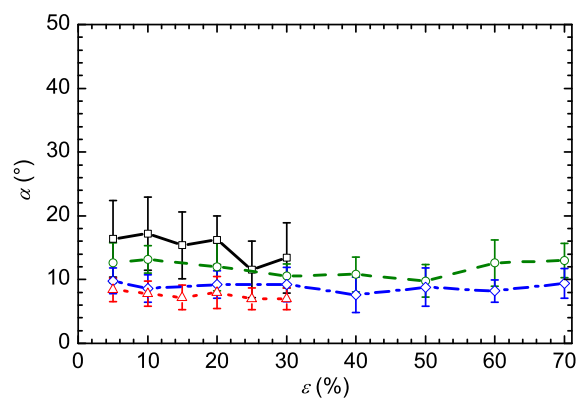


Figure 18. Water droplet sliding angles as a function of strain ( $\epsilon$ ) for coatings deposited on silicone rubber and polyester fabric. 10 sliding angle measurements were averaged for each data point. Uncoated silicone rubber did not allow droplet sliding even when inverted. The uncoated fabric showed inconsistent sliding angles in the range of  $30^\circ$  to  $90^\circ$ . SC1 on silicone rubber (--- $\triangle$ ---); SC1 on fabric (--- $\diamond$ ---); SC2 on silicone rubber (— $\square$ —); SC2 on fabric (--- $\circ$ ---).

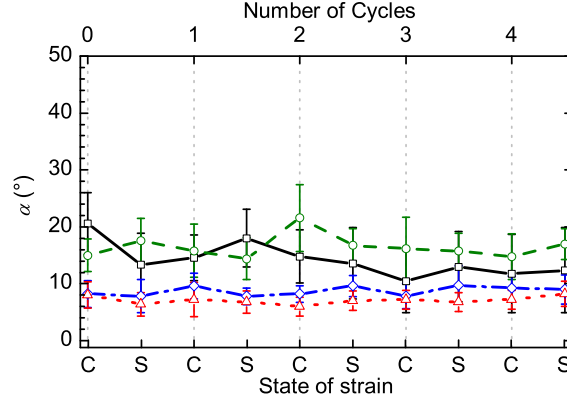


Figure 19. Water droplet sliding angles ( $\alpha$ ) for coatings deposited on silicone rubber and polyester fabric at both stretched (S) and contracted (C) conditions. Coated silicone rubber substrates were cyclically stretched to 30% strain, while coated fabric substrates were cyclically stretched to 70% strain. 10 measurements were averaged to obtain each data point. SC1 on silicone rubber (--- $\triangle$ ---); SC1 on fabric (--- $\diamond$ ---); SC2 on silicone rubber (— $\square$ —); SC2 on fabric (--- $\circ$ ---).

the variations in the composite coating's surface texture are small compared to the droplet size, and that they are uniform throughout the surface. If those criteria are satisfied, then increasing liquid repellency as a function of roughness can still be interpreted under the framework of the Wenzel and Cassie-Baxter equations (144). For heterogeneous coatings with well dispersed filler particles and self-similar surface features (see Figure 14) with size well below that of the water droplet (dia. 2.8 mm), the increased water repellency of these coatings due to increased surface roughness can be interpreted under the Wenzel and Cassie-Baxter models.

Figure 15 shows  $\theta^*$  measurements on composite coatings with varying filler content and deposited on glass slides. The three curves represent composite coatings prepared using either PTFE particles only, CB particles only, or PTFE and CB particles in a 9:1 PTFE:CB wt. ratio. The figure shows that increasing the concentration of CB in the dispersion results in a corresponding increase in  $\theta^*$  for the resulting composite coating. For a CB concentration of  $w_p = 57$  wt.% (2 wt.% in dispersion),  $\theta^* = 136^\circ$ , which is higher than the coatings containing PTFE and PTFE+CB at that same filler concentration. This indicates CB as an optimal nanofiller when low loading is a factor. On the other hand, PTFE filler particles increase coating roughness on the submicrometer scale, and lower the overall surface energy of the composite. Their ability to be dispersed and sprayed more easily at higher concentrations than their CB counterparts justify PTFE particle use in larger proportion. Figure 15 demonstrates a steady increase in  $\theta^*$  with increasing PTFE content, reaching a maximum of  $144^\circ$  at  $w_p = 84$  wt.% (8 wt.% of dispersion). The combination of PTFE with CB (PTFE+CB) also shows a steady increase in  $\theta^*$  with filler content, reaching a maximum of  $144^\circ$  at  $w_p = 82$  wt.% (7 wt.% of dispersion). The composite coating with PTFE and CB achieves its maximum  $\theta^*$  at a slightly lower level of particle concentration than PTFE alone.

It has been argued that superhydrophobicity should be characterized by low-contact angle hysteresis (132), or low sliding angles, as such quantities quantify readiness of water droplet movement (water repellency). Figure 16 shows water droplet sliding angle (sliding angle) measurements of composite coatings deposited on glass slides for different fillers and their change with varying filler content. The two curves depicted in Figure 16 represent composite coatings

prepared using either only PTFE particles or PTFE and CB (PTFE+CB) particles in a 9:1 PTFE:CB wt. ratio. The figure demonstrates that adding increasing amounts of PTFE to the dispersion, results in a general reduction in water droplet sliding angle, which ultimately attains a value  $10^\circ \pm 2$  at  $w_p = 82$  wt.% (7 wt.% of dispersion; composite coating SC2, Table III). Figure 16 also shows the gradual reduction in sliding angle with added PTFE+CB fillers, with the composite coating displaying a sliding angle of  $10^\circ \pm 3$  at  $w_p = 77$  wt.% (5 wt.% of dispersion; composite coating SC1, Table III), and dropping even lower at higher filler content. While previous works have demonstrated superhydrophobic spray cast coatings with hierarchical structures (117; 114), the goal of combining both CB and PTFE here was to achieve superhydrophobicity at the lowest possible level of filler particle concentration in order to maximize the amount of NBR in the final composite coating, thus preserving the coating's mechanical integrity. By utilizing a PTFE+CB combination, the  $w_p$  necessary for the self-cleaning property was lowered by 5.5 wt.% (2 wt.% of dispersion) over just PTFE alone. It is also interesting to note the relatively large error bar of the sliding angle for the PTFE+CB case at  $w_p = 72$  wt.% (4 wt.% dispersion). At this point, the surface transitioned from a sticky Wenzel state to a Cassie-Baxter state, which is characterized by low sliding angles. The large error bar is attributed to the transition between the two wetting states. Since Figure 15 demonstrates increasing  $\theta^*$  for increasing filler content, and since the  $\theta^*$  for PTFE+CB at  $w_p = 66$  wt.% (3 wt.% dispersion) is sufficiently high to guarantee hydrophobicity but the droplet still remains pinned to the surface even when tilted, the droplet must be in a Wenzel state of wetting. On the other hand, at  $w_p = 72$  wt.% (4 wt.% dispersion) no droplet pinning occurs and

the droplet must be in a Cassie-Baxter state of wetting. This interpretation is supported by the decrease of the sliding angles and the corresponding standard deviations with increasing filler concentration, which indicates that the droplets remain in the Cassie-Baxter wetting state.

Repellency to lower surface tension liquids was also investigated to explore the limits of the present composite coatings. A mixture water+IPA (9:1 wt. ratio water:IPA, surface tension  $40.42 \text{ mN m}^{-1}$ ) (117) was used as a stronger challenge of liquid repellency. Neither coating SC1 or SC2 displayed any droplet sliding behavior, indicating that the water+IPA droplets were in a Wenzel state of wetting. However, the corresponding contact angle values were  $126 \pm 3$  (SC1) and  $104 \pm 3$  (SC2), indicating that the coatings did display mild solvent repellency. Steele et al. (116) showed that in order to produce surfaces repellent to such low surface tension liquids, great care must be taken to contain very low surface energy groups while having the polymer matrix itself develop its own surface texture features (*e.g.*, polymer cells, pores, etc).

For the CB-only filled coatings, the content of the dispersion reached up to 2 wt.%. No higher CB content was utilized because of clogging of the sprayer during experimentation, corresponding to device limitations. The clogging was attributed to the apparent increase in dispersion viscosity and the tendency of the CB particles to aggregate and clog the sprayer. Previous studies have reported that raising the nanoparticle volume fraction in a suspending liquid can result in disproportionate increases in dynamic viscosity as compared with the pure dispersing fluid (145; 146; 147; 148). Moreover, undispersed agglomerates, which may persist even after sonic bath treatment (149), can cause increased viscosity in nanoparticle dispersions as well (146; 150). Figure 17 confirms the presence of CB aggregates. These aggregates were



obtained by drying a small amount of the dispersion placed on a holey carbon film supported by a standard electron microscope grid. Since the limits of breaking up CB aggregates were apparently reached for our sonicator, efforts were made to lower the volume fraction of the nanoparticles (to reduce viscosity) by diluting the dispersion with increased acetone. However, this resulted in large amounts of acetone reaching the surface and causing nonuniform coverage of the substrates by the composite coating.

Figure 18 displays the effect of strain on droplet sliding angle for coatings SC1 and SC2 deposited on silicone rubber and polyester fabric substrates. It is clear that SC1 preserves the self-cleaning property (sliding angles  $< 10^\circ$ ) for both silicone rubber and polyester fabric substrates throughout the strain levels investigated. Stretching was ceased at 30% strain for the silicone rubber substrate because visual crack formation of the coating began to occur beyond that level. Visual crack formation of the coating on the polyester fabric substrate was never noted, but permanent deformation to the substrate began to occur beyond 70% of strain and for this reason, the straining of the fabric was ceased at that level. It is important to note that in both cases, the strain was not ceased due to a loss of superhydrophobicity. Michielsen and Lee (151) utilized Cassie-Baxter theory (70) in its original form (*i.e.*, not simplified to liquid in contact with a flat porous surface) to review the relationship between surface tension and roughness for artificially made superhydrophobic textiles. In that study, the wetting behavior was controlled by varying the geometric structure of the fabric; surface energy was controlled by applying different chemical treatments. In the present study, wetting behavior is influenced solely by the composite coating itself, as roughness is affected by the filler particles, while surface

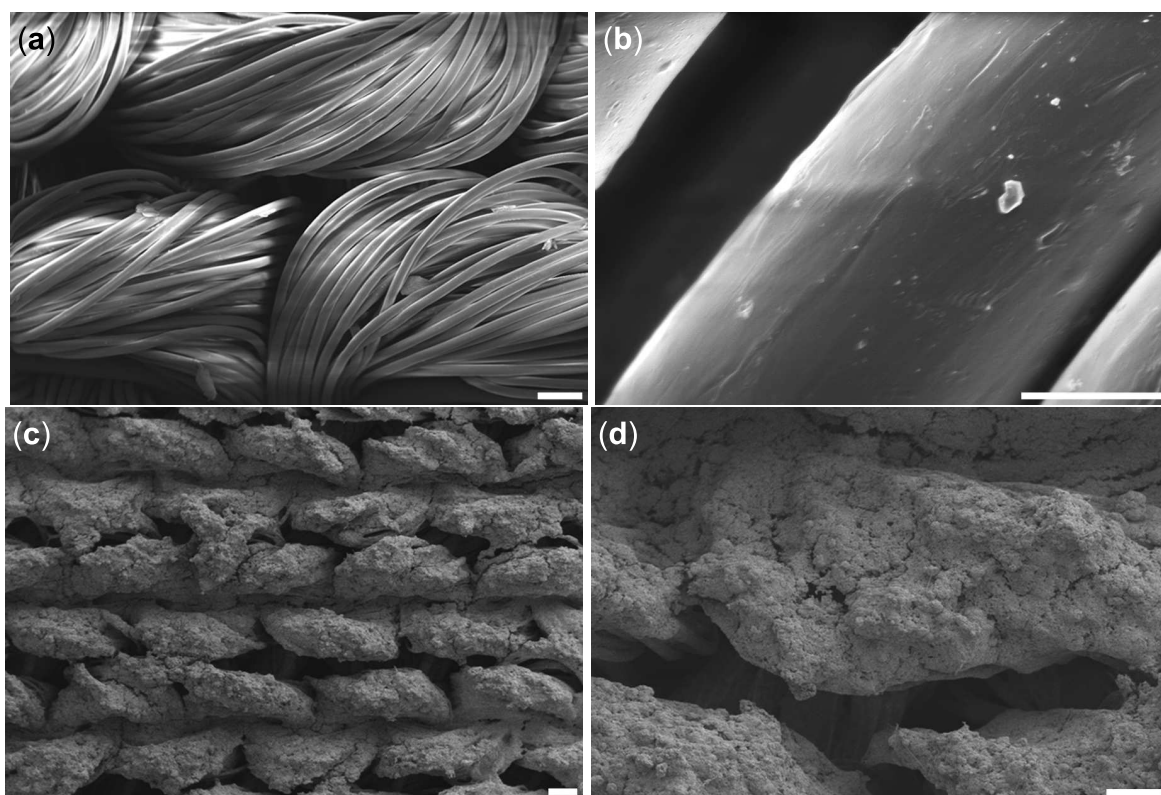


Figure 20. ESEM images of the uncoated polyester fabric at (a) low-magnification (50  $\mu\text{m}$  scale bar), and (b) higher magnification (5  $\mu\text{m}$  scale bar). ESEM images of composite coating SC1, deposited on polyester fabric, unstrained, demonstrating conformal coating of the fabric fibers at (c) low magnification (200  $\mu\text{m}$  scale bar), and (d) higher magnification (50  $\mu\text{m}$  scale bar).

energy is influenced both by the rubber matrix and the particles. If the geometric structure of the underlying textile did significantly affect the wettability of the surface, then there would be a measurable difference in wettability between a flat coated substrate (*e.g.*, glass slide, silicone rubber) and a textured coated substrate (*e.g.*, textile). Figure 18 shows that the coating when on a flat substrate (silicone rubber) has similar droplet sliding angles as when on the fabric for varying stretched states. This indicates that the fabric's surface texture (*i.e.*, roughness, which is also expected to change with stretching) is not contributing to superhydrophobicity. One of the goals in developing the present coating system was to be able to apply it to a variety of flexible substrates without relying on each substrate's inherent roughness to create superhydrophobicity.

Figure 19 shows sliding angles for coatings SC1 and SC2 deposited on fabric and silicone rubber substrates and their values during cycling at their corresponding strain limits. SC1 remains self-cleaning on both silicone rubber and polyester fabric beyond the four strain cycles. Coating SC2 with sliding angles between  $10^\circ$  and  $20^\circ$  is not quite self-cleaning, but maintains its superhydrophobic property throughout and beyond the four strain cycles. It is argued that the higher strains achievable with the coated fabric (without visual crack formation) were due to the fact that the coating conformed to the fibers of the fabric rather than plugging its pores. A conformal coating is supported by the ESEM images of Figure 20 where the coating clearly conforms to the bulk fibers. Choi et al. (135) also demonstrated a conformal style coating for their strained polyester fabrics with tunable oleophobicity. In Figure 19, we present only a few cycles of straining to show that superhydrophobicity is maintained after repeated straining and

contracting. Abrupt failure of the coating was not observed after the four strain-contraction cycles; moreover, loss of superhydrophobicity was not observed even after one-hundred strain-contraction cycles, although the coating did begin to show slow mechanical degradation with increasing number of cycles.

Figure 21(a)-(c) present ESEM images of coating SC1 deposited on stretchable indium foil. Once coated, the indium foil was strained to 18%. Figure 21(a) shows the presence of crack-like defects, which are randomly distributed on the coating, but have a preferred direction of propagation perpendicular to the applied tension (152). During the formation of the crack-like structures, nanofibers formed from the rubber binder were seen to bridge the microcracks; (c). The formation of small fibers is common in fracture of glassy thermoplastics, where these fibers are referred to as fibrils, and the effect associated with their formation is referred to as crazing (153). As seen in (b), the fibril orientation is perpendicular to the direction of crack propagation; the presence of fibrils is also quite homogeneous with respect to the depth of the crack; (c). The average diameter of the observed fibrils is  $70 \pm 33 \text{ nm}$ , which is of the same order with previously observed polymer fibrils (5-30nm dia.) (153). Crazing is known to increase energy dissipation and fracture toughness, due to the ability of the fibrils to support some load. While it is unclear whether the fibrils themselves increase the fracture toughness of the present composites, these fibrils play a positive roll in keeping the coating intact and delaying macroscopic crack formation. It is also interesting to note the shape of the fibrils themselves, which appear to be cylindrical but also decorated with ‘pearls’. Periodic beads seem to form

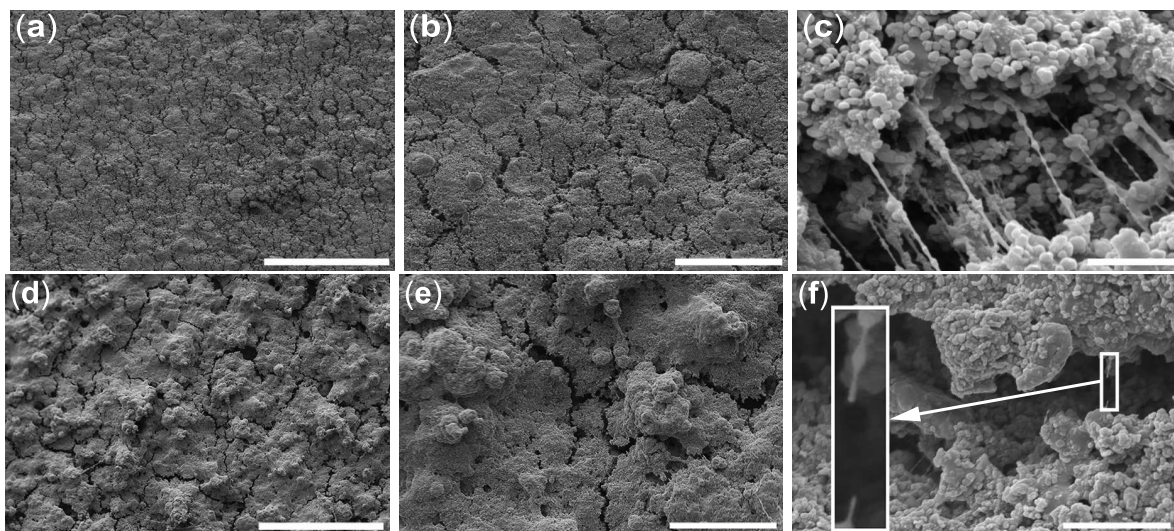


Figure 21. (a)-(c) ESEM images of composite coating SC1 (deposited on indium foil, strained to 18%) at different magnifications increasing from left to right showing crazing. (d)-(f) ESEM images of composite coating SC1 deposited on silicone rubber relaxed after stretching to 30% strain. The inset in (f) displays a magnified image of broken fibrils. Scale bars ( $\mu\text{m}$ ):

(a) 200; (b) 50; (c) 2; (d) 200; (e) 50; (f) 5.

along the entire length of the individual fibrils, as previously observed in nanofibers electrospun from polymer solutions of low viscoelasticity (154; 155).

Figure 21(d)-(f) present ESEM images of coating SC1 applied on stretchable silicone rubber. Once coated, this substrate was stretched to 30% strain and then allowed to relax. Figure 21(d)-(f) display images of the coating surface at its relaxed state (*i.e.*, 0% strain) and reveal the presence of microcracks. Prior to crack formation, the composite coating appears to

have formed fibrils, which broke probably under excessive strain. Remnants of broken fibrils in Figure 21(f) indicate their earlier presence under reduced strain. So while superhydrophobicity of the composite coating on silicone rubber persists for stretching between 0-30% strain, coating fracture and thus mechanical failure occurs at strains below 30%. This low level of strain required for the composite coating to fracture, when compared to other NBR composites, is attributed to the high level of particle filler concentration required for superhydrophobicity (3.3:1 filler particle:NBR mass fraction). It should be noted, though, that flaking off of the coating, as previously observed for other superhydrophobic surfaces undergoing significant stretching, is not observed for the levels of strain investigated here.

## CHAPTER 4

### FLUOROPOLYMER BLENDS: MULTIFUNCTIONAL LIQUID REPELLENT NANOCOMPOSITES

This chapter is reprinted (adapted) with permission from Industrial & Engineering Chemistry Research, 50, Thomas M. Schutzius, Ilker S. Bayer, Manish K. Tiwari, and Constantine M. Megaridis, 11117–11123, Copyright 2011, American Chemical Society (87).

#### 4.1 Introduction

Fluoroacrylic polymer-based coatings are of high interest due to their unique surface properties, such as exceedingly low surface energy, low friction coefficients, repellency to both oil and water, and relatively low permeability to most gases (156; 157; 158). Among them, perfluoroalkyl ethyl methacrylate copolymers (PFEMA) have been characterized for water as well as oil repellency applications (159). Due to their environmental friendliness, water-dispersed fluorinated acrylic copolymers—which we designate here by the umbrella term PMC (*e.g.*, perfluoroalkyl methacrylate copolymers)—have been approved for industrial use. These compounds can be synthesized by conventional free radical polymerization in various liquids, including non-solvents, such as water. However, processing in water poses challenges in controlling molecular weight distribution and composition, as needed for attaining the desired physical properties. In addition, there are environmental concerns about the allowable length (*e.g.*, molecular weight) of the perfluoroalkyl group due to adverse bioaccumulation rates (91; 92; 94). The US Environ-



mental Protection Agency (EPA) has raised concerns over chemicals that can break down into PFA (perfluorinated acids), and studies have shown that the bioaccumulation rate in rainbow trout of perfluoroalkyl carboxylate and perfluoroalkyl sulfonate (two types of PFA) are generally proportional to the length of the original perfluoroalkyl chain, with the type of PFA also affecting bioaccumulation rates (92; 91). Although PFA compounds are prevalent, studies outlining their toxicity thresholds are lacking (94). A recent EPA study expressed concern that current maternal concentrations of PFOA (perfluorooctanoic acid) have the potential to cause adverse effects in human offspring (94; 93). According to the EPA's PFOA Stewardship Program, an invitation was made to eight major fluoropolymer and telomer manufacturers (DuPont, 3M, etc.) to commit towards elimination of precursor chemicals that can break down into PFOA (160). The PMC utilized in the present study was created in response to this EPA initiative, and would not break down into PFOAs in the environment. Since this copolymer has restricted molecular weights due to its processing technique as well as environmental impact, its mechanical properties are expected to be degraded. One way to circumvent this problem could be to blend the PMC with a durable biocompatible polymer, preferably fluorinated (since water and solvent repellency is the ultimate application), in order to improve the overall performance of the final coating.

Poly(vinylidene fluoride) (PVDF) is a hydrophobic fluoropolymer with excellent electro-mechanical properties and resistance to harsh environments (*e.g.*, chemicals, heat, etc.) and finds application in the chemical processing industry (*e.g.*, fluid handling systems) or as the base resin for long-life coatings of exterior surfaces (*e.g.*, aluminum, wood, masonry, etc.) (161).



PVDF is also used in various biomedical applications (162). As such, PVDF could offer a possible solution to the PMC durability problem, if a proper solution blending process were developed. Since PVDF resists most chemicals, it is only soluble in a limited number of solvents (163). It also has relatively poor adhesion due to its inherent hydrophobic property. This problem can be surmounted by blending with PMC, due to the latter's acrylic functionality. More specifically, blending is not straightforward, since PMC is available as an aqueous based dispersion (due to environmental restrictions on spray coating applications), and blending water-based PMC directly with PVDF would phase-invert PVDF from the solution (164; 165). Blending PVDF in solution with a non-solvent (such as water) is usually done for the purposes of generating phase inversion PVDF membranes (166; 167; 165; 168; 169; 164). Bottino et al. (163) showed that PVDF does not dissolve in most conventional solvents but is generally soluble in polar, aprotic solvents, such as NMP and dimethylformamide (DMF). Generally, previous studies on PVDF phase inversion focused only on adding non-solvents (*e.g.*, water) to 'good' PVDF solvents and not to 'poor' solvents or 'good-poor' solvent blends (NMP-acetone), with the general trend being the better the PVDF solvent, the higher the concentration of non-solvent before phase inversion occurs (164). Other authors have reported phase inversion membranes by using 'good-poor' solvent blends, where the 'good' solvent has a high boiling point and a strong affinity for water while the 'poor' solvent has a low boiling point, hence when the 'poor' solvent evaporates, water vapor is absorbed, and phase inversion occurs. However, isothermal quaternary diagrams designating water concentrations necessary for this type of phase inversion process are absent (170; 171; 172). For spray applications 'good' PVDF sol-

vents are not suitable in high concentrations due to their high boiling points (*i.e.*, non volatile), therefore, such solutions are usually diluted with a low-boiling point ‘poor’ PVDF solvent (*e.g.*, acetone) to facilitate drying (115; 117).

Recently a number of studies have been undertaken to fabricate PVDF-based composite films displaying high water and solvent repellency by dispersing sub-micron and nano-sized particles, such as poly(tetrafluoroethylene) and/or ZnO in the PVDF matrix (115; 117; 89). One of the most studied PVDF systems is PVDF-clay nanocomposites. Previous works have shown dramatic mechanical property improvements with the addition of such fillers as well as improved crystallinity control (for the purposes of producing a thermally stable beta phase for application as a piezoelectric and pyroelectric material) (173; 174; 175; 176; 177; 178; 179; 180). Clay has advantages over other fillers in that it can be delaminated from its original layered structure of silicate platelets thus producing discrete, nanoscale silicate platelets (NSPs). These NSPs are polydisperse in size, generally exhibit high aspect ratios and can self-assemble into hierarchical structures necessary for the ‘lotus-effect’ (127; 97). Bayer et al. (86) utilized NSPs in polyurethane-based spray cast composites for producing superhydrophobic coatings. These nanoclays were surface modified with fatty-amino/amine functionality to render them hydrophobic.

We report a facile solution-blending method to disperse PVDF in a water-based PMC solution using suitable co-solvents under pH control. These highly stable solutions can be solution- or spray-cast to fabricate low-surface-energy polymer films with good substrate adhesion compared to pristine PVDF films. Further, by dispersing high-aspect-ratio nanostructured fillers,

such as organoclay and carbon nanowhiskers (CNWs) in these solutions, water and solvent repellent functional nanocomposite coatings are fabricated by simple spray casting. Although fluoroacrylic copolymers have the desired chemistry for liquid repellency (both to water and oils), they do not possess a high degree of mechanical, thermal and chemical resistance as compared to thermoplastic fluoropolymers. This study therefore investigates the blending of a high performance thermoplastic fluoropolymer (PVDF) with a fluoroacrylic copolymer in aqueous-based solutions to form durable—and yet highly liquid-repellent—polymer nanocomposite coatings.

First we incorporate nanoclay (organoclay) to produce water and water-alcohol repellent composite coatings. Next, we demonstrate the robustness of this approach by replacing the nanoclay filler with acid treated CNWs and produce highly water and water-alcohol repellent nanocomposites with the added property of electrical conductivity. Wetting properties of PVDF-PMC-nanoclay composite coatings are compared with those of PVDF-poly(ethyl 2-cyanoacrylate)-nanoclay composites in order to demonstrate the effect of PMC copolymer on liquid repellency. Wettability is interpreted within the framework of the Wenzel and Cassie-Baxter wetting theories (69; 70).

## **4.2 Experimental**

### **4.2.1 Materials**

PVDF powder (typical size  $231 \pm 66\text{nm}$  based on 40 measurements, particle sizes were measured from ESEM images, melt viscosity: 23500-29500 poise at  $230^\circ\text{C}$ ,  $100\text{ s}^{-1}$ ) was obtained from Alfa-Aesar, USA. Ethyl 2-cyanoacrylate (ECA) monomer, carbon nanowhiskers

TABLE IV

COMPOSITION OF ORGANIC SOLVENT-BASED DISPERSIONS USED TO MAKE  
PVDF-CLAY COMPOSITE COATINGS.

ingredient	concentration (wt.%)
PVDF	2.8
nanoclay	0-8.3
NMP	25
acetone	72.2-63.9 (balance)

(dia. = 110-170 nm, solid core, length = 5-9  $\mu\text{m}$ , >90 wt.% purity), DMF, reagent grade acetone, trifluoroacetic acid (TFA), formic acid, isopropyl alcohol (IPA), and NMP were all obtained from Sigma Aldrich, USA. Nanoclay, Nanomer<sup>®</sup> I.31PS, which is a montmorillonite clay, surface-modified with 15-35 wt.% octadecylamine and 0.5-5 wt.% aminopropyltriethoxysilane, was procured from Sigma Aldrich, USA. The aqueous fluorinated acrylic copolymer dispersion, Capstone<sup>®</sup> ST-100 (PMC, 20 wt.% in water) was donated by DuPont, USA. Figure 22 shows an environmental scanning electron (ESEM) micrograph of the nanoclay (organoclay), as purchased. The nanoclay was sonicated in acetone for 5 minutes, blended with a small amount of ECA (clay:ECA 10:1 wt. ratio) to promote adhesion with the substrate, and subsequently dropcast onto aluminum foil. The dry samples were imaged with a Philips XL30 ESEM after

being sputter coated with an 8nm gold-palladium layer to facilitate imaging. The image in Figure 22 shows discrete, delaminated clay platelets, each having microscale size. The edges of these clay platelets exhibit nanometer-scale features, which together with the microscale features, produce the hierarchical texture required for super-repellency.

#### 4.2.2 Procedure

10 wt.% PVDF solutions were prepared by dissolving PVDF powder in NMP under slow mechanical mixing at 40°C for 4 hours. 10 wt.% PMC solutions in an acetone-water-TFA mixture were obtained by first treating acetone (neutral pH) with a small amount of TFA. With the acetone-TFA mixture under mechanical mixing at room temperature, 20 wt.% PMC

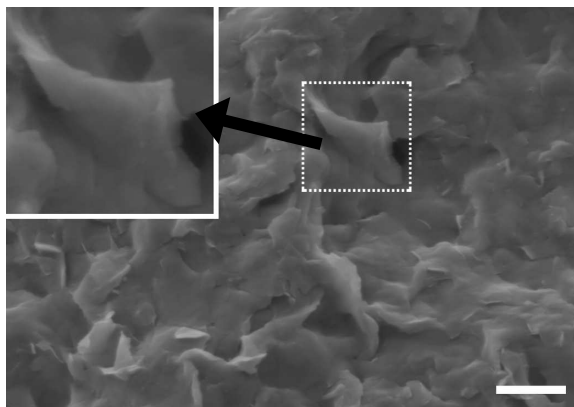


Figure 22. ESEM image of nanoclay platelets demonstrating partial exfoliation. A small amount of ethyl 2-cyanoacrylate monomer was added to facilitate adhesion of the clay to the substrate for imaging purposes (10:1 clay:polymer wt. ratio). The inset shows a magnified image of the area marked by the dotted box. Scale bar is 1  $\mu\text{m}$ .

TABLE V

COMPOSITION OF ORGANIC SOLVENT-BASED DISPERSIONS USED TO MAKE

PVDF-PECA-CLAY COMPOSITE COATINGS.

ingredient	concentration (wt.%)
PVDF	1.7
PECA	1.1
NMP	6.7
DMF	5.3
nanoclay	0-8.3
acetone	85.2-76.9 (balance)

in water was added dropwise until a 10 wt.% stock solution of PMC in acetone-water-TFA (44.5:44.5:1 wt. ratio) was obtained. To determine the onset of phase inversion, 10 wt.% PVDF in NMP was first diluted with acetone and placed under mechanical mixing. With the PVDF-acetone-NMP solution under mechanical mixing at room temperature, water was introduced to this solution either as pure water or water-acetone 1:1 wt. mixture until the PVDF phase inverted (see Figure 23a). Similarly, in separate experiments the 10 wt.% PMC stock solution was added dropwise until PVDF phase inverted (see Figure 23b). A backlit optical image acquisition setup was employed to determine when PVDF phase inverted based on the changes in the turbidity of the multicomponent solutions. To prepare stable PVDF-PMC blends, PMC dropwise addition must be ceased below the phase inversion threshold (see Figure 23).

A co-solvent based technique (117; 181) for controlled polymerization of the ethyl 2-cyanoacrylate monomer to form poly(ethyl 2-cyanoacrylate) was employed to facilitate blending with PVDF in solution. PVDF powder was dissolved in NMP at 40 °C in separate solutions under constant mechanical stirring to produce both 10 wt.% and 20 wt.% PVDF stock solutions. In preparation for addition to either the PVDF solution or PVDF-PECA solution, the organoclay was first dispersed in acetone under sonication for 30 min. For PVDF-clay composites, the solution-processed PVDF was added directly to the acetone-clay suspension at room temperature and then shaken mechanically (concentrations listed in Table IV). For PVDF-PECA-clay composites, PVDF and PECA were blended into the acetone-clay suspension at room temperature at

TABLE VI

COMPOSITION (IN WT.% OF DISPERSION) AND CORRESPONDING NAMES OF  
ACETONE/WATER-BASED DISPERSIONS USED TO MAKE PVDF-PMC-CLAY  
COMPOSITE COATINGS.

ingredient	PVDF:PMC		
	2:1 (wt.%)	1:1 (wt.%)	2:3 (wt.%)
PVDF	1.8	1.4	1.1
PMC	0.9	1.4	1.7
NMP	16.7	12.5	10.0
water	3.7	5.5	6.6
TFA	0.1	0.1	0.1
nanoclay	0.0-4.4	0.0-4.4	0.0-4.4
acetone	76.8-72.4	79.1-74.7	80.5-76.1



TABLE VII

COMPOSITION OF ACETONE/WATER-BASED DISPERSION USED TO MAKE  
PVDF-PMC-CNW COMPOSITE COATING REPELLENT TO BOTH WATER AND  
WATER+IPA (0.17 CNW MASS FRACTION).

ingredient	concentration (wt.%)
PVDF	0.9
PMC	0.9
NMP	8.3
water	3.7
formic acid	19.3
CNW	0.7
acetone	66.2

a fixed weight ratio of 3/2 (PVDF/PECA) and then mixed mechanically (concentrations listed in Table V).

For preparing PVDF-PMC-clay composites, 10 wt.% PVDF in NMP was first diluted with acetone under mechanical mixing at room temperature. With the PVDF-acetone-NMP solution still under mechanical mixing, the 10 wt.% PMC stock solution (in acetone-water-TFA) was added dropwise until the appropriate concentration was achieved; the targeted concentration

was below the phase inversion threshold for PVDF (see Figure 23). The resulting dispersion was removed from mechanical mixing. Organoclay was dispersed in acetone and sonicated with a probe sonicator for 30 min to ensure a stable dispersion. Finally, the PVDF-PMC-acetone-water-TFA solution was blended with the acetone-clay suspension at room temperature and shaken mechanically to produce the final dispersion for spray; see Table VI for specific concentrations of each ingredient.

The procedure for preparing PVDF-PMC-CNW composites was similar to that of PVDF-PMC-clay composites, except that one carboxylic acid (TFA) was replaced by another, formic acid, which was also used to treat the CNWs. Moreover, since formic acid is a much weaker acid compared to TFA, it can be directly blended with 20 wt.% PMC in water without PMC precipitating out of solution. To begin, 10 wt.% PVDF in NMP was diluted with acetone under mechanical mixing at room temperature. Then, in a separate vial under mechanical mixing, 20 wt.% PMC in water was diluted with formic acid until a 10 wt.% solution of PMC was attained. Next, the PVDF-acetone-NMP solution was placed under mechanical mixing at room temperature and the 10 wt.% PMC in formic acid-water solution was combined with it. In a separate vial, CNWs and formic acid were combined and placed under sonication (sonic bath) for 5 min in order to acid treat the CNWs. Next, acetone was added to dilute the CNW-formic acid suspension (to reduce viscosity), which was subsequently placed under sonication (probe sonicator) for 30 min. Finally, the PVDF-acetone-NMP-PMC-formic acid-water solution was combined with the CNW-formic acid-acetone suspension to yield the final spray dispersion.

Table VII lists a typical formulation with specific concentrations of each material in the final dispersion for producing water and water-alcohol repellent coatings.

Once the dispersions were generated, they were spray cast as coatings on aluminum foil as well as on cellulosic substrates (*e.g.*, paper) to demonstrate their water repellency despite being applied on highly-hydrophilic surfaces. Spraying was performed with a double action, siphon feed, internal mix, air brush with a 0.73 mm spray nozzle (Paasche VL, USA) at varying distances (20-30 cm). Coated substrates were then placed in an oven at 80°C for one hour to dry.

#### **4.2.3 Characterization**

Wettability and spatial heterogeneity of the composite coating surfaces were quantified by measuring apparent contact angles (static, advancing, receding) of 8  $\mu\text{L}$  water and water-IPA 9:1 wt. mixture droplets. A backlit optical image acquisition setup was used to measure apparent static contact angles, and a high-speed digital camera (Redlake MotionPro) was used to measure apparent dynamic advancing and receding contact angles. ESEM images of the coating's surface were obtained with a Philips XL30 ESEM-FEG. All samples were first sputter coated with an 8 nm layer of gold-palladium to better facilitate imaging. Electrical conductivity measurements of the CNW-based superhydrophobic coatings were performed with a Mastech MY-64 multimeter and the two-probe method. Conductive silver paint electrodes were applied on the composite surfaces to minimize contact resistance during electrical measurements. CNW-based superhydrophobic coatings were spray cast on insulating paper board substrates to eliminate any substrate effects during electrical measurements.

### 4.3 Results and Discussion

Figure 23a shows that the maximum concentration of water in this isothermal quaternary system (PVDF, NMP, acetone, water) before phase inversion occurs at approximately 15 wt.% of total solution for PVDF concentrations ranging from 0.5-4 wt.% of solution. Yeow et al. (164) studied phase inversion of PVDF from a number of PVDF/solvent/non-solvent systems commonly used in PVDF membrane fabrication processes. The four different solvents studied by Yeow et al. (164) were N,N-dimethylacetamide (DMAc), NMP, DMF and triethyl phosphate (TEP), while water was the only non-solvent. They reported that for PVDF concentrations from 0.5-4 wt.% of total solution, phase inversion for TEP, for instance, occurred around 5-12 wt.% water in total solution, while for DMAc it varied from 12-22 wt.% water in total solution. Although the present NMP-acetone solvent mixture is not better than DMAc in this capacity, the system can accommodate more non-solvent (water) than TEP in the ranges studied. Increasing concentrations of PVDF also led to a different mechanism of phase separation. For low concentrations, the end of titration was marked by a transition from a clear solution to a turbid solution and then to complete polymer aggregation (refer to the inset images in Figure 23a). For higher concentrations of PVDF (beyond 4 wt.% of total solution), aggregation of larger molecules was observed first, instead of turbidity. The difference in phase inversion mechanisms can be explained as follows. At low concentrations of PVDF, the solvent-solute effect dominates the solution behavior, whereas for higher PVDF concentrations, the macromolecule-macromolecule effect dominates (164).

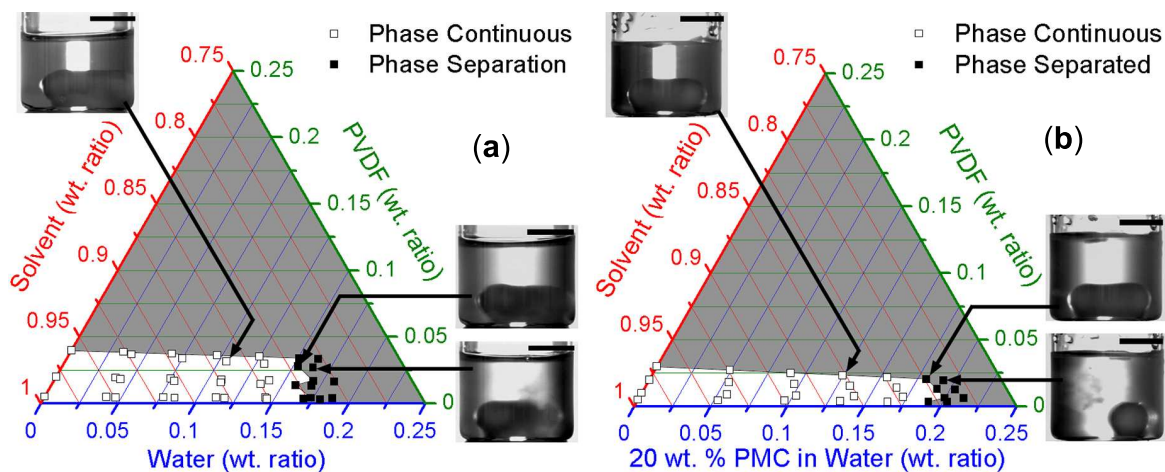


Figure 23. Quaternary and sexternary phase diagrams of the solutions utilized for spray without any clay fillers. Filled symbols indicate PVDF phase separation from liquid to a solid state. The insets display images of vials containing solutions with the specified compositions; scale bar is 10 mm. The magnetic stir bar can be seen at the bottom of each vial. (a) PVDF, solvent (acetone, NMP), water phase diagram; (b) PVDF, solvent (acetone, NMP, TFA), 20 wt.% PMC in water. For both (a) and (b), NMP was kept at a constant 9:1 wt. ratio with respect to PVDF. The concentration of TFA in the total solution was  $< 0.2$  wt.% TFA. Gray areas indicate unstable or phase inverted regimes.

Figure 23b is a sexternary phase (PVDF, NMP, acetone, water, PMC, and TFA) diagram that shows the maximum level of PMC in water solution before phase inversion is about 18 wt.% of total solution. It is instructive to compare Figure 23a with Figure 23b. We see that the titration end points of water and PMC solution in water have similar concentration levels. For water titration, phase inversion occurred at 15 wt.% of solution, whereas for 20 wt.% PMC in water titration, phase inversion occurred at 18 wt.% of total solution. Considering that the PMC dispersion is 80 wt.% water, then the concentration of water in the sexternary system when phase inversion occurs is 14.4 wt.% of total solution, which is comparable to the 15 wt.% water phase inversion concentration observed for the quaternary system in Figure 23a. At the point of phase separation, the concentration of PMC was 3.6 wt % of total solution. Addition of the aqueous-based PMC solution to a 3 wt.% PVDF solution containing co-solvents NMP and acetone (primary solvent & low-boiling point) up to 3.6 wt.% PMC final concentration without phase separation is non-trivial for spray applications, where the total solids concentration is generally kept at 4–24 wt.% of dispersion in order to reduce problems caused by viscoelasticity and nozzle clogging (117). Also, reduction in the concentration of the high boiling point solvent (NMP) by utilizing acetone instead should reduce problems of polymer composite coating non-uniformities due to substrate wetting/dewetting and ‘coffee-stain’ phenomena (116).

Adding nanoclay, which has both micro and nano scale features, to a dispersion is intended to affect the surface texture of the resulting spray cast composite coating. It was hypothesized that these clay platelets, after being introduced into the composite coatings, would self-assemble into hierarchical micro-to-nanoscale structures, as already demonstrated by Lin et al. (97) for

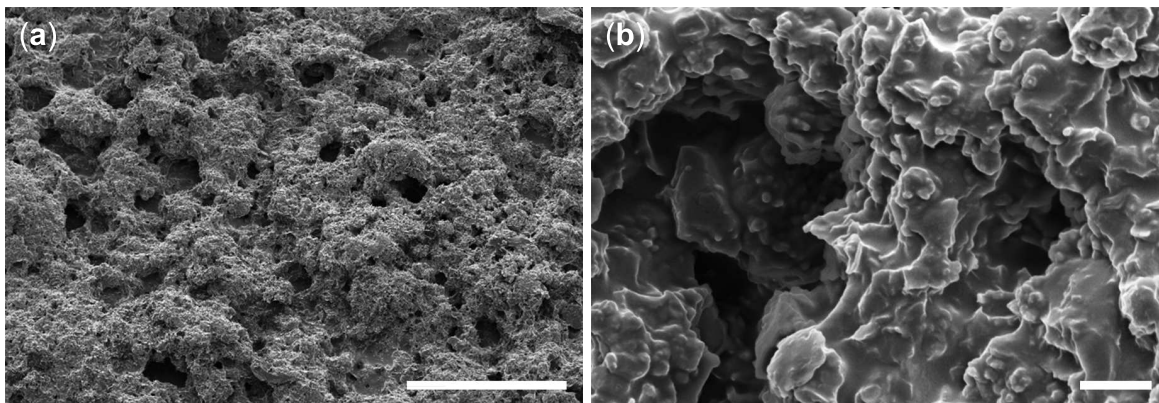


Figure 24. ESEM images of PVDF-PMC-clay composite coatings. (a) 2:3 wt. ratio PVDF:PMC and  $w_p = 0.29$  (100  $\mu\text{m}$  scale bar); (b) 1:1 wt. ratio PVDF:PMC and  $w_p = 0.29$  (2  $\mu\text{m}$  scale bar).

nanoclay platelets functionalized with hydrophobic macromolecules. Such structures are known to facilitate a high-degree of water repellency (lotus effect) (127; 128; 129). Figure 24 shows ESEM micrographs of two spray cast PVDF-PMC-clay composite coatings. Repeating micro and nanoscale features (due to clay) are apparent in these composite coatings; this affects surface wetting of the composites. Figure 25 demonstrates the effect of increasing nanoclay concentration on water contact angle values for PVDF, PVDF-PECA, and PVDF-PMC coatings. For all coatings, the contact angle values increase with increasing clay content. A distinct difference between the values for PVDF-clay and PVDF-PECA-clay composite coatings compared with the values for PVDF-PMC-clay is clear. The inclusion of PMC dramatically raises the hydrophobicity of the coatings. It is known that contact angles are affected by two factors,

*i.e.*, surface energy and surface roughness. Based on the inspection of a number of electron microscope images, PMC in the composite was not found to generate surface roughness in the form of polymer cells when spray cast from these multicomponent systems when compared to a previous study (116). Furthermore, wetting measurements indicated that PVDF-clay and PVDF-PECA-clay composite coatings, when cast on paper, do not demonstrate excellent water-repellency, indicating that to achieve superhydrophobicity with PVDF-clay based composites, a PVDF compatible fluoroacrylic component is required.

Figure 26a shows high water contact angle hysteresis values for high-concentrations of clay filler in PVDF composite coatings ( $w_p = 0.75$ ), while Figure 26b shows low water contact angle hysteresis for medium levels of clay concentration in PVDF-PMC-clay composite coatings ( $w_p = 0.375$ ). Comparison of these two graphs indicates that inclusion of PMC causes a dramatic reduction in contact angle hysteresis even with decreased nanoclay content. Tiwari et al. (117) showed that for PVDF-based composite coatings obtained by spray casting, a minimum of  $w_p = 0.75$  is required in order to obtain superhydrophobicity and self-cleaning behavior. However, by utilizing PMC and the high aspect ratio clay filler, it is possible to reduce the filler weight concentration levels significantly for a comparable level of repellency performance. Figure 27 shows that the developed coatings also resist low surface tension aqueous solutions, such as water-IPA 9:1 wt. mixture, with static contact angles exceeding  $150^\circ$  and reasonably low contact angle hysteresis.

To demonstrate the flexibility of the present method in accommodating various fillers, fluoropolymer dispersions with CNWs were also prepared and tested. CNWs were treated with



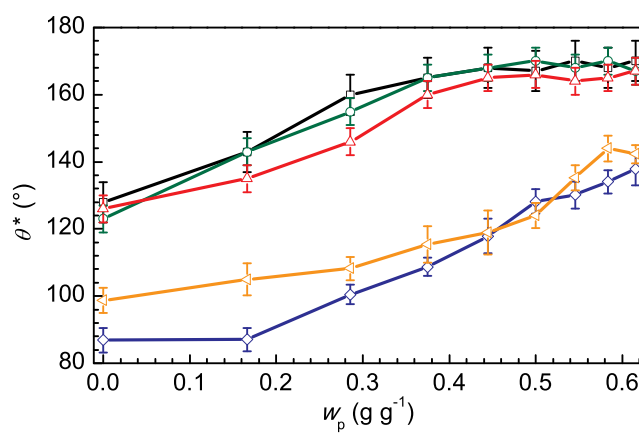


Figure 25. Sessile contact angle ( $\theta^*$ ) vs. nanoclay mass fraction ( $w_p$ ) for PVDF-clay, PVDF-PECA-clay, and PVDF-PMC-clay nanocomposites spray deposited on plain paper.

Varying concentrations of polymers were used and are defined as: PVDF ( $\text{---}\diamond\text{---}$ ), PVDF:PECA 3:2 ( $\text{---}\triangle\text{---}$ ), PVDF:PMC 1:1 ( $\text{---}\circ\text{---}$ ), PVDF:PMC 2:3 ( $\text{---}\square\text{---}$ ), and PVDF:PMC 2:1 ( $\text{---}\triangle\text{---}$ ). Increases in contact angle values were not appreciable beyond the mass fractions investigated here and are therefore not shown.

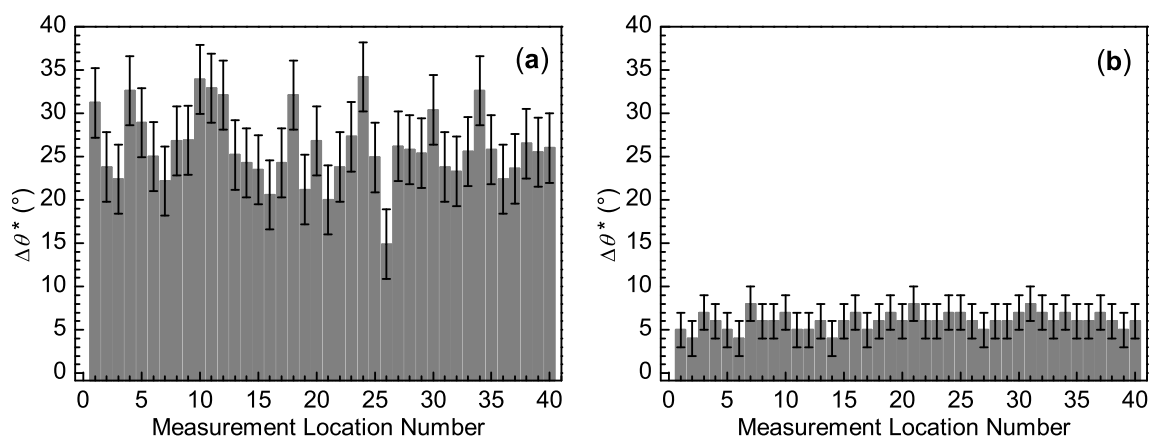


Figure 26. Water contact angle hysteresis ( $\Delta\theta^*$ ) for (a) PVDF-clay and (b) PVDF-PMC-clay nanocomposite coatings spray cast on plain paper. Each bar represents a measurement at a single location on a large-area sample. For (a)  $w_p = 0.75$  with a corresponding water sessile contact angle of  $143 \pm 4$  deg. For (b) the PVDF:PMC wt. ratio is 1:1, and  $w_p = 0.375$ . The corresponding water sessile contact angle is  $164 \pm 4$  deg.

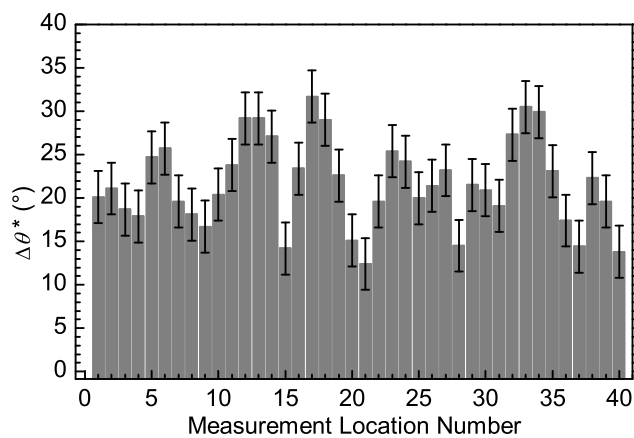


Figure 27. Water-IPA (9:1 wt. ratio) droplet hysteresis ( $\Delta\theta^*$ ) measurements for PVDF-PMC-clay nanocomposite coating spray cast on aluminum foil. For this particular coating, the polymer is a mixture of 1:1 wt. ratio PVDF:PMC, and  $w_p = 0.375$ . The water-IPA sessile contact angle for this coating is  $154 \pm 4$  deg.

formic acid before being added into the polymer blend dispersions. Figure 28 displays the surface morphology of the CNW composites ( $w_p = 0.09$ ), whose hierarchical surface structure is caused by the random assembly of the protruding CNWs within the polymer matrix. Figure 29 displays sessile contact angle (CA), electrical conductivity, and contact angle hysteresis measurements as a function of CNW concentration in the composite coatings. Comparison with clay shows that super-repellency ( $CA > 150^\circ$  and low CA hysteresis) was achieved at a  $w_p = 0.09$ , whereas for nanoclay composites  $w_p = 0.29$  was required. Figure 29 also plots CA and CA hysteresis values for the water-IPA mixture. For both liquids, phobic behavior is attained at a lower filler concentration in the case of CNWs, as compared with nanoclay. However, increasing the concentration of the CNWs beyond a certain level results in partial loss of repellency to the water-IPA mixture. This can be attributed to a possible transition from a Cassie-Baxter (70) wetting state to a Wenzel (69) wetting state. Although, the needle-like protruding structures (see Figure 28) due to the random assembly of CNWs in the hydrophobic polymer matrix are advantageous for the lotus effect with low surface tension liquids, coverage of the CNW solvent-philic surfaces with the low-surface energy polymer blend is also essential. Increasing CNW concentration in the composite probably reduces coverage of the CNWs by the polymer, thus exposing regions on the surface with relatively high surface energy, which are thus wetted by the liquid. As shown in Figure 29, water droplet CA and CA hysteresis do not seem to respond to changes in CNW concentration. In other words, the lotus effect is durable for water for the CNW concentrations used in the present composites.

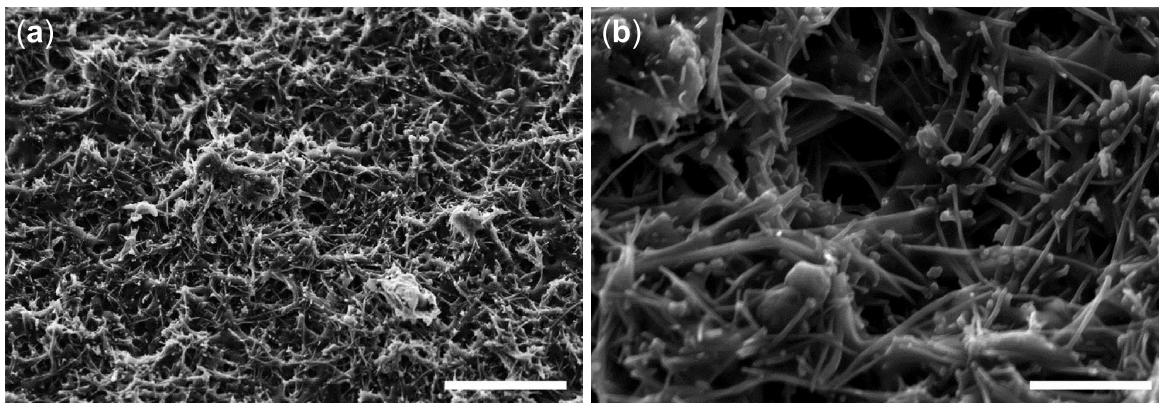


Figure 28. (a) ESEM micrograph of surface morphology of a PVDF-PMC-CNW composite coating with  $w_p = 0.09$  (20  $\mu\text{m}$  scale bar). (b) Higher magnification image showing composite surface morphology made up of randomly assembled CNWs, some of which form needle-like features protruding from the hydrophobic polymer matrix (5  $\mu\text{m}$  scale bar).

Finally, as Figure 29 also demonstrates, the fluoropolymer blend/CNW composite coatings are also electrically conductive. The electrical conductivity of these composites exceeds  $10 \text{ S m}^{-1}$  making these coatings suitable for various applications such as microfluidics, electrically activated liquid delivery, special electrodes for solid and liquid state batteries, electromagnetic interference (EMI) filters, etc.

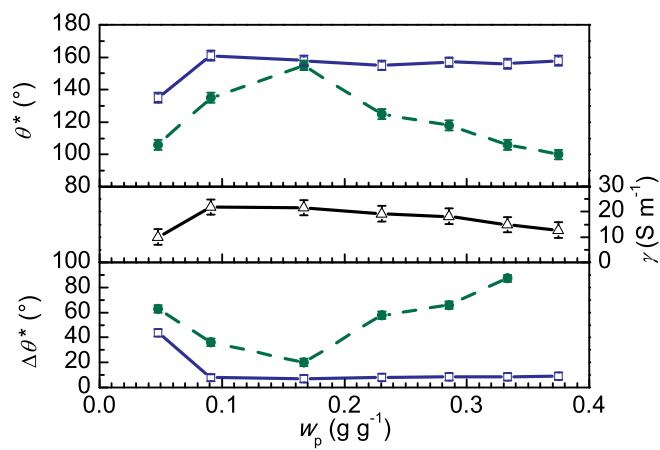


Figure 29.  $\theta^*$ ,  $\gamma$ , and  $\Delta\theta^*$  as a function of CNW mass fraction,  $w_p$ . The polymer is a blend of PVDF and PMC (1:1 wt. ratio). For  $\theta^*$  and  $\Delta\theta^*$ , the unfilled squares correspond to water, while filled circles correspond to a water-IPA mixture (9:1 wt. ratio) with surface tension of  $40.42 \text{ mN m}^{-1}$ . Each point marks the average of five measurements.

## CHAPTER 5

### WETTABILITY ENGINEERED SURFACES: HANDLING LOW SURFACE TENSION LIQUIDS

This chapter was published in: T. M. Schutzius, M. Elsharkawy, M. K. Tiwari and C. M. Megaridis, Lab Chip, 2012, 12, 5237 DOI: 10.1039/C2LC40849J - Reproduced by permission of The Royal Society of Chemistry (46).

#### 5.1 Introduction

Surfaces and coatings with patterned wettability (*e.g.*, hydrophobic, hydrophilic) have shown potential applications in microfluidics (182), fog capture (43) and pool boiling (38). With recent advancements, surfaces with adjacent superhydrophobic and superhydrophilic regions are feasible at a reasonable cost; with properly designed patterns, one can produce microfluidic paths where water is confined and transported by surface tension alone (*i.e.*, surface tension confined tracks) (183; 184; 185). The surface tension ( $\sigma_{lv}$ ) of water is relatively high ( $\approx 72 \text{ mN m}^{-1}$ ) as compared with oils ( $\approx 25 \text{ mN m}^{-1}$ ) and organic solvents ( $\approx 20 \text{ mN m}^{-1}$ ). This makes the design of STC channels for oils and organic solvents more difficult. Zimmermann et al. (186) demonstrated an excellent route to attaining spatial domains of superoleophobicity and superoleophilicity; however, the apparent CA value for hexadecane ( $\theta_{\text{C}_{16}\text{H}_{34}}^*$ ) on the oleophobic domain was  $\sim 140^\circ$  (not quite in the super-repellent regime), with no report of liquid sliding behavior or STC channel velocities, and no wettability mention for alcohols.

In one application, Chang et al. (187) used oleophobic/oleophilic patterning to produce microchips by a capillary-driven, self-assembly process. In another publication, Kobaku et al. (39), fabricated site-selective, self-assembling surfaces for low-surface tension liquids; the patterned superomniphobic-superomniphilic surfaces targeted applications ranging from surface directed microchannels for liquid phase reactions, to site-selective condensation of heptane vapors, and preferential nucleation of methanol under boiling conditions. Such self-assembling surfaces also can enable low-cost patterning of solution-processed polymers or suspensions of micro/nanoparticles. It should be noted that the focus of that work was on site-specific self-assembly, while the emphasis of the present work is on facile pumping of low-surface tension liquids and low-cost, large-area fabrication. Despite many attractive application prospects in synthetic biology, chemistry and heat transfer, only limited literature exists today on substrates with spatially-patterned wettability for low surface tension liquids.

We report a facile method to produce large-area, STC tracks for low-surface tension liquids. These 2-D tracks attain liquid velocities approaching  $3 \text{ cm s}^{-1}$  for low-viscosity liquids, thus bridging a gap in the literature for unassisted, capillary driven, open channel micro-fluidic transport of oils, solvents and alcohols. The STC tracks are fabricated from spray coating a fluoroacrylic-carbon nanofiber dispersion to form a superoleophobic surface, which is subsequently patterned with a paraffin wax-hexane solution to form wettable tracks. To demonstrate the facile nature of the present technique, the wax patterning is done by a continuous fountain-pen printing method—a relatively simple process. However, the technique should be amenable to other finer-scale liquid patterning processes (*e.g.*, ink-jetting, etc.), which can attain spatial



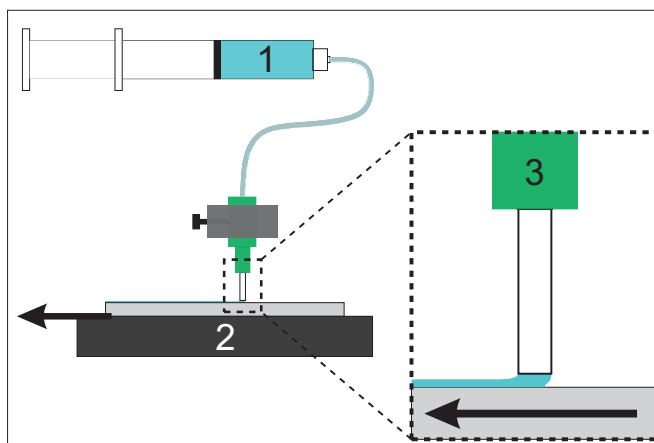


Figure 30. Continuous fountain-pen printing setup: 1) Syringe containing wax-hexane solution (dispensed by an automated syringe pump, not pictured); 2) linearly translating substrate (attained by a computer controlled linear actuator, not pictured); 3) detail showing polypropylene nozzle dispensing wax-hexane solution onto the coated (oleophobicized) glass slide, substrate moving right-to-left, nozzle held at a fixed position.

resolutions in the micrometer regime. Spontaneous transport of water (which only partially wets the wax) in the tracks is not observed; however, anisotropic wetting behavior is seen,<sup>(188)</sup> as mm-size water droplets slide under the influence of gravity along the track direction, but remain pinned when tilted against the non-wettable curbs <sup>(189)</sup>. In this case, tracks act to guide sliding water droplets with the aid of gravity.

## 5.2 Experimental

### 5.2.1 Materials and Procedure

The dispersion formulation used to form the superoleophobic base coating has been reported elsewhere (88); a brief description is given here for completeness. First, carbon nanofibers (CNF), (PR-24-XT-HHT; Pyrograf III) were acid treated with acetic acid (99.9 wt.%, ACS Certified, Fisher Scientific) and bath sonicated (output power 70 W; frequency 42 kHz; Cole-Parmer, Model 08895-04) for 10 min. producing a ‘mud-like’ material (2.5 wt.% CNF in acetic acid), which was subsequently diluted with acetone (0.9 wt.% CNF in acid and acetone) and probe sonicated (750 W, 13 mm probe dia., 40 % amplitude, 20 kHz frequency, Sonics & Materials, Inc., Model VCX-750) for 1.5 min. Separately, an aqueous fluoroacrylic copolymer dispersion (PMC, 20 wt.% in water, Capstone ST-100, DuPont) was diluted with acetic acid and then acetone to form a 2.9 wt.% PMC stock solution (1:2.5:5 wt. ratio of water:acetic acid:acetone). This stock solution was then added to the stable CNF-acetone-acetic acid suspension (1:1.5 wt. ratio PMC:CNF), which was then bath sonicated for 10 min until a stable dispersion was formed. The dispersion was subsequently spray cast with an airbrush (Paasche VL siphon feed, 0.78 mm spray nozzle) onto aluminum plates or glass slides using compressed air (2.1 bar). The coatings were initially dried by a heat-gun (Proheat<sup>®</sup> Varitemp<sup>®</sup> PH-1200, 1300 W max) for several minutes and were then placed in an oven at 70 °C for 60 min to dry completely, thus forming the oleophobic base coating for the subsequent step (wettability patterning). For that, a 1 wt.% (0.7 vol.%) solution of paraffin wax (melting point 53-57 °C , Sigma-Aldrich) in hexane (> 98.5%, ACS reagent, Sigma-Aldrich) was formed by adding wax

to hexane and shaking mechanically for several minutes at room temperature. Patterning was done by a continuous fountain-pen printing technique (see Figure 30) whereby the wax solution was dispensed with a syringe pump (Cole-Parmer, 74900 Series) out of an 18 gauge polypropylene needle (1.27 mm outer dia., 0.84 mm inner dia., 12.7 mm length; EFD<sup>®</sup>) at 15  $\mu\text{L min}^{-1}$ ; the needle was kept at a fixed distance of 250  $\mu\text{m}$  above the coating, while the substrate was translated at a fixed speed (3.7  $\text{mm s}^{-1}$ ; Velmex translation stage). Patterned areas were subsequently dried quickly with the heat-gun. Track widths of  $\approx 1$  mm were readily formed under these process parameters. Since the track width is proportional to the needle diameter, features well below 1 mm were also printed with a 31 gauge needle (0.24 mm outer dia., 0.1 mm inner dia.). Figure 30 shows a description of the fountain-pen printing setup.

### 5.2.2 Characterization

Wettability characterization was done by measuring advancing and receding contact angle (CA) values for uniform wettability areas by the sessile drop method, whereby 5-10  $\mu\text{L}$  of each probe liquid was dispensed (advancing measurement) and removed (receding measurement). Advancing and receding CAs were captured with a high-speed, backlit image acquisition setup (Redlake MotionPro); a different spot location on the coated substrate was used for each measurement. The morphology of the unpatterned and patterned, spray deposited coating was characterized by scanning electron microscopy (SEM) analysis (Hitachi S-3000 N). All samples were coated with a conforming 4 nm layer of Pt/Pd prior to SEM imaging. Liquid transport along the patterned STC tracks was captured with a high-speed camera (frame rate 50  $\text{s}^{-1}$ , Redlake MotionPro) and was used to measure flow velocity. For each experiment, a droplet of

the appropriate fluid (3.7  $\mu\text{L}$  acetone; 3.8  $\mu\text{L}$  ethanol; 4.5  $\mu\text{L}$  hexadecane) was placed at one end of a 1 mm x 25 mm track and the impending flow was visualized at high speed from above.

### 5.3 Results and Discussion

TABLE VIII

APPARENT ADVANCING CONTACT ANGLE AND RECEDING CONTACT ANGLE  
VALUES FOR LIQUIDS OF DIFFERENT SURFACE TENSIONS ON A  
SUPEROLEOPHOBIC PMC-CNF COATING (60 WT.% CNF); VALUES OBTAINED  
FROM HANDBOOK.<sup>10</sup>

liquid	$\sigma_{lv}$ (mN m <sup>-1</sup> )	$\theta_a^*$ (°)	$\theta_r^*$ (°)
water	71.99	$160 \pm 3$	$156 \pm 3$
DMSO	42.92	$155 \pm 3$	$152 \pm 4$
hexadecane	27.05	$157 \pm 2$	$142 \pm 9$
ethanol	21.97	$144 \pm 3$	$\approx 0$
isopropanol	20.93	$125 \pm 4$	$\approx 0$
hexane	17.89	$49 \pm 7$	$\approx 0$

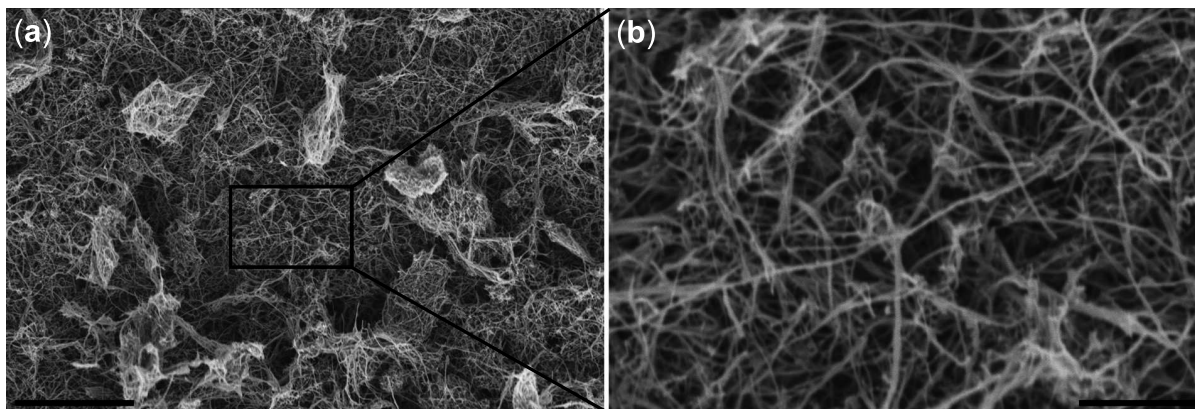


Figure 31. SEM micrographs of a superoleophobic, spray-deposited, fluoroacrylic/CNF composite coating with  $w_p = 0.60$  CNF at (a) low-magnification and (25  $\mu\text{m}$  scale bar) (b) high-magnification (5  $\mu\text{m}$  scale bar).

Over the past few years, many studies have investigated liquid repellent surfaces generated from spray deposited polymer-particle dispersions; the polymer acts to reduce surface energy and the role of the filler is to create surface texture (115; 117). In the present coatings, the overlapping CNF particles create inherently re-entrant textures (see Figure 31), which are necessary for superoleophobicity ( $\theta_a^* > 150^\circ$ ; see Table VIII) (77). Table VIII shows that the self-cleaning behavior of the coating (*i.e.*, low CA hysteresis) is lost with lower surface tension liquids, such as alcohols. However,  $\theta_a^*$  retains values indicating that alcohols do not spread

---

<sup>10</sup>Values for surface tension obtained from the *CRC Handbook of Chemistry and Physics, 2005, 85 ed.*

spontaneously on these coatings. For the case of ethanol,  $\theta_a^*$  is relatively high, implying a non-trivial differential pressure across the droplet interface (*i.e.*, Laplace pressure). Recently, high Laplace pressures inside water droplets interacting with superhydrophobic surfaces have been shown to be useful for self-pumping, superhydrophobic-patterned surface microfluidic (S<sup>2</sup>M) platforms, where liquid motion is induced by the merging of a larger droplet with a smaller droplet, both of which are connected by a microchannel (190). For water, contact angle hysteresis has been shown to be important in two-dimensional lab-on-paper devices where water contact angle hysteresis is selectively increased in predefined areas on a superhydrophobic paper—so called hysteresis enabled lab-on-paper (HELP); such an approach enables one to perform storage, guided transport, mixing and sampling of test liquids (191). Such clever techniques can be extended to low-surface tension liquids only if the surfaces contain wettability patterns capable of confining low-surface tension fluids, which is non-trivial to achieve. Our facile approach to form such patterns uses an approach that circumvents sophisticated top-down microfabrication steps. In addition, our technique—wherein we apply wax solution locally to selectively increase the surface energy on predefined tracks—results in considerable materials saving. We focus on pumpless transport of low-surface tension liquids in open, surface-tension-confined tracks by capillary action—a different mechanism than in the S<sup>2</sup>M and HELP devices, which are mentioned here only to show the wide variety of potential applications of the present approach.

On smooth surfaces with high surface energy, droplets may occupy one of two possible wetting states: 1) total wetting, or 2) partial wetting. The specific wettability state can be

predicted using the spreading parameter  $S$  (see Equation 1.1). The critical surface tension of the solid, which is denoted by  $\sigma_c$ , corresponds to  $S = 0$ .  $S > 0$  (*i.e.*,  $\sigma_{lv} < \sigma_c$ ) predicts total wetting (*i.e.*, equilibrium CA  $\theta_e = 0$ ), while  $S < 0$  corresponds to partial wetting (*i.e.*,  $\theta_e \neq 0$ ).  $S = 0$  marks the transition between the two wetting states. For liquids satisfying the condition  $S > 0$ , spontaneous transport in STC channels is expected *a priori*; however, for liquids with  $S < 0$ , spontaneous liquid spreading is not guaranteed. The above discussion applies for smooth surfaces. For rough surfaces, partial wetting may give rise to a situation referred to as *hemi-wicking* (71), where the liquid invades the texture but leaves exposed a portion of the solid. This configuration is thermodynamically favored when  $\theta_e$  satisfies the inequality in Equation 1.7. Estimates of equilibrium CA on paraffin wax ( $\theta_{e, \text{wax}}$ ) for several of the probe liquids utilized in this study can be found in Fox & Zisman (192); in general,  $\sigma_c$  for the  $\text{CH}_3$  and  $\text{CH}_2$  bonds (*i.e.*, paraffin wax) is in the range of 22-31 mN m<sup>-1</sup> (193), which overlaps with the surface tensions of the organic probe liquids investigated herein (see Table VIII). Considering the case where  $\Phi_{sl} \ll 1$  (*i.e.*, large area fraction of liquid in channels), Equation 1.7 becomes

$$\cos \theta_c \approx \frac{1}{R}. \quad (5.1)$$

When  $\sigma_c$  and  $\sigma_{lv}$  are comparable—as is the case here—then from Young’s relation (58) it follows that  $\theta_e$  should be relatively low; for hexadecane (192)  $\theta_{e, \text{wax}} = 27^\circ$ . Setting  $\theta_{e, \text{wax}} = \theta_c = 27^\circ$  and substituting into Equation 5.1, it follows that  $R = 1.06$ , implying that for the case of  $S < 0$  (partial wetting), only a relatively small amount of surface roughness is required to

produce hemi-wicking behavior. This level of roughness is well below that achieved by spray cast coatings which contain high concentrations of filler particles (*cf.* Figure 31,  $w_p = 0.60$  CNF). So if the wax were deposited as a conformal, thin layer onto the highly textured coating, then it would be possible to produce hemi-wicking behavior. The wax should be solution-processed with a low-surface tension liquid so as to partially wet ( $S < 0$ ) the underlying textured surface, and ultimately, produce patterns on the highly liquid-repellent coating. From Table VIII we deduce that hexane does not fully wet the CNF coating, so this liquid offers an appropriate choice for patterning wettable tracks on top of the superhydrophobic terrain; fully wetting liquids, which spread uncontrollably, would make it extremely difficult to pattern with good resolution. When applying the wax coating, it is necessary to preserve the underlying surface texture, otherwise the desired hemi-wicking behavior may not be attained. The deposited wax thickness is a function of printing speed, wax-hexane solution flow rate, the printing nozzle diameter and solution concentration. From Figure 31, the surface texture appears to have four apparent length scales: 1) micro-clusters of CNFs (see **a**; with length scale  $\approx 10\mu\text{m}$ ), 2) CNF diameter (see **b**;  $\approx 100$  nm (88)), 3) CNF length ( $\approx 10\text{--}30\mu\text{m}$  (88)) and 4) pores in-between adjacent CNFs (see **b**;  $\approx 1\mu\text{m}$ ). If one wishes to preserve coating feature sizes larger than  $\approx 1\mu\text{m}$  (*i.e.*, the large micro-clusters seen in Figure 31), then one must ensure that the wax film thickness is approximately the same or below this value. The substrate linear translation speed ( $u_t$ ) and dispensing volumetric flow rate ( $Q$ ) are related through  $Q \sim u_t h_{\text{film}} d_n$ , where  $d_n$  is the inner diameter of the nozzle and  $h_{\text{film}}$  is the film thickness of the deposited wax-hexane solution. The relation between the film thickness of the wax-hexane solution and the



dry wax coating thickness ( $h_{\text{wax}}$ ) is  $h_{\text{wax}} = ch_{\text{film}}$ , where  $c$  is the volumetric concentration of wax in hexane. Taking  $Q=15 \text{ } \mu\text{L min}^{-1}$ ,  $h_{\text{film}} \approx 100 \text{ } \mu\text{m}$  and  $d_n=0.84 \text{ mm}$ ,  $u_t$  becomes  $3.0 \text{ mm s}^{-1}$ . Our substrate velocity in the track deposition experiments was  $3.7 \text{ mm s}^{-1}$ , which is comparable to the calculated value. We applied three successive layers of 0.7 vol.% solution on each area to produce the desired wetting behavior (*i.e.*, capillary driven flow), which implies an overall wax-layer thickness of  $\approx 2 \text{ } \mu\text{m}$ . Thicker, as well as thinner, wax layers resulted in channels with unfavorable capillary behavior (*i.e.*, no liquid movement). Figure 32 presents SEM micrographs of a wax-patterned, composite coating. We see that most of the low-lying valleys have been filled, but the micro-cluster texture remains in the areas protruding above the polymer. The space between adjacent micro-clusters forms a channel, as is evident from Figure 32b. The average micro-cluster interspacing was estimated to be  $18 \pm 7 \text{ } \mu\text{m}$ , as based on 66 distinct measurements.

An important property of microchannels is the fluid advancing velocity. For our STC tracks, the dynamic transport is affected by both viscous and capillary forces (194). We assess the moving liquid front's velocity by modeling the liquid advancement as capillary driven impregnation of the liquid into the pores of the rough underlying surface. The pores can be imagined as small channels in their own right. A balance of capillary and viscous forces yields (195)

$$u_m \sim \frac{\Delta p d_{\text{pore}}^2}{\mu x} \sim \frac{\Delta \sigma d_{\text{pore}}}{\mu x}, \quad (5.2)$$

where  $\Delta p \sim \Delta \sigma / d_{\text{pore}}$  represents the Laplace pressure due to the presence of a curved

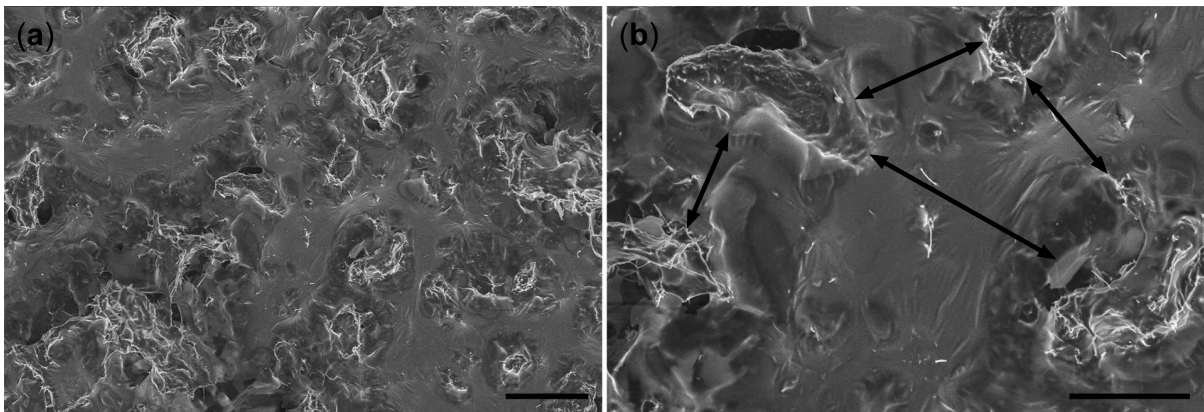


Figure 32. SEM micrographs of a wax-coated, fluoroacrylic/CNF ( $w_p = 0.60$  CNF) composite coating at (a) low-magnification (50  $\mu\text{m}$  scale bar) and (b) high-magnification (25  $\mu\text{m}$  scale bar). Arrows in (b) demonstrate example measurements of the interspacing values between micro-texture features that remain exposed after wax-patterning.

TABLE IX

MEASURED AND PREDICTED AVERAGE SPEEDS FOR FLUIDS OF DIFFERENT DYNAMIC VISCOSITY (VISCOSITY VALUES OBTAINED FROM HANDBOOK<sup>11</sup>) TO TRAVERSE A LENGTH IN 1 MILLIMETER-WIDE STC TRACKS.

liquid	$\mu$ (mPa s)	$\Delta x$ (cm)	$\frac{\Delta x}{\Delta t}$ (cm s <sup>-1</sup> )	$u_m$ from Equation 5.2 (cm s <sup>-1</sup> )
acetone	0.306	1.03±0.01	3.1±0.5	13.8
ethanol	1.074	1.08±0.06	1.2±0.3	3.68
hexadecane	3.032	1.08±0.06	0.7±0.1	1.61

liquid-vapor interface (in between the protrusions seen in Figure 32b),  $d_{\text{pore}}$  is the average pore diameter (selected values depicted by the arrows in Figure 32b),  $\mu$  the dynamic viscosity of the fluid and  $x$  the position of the advancing liquid front, which varies with time;  $\Delta\sigma = \sigma_{\text{sv}} - \sigma_{\text{sl}}$  describes the surface energy change as the fluid column advances. For highly wetting cases (*i.e.*,  $\theta_e \approx 0$ ) where  $\sigma_{\text{sv}} \gg \sigma_{\text{sl}}$  (*e.g.*, for hexadecane) (192), from Young's relation (58)  $\sigma_{\text{sv}} \approx \sigma_{\text{lv}}$ , and we deduce  $\Delta\sigma \approx \sigma_{\text{lv}}$ . Stated simply, for highly wetting situations  $\Delta\sigma$  can be approximated by the surface tension of the liquid. Table IX presents the measured velocity ( $\frac{\Delta x}{\Delta t}$ ) of the advancing liquid front for the first 1.0 cm of travel, as well as the values computed from Equation 5.2

---

<sup>11</sup>Values for viscosity obtained from the *CRC Handbook of Chemistry and Physics, 2005, 85 ed.*

for  $d_{\text{pore}} = 18 \text{ } \mu\text{m}$  (the previously measured average pore scale). The order of magnitude agreement between the predictions and the measurements is quite good, although we have neglected the energy cost of generating new free surface as the liquid flows along the STC tracks and through the obstacles posed by the CNF protruding clusters. The data listed in Table IX shows that Equation 5.2 overestimates the measured velocity more for the case of acetone and ethanol, as compared with hexadecane. The reason for this discrepancy may be due to the approximation of  $\Delta\sigma$ . In the case of alkanes, it is known that the magnitude of the previously neglected term,  $\sigma_{\text{sl}}$ , is less than in the case of oxygen-containing liquids (192). Considering that  $\theta_{\text{e, wax}} = 33 \pm 2^\circ$  for ethanol (196) and  $27^\circ$  for hexadecane (192), from Young's relation the respective values for  $\Delta\sigma$  are 18.4 and 24.1 mN m<sup>-1</sup>. The error of the approximation  $\Delta\sigma \approx \sigma_{\text{lv}}$  is then 19% and 12%, respectively for ethanol and hexadecane. Therefore, for liquids containing oxygen (such as ethanol), one should exercise reserve in applying this approximation. On the other hand, for highly volatile liquids like acetone, this approximation may be the only possible approach due to difficulties associated with measuring  $\theta_{\text{e}}$  on wax (rapidly changing liquid volume due to evaporation). In this case, one should expect that  $\Delta\sigma$ , and ultimately  $u_{\text{m}}$ , would be overestimated (as seen in Table IX). Figure 33 draws the measured values of the liquid wetting front position along an STC track as a function of time for liquids of different viscosity and comparable surface tension (acetone, ethanol, hexadecane; see Figure 34 for an image sequence of hexadecane transport on a straight track). As expected, increasing viscosity (from acetone to ethanol to hexadecane) results in slower liquid velocities on the respective

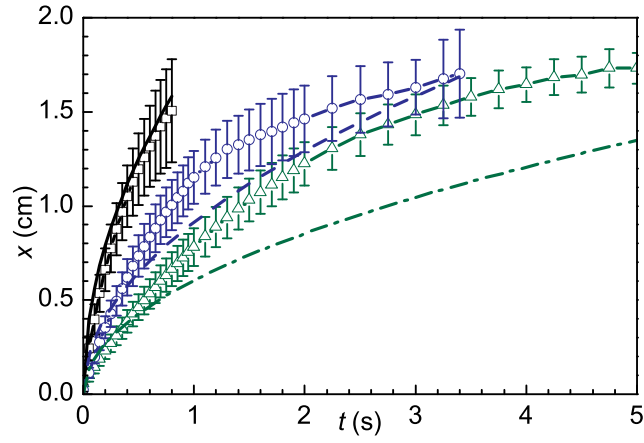


Figure 33. Measured data for liquid wetting meniscus position ( $x$ ) as a function of time ( $t$ ) for

acetone ( $\text{—}\square\text{—}$ ; average of 10 trials), ethanol ( $\text{--}\circ\text{--}$ ; average of 14 trials) and hexadecane ( $\text{--}\triangle\text{--}$ ; average of 14 trials) flowing in wax-patterned STC tracks.

Washburn theory prediction of  $x$  vs.  $t$  for acetone (solid line), ethanol (dashed line) and hexadecane (dot dashed line) for liquid flow in wettable  $18\text{ }\mu\text{m}$  pores (from Equation 5.3).

Inset is a top-view image of horizontally-placed patterned tracks with ethanol advancing by capillary action.

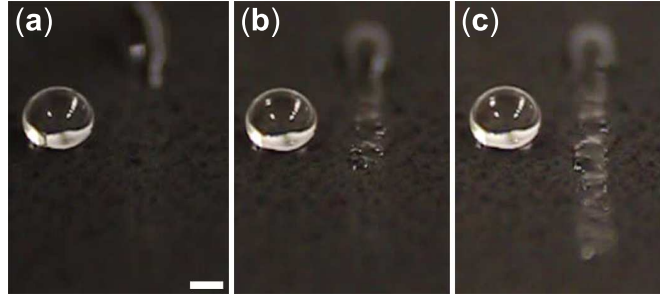


Figure 34. STC line tracks printed with wax on a superoleophobic fluoroacrylic/CNF composite coating. Two identical hexadecane droplets are placed, one outside the wax-coated area (left), and the other (top middle) on the wax line at (a)  $t=0s$ , (b)  $t=1s$  and (c)  $t=3s$ . Note how the fluid advances along the straight track via capillary action. Scale bar is 1.0 mm.

track. In order to better describe the wetting behavior (*i.e.*, liquid penetration), we utilize the familiar Washburn equation (194)

$$x = \sqrt{\frac{\sigma_{lv} d_{pore} t}{4\mu}}, \quad (5.3)$$

which is also plotted in Figure 33 for acetone, ethanol and hexadecane with  $d_{pore} = 18 \mu m$ . The trends are quite consistent, although it appears that Equation 5.3 significantly underestimates the advancing wetting front for hexadecane, as compared with acetone and ethanol. This is a complex issue and at its core demonstrates the limitations of the applicability of Washburn's equation to the present data sets. First, Washburn's equation neglects the generation of new free surface (costly in terms of energy), which should ultimately slow the velocity of the advancing liquid. For the idealized case of wetting of pillars—where the tops of the pillars are also wet

(*i.e.*,  $\theta_e \approx 0$ )—the percentage of surface energy consumed by generating a new free surface as a liquid advances is  $1/(1 + R)$  (58). Even for a highly rough case with  $R = 3$  (71), the relative amount of surface energy consumed by free surface generation is 25%. Lower values of  $R$  would raise this estimate. Ultimately most important is the effective pore size or characteristic length scale. It is tempting to idealize a textured surface as a series of hollow cylinders due to the ease of which one can model fluid transport in between such cylinders. While we performed SEM and measured characteristic length scales that we felt were representative of an effective micro-channel width (idealized as a pore in Equation 5.3), this characteristic length scale had a standard deviation of almost 60% around its mean value, which highlights the large discrepancy from the idealized case. Nevertheless, despite its potential short-comings, Equation 5.3 models the wetting behavior for acetone and ethanol quite well. Patterning the wettability of surfaces is likely to have a wide palette of applications that vary depending on the surface tension of the liquid being used. As an example, the method could be employed for facile fabrication of surfaces with anisotropic wettability (188). The following illustrates how the method could be implemented to gain directional movement control of small liquid volumes on a pre-patterned surface. Since we utilized wax in the oleophilic tracks, it is expected that these tracks would be partially-to-fully superhydrophobic. Figure 35(a) is a schematic demonstrating the anisotropic wetting of mm-sized water droplets (blue) inside a mm-wide STC track, where  $\alpha$  and  $\beta$  define the tilting angles around two orthogonal axes. Figures Figure 35(b)-(c) show the shape of the water droplet placed on a line STC track in an untilted ( $\alpha = 0^\circ$ ) and tilted ( $\alpha = 90^\circ$ ) state, respectively (**b-c** camera view fixed). In **c**, note the non-circular solid-liquid contact area of

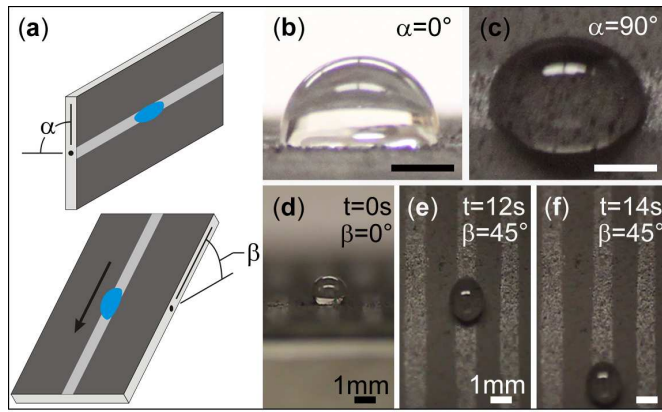


Figure 35. (a) Schematic of anisotropic wetting of water droplets placed in line STC tracks.  $\alpha$  and  $\beta$  define tilting angles with respect to axes parallel and normal to the track, respectively; droplets remain pinned for  $\alpha > 0^\circ$  and slide for adequate values of  $\beta > 0^\circ$ ; (b)-(c) demonstrate the confinement of a water droplet (*i.e.*, no mobility) even for  $\alpha = 90^\circ$ ; (d)-(f) demonstrate droplet sliding action for  $\beta = 45^\circ$  in the time period  $t = 0$  to 14 s. Inset scale bars are all 1 mm and the droplet volume is 10  $\mu\text{L}$ .



the water droplet, which remains immobile and pinned against the hydrophobic curbs. Figures Figure 35(d)-(f) show an image sequence of a water droplet on a track in an untilted and tilted state; the droplet demonstrates its mobility in Figs. Figure 35(e)-(f). The required minimum angle  $\beta$  for droplet sliding was  $25 \pm 4^\circ$ —an increased value over unpatterned (superhydrophobic) areas of the coating where droplets slid at tilt angles below  $10^\circ$ . The anisotropic wetting property can be exploited in these open tracks to guide large water droplets with the aid of gravity. The sine of the minimum sliding angle of a droplet with an idealized rectangular solid/liquid contact area can be calculated as  $(l_{\text{track}} \sigma_{\text{lv}} (\cos \theta_r^* - \cos \theta_a^*)) / (\rho V g)$ , where  $l_{\text{track}}$  is the width of the wettable track,  $\rho$  the fluid density,  $V$  the droplet volume, and  $g$  the acceleration of gravity (75; 76). From the above expression, we see that by reducing  $l_{\text{track}}$ —the patterned track width—we can reduce the overall sliding angle of the droplet, *i.e.*, increase the mobility of the droplet on the track.

## CHAPTER 6

### WETTABILITY ENGINEERED SURFACES: THERMAL STABILITY AND SCALABILITY

This chapter and its associated appendix (Appendix A) were published in: T. M. Schutz-  
ius, I. S. Bayer, G. M. Jursich, A. Das and C. M. Megaridis, *Nanoscale*, 2012, 4, 5378 DOI:  
10.1039/C2NR30979C - Reproduced by permission of The Royal Society of Chemistry (48).

#### 6.1 Introduction

Polyhedral oligomeric silsesquioxanes or, in short polysilsesquioxanes (POSS), are organici-norganic hybrid materials having unique molecular structures (197). POSS resins are a class of silicon compounds with the empirical formula  $\text{RSiO}_{1.5}$ , where R denotes hydrogen or an alkyl, alkylene, aryl, or arylene group. The POSS name is derived from one and one half (1.5) or sesquistoichiometry of oxygen bound to silicon. POSS molecular building blocks can be tuned for desired optical, structural and mechanical properties (198). The most common form of POSS is a three dimensional Si–O cage framework, commonly known as a POSS nanocage. Among POSS compounds, solution-processable hydrogen silsesquioxane (HSQ) or methylsilsesquioxane (MSQ) resins generally find applications as low-dielectric materials for integrated circuit devices (199; 200; 201; 202; 203; 204) and are also used as an alternative route to produce silica coatings (205; 206). For high temperature applications, POSS resins may have greater advantages over their organic polymer counterparts due to their inherently higher bond strength (207; 208).

Silsesquioxanes can be produced with a variety of pendant chemical groups (*i.e.*, alkyl, aryl, etc.), thus allowing appreciable solubility in organic solvents for solution processing; MSQ is expected to be hydrophobic due to the presence of methyl groups. Further enhancement of film hydrophobicity may be attained by introducing hydrophobic inorganic nanoparticles, such as hydrophobic fumed silica (*i.e.*, silica modified by silanes or siloxanes), into the MSQ film. These filler particles not only lower the surface energy of the films, but also affect surface texture, two factors known to significantly influence hydrophobicity (115; 117). With proper combination of hydrophobic nanoparticles, it seems possible to achieve superhydrophobic coatings based upon POSS materials, thereby circumventing problems associated with organic polymers, and in turn, offering improved coating thermal stability and scratch resistance. Finally, due to the ability of POSS to oxidize (206) and generate hydrophilic functional groups (*i.e.*, silanol) (205), it may be possible to induce spatially abrupt wettability transitions in such coatings (from superhydrophobic to superhydrophilic) if, for example, hydrophobic Si-CH<sub>3</sub> bonds of MSQ were to be replaced with hydrophilic functional groups in select locations. Similar logic applies for silane or siloxane modified silica (*e.g.*, HFS) as under oxidizing conditions silicon will readily abandon linkages with hydrogen or carbon in preference for oxygen, thus inducing hydrophilicity (207). If it is possible to induce a wettability transition to a POSS nanocomposite coating by a fast thermally assisted process—such as with flame exposure or laser irradiation—then one may be able to fabricate chemically stable surfaces patterned with superhydrophobic and superhydrophilic area regions by large-area processing. With laser-beam heating, patterning the wettability at the micrometer scale may be possible.

The advantages of alternating hydrophobic-hydrophilic areas have been extolled in a recent patent (209), where a sol-gel method was used to apply transparent superhydrophobic silica coatings whose wettability could be locally modified continuously from superhydrophobic to superhydrophilic by masked UV exposure. In the open literature, alternating superhydrophobic-superhydrophilic area patterns with well-defined repeatable features have been reported only by a handful of groups. For example, Zhai et al.(43) generated hydrophilic patterns on superhydrophobic surfaces by selective deposition of polyelectrolyte/water/2-propanol mixtures; such surfaces mimic the water harvesting behavior of the *Stenocara* beetle's back (42). Garrod et al. (210) utilized a two-step, plasma chemical approach to generate said surfaces; their applications include fog harvesting, microfluidics, and biomolecule immobilization. Other reported patterning approaches include photo degradation of hydrophobic chemistry (211; 212), and photo-induced modification of hydrophobic/hydrophilic chemistry (213). In addition, highly desirable surface-tension-confined (STC) micro channels in two (182) and three dimensions (183) can also be realized through wettability patterning techniques. UV-irradiation has been used (214) to generate such micropatterns. Most recently, Zahner et al.(185) used UV-initiated photo grafting to generate virtual microfluidic channels in the form of superhydrophilic micropatterns on a superhydrophobic porous polymer film; one possible application is two-dimensional peptide separation (184). However, most of these patterning techniques require the use of masks (*e.g.*, plasma chemical (210), photo degradation techniques (211; 212), photo-induced technique (213), UV-irradiation (214; 185)) or closed chambers (210). Masks limit the flexibility in changing the type of pattern on-the-fly, while chambers limit scalability and increase the patterning

costs. Finally, in some superhydrophilic patterning techniques, the property is not permanent, as is the case with UV-irradiation of TiO<sub>2</sub> containing coatings (214). Such coatings also require large concentrations of filler particles to attain superhydrophilicity (214), which may reduce their adhesion and durability as compared with other coating systems. None of the previous works on superhydrophobic-superhydrophilic area patterning involved silsesquioxanes.

We report herein spray-based fabrication of large-area superhydrophobic MSQ-HFS nanocomposite coatings, which are capable of becoming superhydrophilic when thermally treated by simple flame or laser exposure. Micro-patterned wettability—with alternating areas of superhydrophobicity and superhydrophilicity—is demonstrated for the first time using localized thermal treatment applied by computer controlled CO<sub>2</sub> (infrared) laser irradiation in open air. Open STC micro-channels are thus formed by large-area, two-step processing (*i.e.*, spray and laser treatment). Spray deposition and CO<sub>2</sub> laser processing (thermal treatment) are two efficient industrial processes, making them ideally suited for large-area applications. It takes seconds of laser treatment to form a 0.1 m long open STC micro-channel. Applications are envisioned in microfluidics and other small liquid volume handling technologies. Due to their ability to withstand temperatures well above the boiling point of water, one possible application of such patterned binary-wettability coatings is in the area of enhanced heat transfer (*e.g.*, pool boiling). The present technique is not substrate limited, therefore such patterns can be applied on thermally-conductive materials (*e.g.*, metals), which are necessary in heat transfer applications at elevated temperatures. This feature, along with the thermal stability of the present patterns, opens new horizons in technologies involving high temperature fluids.

TABLE X

COMPOSITION OF DISPERSIONS USED TO MAKE MSQ-HFS COATINGS.

ingredient	concentration (wt.%)
20 wt.% MSQ in alcohol	16.7
hydrophobic fumed silica	0.0-8.3
isopropanol	83.3-75.0

## 6.2 Experimental

### 6.2.1 Materials

The materials used were: isopropanol (IPA, Sigma-Aldrich, USA), methylsilsesquioxane resin (Gelest, Inc.; 19-21 wt.% in a mixture of methanol, n-butanol, and isopropanol), and hydrophobic fumed silica, Aerosil®; silane or siloxane modified silica).

### 6.2.2 Procedure

In a 20 mL glass vial, hydrophobic fumed silica and IPA were combined and sonicated (Sonics®, 750 W, High Intensity Ultrasonic Processor, 13 mm diameter tip at 30 % amplitude) to form a suspension. Once a stable HFS-IPA suspension was formed, the MSQ solution in alcohol was added, and the entire dispersion was sonicated until a stable dispersion formed. Typical sonication procedures lasted 1-2 min under ambient conditions; longer sonication times resulted in undesirable boiling loss of the alcohol solvents. Stable dispersions (Table X) were

then spray cast with an airbrush atomizer (Paasche VLS, siphon feed, 0.73 mm nozzle) onto stainless steel, aluminum foil, copper, quartz, and glass slide substrates at a spray distance of 10 cm and were subsequently heated with a heat gun (Proheat<sup>®</sup> Varitemp<sup>®</sup> PH-1200, 1300 W max) to immediately remove solvents, and an oven at 130°C for 1 hr to allow the coating to dry. Alternatively, thermal treatment—for the purposes of inducing a wettability transition—was done with either a propane flame or a CO<sub>2</sub> laser (100 W max, 25  $\mu$ m spot size, mounted on a computer-controlled 3-axis stage; output power is controlled by a percentage of maximum power, *i.e.*, 1.0% power corresponds to  $\sim$ 1 W). For some samples, laser patterning was used to form repeating islands of either hydrophobic or hydrophilic nature.

### 6.2.3 Characterization

Environmental scanning electron microscope (ESEM, Philips XL30 ESEM-FEG) and scanning electron microscope (SEM, Hitachi S-3000N, variable pressure) images were obtained after samples were sputter-coated with a conformal 5 nm thick layer of Au-Pd or Pt-Pd. X-ray photoelectron spectroscopy (XPS, Kratos AXIS-165) was performed on heat gun-treated, flame-treated, and laser-treated MSQ-HFS coatings deposited on stainless steel, to investigate the effect of thermal treatment on the surface chemistry of the coating. Thermogravimetric analysis (TGA) was performed to determine degradation temperatures and reveal the related mechanisms. Sessile, advancing and receding contact angle values were obtained with a backlit, optical, high speed image acquisition setup (Redlake MotionPro) utilizing 10  $\mu$ L water droplets. Coating heat treatment—for the purposes of analyzing the effect of temperature on wettability—was done with a standard hot-plate. Each sample was kept at a constant, elevated

temperature for 1 hr (*e.g.*, 200°C, 300°C, etc.) and then was removed and allowed to cool down to ambient temperature. Each sample was subsequently characterized by sliding angle measurements with 5.0  $\mu\text{L}$  water droplets on a tilting stage with 1° accuracy.

### 6.3 Results and Discussion

The purpose of introducing hydrophobic, inorganic nanoparticles into the spray dispersion is to affect the coating surface texture resulting after application and drying—a well-established approach for achieving superhydrophobicity (115; 117; 114). Figure 36a illustrates the characteristic micro-cluster surface morphology of a MSQ-HFS coating ( $w_p = 0.5$ ) applied by spray, while the higher magnification image in Figure 36b displays the resulting nanotexture due to HFS particles embedded in the MSQ matrix. Such hierarchical surface texture is known to produce superhydrophobicity on both artificial and natural surfaces. Figure 37a presents the advancing ( $\theta_a^*$ ) and receding ( $\theta_r^*$ ) contact angles as functions of HFS concentration in the MSQ matrix. The two curves display trends similar to those seen in the classic experiments of Johnson and Dettre (113) where advancing and receding contact angles were quantified with respect to increasing substrate roughness. Contact angle hysteresis ( $\Delta\theta^* = \theta_a^* - \theta_r^*$ ) initially increases with HFS filler content (*i.e.*, surface roughness), followed by an abrupt decrease as the HFS concentration increases further, indicating a wetting state transition (*i.e.*, Wenzel to Cassie-Baxter) (69; 70). Beyond a  $w_p = 0.5$ , the coating becomes superhydrophobic (*i.e.*,  $\theta_a^* > 150^\circ$ ). The Cassie-Baxter (non-wetting) state should be realized if the true (Young's) contact angle ( $\theta_e$ ) satisfies Equation 1.6. For very rough surfaces with a high concentration of filler particles or rough surface texture due to the spray process itself, it follows that  $R \gg \Phi_{sl}$ , and the cosine



of the critical angle,  $\theta_c$ , is proportional to  $-R^{-1}$ ; thus, for highly rough, hydrophobic surfaces ( $\theta_e > 90^\circ$ ), the value of  $\theta_c$  from Equation 1.6 decreases, and Cassie-Baxter becomes the most probable wetting state, not considering metastable wetting states. As shown in Figure 37a, the contact angle hysteresis is  $8^\circ$  at  $w_p = 0.6$ , which designates a self-cleaning surface (droplets roll off the surface under only a slight substrate tilt). Further rise in hydrophobic filler concentration results in a further decrease of contact angle hysteresis. Figure 37b presents sessile contact angle values ( $\theta^*$ ) for the previously characterized coatings, before and after flame treatment. For all cases where HFS filler is incorporated into MSQ, the coatings achieve a zero-valued or immeasurably small apparent contact angle after flame treatment, thus indicating superhydrophilicity. Refer to Figure A1 for a sequence of images demonstrating flame treatment and the subsequent superhydrophilic property. The dramatic transition from non-wetting to fully-wetting state should be observed if the cosine of  $\theta_e$  satisfies the condition in Equation 1.7 ( $0^\circ < \theta_c < 90^\circ$ ). If the condition for  $\theta_e$  in Equation 1.7 is satisfied, then the liquid penetrates the surface texture but partial wetting remains due to islands emerging above the absorbed film (*i.e.*,  $\theta_e \neq 0^\circ$ ) (58). Regarding morphological changes as a result of brief flame treatment, the coating is not observed to undergo drastic changes, *i.e.*,  $R$  remains relatively high. In the limit of  $\Phi_{sl} \ll R$ , Equation 1.7 becomes

$$\theta_e < \theta_c \text{ with } \cos \theta_c \approx \frac{1}{R}. \quad (6.1)$$

Therefore, for highly rough, hydrophilic surfaces ( $\theta_e < 90^\circ$ ), the value of  $\theta_c$  from Equation 1.7 is high, and the superhydrophilic state becomes most probable.

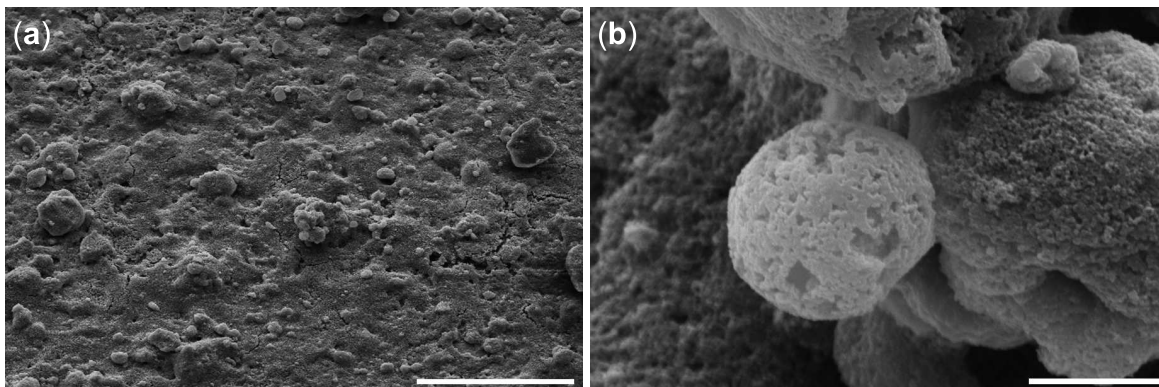


Figure 36. ESEM images of superhydrophobic MSQ-HFS coating ( $w_p = 0.5$ ) with increasing magnification from (a) to (b). (a) 50  $\mu\text{m}$  scale bar (b) 2  $\mu\text{m}$  scale bar.

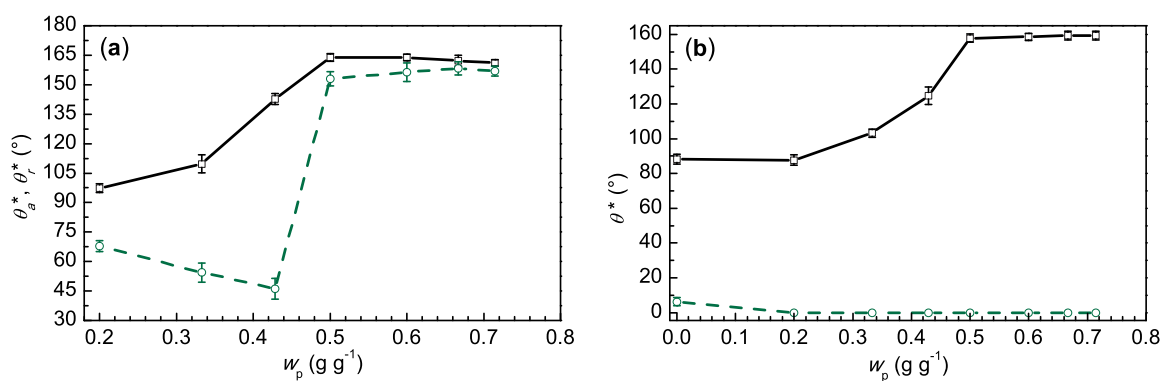


Figure 37. (a) Apparent advancing ( $\theta_a^*$ ; —□—) and receding ( $\theta_r^*$ ; ---○---) contact angles vs. filler particle concentration ( $w_p$ ). (b) Sessile ( $\theta^*$ ) contact angle vs.  $w_p$  for untreated (—□—) and flame treated (---○---) coatings.

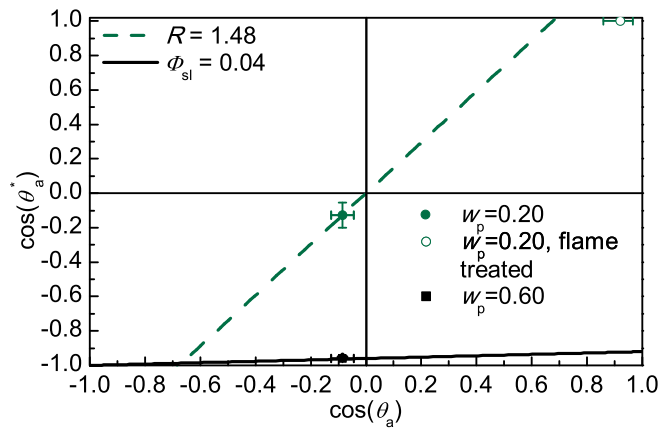


Figure 38. Apparent advancing contact angle  $\theta_a^*$  for spray cast, HFS filler-containing coatings vs.  $\theta_a$  for spin-coated MSQ (plotted in terms of their cosines). Coatings contain different concentrations of HFS, as indicated in the legend. Unfilled data points indicate flame-treated coatings. Plotted lines are for the two wetting theories; the dashed line is for Wenzel (Equation 5 with  $R = 1.48$ ), while the solid line is for Cassie-Baxter (Equation 4 with  $\Phi_{sl} = 0.04$ ).

To delineate the effects of HFS filler content (which affects texture) and thermal treatment (which affects surface energy), Figure 38 presents apparent advancing contact angles for spray cast MSQ-HFS composite films vs.  $\theta_a$  of spin-coated MSQ before and after flame treatment. The values of  $\theta_a$  for spin-coated MSQ before and after flame treatment were measured to be  $95^\circ$  and  $23^\circ$ , respectively. Two concentrations of HFS ( $w_p = 0.2$  and  $0.6$ ) are represented in Figure 38. Also plotted in the same figure are the lines for two theoretical cases, namely Cassie-Baxter (Equation 1.5 for  $\Phi_{sl} = 0.04$ ) and Wenzel (Equation 1.3 with  $R = 1.48$ ). As stated previously, for the heat-treated (wetable) MSQ,  $\theta_a = 23^\circ$ . Taking  $\theta_a$  as a conservative approximation of  $\theta_c$ , and substituting into Equation 6.1, we see that the lower threshold value of  $R$  for the validity of Equation 6.1 comes as,  $R^* = 1/\cos \theta_a \approx 1.1$ , which is an easily attainable roughness ratio. It is possible to quantify the roughness ratio of the coating prior to flame treatment by utilizing Equation 1.3; the only requirement is that the liquid droplet be in a Wenzel wetting state. At  $w_p = 0.2$ , the measured  $\theta_a^*$  value is relatively small ( $\sim 97^\circ$ ; see Figure 37a) and the hysteresis is high ( $\sim 30^\circ$ ; Figure 37a), which are characteristic traits of droplets in a partially wetting Wenzel state, thus allowing use of Equation 1.3 to quantify  $R$  (note that this particular point falls in the hydrophobic regime of Figure 38 and is prior to coating flame treatment). The dashed line Wenzel fit with  $R = 1.48$  shows that the  $w_p = 0.2$  coating is consistent with a roughness value sufficiently higher than the threshold value of 1.1, thus allowing the most stable wetting state, *after flame treatment*, to be superhydrophilic (assuming negligible morphological changes due to flame treatment).<sup>12</sup> Intuitively this corresponds to a MSQ-HFS film that is sufficiently wettable (*i.e.*, possesses high surface energy) to require only

a low level of roughness for superhydrophilicity to be energetically favored. Also in Figure 38, the data point for untreated  $w_p = 0.6$  coating resides in the lower left quadrant, suggesting that the water droplet is in a stable Cassie-Baxter wetting state, and not a metastable one (metastable states generally reside in the lower right quadrant of Figure 38). Thus, this point can be fitted with the Cassie-Baxter curve,  $\Phi_{sl} = 0.04$ , suggesting a very low fraction of the textured solid being in contact with the beaded liquid.

CO<sub>2</sub> lasers offer a controlled approach to thermal treatment due to their ability to deliver high levels of energy to localized surface areas. Since most materials are opaque at 10  $\mu\text{m}$  (laser wavelength), CO<sub>2</sub> lasers offer a robust approach to surface heat treatment. Heating can be regulated by tuning beam size and energy, as well as beam exposure. Figure 39 quantifies the effect of laser treatment on wettability of pure MSQ and MSQ-HFS films as a function of laser exposure. For these tests, laser power was held constant at  $\sim 1$  W and the laser translation speed was varied. For sufficiently high fluence (*i.e.*,  $\phi > 150 \text{ J cm}^{-2}$ ), the films underwent a wettability transition to complete wetting, as indicated by the very low values of  $\theta^*$  in Figure 39, and as previously observed for the flame-treated films (*cf.* Figure 37b). It is instructive to compare the temperature ranges attained in both thermal treatment processes. In the case of propane flames, the flame temperature is  $\sim 2200$  K. For laser treatment, direct temperature measurement is difficult due to the low exposure time to the laser beam. For a laser spot diameter  $d_L$  of  $\sim 25 \mu\text{m}$

---

<sup>12</sup>While local gas temperatures in propane flames can rise to 2200 K, small propane flames impinging onto coated bulk surfaces for 1-2 seconds are not capable of raising coating temperatures up to the melting point of silica ( $\sim 1900$  K). Consequently, during flame treatment, the coating temperatures stay well below this critical value, thus eliminating the possibility of significant morphological changes in the coating texture. See Figure A6 for SEM images of a flame-treated MSQ-HFS coating.

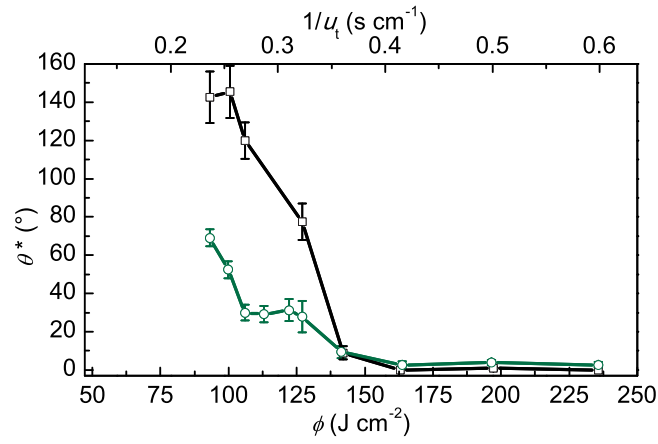


Figure 39. Sessile contact angle ( $\theta^*$ ) vs. laser fluence ( $\phi$ ) of the coating (bottom axis) and laser translation speed ( $u_t$  top axis; laser irradiance was held constant at  $I = 0.2 \text{ MW cm}^{-2}$ ).

The filler concentration was  $w_p = 0.5$  ( $\text{—}\square\text{—}$ ) and  $w_p = 0.0$  ( $\text{--}\circ\text{--}$ ). All further laser

processing was done with  $u_t = 2 \text{ cm s}^{-1}$ .

and a translation speed ( $u_t$ ) of  $2.0 \text{ cm s}^{-1}$  (the speed used for all subsequent laser treatments), the exposure time scales like  $d_L/u_t \approx 1 \text{ ms}$ . The corresponding rise in surface temperature ( $\Delta T$ ) can be estimated using an expression applicable for a semi-infinite solid medium heated on a spot (see Equation A1) (215; 216). After only  $t = 0.025 \text{ ms}$ ,  $\Delta T$  becomes  $2230 \text{ K}$  which is sufficient to cause silica boiling. Significant removal of coating material should be expected as thermal treatment extends far further than the time required to reach temperatures required for wetting transitions, potentially resulting in channel formation (for a single laser pass) or a thinner coating (for total surface treatment), the latter being advantageous for heat transfer applications, where the thermal resistance associated with thicker coating treatments must be minimized.

It is important to establish the minimum spatial feature size during  $\text{CO}_2$  laser processing. The diameter of the focused laser spot is defined as

$$d_L = \frac{4}{\pi} \lambda \frac{l_{\text{focal}}}{d_{L,0}}, \quad (6.2)$$

where  $l_{\text{focal}}$  is the beam focal length,  $d_{L,0}$  the initial beam diameter, and  $\lambda$  the beam wavelength (217). We employed a high power density lens with a  $25 \text{ }\mu\text{m}$  spot diameter. Optimization of the laser-lens-to-substrate distance was done by observing when superhydrophilicity was or was not achieved (see Figure A2). It is also important to understand the wetting transition between hydrophobic and hydrophilic areas, and more importantly, the spatial extent of this transition. A sharp transition will allow the surface to confine liquids, which has important ramifications on microfluidics and lab-on-a-chip applications.

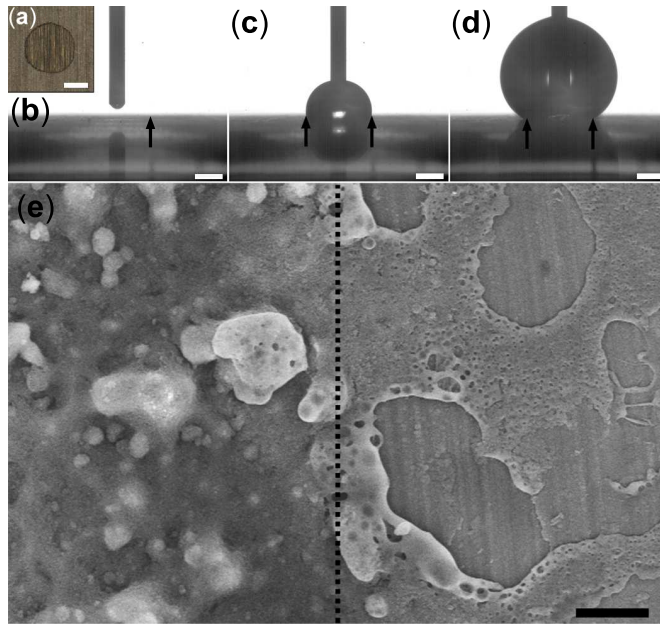


Figure 40. A sequence of images showing an advancing water contact angle measurement at the transition between a superhydrophilic (laser patterned) and the surrounding superhydrophobic area. Inset in (a) shows the laser patterned, hydrophilic, circular spot on the superhydrophobic coating ( $w_p = 0.6$ ) prior to water droplet deposition (scale bar is 500  $\mu\text{m}$ ). The scale bars in (b)-(d) are 500  $\mu\text{m}$ . Arrows in (b)-(d) mark the outer extent of the patterned area. Part of the needle in (d) is obscured by the liquid. (e) is a SEM micrograph depicting the transition area with a vertical dashed line separating the hydrophobic (left) from the hydrophilic area (right). The scale bar in (e) is 20  $\mu\text{m}$ .



Figure 40a presents a CO<sub>2</sub> laser patterned hydrophilic circular spot in a hydrophobic background. Figure 40b-d presents a hydrophilic spot being characterized by an advancing water contact angle measurement; the edges of the hydrophilic spot are marked by dark arrows. As the water is dispensed from the needle, the droplet readily advances to the edge of the hydrophilic pattern, and once there, it pins. The droplet remains pinned at that location as it grows above it, until it achieves a high contact angle value, and begins to advance once again, but this time with a high contact angle, indicating superhydrophobicity. This experiment demonstrates the spatially abrupt wettability transition on the patterned surface. SEM analysis also confirms a sharp transition of the coating from superhydrophobic to superhydrophilic, as shown in Figure 40e, left-to-right through the dashed-line boundary. Figure 41a-d shows examples of STC microchannels with and without deposited water; e-f show SEM micrographs of the channels with increasing magnification. It is obvious that laser-treatment ( $I \approx 0.2 \text{ MW cm}^{-2}$ ,  $d_L = 25 \text{ }\mu\text{m}$ ,  $u_t = 2.0 \text{ cm s}^{-1}$ ) has removed much of the coating material, thus creating a physical channel. Figure 41g shows a high-magnification micrograph of the patterned area where laser treatment caused cellular morphology. While during flame treatment the pre-existing surface roughness remained relatively unchanged (as confirmed from SEM analysis; see Figure A6), the laser treatment actually produced its own unique surface texture, facilitating superhydrophilicity. Figure 41f actually shows coating areas that have been completely stripped by the laser processing; these areas form apparently bare islands with the remaining coated sections percolating, thus allowing superhydrophilicity to persist. Further optimization of spray processing (*i.e.*, increased coating thickness) should reduce the likelihood of bare-island formation. An

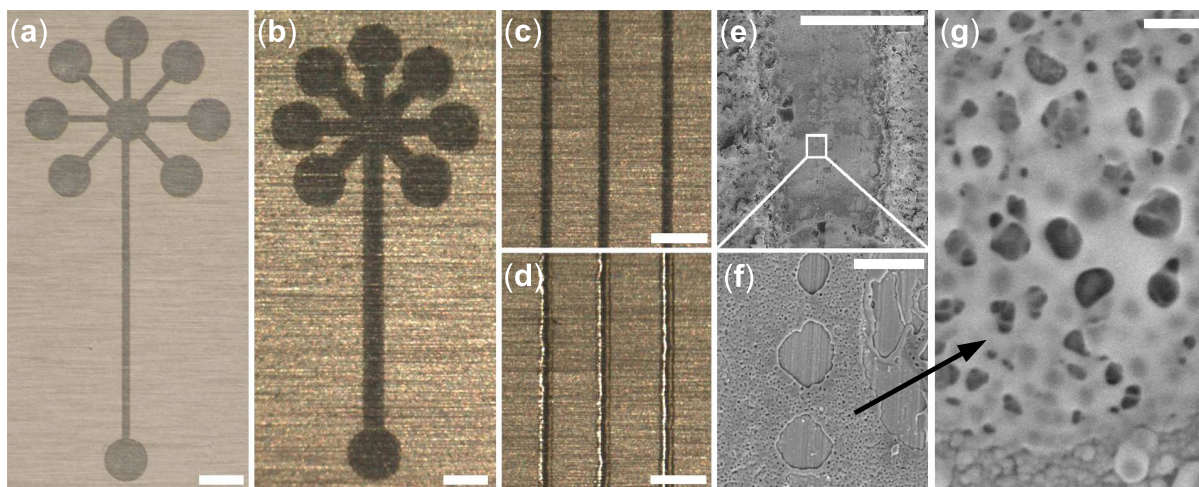


Figure 41. (a) Photographic and (b) optical microscope images of superhydrophilic patterns (dark) on a superhydrophobic MSQ-HFS coating; (c) hydrophilic, laser patterned lines (dark), and (d) surface-tension-confined channel showing wetting of the lines in (c) by water through capillary action. (e)-(f) SEM images of a STC channel with increasing magnification; (g) SEM image of a laser patterned area revealing porosity. For 0.18 mm-wide STC channels, the water propagation velocity was measured to be  $2.5 \text{ mm s}^{-1}$ . Scale bars: (a) 2 mm; (b) 500  $\mu\text{m}$ ; (c)-(d) 1 mm; (e) 200  $\mu\text{m}$ ; (f) 10  $\mu\text{m}$ ; (g) 2  $\mu\text{m}$ .

important property of STC channels is the average flow velocity of water in them. In the case of a 7.2 mm-long 0.18 mm-wide channel formed with the present procedure, the average water flow velocity was  $2.5 \text{ mm s}^{-1}$ , which is comparable to speeds attained by others in similar sized channels (185).

Laser-treated areas appear visually different than non-treated areas. As shown before (Figure 41), laser processing removes the top portion of the coating. The resulting surface is a thin, glassy coating devoid of the micro-features originating from spray application and appears more optically transparent (see Figure A3). For heat transfer applications, a thin coating or surface treatment is desirable, as minimal thermal resistance is required. For pool boiling applications, it has been recently reported that selective patterned areas of hydrophobicity and hydrophilicity on surfaces, improves heat transfer characteristics (*i.e.*, heat transfer coefficient, critical heat flux) (38). The demonstrated feature sizes were in the  $\sim 100\ \mu\text{m}$  range with either hydrophobic or hydrophilic networks. Figure 42a-b show laser patterning of similar  $\sim 100\ \mu\text{m}$  repeatable feature sizes of either hydrophobic or hydrophilic nature, while c shows what happens when the patterned surface shown in Figure 42b is subjected to nucleate boiling conditions; the hydrophobic islands act as preferred nucleation sites for boiling, in line with previously reported results (38). An important property of these MSQ-HFS films is their ability to maintain extreme wetting properties during and after heating. Determination of the temperature at which these surfaces change wettability is important. Figure 43 presents water droplet sliding angle measurements as a function of temperature treatment of the coating on a hot plate for one hour. At treatment temperatures below  $300^\circ\text{C}$ , the sliding angles are well below  $10^\circ$ , indicating self-cleaning ability for these coatings. For treatment above  $300^\circ\text{C}$ , the coating begins to undergo a change in its superhydrophobic property. After treatment at  $500^\circ\text{C}$ , the coating ceases to display droplet sliding behavior with the water droplets remaining pinned, indicating a full-loss of superhydrophobicity and the Cassie-Baxter wetting state, and marking a *temperature limit*

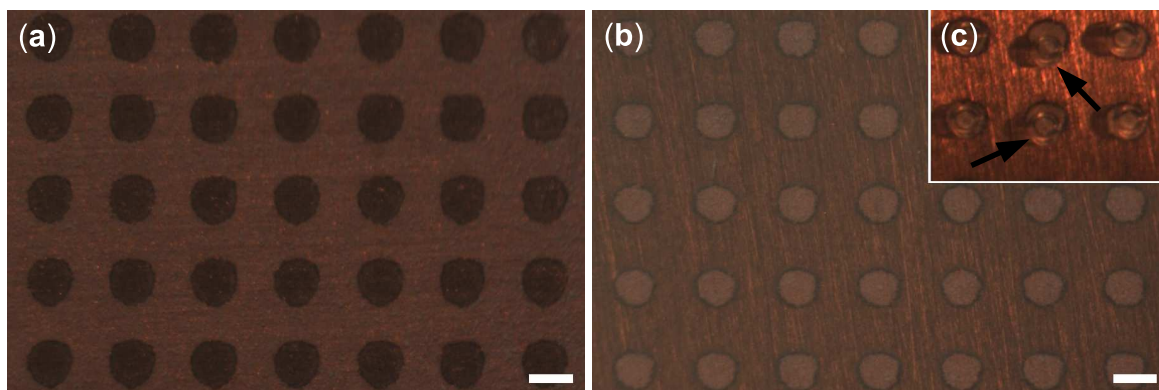


Figure 42. Superhydrophobic MSQ-HFS coating deposited onto copper substrates and laser-processed to create hydrophilic patterns. (a) Superhydrophobic spots on superhydrophobic background; (b) Superhydrophobic spots on superhydrophilic background; (c) pattern from (b) placed in a water bath and subjected to heating; the hydrophobic islands act as preferred gas nucleation sites—arrows indicate vapor bubbles that grow gradually and detach before this cycle repeats itself over and over. Both scale bars are 400  $\mu\text{m}$ .

for the application of this coating. The ability to maintain superhydrophobic behavior even after thermal treatment at 300 °C (*i.e.*, no degradation, no melting, etc.) puts this composite coating in class with some of the high-performance thermoplastics which have melting points above 300 °C (*e.g.*, poly(ether ether ketone)).

In order to further explore the thermal properties of the MSQ and HFS coating ingredients, Figure 44 presents two separate TGA plots, one for HFS a and the other for pure MSQ b. In the case of HFS tested under nitrogen atmosphere conditions, no significant mass loss was detected,

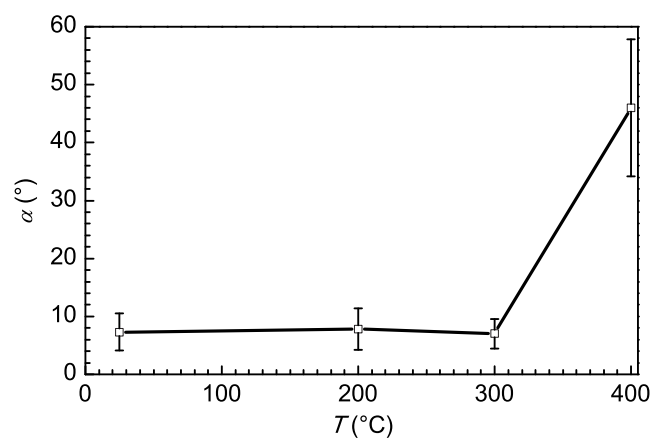


Figure 43. Water droplet sliding angle ( $\alpha$ ) vs. treatment temperature ( $T$ ) of a superhydrophobic coating ( $w_p = 0.6$ ). Coatings were treated for 1 hr on a hot plate in open air. At 500  $^{\circ}\text{C}$  treatment temperature, the water droplet ceased to slide, indicating full-loss of the superhydrophobic property of the coating.

while under oxidative conditions of artificial air (80% N<sub>2</sub> , 20% O<sub>2</sub>), a 2.3 wt.% mass loss was detected between 530-630°C. It is suggested that this mass loss is attributed to oxidation of alkyl groups in the HFS, which results in formation of –OH containing function groups and evolution of volatile CO, CO<sub>2</sub> and H<sub>2</sub>O. According to the manufacturer, the concentration of carbon in the HFS, as induced by the wettability modification of silica, is in the range of 0.7-1.3 wt.%. This is quite close to the TGA mass loss (2.6 wt.%) seen in the oxidizing atmosphere, and thus carbon presence in the HFS could be responsible for this mass reduction. HFS becomes dispersible in water after thermal treatment at 900°C in artificial air (see inset image in Figure 44a, vial 3) and retains its white color (*i.e.*, no pyrolysis), supporting alkyl group oxidation as the probable mass loss mechanism. For MSQ in Figure 44b, the TGA shows three significant mass losses at 159°C, 377°C, and 719°C for oxidizing conditions (artificial air) and at 154°C, 406°C, and 771°C for inert conditions (nitrogen). Regarding the first mass loss (159°C), the coating remains self-cleaning after thermal treatment at 200°C (see Figure 43), so this mass loss is irrelevant in the context of superhydrophobicity. A previous study attributed such mass loss to condensation of silanol groups and loss of siloxane (218). For the mass loss of MSQ at medium temperature (300-500°C), this is the temperature range where loss of superhydrophobicity is observed. The effect of mass loss on wettability at ~400°C is unclear, but the associated loss of superhydrophobicity there may be due to MSQ melting, which affects surface texture—a major factor in superhydrophobicity—more than it is due to chemical changes and mass loss of MSQ. At 500°C, the coating begins to undergo a color change from its original white to black, and chemical changes begin to play a prominent role. Heating MSQ in air or O<sub>2</sub> above

600°C results primarily in the formation of  $\text{SiO}_2$ , which is used for production of silica glasses (205). In the case of flame or laser treatment in open air, one can expect more extreme thermal treatment than that delivered by TGA testing; transformation of hydrophobic methyl groups to hydrophilic  $-\text{OH}$  groups can thus be expected.

High-resolution XPS analysis of silicon, oxygen, and carbon was done on untreated, flame treated, and laser treated MSQ-HFS ( $w_p = 0.5$ ) coatings. This analysis supported the TGA data, in turn, suggesting increased concentration of Si-O bonding and reduced concentration of Si-R bonding (*i.e.*, methyl) with heating, both consistent with the observed increased silica concentration and decreased hydrophobicity (Figure A4).

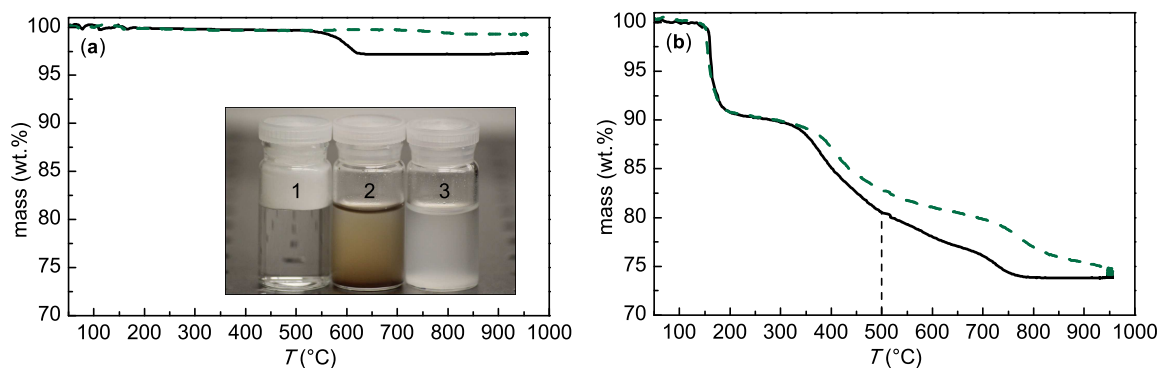


Figure 44. TGA plot (mass vs.  $T$ ) for (a) HFS, and (b) MSQ under different gas atmospheres (nitrogen  $---$ , air  $—$ ). The inset in (a) shows three 15 mL glass vials containing 10 g of water and 0.07 g HFS. The HFS contained in vial 1 was not subjected to prior TGA treatment, while the HFS in vials 2 and 3 was. For the HFS in vial 2, TGA was performed under nitrogen conditions. For vial 3 it was run under artificial air conditions. In (b), the dotted (...) drop-down line denotes the thermal treatment temperature (1 hr, open air, hot plate) for a superhydrophobic coating ( $w_p = 0.6$ ) above which total loss of droplet sliding behavior was observed (see Figure 43). This temperature marked the beginning of the wettability transition.



## CHAPTER 7

### WETTABILITY ENGINEERED SURFACES: SHAPING AND MOBILIZING LIQUID $\mu$ -VOLUMES

#### 7.1 Introduction

Water droplet impact on solid surfaces—while being a historic field with contributors dating back 100 years—has only recently been well analyzed for surfaces with extreme wetting properties (*e.g.*, superhydrophobic). Such surfaces are generated by coupling proper surface morphology with proper surface energy (72). In general, the rougher a hydrophobic surface is (*i.e.*, micro, nano roughness), *ceteris paribus*, the more likely it is to become superhydrophobic; the inverse is true of a hydrophilic surface: the rougher they are, the more they tend towards superhydrophilic surfaces (58). Fluid mechanics research on such surfaces has been made widely available due to the wide-range of micro/nano-fabrication techniques that are now readily available for their synthesis (219; 220). So while such surfaces that are entirely superhydrophobic or superhydrophilic are important, recent work has shown that surfaces with patterns of superhydrophobicity or superhydrophilicity are also of great importance for application in surface microfluidics—due to their ability to confine and transport liquids in a facile manner (185; 46). They are also important for the non-isothermal problems, specifically pool boiling (221) and icing (222). These surfaces also now have a myriad of synthesis techniques (223), enabling a wider range of bench-top experiments. However, while many of their applications are owed

to fluid dynamic applications, relatively little research has been dedicated to their study with regards to dynamic fluid events such as droplet impact (224). This work aims to bridge that specific gap and to show possible research and industrial applications.

We present a novel application of wettability patterned surfaces, specifically superhydrophobic/hydrophilic surfaces, for the purposes of rapid micro-volume shaping through droplet impact. In previous research on such surfaces, a great deal of the liquid volume was “ejected” during the droplet impact process (224); our surfaces are capable of forming stable annuli without loss of liquid volume, which is extremely important for lab-on-a-chip style applications. In our research we show how simple surface chemistry modification dramatically alters the dynamic behavior of impinging droplets for the purposes of forming complex annular and cross shapes (*e.g.*, Swiss flag), which are important for many surface microfluidic applications (211). One major step in forming annuli-like patterns is the generation of an air cavity or dry region at the center of the liquid droplet (lens) by a well controlled, repeatable process. Previous research has shown that by rotating the plate (225) or by impinging an air stream (226), one can produce air cavities or dry regions in a liquid lens or film. We demonstrate that it is also possible to form stable air cavities in liquid lenses—for the purposes of complex droplet  $\mu$ -volume shaping—by droplet impact on wettability engineered surfaces. We also show the ability to mobilize (propel) droplets (*e.g.*, sling-shot) and cut them (*e.g.*, superhydrophobic scalpel (227)) through proper surface design. Models are developed to aid in the design of wettability engineered surfaces and to understand fluid dynamic behavior for applications in surface microfluidic platforms.

## 7.2 Experimental

### 7.2.1 Materials

The materials utilized in this study, as well as their commercial origins, are as follows: fluoroacrylic copolymer (PMC; 20 wt.% in water; Capstone ST-100, DuPont), hydrophobic fumed silica (HFS; Aerosil R 9200, Evonik), acetic acid (99.7 wt.%; Fisher Scientific), acetone ( $\geq 99.9\%$ ; Sigma-Aldrich), and silver nano-ink (38-40 wt.% in water; PSPI-100, PChem Associates). The substrate utilized in this study was a flexible waterproof microtextured SiC paper (1500 grit; B-99, Fandeli).

### 7.2.2 Procedure

A schematic describing the procedure for synthesizing wettability patterned coatings—as well as their relevant variables—is depicted in Figure 45. The outer and inner annulus radii are defined as  $r_o$  and  $r_i$ , respectively. The line thickness of the outer and inner annuli are defined as  $w_o$  and  $w_i$ , respectively. First, a polymer-nanoparticle dispersion was generated; its purpose was to create a superhydrophobic coating by wet processing methods on a microtextured silicon-carbide substrate. Initially, a nanoparticle suspension was formed by combining HFS and acetone and mechanically mixing at room temperature. Subsequently, the suspension underwent 500 J of probe sonication (750 W, 13 mm probe dia., 40 % amplitude, 20 kHz frequency, Sonics & Materials, Inc., Model# VCX-750). The HFS-acetone suspension was then treated with acetic acid and combined with PMC (20 wt.% in water). The entire dispersion was then mechanically mixed at room temperature to form the final dispersion for drop casting. Refer to Table XI for the specific concentrations of all materials in the dispersion.

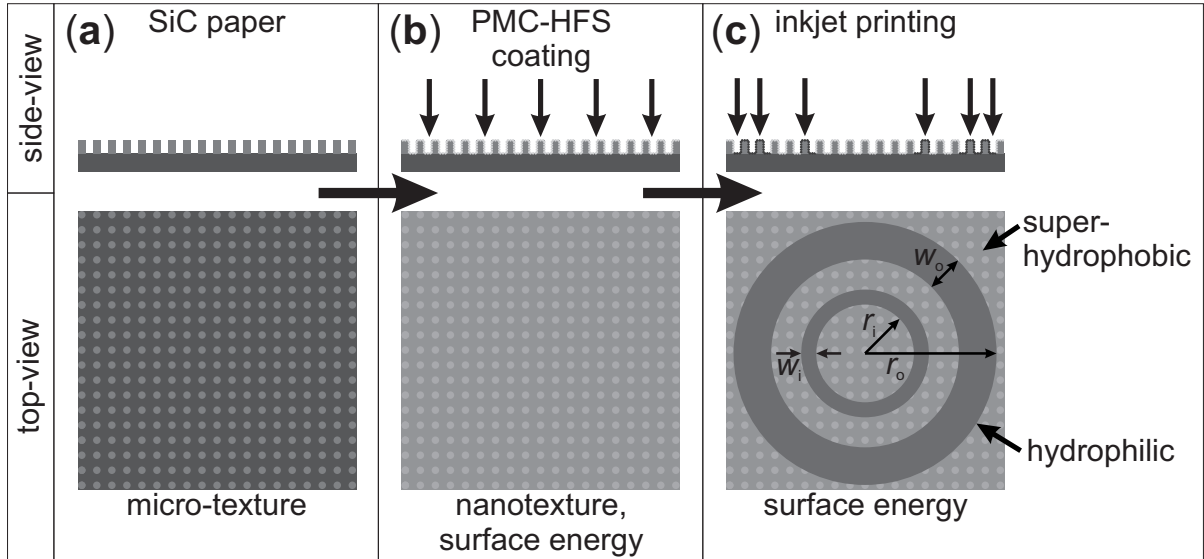


Figure 45. Schematic outlining the procedure for synthesizing the wettability patterned coatings. (a) Begins with a micro-textured SiC substrate; (b) a PMC-HFS composite coating is dropcast onto the SiC substrate forming a superhydrophobic surface; (c) hydrophilic inkjet patterns are successively applied until the desired level of hydrophilicity is achieved.  $r_i$  and  $r_o$  represent the inner and outer radii of the hydrophilic annular patterns, respectively.  $w_i$  and  $w_o$  represent the inner and outer widths of the hydrophilic annular patterns, respectively.

TABLE XI

CONCENTRATIONS OF ALL INGREDIENTS USED IN THE DISPERSION FOR  
GENERATING SUPERHYDROPHOBIC COATINGS BY DROP CASTING METHODS.

ingredients	concentration (wt.%)
acetone	87
acetic acid	6.0
water	4.0
HFS	2.0
PMC	1.0

In order to form a superhydrophobic coating, the PMC-HFS dispersion was drop-cast onto silicon-carbide micro-textured paper (1500 grit) and was allowed to dry for one hour in an oven at 80°C to remove residual solvents. Such a dispersion, with its low surface tension readily wets and wicks along the micro-textured substrate forming a uniform film. What results is a coating with low-surface energy and a high-degree of hierarchical roughness. Subsequently, an ink jet printer (Kodak OfficeHero 6.1) was used to apply ink in the areas desired to be hydrophilic. One layer of the following colors is applied successively to the areas desired to be hydrophilic: magenta, yellow, cyan and gray (50 % black). Different ink colors were used for each printing step to ensure that the same area was being treated each time. Areas that had multiple colors

printed on them appeared black; regions that printed incorrectly (spatially) would appear in their inherent color and thus expose a misprint. After each ink layer is applied the ink is dried by gentle blowing with a hot air gun for 30 seconds. What results is a coating on paper with domains of superhydrophobicity and hydrophilicity, which we term wettability patterned (WP).

### 7.2.3 Characterization

Wettability characterization—on uniform wettability areas—was done by measuring advancing ( $\theta_a^*$ ) and receding ( $\theta_r^*$ ) water contact angle values by the sessile drop method, whereby 5-10  $\mu\text{L}$  of the probe liquid (water) was inflated (advancing CA) and deflated (receding CA). Measurements of  $\theta_a^*$  and  $\theta_r^*$  were made with images captured with a high-speed, backlit image acquisition setup (Redlake MotionPro). A different location on the substrate was used for each individual CA measurement. Dynamic water droplet behavior (*e.g.*, drop impact) on the substrates was captured with a modified version of the aforesaid image acquisition setup (see Figure B1). The setup, all on a floating optical table, included a cold light source (Fostec 8375), high-speed camera (Redlake MotionPro), syringe pump (Cole Palmer 74900 Series), and needle (32 gauge, stainless steel, EFD). All optical and dispensing components were mounted on linear stages to allow for precise motion. The distance from the tip of the needle to the surface of the sample  $L$  can be varied in order to control the Weber number with  $We = (\rho U_0^2 D_0) / \sigma_{lv}$ , where  $\rho$  and  $\sigma_{lv}$  are the density and surface tension of water, respectively;  $U_0$  and  $D_0$  are the velocity and diameter of the impinging droplet, respectively. We define  $U_0$  through the following relation (neglecting air resistance)  $U_0 = \sqrt{2gL}$  where  $g$  is acceleration due to gravity and  $L$  is the distance between the dispensing needle and the substrate (see Figure B1).

This approximation was validated by measuring the velocity of the droplet at impact for the Weber numbers investigated in this study:  $We = 60, 80, 100$  gave errors of 2%, 3%, and 4%, respectively. A force balance, supporting this approximation, is also given in Appendix B.2.  $D_0$  is defined as  $D_0 = \left(\frac{6}{\pi}V\right)^{1/3}$  where  $V$  is the volume of the droplet. For droplet impact onto annular wettability patterns,  $We$  is kept in the range of 60 to 100. Deionized water with a drop diameter of  $D_0 = 2.1$  mm was used for all experiments. Morphological characterization of micro-textured SiC in uncoated and coated states was performed with a scanning electron microscope (SEM; Hitachi S-3000 N). All samples were coated with a conformal 8.0 nm layer of Pt/Pd to facilitate imaging.

### 7.3 Results and Discussion

Prior to considering droplet impact on wettability patterned surfaces, it is instructive to consider the intricacies of drop impact on superhydrophobic surfaces. While most superhydrophobic surfaces have the ability to shed droplets from a sessile condition (*i.e.*, self-cleaning)—where droplets reside in the so-called Cassie-Baxter (70) wetting state—not all of them can repel impacting droplets. Droplets that are not repelled by superhydrophobic surfaces are said to undergo “impalement” or a transition to the so-called Wenzel wetting state (69). Deng et al. (228) presents design criteria for resisting impalement of impinging droplets with speeds  $O(1)$ - $O(10)$  m s<sup>-1</sup>; the conclusion is that such superhydrophobic surfaces should have  $\sim 100$  nm (hydrophobic) surface texture features (*e.g.*, pores, etc.), since the pressure required to impale the surface scales as the Laplace pressure of the maximum deformation of the water-air interface between surface textures. For porous structures, the capillary pressure can be calculated as

$p = -2\sigma_{lv} \cos \theta_a / r_{\text{pore}}$ , where  $\theta_a$  is the advancing contact angle on a flat surface and  $r_{\text{pore}}$  is the radius of the pore; therefore, the smaller the  $r_{\text{pore}}$  is, the more likely a superhydrophobic surface is to resist impalement. In the case of this study, hydrophobic silica nanoparticles, coated with a fluoropolymer, were utilized to generate the required hydrophobic nano-scale surface texture in order to resist droplet impalement. In order to generate hierarchical micro-to-nano surface structures—which are well known for their role in enhancing hydrophobicity—the PMC-HFS composite coating was deposited onto a flexible micro-textured SiC substrate (see Figure B2 for micrographs). The PMC-HFS composite coating, when deposited onto the SiC substrate, displayed the following wetting characteristics:  $\theta_a^* = 166 \pm 1^\circ$  and  $\theta_r^* = 155 \pm 6^\circ$  (see Table XII). Water droplets had a high degree of mobility, and the coating was able to resist water droplet impalement even for  $U_0 > 3.5 \text{ m s}^{-1}$ , making the coating well suited for a droplet impact study.

Once the superhydrophobic composite coating was formed, inkjet printing of standard color and black inks onto the coating was utilized to modify its surface energy, and not surface texture, in a spatial manner. Since the coating was inherently non-wettable, it initially did display repellency towards the liquid inks during processing; however, if multiple printing steps were performed on the same region then the surface displayed a high-degree of printing uniformity. The ink patterned regions on the PMC-HFS composite coating displayed the following wetting characteristics:  $\theta_a^* = 93 \pm 5^\circ$  and  $\theta_r^* \approx 0^\circ$  (Table XII). While  $\theta_a^*$  is actually high enough to deem this ink coating hydrophobic, the extremely low value for  $\theta_r^*$  indicates that for receding contact line conditions—which are of great importance for droplet rebound situations—this coating will behave as hydrophilic. Not only that, the ink coating regions will act to pin, or arrest, the



TABLE XII

WATER CONTACT ANGLE VALUES ON MICRO-TEXTURED SILICON-CARBIDE SURFACES (SANDPAPER) FOR THREE CASES: 1) UNCOATED; 2) PMC-HFS COMPOSITE COATING; 3) INK COATED ON PMC-HFS COMPOSITE.

	uncoated (°)	PMC-HFS (°)	ink coated (°)
$\theta^*$	93±17	159±16	83±23
$\theta_a^*$	97±3	166±1	93±5
$\theta_r^*$	≈ 0	155±6	≈ 0

motion of the contact line due to its high value of contact angle hysteresis,  $\Delta\theta^* = \theta_a^* - \theta_r^*$ . Such behavior can be quite useful for constraining droplet motion during extremely dynamic fluid events as will be shown later.

Since these wettability patterned coatings displayed ideal wetting characteristics—superhydrophobic regions resisted droplet impalement and hydrophilic regions arrested contact line motion—studies on complex drop formation were undertaken. Figure 46 presents the advancing and receding contact line behavior of impinging droplets ( $We = 80$ ) on the superhydrophobic coating, hydrophilic ink coating, and the hydrophilic annular patterns of varying radii ( $r_o$ ) but constant line thickness ( $w_o$ ). Prior to considering complicated annular patterns, it is instructive to compare the dynamic wetting behavior of water—as a result of drop impact—on the

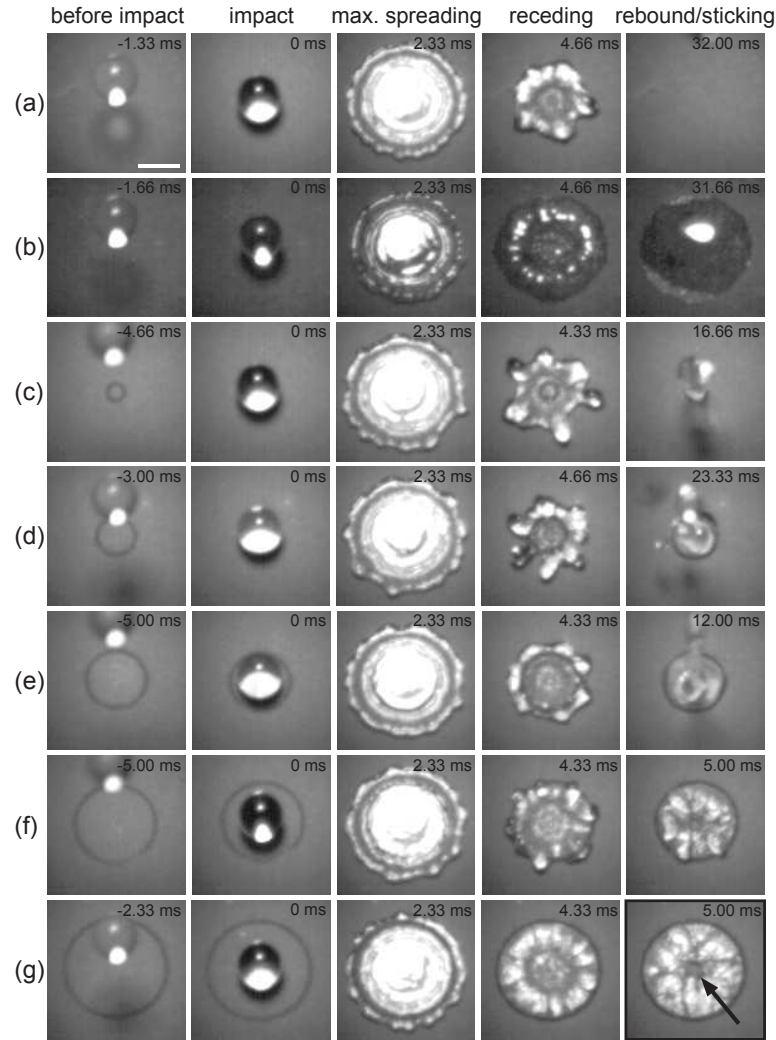


Figure 46. Drop impact at  $We=80$  on superhydrophobic-paper (a), entirely wettability patterned paper (b), hydrophilic ring pattern on hydrophobic background with  $r_o =$  (c) 0.5 mm, (d) 1 mm, (e) 1.5 mm, (f) 2 mm and (g) 2.5 mm, and  $w_o=0.20$  mm. The inset scale bar is 2.0 mm.

superhydrophobic (Figure 46a) and hydrophilic (Figure 46b) coatings. The spreading behavior of the water droplets in their early stages of drop impact ( $t \approx 0 - 2$  ms) are quite comparable on both surfaces.

Clanet et al. (229) showed that for droplet impact of low-viscosity fluids (*e.g.*, water) on solid surfaces, the early stage dynamics for non-wettable and partially-wettable surfaces are quite similar, with the maximal spreading diameter,  $D_{\max}$ , scaling as

$$D_{\max} \sim D_0 We^{1/4}. \quad (7.1)$$

The flattening behavior of the droplets in both cases are due to an effective acceleration,  $\gamma$ , which scales as  $\gamma \sim U_0^2/D_0$  and dominates the gravitational field (229). For the experiments herein,  $We = 80$  ( $D_0 = 2.1$  mm); substituting those values into Equation 7.1 we see that  $D_{\max} = 6.2$  mm. This value compares quite well with that observed for superhydrophobic and hydrophilic surfaces (see Figure 46 (a)-(b) max spreading). While the early (advancing) stages compared well, the drop impact behavior during the later stages ( $t \approx 2 - 30$  ms; receding) is markedly different.

In the case of droplet impact on the superhydrophobic surface, some surface energy—as a result of the increase in free surface area—is converted back to kinetic energy and therefore facilitates droplet “rebound”. This is made possible by the low-viscosity of water and the high mobility of the droplet on the surface. In the case of droplet impact on the hydrophilic surface, such a conversion of surface energy to kinetic energy is not observed, and the droplet does not

rebound; its final conformation is a puddle. The low-mobility of the contact line during the receding stage of droplet impact is due to the low apparent receding contact angle,  $\theta_r^* \approx 0^\circ$ .

Figure 46 (c)-(g) show drop impact on wettability patterned coatings with a constant  $w_o$  (200  $\mu\text{m}$ ) and varying  $r_o$ . As was the case with the homogeneous hydrophilic (ink) coating, the hydrophilic annular patterns do not affect the advancing contact line behavior during droplet impact; however, the receding contact line behavior is once again dramatically affected. What is interesting to note is the dramatic effect that a relatively small amount of well placed ink can have on energetic droplet impact dynamics. In most cases, the wettability patterns act to resist droplet rebound, which is rather expected. However, in one special case, when  $D_{\text{max}} \sim 2r_o$  (Figure 46(g)), something important happens. The receding contact line motion is interrupted by the hydrophilic pattern and a liquid lens is formed. Subsequently, rupture of the liquid lens occurs at the center of the droplet. This is a non-trivial result as this allows one to possibly form complicated shapes which require hollow centers (*e.g.*, annuli). However, this type of wettability pattern (low  $w_o$ ) was not suitable for further analysis (or applications) since it had a low-degree of droplet adhesion; therefore, the value of  $w_o$  was increased.

Prior to considering the experimental details of annular droplet shaping further, it is instructive to consider two things theoretically: 1) The stability of a static liquid droplet in contact with a solid surface subjected to gravity; 2) the stability of a hole in a (static) liquid droplet in contact with a solid surface. For a large liquid droplet having a radius much larger than the capillary length,  $l_{\text{cap}} = \sqrt{\sigma_{\text{lv}}/(\rho g)}$ , the gravity dominates. Its stability in contact with solid surfaces depends on its thickness,  $h_l$  (58). If  $h_l$  is less than a critical thickness value

$h_{l,c} = 2l_{\text{cap}} \sin(\theta_e/2)$ , where  $\theta_e$  is the equilibrium contact angle, then the droplet is unstable (58). For a water droplet on a hydrophilic surface ( $\theta_e = 10^\circ$ ),  $h_{l,c} \approx 0.5\text{mm}$ . For superhydrophobic surfaces,  $h_{l,c} = 2l_{\text{cap}} \sin(\theta^*/2)$ ; substituting appropriate values ( $\theta^* = 150^\circ$ ), we see that  $h_{l,c} = 5.2\text{mm}$ , which is much greater than the maximum height of the liquid lens generated in Figure 46(g) ( $h_{l,\text{max}} \approx 0.50\text{ mm}$ ); therefore, the observed instability of the liquid lens should be expected. Liquid films can be destabilized in a variety of ways; however, since in this study destabilization of liquid lenses (films) was always preceded by the formation of a hole, let us consider the requirements for this configuration and its subsequent growth.

The configuration of the liquid lens during hole formation is presented in Figure 47. The hole is assumed to be axisymmetric and has a volume of  $V_h = \pi r_h^2 h_h$ , where  $r_h$  and  $h_h$  are the radius and height of the hole, respectively. In order to understand if a given hole is stable—and therefore capable of growing—it is necessary to compute whether a hole is energetically favorable. With the maximum lens thickness being less than the capillary length, we can neglect gravitational effects and assume that the lens conforms to the shape of a spherical cap (58).  $\Delta E$  can then be defined as (224)

$$\Delta E = E_2 - E_1 = \sigma_{lv} \left[ 2\pi r_h h_h - \pi r_h^2 (1 - \cos \theta_{CB}^*) \right], \quad (7.2)$$

where the apparent contact angle  $\theta_{CB}^*$  can be defined by the Cassie-Baxter equation, for droplets in a Cassie-Baxter state, as  $\cos \theta_{CB}^* = -1 + \Phi_{sl} (\theta_e + 1)$ , where  $\Phi_{sl}$  is the liquid-solid fractional area ( $\Phi_{sl} \leq 1$ ) (70; 58). Previous analysis (224) neglected the effect that a displaced liquid volume—as a result of hole formation—had on the shape of the liquid lens. In this analysis,

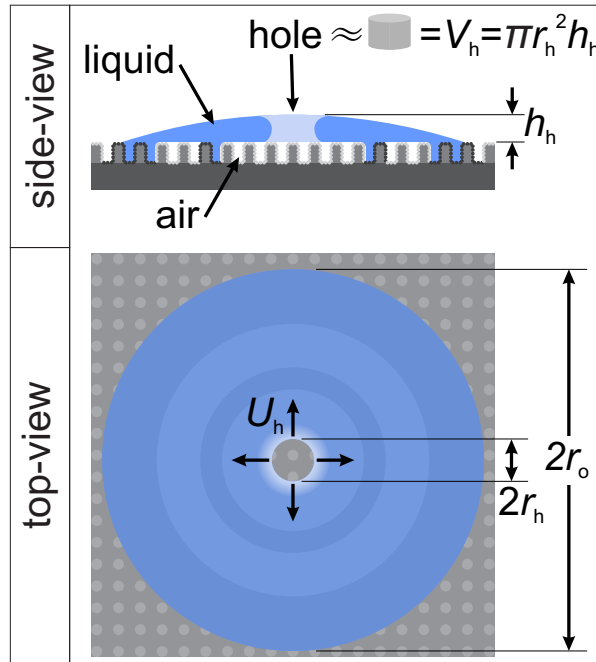


Figure 47. Schematic illustrating hole formation in a thin liquid lens formed through droplet impact on a wettability patterned surface.  $V_h$ ,  $h_h$ ,  $U_h$ ,  $r_h$ , and  $r_o$  represent the approximate volume of the hole, the approximate height of the hole, the velocity of the hole expansion, the radius of the hole, and the outer radius of the wettability patterned annulus, respectively.

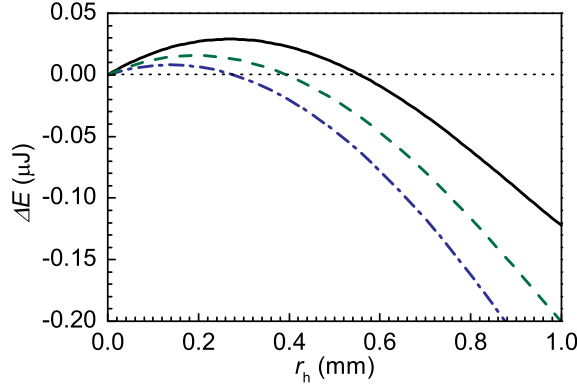


Figure 48. Plot of  $\Delta E$  vs.  $r_h$  for a liquid lenses of varying initial droplet diameter ( $D_0$ ) and constant annular pattern conditions,  $r_o = 2.5$  mm. The liquid displaced by generating a hollow cylinder of volume  $V_h$  in the center of the lens was accounted for in this model. The following values of  $D_0$  were used: 2.1 mm (—), 1.9 mm (---), and 1.7 mm (- - - -).

we held  $V$  constant, and therefore accounted for the change in lens shape as a result of hole formation (see Appendix B.2.1 for a detailed analysis). The displaced liquid in the lens should act to increase the maximum height of the lens; therefore, from Equation 7.2 this results in a higher (positive) value of  $\Delta E$  and makes hole formation energetically less favorable. Accounting for the displaced liquid volume increased  $r_{h,c}$  by 9%. Figure 48 presents a plot of  $\Delta E$  vs.  $r_h$  and shows the transition point ( $\Delta E = 0$ ,  $r_h = r_{h,c}$ ) to where hole formation is energetically favorable ( $\Delta E < 0$ ) for a series of liquid volumes. For  $D_0 = 2.1$  mm,  $r_{h,c} = 0.56$  mm, and as  $D_0$  decreases so does the  $r_{h,c}$ , which is intuitive. Now that the physical requirements for hole

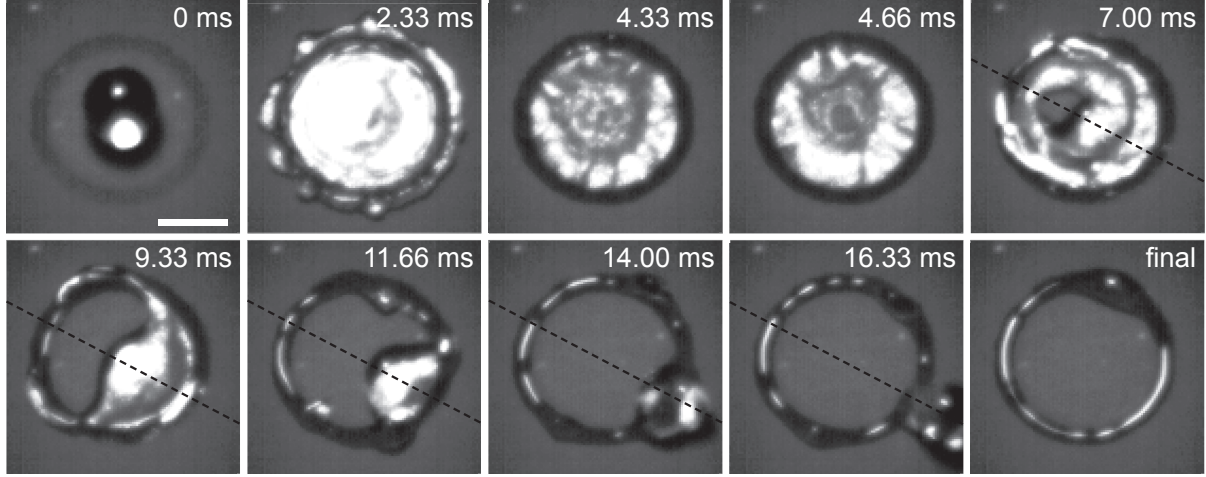


Figure 49. Impact on a hydrophilic annulus with  $r_o = 2.5$  mm and  $w_o = 0.50$  mm width for  $We = 80$ . The dotted line indicates an axis of symmetry as well as the propulsion direction of the eventual droplet.

formation in liquid lenses have been treated, droplet impact on a variety of increasing complex annular patterns can be considered.

Figure 49 presents a water droplet impacting ( $We = 80$ ) on an annular pattern with an increased value of  $w_o$  ( $r_o = 2.5$  mm;  $w_o = 0.50$  mm). At  $t = 6.0$  ms, the first stable hole is observed with  $r_h \approx 0.49 \pm 0.06$  mm, which is of the same magnitude as that shown in the previous analysis. In the early stages of growth, the hole expansion velocity ( $U_h$ ) can be estimated by balancing surface tension force with inertial force. For liquid films disintegrating in open air,  $U_h$  can be defined by the Taylor-Culick formula (230; 231),  $U_h = \sqrt{\frac{2\sigma_{lv}}{\rho h}}$ , where  $\bar{h}$  is the nominal



thickness of the liquid film. If one assumes that the liquid dynamics on a superhydrophobic surface ( $\theta_{CB}^* = 150^\circ$ ) are similar to those in open air ( $\theta_{CB}^* = 180^\circ$ ) (224), and that  $\bar{h} \approx h_h$ ,  $U_h \approx 0.5 \text{ m s}^{-1}$ . For the annular pattern considered here ( $r_o = 2.5 \text{ mm}$ ), the time scale comes as  $t_h \approx r_o/U_h \approx 5 \text{ ms}$ . The actual ring expansion process in Figure 49 takes  $\approx 10 \text{ ms}$  to complete, which is of a comparable magnitude. The hole expansion process eventually results in a ejection of a portion of the droplet from the annular pattern. What is interesting to note is the direction that the droplet was ejected in. In hole expansion processes that are asymmetric (*i.e.*, off center), the droplet ejection direction is along a straight line connected by the center of the hole and the center of the annulus, as was previously demonstrated by Kim et al. (224). This is due to the hole expansion process being symmetric about this line. Hole expansion behavior, as well as droplet propulsion, will be investigated in further detail in a later section.

One of the main issues with shaping liquids via droplet impact on wettability patterns was that in many cases liquid was ejected. By designing patterns that can account for the final conformation of the droplet, it may be possible to prevent discharge. If we assume that in the final configuration the annulus is continuous and satisfies the condition  $\theta^* = 90^\circ$ , the volume of the liquid annulus can be approximated as half the volume of a torus ( $V_{\text{tor},1/2}$ ; see Appendix B.2.2 for a detailed analysis). For the following conditions,  $V_{\text{tor},1/2} = 4.7 \mu\text{L}$  (the volume for all droplets used in this study) and  $r_o = 2.5 \text{ mm}$ , from Equation B9  $r_i$  can be computed as  $1.528 \text{ mm}$ . In practice,  $r_i$  was decreased to ensure that the final annulus was symmetric (*i.e.*,  $\theta^* < 90^\circ$ ). Figure 50 presents a drop impact sequence that forms a liquid annulus without mass loss;  $r_i$  for this functioning wettability pattern was  $1.35 \text{ mm}$ , which represents a 12% decrease

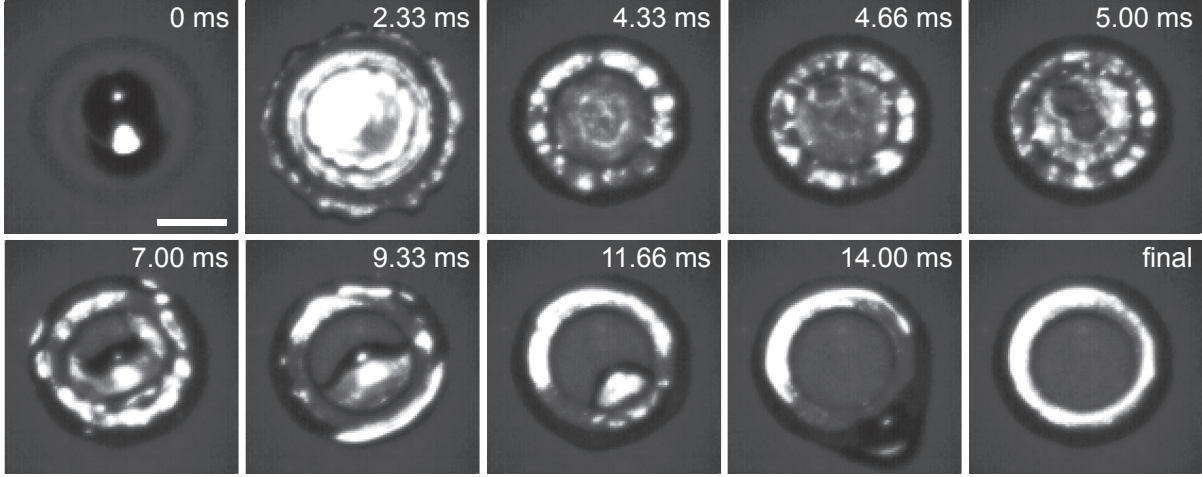


Figure 50. Droplet impact ( $We = 80$ ) on concentric hydrophilic annular patterns with the following properties:  $r_o = 2.5$  mm,  $w_o = 0.50$  mm,  $r_i = 1.35$  mm, and  $w_i = 0.20$  mm.

compared with the  $r_i$  value obtained from the idealized torus, a reasonable deviation in-line with the previous analysis. For the wettability pattern in Figure 50, note that the pattern is not continuous; rather, there are two concentric annuli with an outer and inner radii of  $r_o$  and  $r_i$ , respectively, and a distinct superhydrophobic region separating them. Concentric annuli were chosen since the droplet wetting behavior (contact angle) is only affected by the regions located near the contact line; “filling” in the annuli to form one “thick” annulus is both unnecessary and may lead to misunderstanding (232; 233). The thickness of the inner annulus ( $w_i$ ) was limited by the patterning resolution ( $O(100 \mu\text{m})$ ); any thickness less than that would not produce a continuous well-behaving pattern. The outer annulus thickness ( $w_o$ )

was determined experimentally, and then validated theoretically; for a given value of  $We$ ,  $w_o$  was incrementally increased until the pattern was capable of stabilizing a liquid lens during vigorous droplet impact. In practice,  $w_o$  was set to  $\approx 500 \mu\text{m}$  in order to suppress liquid lens detachment (*i.e.*, increase adhesion). It was previously shown that liquid lens detachment from wettability patterns can arise due to hole formation near the wettability transition as a result of air-bubble entrainment due to the fast moving contact line crossing from a Cassie-Baxter (70) to a Wenzel (69) wetting state (224). By increasing  $w_o$ , the spatial locations of the entrained air bubbles at the wettability transition are moved towards the center of the annulus; since the thickness of the liquid annulus also increases with proximity to its center, it is hypothesized that hole formation in liquid lenses at the wettability transition becomes energetically less favorable. In fact, for air-bubbles that are capable of forming penetrating holes of radius  $\sim 90\mu\text{m}$  at the wettability transition ( $D_0 = 2.1 \text{ mm}$ ,  $r_o = 2.5 \text{ mm}$ )—an approximate sized hole reported in a previous analysis (224)—once  $w_o$  becomes greater than  $150 \mu\text{m}$ , it is no longer energetically favorable for those holes to form and therefore destabilize the liquid lens. See Appendix B.2.3 for a detailed analysis of this.

For relatively high values of  $We$  ( $\approx 80$ ), it was observed that stable penetrating holes appeared very early in the process. If we consider  $t = 0 \text{ ms}$  to be the moment just before drop impact, then the first stable penetrating hole in the liquid lens would appear at  $t \approx 5 \text{ ms}$  (*cf.* Figures Figure 49 and Figure 50). The process of hole formation here is difficult to interpret due to the high-level of dynamics. However, if the value of  $We$  was reduced slightly to  $\approx 60$ , and  $r_o$  reduced to  $2.34 \text{ mm}$ , then a penetrating hole did not appear until much later,  $t \approx 15$

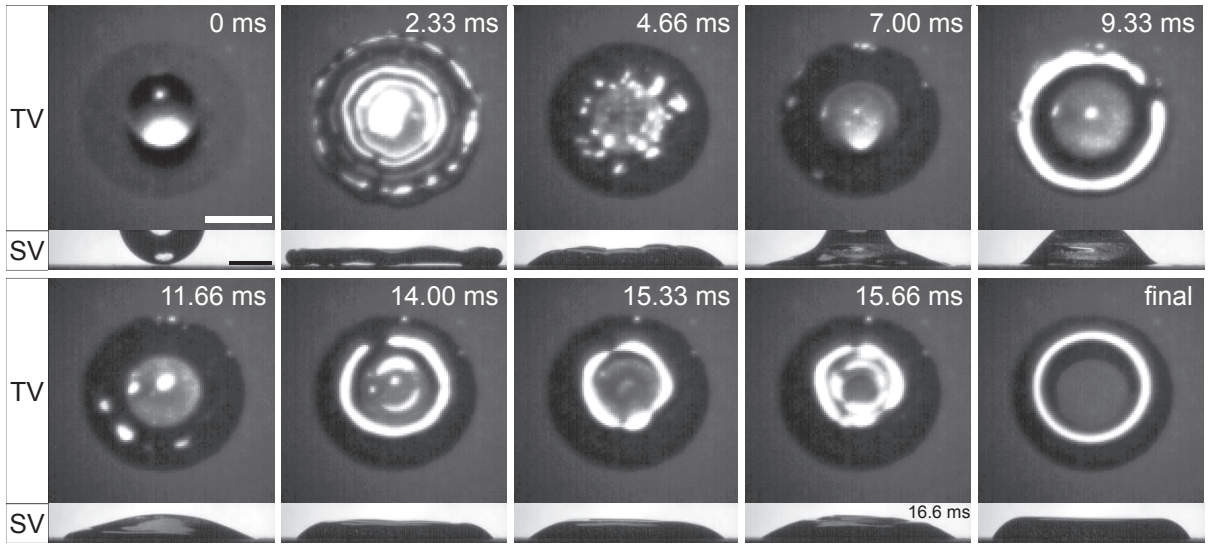


Figure 51. Droplet impact ( $We = 60$ ) on a hydrophilic annulus with  $r_o = 2.34$  mm and  $w_o = 1.3$  mm width. Both top (TV) and side (SV) views are shown and is noted on the left of the image. Scale bars: top view is 2.0 mm; side view is 1.0 mm. The time (in ms) for top and side views are synchronized unless otherwise stated in the side view images.

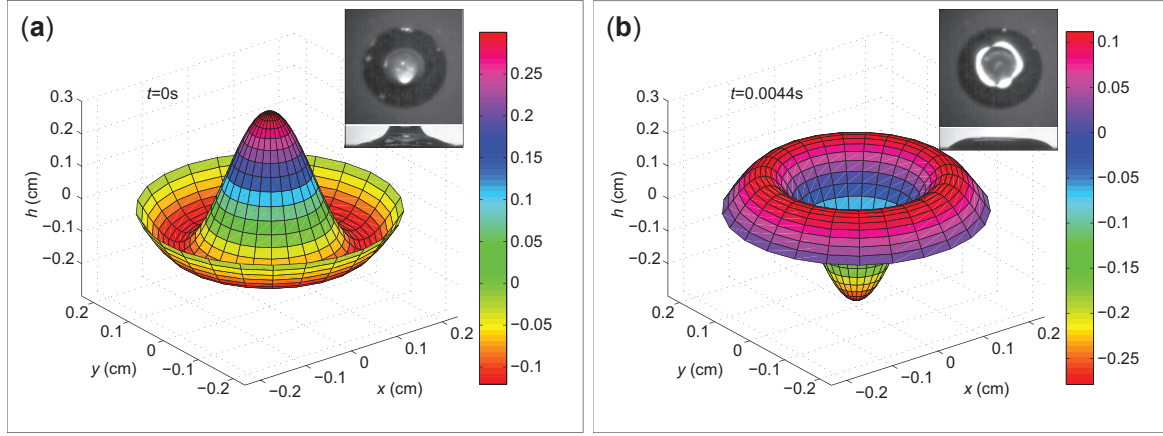


Figure 52. Plots of displacement ( $h$ ) vs. spatial coordinates ( $x$  and  $y$ ) for a vibrating circular membrane with  $m = 0$  and  $n = 2$ ; this is the so-called (0,2) mode. The parameters used were  $c = 1.45 \text{ m s}^{-1}$ ,  $r_o = 2.34 \text{ mm}$ , and  $h_{\max} = 3.0 \text{ mm}$ . The time  $t$  is (a) 0 ms and (b) 4.4 ms.

Inset images are from Figure 51 at (a)  $t = 7.00 \text{ ms}$  and (b)  $t = 15.33 \text{ ms}$ .

ms (see Figure 51), allowing a portion of the kinetic energy from the droplet impact process to be dissipated and the penetrating hole formation process to be much more elucidating. Such penetrating holes (air cavities)—which form a well-defined torus—have been observed before during droplet impact on superhydrophobic surfaces and are commonly referred to as “dry-out” events; viscous effects are small and topology is controlled by a competition between surface tension and inertia forces (234; 235). In these cases, the air cavities collapse and lead to the ejection of a very thin jet (234; 235). In the present case, no jet ejection is observed since the hole expands rather than contracts.

If we focus on the dynamics in Figure 51 beginning at  $t = 7.0$  ms and ending at 15.33 ms—for an overall time change of  $\Delta t = 8.33$  ms—we can gain some insight into the timing of a penetrating hole as well as its characteristic length scale. At  $t = 7.0$  ms, the droplet has already undergone an advancing and receding stage and is beginning to advance again. The shape of the droplet at this point is nipple-like. The subsequent oscillation of the droplet is reminiscent of the behavior of a circular elastic membrane (clamped at its boundary) where its deflection from the horizontal is represented as  $h$  and evolves in time according to the two-dimensional wave equation (axisymmetric; see Appendix B.2.4); the simplest analytic solution that most closely represents the aforesaid wave-dynamics is the normal mode of oscillation with parameters  $m = 0$  and  $n = 2$  (see Figure 52), where  $m = 0$  comes from the Bessel function  $J_m = J_0$  and  $n = 2$  comes from the root number of the aforesaid Bessel function  $z_{mn} = z_{02}$ . The length-scale of the first visible penetrating hole was measured to be  $r_h \approx 0.4$  mm, and it is instructive to compare this length scale with that of the wavelength of the vibrating circular membrane,  $\lambda$ . The characteristic natural frequency of the vibrating circular membrane ( $m = 0$ ,  $n = 2$ ) is  $f = c(z_{02}/r_o)$  where  $c$  is the wave speed; therefore, the wavelength is  $\lambda = z_{02}/r_o = 2.36$  mm ( $z_{02} = 5.52$ ). From this we see that the diameter of the penetrating hole ( $2r_h$ ) is of the order of half of the wavelength  $\lambda$ , which accounts for this length scale. The time it takes to form a penetrating hole—from time  $t = 7.0$  ms—is dictated by the wave speed ( $c$ ) and the distance that the wave has to travel. This time can be recovered by also considering the circular vibrating membrane example. From Figure 52, we see that the time to go from a nipple configuration (compare with Figure 51  $t = 7.00$  ms, side-view) to a dimple configuration (*i.e.*, just prior to a

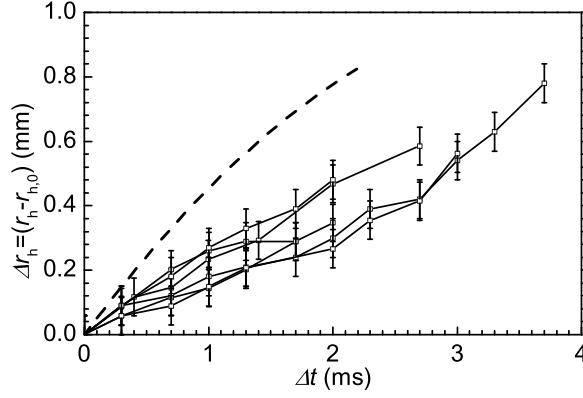


Figure 53.  $\Delta r_h = r_o - r_{o,i}$  ( $r_{o,i}$  is the initial hole radius) vs.  $\Delta t$ ; the hole formed after droplet impact ( $We = 60$ ) on a hydrophilic annuli with the following properties:  $r_o = 2.34$  mm and  $w_o$  varies between 0.8-1.3 mm. 6 trials total. Equation 7.3 is plotted (— —) for  $D_0 = 2.1$  mm and  $r_{h,0} = 0.373$  mm, which was the average value initial hole radius for the experimentally measured cases.

penetrating hole; compare with Figure 51  $t = 15.33$  ms) takes  $\Delta t = 4.4$  ms; the real situation takes  $\Delta t = 8.33$  ms; however, the timescales are still quite comparable. The discrepancy is likely due to the assumption of  $c = U_0$ . Another means to estimating that timescale would be to take the ratio of outer lens radius to impact velocity,  $r_o/U_0 \approx 2$  ms. Once again the discrepancy is due to estimating the wave velocity as the impact velocity. Now that the penetrating hole time and length scales have been considered, it is necessary to consider the hole expansion speed for the previous conditions.

Figure 53 presents a plot of the differential of hole radii ( $\Delta r_h$ )—which is defined with respect to its initial radius ( $r_{h,0}$ )— $\Delta r_h = r_h - r_{h,0}$  vs. time ( $t$ ). As was shown by Kim et al. (224), the hole expansion velocity can be derived by balancing surface tension ( $F_\sigma = 2\pi r_h \sigma_{lv} (1 - \cos \theta_{CB}^*)$ ) and inertial forces ( $F_\rho = 2\pi \rho r_h \bar{h} U_h^2$ ). However, if instead of utilizing a nominal film thickness in the inertial force approximation, one employs the actual hole height,  $h_h$ , which varies depending on the hole size, one can define  $\Delta r_h$  as

$$\Delta r_h(t) = \sqrt{\frac{2\sigma_{lv}}{\rho h_h(t)}} t, \quad (7.3)$$

where for  $\theta_{CB}^* = 160^\circ$  the following approximation was made  $\cos \theta_{CB}^* = \cos 160^\circ \approx -1$ . Once again, we held  $V$  constant, and therefore accounted for the change in lens shape (*i.e.*,  $h_h$ ) as a result of hole formation (see Appendix B.2.1 for a detailed analysis). Figure 53 also plots Equation 7.3 for the same parameters used in the experimental case ( $D_0 = 2.1$  mm,  $r_o = 2.34$  mm) and the value of  $r_{h,0}$  used was the average of the experimental cases, 0.373 mm. It is apparent that Equation 7.3 overestimates  $\Delta r_h$  and therefore  $U_h$ ; however, the trends are similar and the magnitudes are close. Previous analysis suggests that  $U_h$  should be constant; however, our analysis suggests that by accounting for the change in lens shape as a result of hole expansion, that the velocity should decrease in time as a result of increased  $h_h$ . This is however not perceptible in the experimental data due to limitations (resolution) with our high-speed image acquisition setup.

Using the same drop impact technique shown in the formation of the ring (Figure 51), it is possible to create droplet patterns which are not radially symmetric. To demonstrate this,



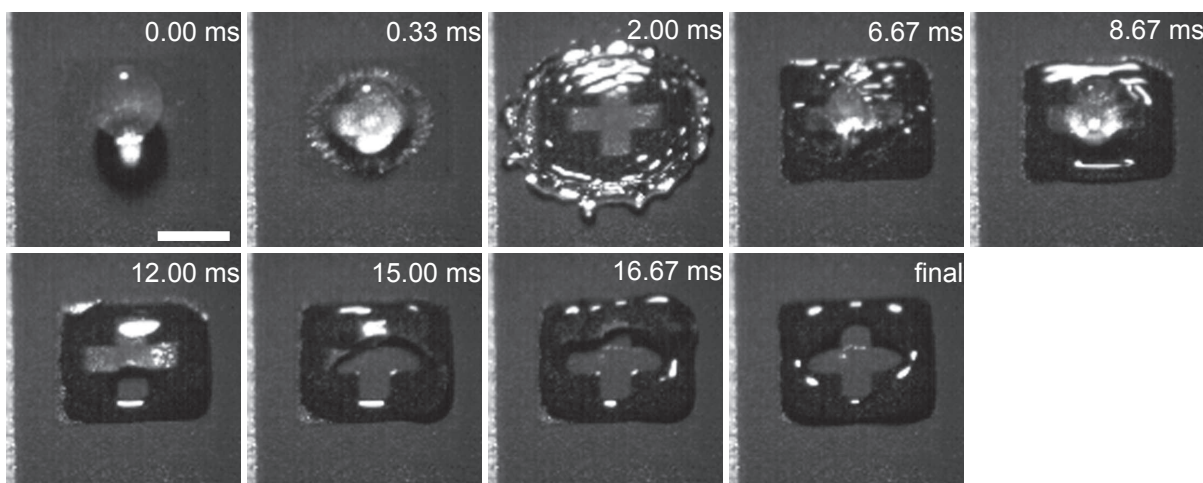


Figure 54. Droplet impact ( $We=100$ ) on a wettability patterned square with sides of 4.5 mm and a 2.7 mm by 0.866 mm hydrophobic cross. Scale bar shown is 2.0 mm.

Figure 54 presents droplet impact experiments on a cross wettability pattern. The hydrophilic square has an outer dimension of 4.5 mm and the centered inner hydrophobic cross has dimensions 2.7 mm x 0.866 mm. A penetrating hole forms in the liquid film—at the wettability transition—which grows to take up the shape of the hydrophobic cross, as previously shown for annular patterns. The cross pattern has shown to be very repeatable and consistent, even when the droplet impacts slightly off center, a hole would still form with no satellites. One possible application of this process is rapid soft (water) templating for the purposes of forming films of complex geometries.

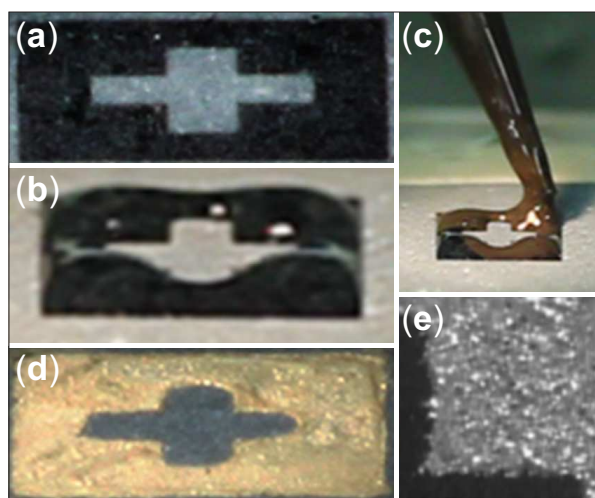


Figure 55. The process used to create a silver cross outline from a wettability pattern: (a) Hydrophilic cross outline pattern on the superhydrophobic surface. The hydrophilic square has sides of 4.5 mm and the centered inner hydrophobic cross is of dimensions 2.7 mm by 0.866 mm; (b) drop impact onto the hydrophobic cross ( $We = 100$ ) leaves a water template of the desired pattern; (c) silver nanoparticle ink is dispersed throughout the water template; (d) silver film after low-temperature sintering; (e) microscopic view of (d) shows the silver formed on the hydrophilic patterned section and did not extend onto the hydrophobic area.

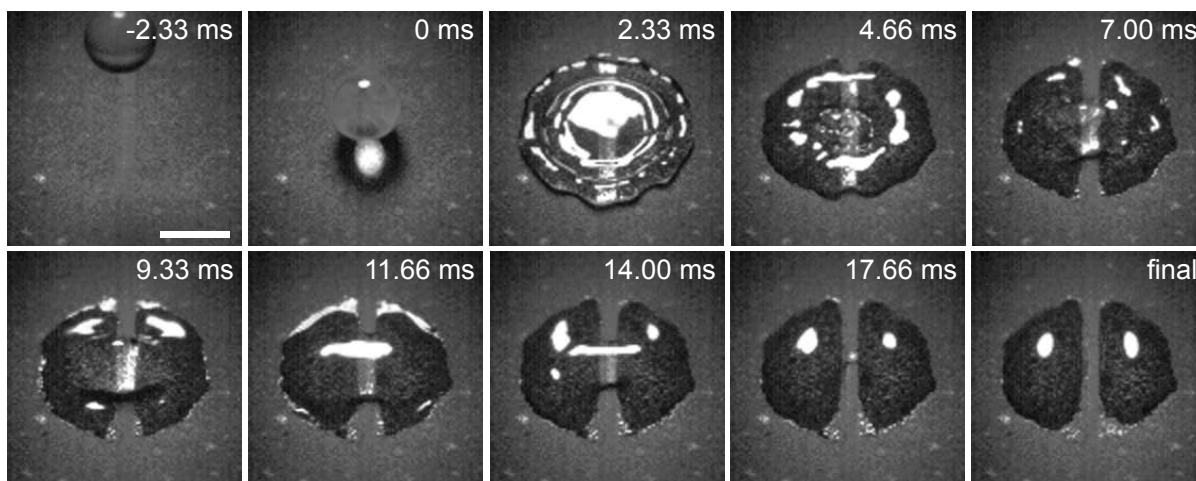


Figure 56. Droplet impact on a superhydrophobic line with a width of 0.5 mm at  $We=60$ .

Scale bar is 2.0 mm.

To demonstrate this technique, a low-temperature sintering silver nanoparticle ink was added to the water template to create a thin conductive silver cross. The process used is shown in Figure 55. Silver nanoparticle ink was added to the water template by a pipette shown in Figure 55c. The sample was put in a dry air convention oven at  $120^{\circ}\text{C}$  for 180 s to allow for the ink to form silver; the manufacturer states that if conditions are optimized then this type of silver can sinter in seconds. Taking a close look at one of the corners of the silver cross (Figure 55e), it can be seen that the silver was formed on the hydrophilic pattern and did not extend onto the hydrophobic surface after silver was formed.

While the previous work emphasized complex shaping—in a well controlled manner—of liquid droplets with droplet impact on wettability patterned surfaces, the fact that advancing contact line behavior is inertia dominated and receding contact line behavior is wettability dominated can be used to also split liquid micro-volumes. Figure 56 shows a sequence of snapshots of a water droplet impacting on a superhydrophobic line of width 0.5 mm at a  $We = 60$ . Left and right from the hydrophobic line the surface is hydrophilic. After the impact the drop reaches its maximum spreading radius. The shape of the contact line is slightly irregular due to the differences in wettability of the surface. From the maximum spreading radius the contact line on the hydrophobic part of the surface recedes quickly while the rest of the contact line being pinned on the hydrophilic parts of the surface only slightly recedes. As a result a liquid bridge between two main parts of the drop forms and finally the bridge collapses leading to a separation of the drop—in under 18 ms—into two drops of equal size; therefore, this wettability pattern acts as a kind of “scalpel” (227). Experiments at low values of  $We$  ( $We < 30$ ) show that with the investigated surfaces splitting is not possible (see Figure B8), suggesting the large role that inertia plays in the process. As the width of the superhydrophobic line becomes larger, the droplet requires a larger value of  $D_{max}$  in order to reach the hydrophilic regions (*i.e.*, higher  $We$ ), leading to an increased risk of partial rebound and “sling shot” action, resulting in a loss of the liquid volume (Figure B9). This is not desirable behavior for surface microfluidic devices. While most of this discussion is focused in splitting a droplet in two, such wettability engineered surfaces are capable of a much higher rate of droplet sampling. Figure B10 presents a wettability patterned coating capable of rapidly sampling a large number (24 droplets) of small

volumes in  $\sim 0.01$  s. Such behavior may prove useful for rapid sampling surface microfluidic systems.

In order to understand how efficient the aforesaid process is at splitting a droplet, it is instructive to compare the kinetic energy of the impacting droplet with the energy required to split one droplet into two. We achieve this by defining an efficiency parameter  $\eta = \Delta E_\sigma / E_k$ . The energy required to split one droplet into two is defined as  $E_\sigma = 8\pi\sigma_{lv}(D_0/2)^2((0.5)^{\frac{2}{3}} - 0.5)$ , and the kinetic energy of the impacting droplet is defined as  $E_k = \frac{1}{2}\rho(\frac{4}{3}\pi(D_0/2)^3)U_0^2$ . Therefore,  $\eta$  can be written as

$$\eta = \frac{\Delta E_\sigma}{E_k} = \frac{24 \left( \left( \frac{1}{2} \right)^{\frac{2}{3}} - \frac{1}{2} \right)}{We} = \frac{3.12}{We}. \quad (7.4)$$

For the conditions in Figure 56,  $We = 60$ , from Equation 7.4 we see that  $\eta = 0.052$  or 5.2%. While this is a relatively inefficient process, when one considers that each splitting process—achieved through droplet impact on a wettability pattern—only consumes  $5.1 \times 10^{-6}$  J, there does not seem to be much to gain by making the process even more efficient.

Vectoring of a droplet undergoing impact on a wettability patterned surface is also demonstrated; previous approaches have generated surface texture gradients to achieve similar results (236). Figure 57 shows vectoring of a droplet with a line wettability pattern. Vectoring of a droplet occurs due to a difference in the receding contact line speeds, and results in momentum being transferred into the lateral direction. If we consider a simple force balance of inertia and hysteresis, we can resolve the angle of launch and therefore the degree to which momentum is

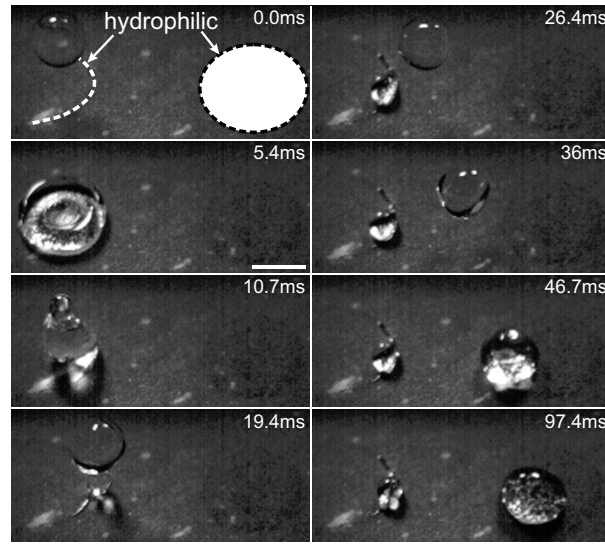


Figure 57. Droplet impact ( $We = 14$ ) on a half-annulus wettability pattern (indicated by a dashed white line) with  $r_o = 1.95$  mm and  $w_o = 0.2$  mm. The droplet is propelled towards a circular wettability pattern (indicated by white filled circular region) with radius 2.0 mm.

The distance between the edge of the half annulus and the closest edge of the circular wettability pattern is 4.0 mm. Inset scale bar is 2.0 mm.

transferred to the lateral direction. From here we can gain insight into how fast droplets can be propelled horizontally with drop impact on wettability patterns. The force due to inertia can be defined as  $F_\rho = \rho V \gamma = \frac{1}{6} \rho \pi D_0^2 U_0^2$  while the force due to surface tension can be defined as  $F_\sigma = \pi r_o \sigma_{lv}$ . In this case,  $\pi r_o$  represents the effective peripheral length of the (impacting) droplet in contact with the wettability pattern. Their ratio can be defined as

$$\frac{F_\rho}{F_\sigma} = \frac{\frac{1}{6} \rho \pi D_0^2 U_0^2}{\pi r_o \sigma_{lv}} = We \left( \frac{D_0}{6r_o} \right). \quad (7.5)$$

If  $D_{\max} \sim 2r_o$ , then from Equation 7.1 we see that  $D_0 \sim 2r_o/We^{\frac{1}{4}}$ . Substituting this into Equation 7.5 we see that

$$\frac{F_\rho}{F_\sigma} = \frac{1}{3} We^{\frac{3}{4}}. \quad (7.6)$$

Substituting  $We = 14$  into Equation 7.6 gives  $\frac{F_\rho}{F_\sigma} = 2.4$ . Noting that  $F_\sigma$  and  $F_\rho$  act parallel and perpendicular to the substrate, respectively, the angle of droplet launch ( $\beta$ ; defined with respect to the horizontal substrate) can be found by taking the inverse tangent of the ratio of their magnitudes

$$\beta = \tan^{-1} \left( \frac{|F_\rho|}{|F_\sigma|} \right) = \tan^{-1} \left( \frac{1}{3} We^{\frac{3}{4}} \right). \quad (7.7)$$

Substituting  $We = 14$  into Equation 7.7 gives  $\beta = 67^\circ$ . With  $\beta$  known, it should now be possible to rectify a horizontal velocity component,  $U_x$ , by projecting the initial impact velocity ( $U_0$ )

in that direction and accounting for energy losses during the collision event by implementing a coefficient of restitution ( $\epsilon$ ). This can be estimated as

$$U_x \approx \frac{\epsilon U_0}{\tan \beta} = \frac{\epsilon U_0}{\frac{1}{3} We^{\frac{3}{4}}}. \quad (7.8)$$

Taking  $U_0 = 0.70 \text{ m s}^{-1}$ ,  $\beta = 67^\circ$ , and  $\epsilon = 0.86$  (237), we see that  $U_x \approx 0.25 \text{ m s}^{-1}$ . The experimentally measured value was  $U_x = 0.16 \pm 0.02 \text{ m s}^{-1}$ , which is about 65% of the theoretically predicted value. The discrepancy may be owed to several facts: 1) The value of  $\epsilon$  used here was for droplet impact on a totally superhydrophobic surface (unpatterned); 2) some portion of the droplet volume remains on the wettability patterned after the droplet is launched (see Figure 57). Both of these facts should force deviations between experimental and theoretical values. While there are deviations, the calculation is of the correct magnitude, and may help in the design of future pumpless surface microfluidic platforms interested in high-transport rates. One interesting thing to note from Equation 7.8 is that  $U_x$  scales like  $U_0^{-\frac{1}{2}}$ , meaning that the higher  $U_0$  is, the lower that  $U_x$  is. This means—rather non-intuitively—that increasing the impact velocity does not maximize  $U_x$ . It suggests that  $U_0$  should be kept relatively small—while still keeping  $We \gtrsim 10$ —in order to maximize  $U_x$ . In fact, large values of  $U_0$  generally resulted in satellite droplets being ejected vertically during droplet vectoring. If we compare  $U_x$  with the meniscus velocities of other fast transport surface microfluidic systems ( $0.4 \text{ m s}^{-1}$  (238),  $0.031 \text{ m s}^{-1}$  (46),  $0.005 \text{ m s}^{-1}$  (185)), we see that it is either quite comparable or even better. This surface microfluidics platform also demonstrated relatively high fluid transport rates of  $Q = \pi (D_0/2)^2 U_x = 540 \text{ } \mu\text{L s}^{-1}$ .



## CHAPTER 8

### CONCLUSIONS AND RESEARCH OUTLOOK

This thesis has considered a variety of research topics which all involve either design, synthesis, or characterization of wettability engineered surfaces; all of the wettability engineered surfaces consisted of either unpatterned or patterned nanostructured composite coatings. The conclusions from each of the previous research topics is discussed below.

#### 8.1 Thesis conclusion

##### 8.1.1 Environmentally Benign Superhydrophobic Coatings

We report for the first time an all-aqueous, fluorine-free dispersion that when spray deposited and dried, forms a superhydrophobic coating. A combination of water-based polyolefin (hydrophobic) solution with a stable exfoliated graphite nanoplatelet (hydrophobic) water suspension form the sprayable dispersion. Both components are stabilized in water through pH modification and charge stabilization. At the optimum xGnP mass fraction of 0.64, the coatings feature contact angles exceeding  $150^\circ$  and contact angle hysteresis below  $10^\circ$ . In addition, the coatings are electrically conducting with conductivity exceeding  $1 \text{ S m}^{-1}$ . The present study offers new insights on synthesizing fluorine-free coatings that are not only environmentally friendly, but also well suited for manufacturing platforms where all-aqueous formulations are preferred.

### **8.1.2 Stretchable Superhydrophobic Composite Coatings**

Stretchable, superhydrophobic, composite coatings were synthesized by solution-based processing of nitrile rubber and two separate particle fillers, poly(tetrafluoroethylene) (submicron-scale) and carbon black (nanoscale); filler mass content was minimized. The ability of these coatings to conform to high strains of the underlying flexible substrate was demonstrated promising application for non-woven substrates. Superhydrophobicity of the coatings was demonstrated for uniaxial stretching up to 30% strain on silicone rubber, 70% strain on polyester fabric, and for cyclic stretching on these two substrates. Water droplet sliding angles—for optimum filler concentrations—were low enough to deem these coatings self-cleaning even under extreme strain. SEM characterization of coatings under strain revealed that fibrils form as a result of crazing, and play a role in delaying the true fracture of the composite at high strains. The present results are important as they offer a facile method to synthesize large-area, flexible, conforming, superhydrophobic coatings with commercially available ingredients.

### **8.1.3 Fluoropolymer Blends: Multifunctional Liquid Repellent Nanocomposites**

Novel fluoropolymer dispersions comprising PVDF and a fluoroacrylic copolymer were prepared in a multi-component solvent system. Stable polymer blend solutions were obtained by initially dissolving PVDF in a co-solvent (NMP, acetone) and then by dropwise addition of water-dispersed fluoroacrylic copolymer under pH control using trifluoroacetic acid or formic acid. Nanostructured organoclay or carbon nanowhiskers can be easily dispersed in these stable polymer solutions for single-step fabrication of superhydrophobic nanocomposites by spray casting. Wettability characterization with water as well as a lower surface tension water-alcohol (9:1

wt. ratio) mixture was performed and revealed very good liquid repellency of these composite coatings. In addition, liquid repellent nanocomposite coatings containing carbon nanowhiskers were electrically conductive, as an added functionality. The concentration of fillers required in these composite coatings for water and water-IPA repellency was compared with a previously reported PVDF-based coating system and showed a dramatic reduction in filler concentration for a certain level of performance, thus promising significant material savings in large-scale applications. Such large-area scalable functional durable superhydrophobic composites can have various potential industrial applications, such as exterior protective coatings, marine and aerospace coatings and electroactive liquid repellent coatings for anti-icing applications to name a few.

#### **8.1.4 Wettability Engineering: Handling Low Surface Tension Liquids**

In summary, we demonstrated the ability to fabricate a surface microfluidic device featuring surface tension confined tracks for pumpless transport of low-surface tension liquids using large-area, scalable techniques—namely spray and continuous fountain pen printing. Low-surface tension liquids, such as acetone, ethanol and hexadecane, attained advancing meniscus velocities up to  $3.1 \text{ cm s}^{-1}$  on said tracks. The meniscus advancement along the tracks was characterized by combining high speed imaging and a scaling analysis of capillary-viscous force balance for liquid impregnation into the surface texture—similar to Washburn’s theory. In a separate application, the tracks were used to allow selective and directionally controlled transport of water droplets in a preferred sliding direction with the aid of gravity. In general, such patterns can find application in low-cost, scalable technologies for lab-on-a-chip and other sur-

face microfluidic devices designed to selectively confine and deliver liquids with a wide-range of surface tensions without the need for pumps. Several other existing surface microfluidic platforms envisioned to benefit from this approach were also presented; currently they are used for water, but with the present approach—and possible modification of the patterning polymer—implementation to low-surface tension liquids may be possible.

#### **8.1.5 Wettability Engineering: Thermal Stability and Scalability**

Thermally-stable (at temperatures below 400°C) polysilsesquioxane-silica superhydrophobic nanocomposite coatings have been demonstrated by spray casting nanoparticle dispersions in alcohol. The coatings, after drying, are intrinsically superhydrophobic, but are capable of becoming superhydrophilic by either flame or CO<sub>2</sub> laser treatment in open air. The latter allows imprinting of superhydrophilic patterns onto the coatings with feature size around ~100 μm. The interface between heat-treated and untreated regions was sharp, as determined by advancing CA and SEM analysis. Chemical analysis suggests that the wettability transition is due to oxidation of hydrophobic methyl groups. Wettability transitions were interpreted within the Wenzel and Cassie-Baxter wetting theories. Simple water pool boiling experiments showed the promise of such patterned surfaces for enhanced heat transfer applications. Water velocities of ~2 mm s<sup>-1</sup> in true micro channels offers promise for fabricating surface tension confined micro-channels (STC). Advantages of the present approach include inherent thermal stability over organic-based coatings, as well as scalability to large-area applications.

### 8.1.6 Wettability Engineering: Shaping and Mobilizing Liquid $\mu$ -Volumes

Wettability engineered surfaces capable of shaping, splitting, and vectoring impacting liquid droplets—without loss of liquid—was demonstrated for lab-on-a-chip style applications. Droplets were shaped into hollow-type patterns such as annuli which are of use for surface microfluidic applications. Such droplet  $\mu$ -volume shaping was employed as a soft (water) template and was used to form complex conductive silver patterns; potential applications include next-generation terahertz devices. Suitable drop impact and thin film rupture models were developed developed to aid in rational design of wettability engineered surfaces. Droplet impact on wettability engineered surfaces was also shown to be efficient as droplet splitting (*i.e.*, superhydrophobic scalpel). Finally, droplet vectoring was also demonstrated. Both the angle and magnitude of droplet vectoring behavior was shown to be consistent with a suitable fluid mechanical model.

## 8.2 Expected research contribution

The research contributions from each of the previous research topics is discussed below.

### 8.2.1 Environmentally Benign Superhydrophobic Coatings

- The first ever water-based, non-fluorinated polymer-nanoparticle dispersion for superhydrophobic coatings by spray was designed and synthesized. This should have a significant impact on industrial and commercial implementation as no harsh solvents or fluorinated compounds are used in synthesizing nor are they contained in the final coating. All ingredients were obtained from commercial sources ensuring the scalability of the dispersion.

- This coating system emphasized multi-functionality so that applications other than liquid repellency would be impacted ensuring wider implementation. In fact, electrically conductive exfoliated graphite nanoplatelets (xGnP)—which can be compared with the wonder material graphene (highly electrically conductive)—were the primary focus of this study.
- Specifically, this coating system is expected to assist in fluid management strategies for disposable non-woven substrates.

### 8.2.2 Stretchable Superhydrophobic Composite Coatings

- The first ever stretchable, superhydrophobic polymer nanocomposite coating was designed and synthesized; applications are envisioned for non-woven and woven substrates.
- The coating demonstrated the operating limits of superhydrophobic polymer composite coatings for application on flexible rubber and polyester woven substrates and a failure mode was identified.
- Its main purpose was to highlight the need for robust mechanical characterization of superhydrophobic coating treatments as many lack durability relative to existing commercial coatings or paints.
- A wettability study was performed on a classic polymer nanocomposite: nitrile rubber and carbon black.

### 8.2.3 Fluoropolymer Blends: Multifunctional Liquid Repellent Nanocomposites

- The first ever superhydrophobic poly(vinylidene fluoride)-nanoclay composite—a classic nanocomposite system known for its excellent mechanical properties—was designed, synthesized, and characterized.
- By selecting a proper nanoparticle and copolymer—for the purposes of reducing surface energy and also enhancing substrate adhesion—this composite coating system demonstrated a 66 wt.% reduction in filler particle concentration (in the dry composite) required for producing water and water-alcohol repellency as compared with a previous superhydrophobic poly(vinylidene fluoride) composite coating system.
- In order to blend the aforesaid high-performance copolymer—a fluoroacrylic copolymer—with solution processed poly(vinylidene fluoride), a detailed analysis of the miscibility was undertaken. It was shown that solution processed poly(vinylidene fluoride) was capable of accepting a non-trivial amount of non-solvent (*i.e.*, water; ~10 wt.%) to its solution without phase inverting, which is an important characteristic for blending poly(vinylidene fluoride) with polymers that were solution processed with non-solvents (*i.e.*, water).
- A wettability study was performed on a classic polymer nanocomposite: poly(vinylidene fluoride) and nanoclay.

### 8.2.4 Wettability Engineering: Handling Low Surface Tension Liquids

- One of the first ever superoleophobic-superoleophilic patterning systems was designed, synthesized, and characterized for pumpless transport of low-surface tension liquids.

- A simple visco-capillary model was developed and implemented which should aid in the rational design of future pumpless surface microfluidic systems.
- Such a simple coating and patterning system should find applications in low-cost, scalable technologies for lab-on-a-chip style applications and combinatorial chemistry. Advantages of this technique are its ability to selectively confine and transport liquids with a wide-range of surface tensions in a pumpless manner.

#### **8.2.5 Wettability Engineering: Thermal Stability and Scalability**

- The first ever spray coating and CO<sub>2</sub> laser patterning technique (scalable) capable of producing binary micropatterns of superhydrophobicity and superhydrophilicity was synthesized and characterized.
- This technique should have impact on rapid prototyping of wettability engineered coatings—for applications in surface microfluidics and multi-phase heat transfer—due to its flexible processing techniques which are capable of being modified on-the-fly.
- This coating system is expected to find broad application in heat transfer applications due its inherent thermal stability (400°C).

#### **8.2.6 Wettability Engineering: Shaping and Mobilizing Liquid $\mu$ -Volumes**

- The second ever report on complex micro-volume shaping through water droplet impact on wettability engineered surfaces was presented.



- Several fluid and thermodynamics models were developed which are expected to aid in rational design of future surface microfluidic platforms employing droplet impact techniques for the purposes of shaping, splitting, and vectoring.
- Droplet vectoring was achieved by spatially altering surface energy; previous reports emphasized surface texture gradients.
- Liquid velocities  $\sim 0.70 \text{ m s}^{-1}$  were achieved, which are among the highest ever reported for water on a surface microfluidic device. Liquid flow rates  $\sim 540 \text{ }\mu\text{L s}^{-1}$  were also achieved which are believed to be among the highest reported for a surface microfluidic device.

### **8.3 Recommendations for future research**

#### **8.3.1 Environmentally Benign Superhydrophobic Coatings**

A great deal of research remains to be done on water-based, non-fluorinated superhydrophobic coating systems. This report represents the first of its kind. Specifically, work remains to be done on making such films more optically transparent for it to realize much wider industrial and commercial implementation.

#### **8.3.2 Stretchable Superhydrophobic Composite Coatings**

Attaining superhydrophobic coating systems capable of withstanding robust mechanical abrasion or strain remains one of the most elusive goals in this particular research area.

### **8.3.3 Fluoropolymer Blends: Multifunctional Liquid Repellent Nanocomposites**

Utilizing poly(vinylidene fluoride) in composite coatings has major advantages—especially if the goal is multi-functionality—as it has excellent piezoelectric properties. By forming nanocomposites of poly(vinylidene fluoride) with nanoclay—and potentially other nano-fillers—one can obtain the necessary crystalline phase for generating its piezoelectric property. Superhydrophobic composite coatings with piezoelectric properties are expected to be of interest to both fundamental research as well as potential fluid management technologies.

### **8.3.4 Wettability Engineering: Handling Low Surface Tension Liquids**

Wettability engineered surfaces for handling of low-surface tension liquids in a pumpless manner is only in its infancy. It is believed that such research can be of great use to combinatorial chemistry or other surface microfluidic systems that are looking to extend into low-surface tension liquids.

### **8.3.5 Wettability Engineering: Thermal Stability and Scalability**

While a great deal of characterization in terms of basic capabilities was performed, much remains to be done on this coating system for multi-phase heat transfer, which is its envisioned application. Specifically, much remains to be done on pool boiling characterization as well as condensation. The latter should be of interest to fluid management technologies such as water collection and fog harvesting.

### **8.3.6 Wettability Engineering: Shaping and Mobilizing Liquid $\mu$ -Volumes**

Since this was only the second report on droplet impact on wettability engineered surfaces for complex droplet shaping, droplet splitting, and droplet vectoring, there is much that remains

to be done on this topic. Testing the presented theories and models should be of a particular interest as well as proving the system as a capable surface microfluidic system (*e.g.*, mixing, etc.). The use of the complex droplet shaping for a soft (water) template should also be of interest.

## APPENDICES

## Appendix A

### SUPPORTING INFORMATION: WETTABILITY PATTERNING

The photographs shown in Figure A1 show the heat-induced change in wettability from superhydrophobic to superhydrophilic. Figure A1a shows three droplets beaded on a superhydrophobic MSQ-HFS coating applied on an aluminum plate. Figure A1b shows the flame treatment using a propane torch; open-air exposure lasted only a few seconds. The flame was operated in the premixed mode, thus assuring the absence of carbonaceous soot (as also affirmed by the blue color of the flame). After flame treatment, the MSQ-HFS coating became superhydrophilic, as shown in Figure A1c, d and e.

In the case of a semi-infinite solid medium heated on a spot, the corresponding rise in surface temperature ( $\Delta T$ ) can be estimated using the following expression

$$\Delta T(t) = \frac{(1-R)I}{K} \left[ \frac{\delta}{\sqrt{\pi}} - \frac{1}{\alpha} \left( 1 - e^{(\alpha\delta/2)^2} \operatorname{erfc}(\alpha\delta/2) \right) \right], \quad (\text{A1})$$

where  $R$  is the surface reflection coefficient,  $I$  the irradiance (uniform source),  $K$  the thermal conductivity,  $\delta$  the diffusion length ( $\delta = 2\sqrt{\kappa t}$ ; with  $\kappa$  being the thermal diffusivity and  $t$  the time), and  $\alpha$  the absorption coefficient (215; 216). With  $R = 0.05$ ,  $K = 0.01 \text{ W cm}^{-1} \text{ K}^{-1}$ ,  $\kappa = 6.0 \cdot 10^{-3} \text{ cm}^2 \text{ s}^{-1}$ ,  $\alpha = 10^3 \text{ cm}^{-1}$  for glass (216), and  $I \approx 0.2 \text{ MW cm}^{-2}$ , Equation A1 predicts that  $\Delta T \sim 2000 \text{ K}$  after only  $t = 0.022 \text{ ms}$ , a temperature that is comparable with the propane flame temperature.

## Appendix A (Continued)

Figure A4a-c, Peak 1 and Peak 2 correspond to Si-R and Si-O bonding, respectively. After thermal treatment, an increase in Peak 2 is observed with a corresponding decrease in Peak 1, which can be interpreted as an increase in Si-O bonding with a decrease in hydrophobic groups, *i.e.*, increased hydrophilicity. d-f, Peak 1 corresponds to Si-O bonding, and its concentration increases from d to e and f, suggesting increased hydrophilicity of the coating. g-i, Peak 1 corresponds to adventitious carbon and/or simple C-H / C-C bonds. Its reduction from g to h and i is indicative of suspected cleavage of methyl groups, and increased hydrophilicity.

Figure A6(a)-(b) presents a sequence of SEM micrographs with increasing magnification from a to b of a spray deposited MSQ-HFS coating ( $w_p = 0.5$ ) after flame treatment. This coating displays the property of superhydrophilicity. Note how the morphology of this coating has relatively little morphological difference as compared with the untreated version of this coating (see Figure 36).

## Appendix A (Continued)

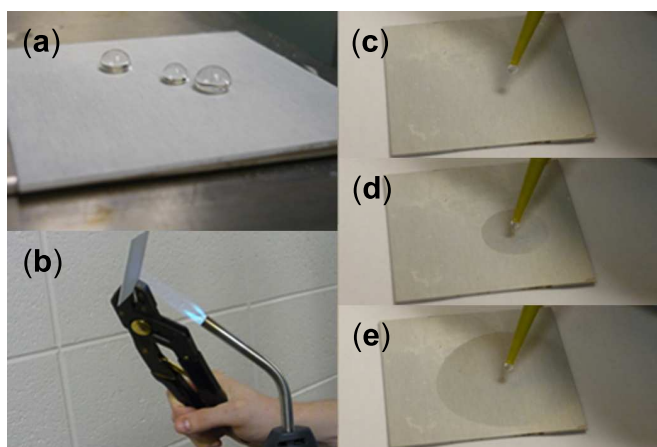


Figure A1. (a) Photograph of beaded water droplets on a MSQ-HFS film applied on an aluminum plate. (b) Flame treatment of the coating shown in (a) using a propane torch for a few seconds from a distance of 5-10 cm. (c) Photograph of the flame-treated coating just before depositing a water droplet ( $> 10 \mu\text{L}$ ). (d) Completely wetting droplet spreading on the flame-treated coating. (e) Completely wetting droplet at its final fully-spread state.

## Appendix A (Continued)

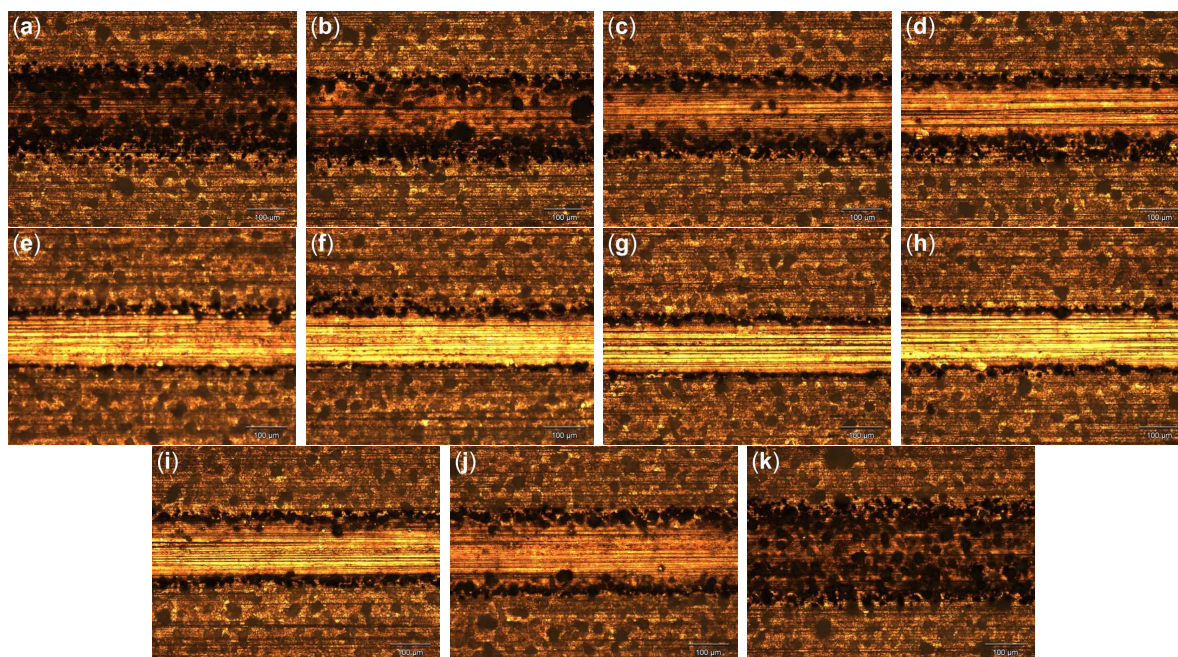


Figure A2. Superhydrophobic MSQ-HFS coatings patterned with a single pass of a CO<sub>2</sub> laser beam at a fixed power (1.0 W) and speed (2.0 cm s<sup>-1</sup>) with a constant focal length and variable distance between the lens and the substrate. The inset scale bars are 100 μm. The distance between the laser (lens) and the substrate is decreasing from (a) to (k). The optimum range is between (e)-(h) with the minimum line width in (g) being 109±6 μm. Inset scale bars in the images are all 100 μm.



## Appendix A (Continued)

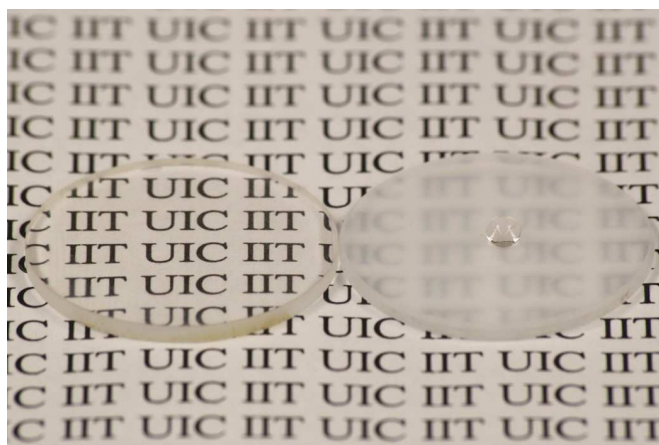


Figure A3. Superhydrophobic MSQ-HFS film deposited onto two quartz substrates (2.54 cm dia.) before (right) and after (left) laser processing, which induces hydrophilicity and increases transparency. A water droplet has been deposited on each surface, but is visible as a bead only on the superhydrophobic disk (right). The droplet on the superhydrophilic disk (left) has fully spread, thus becoming indistinguishable.

## Appendix A (Continued)

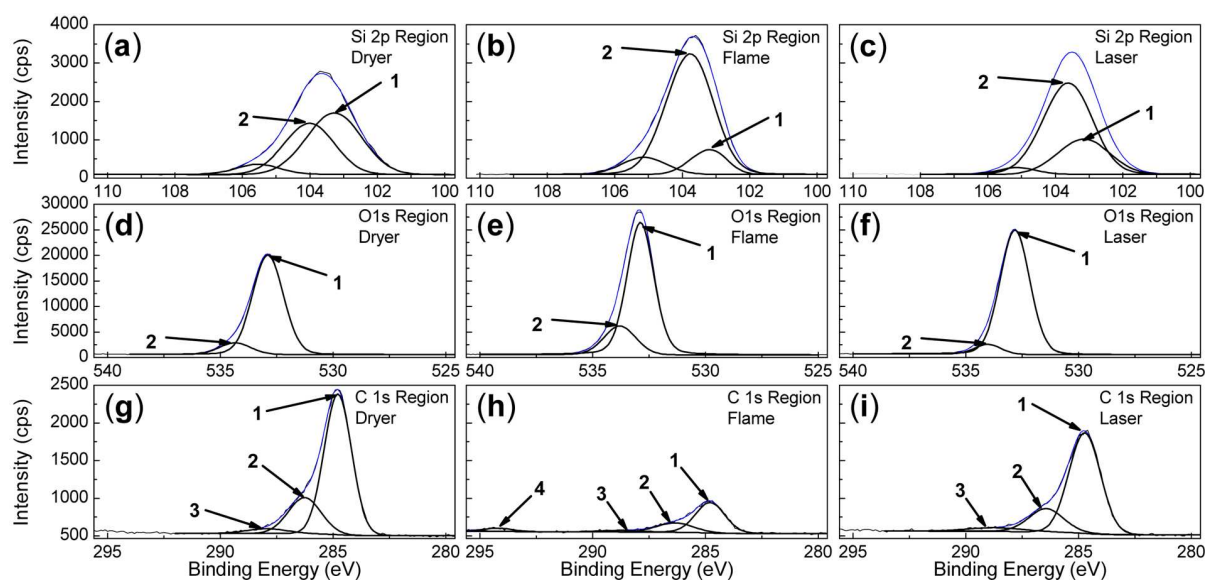


Figure A4. XPS data of untreated (superhydrophobic) and heat-treated (superhydrophilic) MSQ-HFS coatings. (a)-(c) Si 2p region; (d)-(f) O 1s region; (g)-(i) C 1s region. Figures in the left column represent untreated state, while figures in the middle and right columns are the corresponding thermally treated states. Thermal treatment was performed by either a flame ((b), (e) and (h)) or CO<sub>2</sub> laser ((c), (f) and (i)). For a given region, each peak is designated by a number.

## Appendix A (Continued)

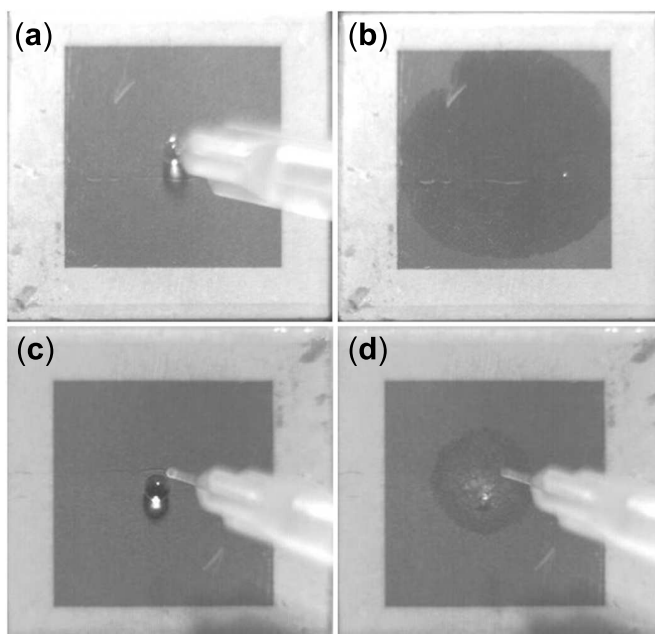


Figure A5. A sequence of images demonstrating the super-wetting behavior of water on laser patterned areas of the MSQ-HFS coating for (a)-(b) room temperature conditions ( $T = 25^{\circ}\text{C}$ ), and (c)-(d)  $T = 138^{\circ}\text{C}$ . The time difference from (a) to (b) is 1.0 s, and (c) to (d) is 0.4 s. Images were captured with a high speed camera mounted overhead at a frame rate of  $250\text{ s}^{-1}$ .

The size of the laser patterned areas is  $6.4\text{ cm}^2$ ; water droplet volumes are  $< 10\text{ }\mu\text{L}$ .

## Appendix A (Continued)

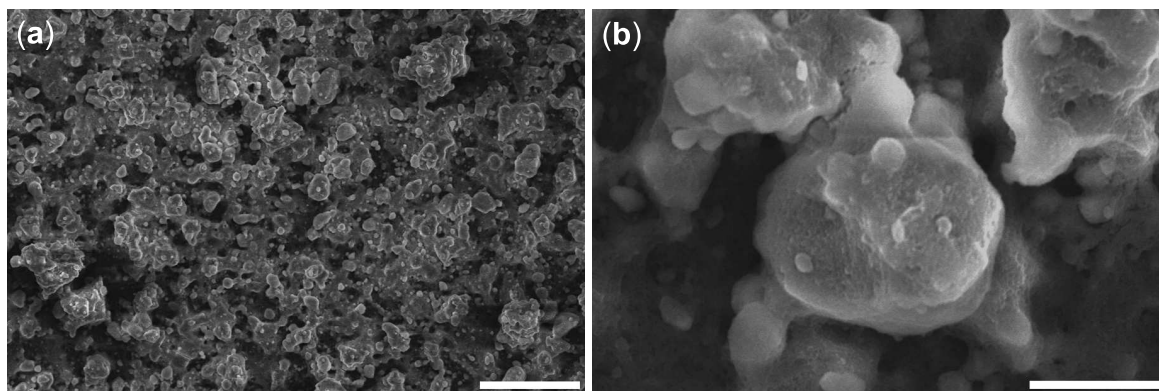


Figure A6. (a)-(b) SEM micrographs of spray deposited MSQ-HFS coatings ( $w_p = 0.5$ ) with increasing magnification left-to-right after flame treatment (*i.e.*, superhydrophilic coating).

Scale bars: (a) 50  $\mu\text{m}$ ; (b) 10  $\mu\text{m}$ .

## Appendix B

### SUPPORTING INFORMATION: DROPLET IMPACT

#### B.1 Fabrication

Figure B2 presents a sequence of images demonstrating the synthesis procedure for obtaining wettability patterned coatings (a-d) as well as the corresponding scanning electron micrographs of the coatings after each processing step at low- (e-h) and high-magnification (i-l).

To illustrate why printing four times on the same spot is useful Figure B2 (g) and (k) show the wettability patterned coating with only one layer of ink (magenta color). It is apparent that only parts of the nanostructure are covered with ink. The final wettability patterned coating, with four layers of ink, is shown in Figure B2 (h) and (l). Most of the nanostructure is covered with the ink, while maintaining a high-degree of surface micro-texture, giving rise to the extremely low value of  $\theta_r^*$ .

#### B.2 Force balance

In order to understand the validity of approximating the impact velocity of the droplet as

$$U_0 = \sqrt{2gL}, \quad (B1)$$

it is necessary to compare the force due to drag ( $F_d$ ) with that due to gravity ( $F_g$ ). In the case of a water droplet traveling through air, the Reynolds number ( $Re$ ) can be calculated as  $Re = D_0 U_0 / \nu$  where  $\nu$  is the kinematic viscosity of air. Substituting appropriate values ( $U_0 \approx 1$

## Appendix B (Continued)

$\text{m s}^{-1}$ ;  $D_0 = 0.002 \text{ m}$ ;  $\nu = 1.6 \cdot 10^{-5} \text{ m}^2 \text{ s}^{-1}$ ) (239), the Reynolds number can be calculated as  $\text{Re} = 125$ , which is a relatively low value.

Assuming that the water droplet travelling through air behaves like a smooth sphere, the drag force  $F_d$  can be calculated from the drag equation as (239)

$$F_d = \frac{1}{2} \rho_a U_0^2 C_{\text{drag}} A, \quad (\text{B2})$$

where  $\rho_a$  is the density of air,  $C_{\text{drag}}$  is the drag coefficient (dimensionless; depends on  $\text{Re}$ ), and  $A$  is the cross sectional area of the sphere ( $A = \pi(D_0/2)^2$ ). For  $\text{Re} \approx 100$ ,  $C_{\text{drag}}$  can be found from standard drag coefficient plots as  $\approx 1$  (239). Substituting the appropriate values into Equation B2 ( $\rho_a = 1.2 \text{ kg m}^{-3}$  (239);  $U_0 \approx 1 \text{ m s}^{-1}$ ;  $A = 3.1 \cdot 10^{-6} \text{ m}^2$ ) gives  $1.8 \mu\text{N}$ . The force experienced by the droplet due to gravity can be calculated as  $F_g = m_d g$  where  $m_d$  is the mass of the droplet and  $g$  is the acceleration due to gravity. Substituting appropriate values ( $g = 9.81 \text{ m s}^{-2}$ ;  $m_d = 4.2 \cdot 10^{-6} \text{ kg}$ ) gives  $F_g = 41 \mu\text{N}$ . So the ratio of  $F_g/F_d$  is  $> 20$  indicating that the drag force is minimal with respect to the gravitational force, so the assumption in Equation B1 holds. We also found that the computed and measured values of  $U_0$  never differed by more than 4%.

### B.2.1 Hole Formation

Considerations on the effect cylindrical (axisymmetric) hole formation has on the shape of a liquid lens are given here. In order to form a cylindrical hole of volume  $V_h = \pi r_h^2 h_h$  in a lens, it is necessary to displace liquid of equal volume. The volume of the lens can be defined as a spherical cap

## Appendix B (Continued)

$$V_l = \frac{\pi h_l}{6} \left( 3r_0^2 + h_l^2 \right). \quad (\text{B3})$$

The volume for a lens with a hole can be approximated as

$$V_{l,h} = \frac{\pi h_l}{6} \left( 3r_0^2 + h_l^2 \right) - \pi h_h r_h^2. \quad (\text{B4})$$

In the case of Equation B3 and Equation B4, it was not possible—for the parameters relevant to this study—to find  $h_l$  as a function of  $V$  and  $r_0$  directly. Therefore, in order to calculate the effect of a hole on the shape of a lens—and the resulting energy state—the following procedure was executed: 1)  $V_l$ ,  $r_0$ ,  $\sigma_{lv}$  and  $\theta_{CB}^*$  were held constant; 2) a value of  $r_h$  was selected; 3) The height of the lens was approximated as the height of the hole,  $h_l \approx h_h$ ; 4) the Newton-Raphson method was used to solve Equation B4 for  $h_h$ ; 4)  $\Delta E$  was computed according to Equation 7.2. The process was repeated by selecting a new value of  $r_h$ .

For the Newton-Raphson method, the following equations were employed

$$h_h^{(n+1)} = h_h^{(n)} - \frac{f(h_h^{(n)})}{f'(h_h^{(n)})}, \quad (\text{B5})$$

where

$$f(h_h^{(n)}) = \frac{\pi h_h^{(n)}}{6} \left( 3r_0^2 + \left( h_h^{(n)} \right)^2 \right) - \pi h_h^{(n)} r_h^2 - V_{l,h}, \quad (\text{B6})$$

and

## Appendix B (Continued)

$$f' \left( h_h^{(n)} \right) = \frac{\pi}{2} \left( r_0^2 + \left( h_h^{(n)} \right)^2 - 2r_h^2 \right), \quad (\text{B7})$$

where the subscript  $n$  represents the index. No more than 10 iterations ( $n \leq 10$ ) were required for  $h_h$  to sufficiently converge. Figure B3 shows how  $h_h$  compares with  $r_h$  for the cases where the shape of the lens is and is not accounted for during hole formation. For  $r_h < 0.2$  mm, neglecting the shape of the lens appears to be a good approximation; however, for  $r_h = 0.52$  mm, it appears that the hole has a measurable impact on  $h_h$  (increased 8.3%) and therefore the shape of the lens. Figure B4 shows how  $\Delta E$  is affected by accounting for the change in lens shape as a result of hole formation. The critical radius for hole formation  $r_{h,c}$  (*i.e.*,  $r_h$  at  $\Delta E = 0$ ) increased by 10% when accounting for the change in lens shape, as expected. Figure B5 presents a plot of the ratio of the initial drop volume  $V_0$  to  $V_h$  vs.  $r_h$ . At  $r_h = r_{h,c} = 0.52$  mm,  $V_h V_0^{-1} = 0.093$ , which represents a non-trivial volume ratio, and acts to show the importance of accounting for the total volume of the lens during hole formation.

### B.2.2 Stable Liquid Annulus

The volume of a liquid annulus which exhibits  $\theta^* = 90^\circ$  can be estimated as half the volume of a torus. The volume of a torus can be defined as

$$V_{\text{tor}} = 2\pi^2 R_{\text{tor}} r_{\text{tor}}^2, \quad (\text{B8})$$



## Appendix B (Continued)

where  $R_{\text{tor}}$  and  $r_{\text{tor}}$  represent the major and minor radii of the torus. The torus minor and major radii were related to the wettability pattern as  $r_i = R - r$  and  $r_o = R + r$ . The half volume of a torus then, cast with the variables relevant to this study came as

$$V_{\text{tor},1/2} = \pi^2 (r_o - r_{\text{tor}}) r_{\text{tor}}^2. \quad (\text{B9})$$

For the purposes of this study, the variable  $r_o$  was generally fixed, so the sought after variable was  $r_{\text{tor}}$  (or  $r_i$ ). By solving Equation B9 for zero, and employing a root solver (MATLAB), one can find  $r_{\text{tor}}$ . Since there were three roots, the one with physical significance was selected. In the case of  $V_{\text{tor}} = 4.7\mu\text{L}$  (*i.e.*, initial drop volume;  $D_0 \approx 2.1$  mm) and  $r_o = 2.500$  mm, the torus tube radius came as  $r_{\text{tor}} = 0.486$  mm; therefore,  $r_i = 1.528$  mm. In an alternative pattern that satisfies the above conditions, consider if  $r_i$  was set to zero, then  $w_o$  would be 0.972 mm. In practice,  $r_i$  was generally decreased to ensure that the final annulus was symmetric, so the value of  $r_i$  found from this analysis represented an upper-bound.

### **B.2.3 Penetrating Hole Formed at the Wettability Transition**

For a more detailed analysis of hole formation in liquid lenses at wettability transitions, please refer to the work by Kim et al (224). A brief discussion is given here for clarity. Figure B6 is a schematic depicting a non-axisymmetric penetrating hole formed in a liquid lens at a wettability transition. Previous analysis showed that for contact lines advancing on a superhydrophobic surface, if their velocities exceed a critical value ( $\sim 0.01$ - $0.1$  m s<sup>-1</sup> for water)—which they did in this study—they can become roughened and can entrain air bubbles until they meet the hydrophilic annulus (224). At the transition—where the liquid lens undergoes a wettability

## Appendix B (Continued)

transition from a Cassie-Baxter to Wenzel wetting state—it tends to entrain larger air bubbles, where airflow (underneath the droplet in a Cassie-Baxter state) following the liquid flow suddenly becomes trapped (224). In the analysis by Kim et al., the first observable penetrating holes—which formed due to the presence of large underlying air pockets—had a radii  $\sim 90\mu\text{m}$ . We hypothesize that by increasing the value of  $w_o$ , eventually one can make it energetically unfavorable for such holes to form/grow. To see this, Equation 7.2 can be employed to calculate whether or not a penetrating hole is energetically favorable or not; however, since in this case  $r_h$  is fixed, and the volume of the hole is small compared with the liquid lens (*i.e.*, does not affect the radius of curvature,  $r_{\text{curv}}$ ;  $V_h/V_0 = 0.0005$ ),  $h_h$  can be defined as

$$h_h = \sqrt{r_{\text{curv}}^2 - (r_o - w_o - r_h)^2} - r_{\text{curv}} + h_{\text{max}}, \quad (\text{B10})$$

where  $h_{\text{max}}$  is the maximum height of the liquid lens (224). With this, Equation 7.2 can be redefined as a function of  $w_o$

$$\Delta E = E_2 - E_1 = \sigma_{lv} \left[ 2\pi r_h \left( \sqrt{r_{\text{curv}}^2 - (r_o - w_o - r_h)^2} - r_{\text{curv}} + h_{\text{max}} \right) - \pi r_h^2 (1 - \cos \theta_{\text{CB}}^*) \right]. \quad (\text{B11})$$

Figure B7 presents a plot of  $\Delta E$  vs.  $w_o$  for the following conditions:  $r_h = 0.09$  mm,  $D_0 \approx 2.1$  mm, and  $r_o = 2.5$  mm. The point of importance is when  $\Delta E > 0$ ; at this point ( $w_o = 0.15$  mm) hole formation for the aforesaid conditions becomes energetically unfavorable. While  $w_o = 0.15$  mm is obviously much less than the value employed in this study,  $w_o = 0.50$  mm,

## Appendix B (Continued)

the previous analysis gives justification as to why the minimum width of a peripheral annular wettability pattern for  $\mu\text{L}$  sized droplets undergoing droplet impact ( $We = O(10 - 100)$ ) is of a sub-millimetric scale, and not say atomic, as might be expected. This may also prove useful in future design of wettability patterns for droplet impact.

### B.2.4 Wave equation: Time to Penetrating Hole Formation; Length Scale

In order to better understand the oscillatory behavior of a water droplet in the later stages of droplet impact on an annular wettability pattern, it is instructive to consider a general case of vibrations on a circular membrane. The wave equation for the axisymmetric case can be written as

$$\frac{\partial^2 h}{\partial t^2} = \frac{c^2}{r} \frac{\partial}{\partial r} \left( r \frac{\partial h}{\partial r} \right), \quad (\text{B12})$$

where  $h$  represents the displacement of the membrane from zero,  $r$  is the radial coordinate, and  $c$  is the speed of the vibration waves. Employing the boundary condition,  $h(r_o, t) = 0$ , the solution, known as a normal mode of oscillation, can be written as (240)

$$h(r, \phi, t) = J_m \left( z_{mn} \frac{r}{r_o} \right) \begin{Bmatrix} \sin(m\phi) \\ \cos(m\phi) \end{Bmatrix} \begin{Bmatrix} \sin(cz_{mn}/r_o) \\ \cos(cz_{mn}/r_o) \end{Bmatrix}, \quad (\text{B13})$$

where  $J_m$  is a Bessel function of order  $m$  and  $z_{mn}$  is the  $n$ th zero of  $J_m$  and  $\phi$  is the polar azimuth. The case of interest is  $m = 0$  and  $n = 2$ , which reduces Equation B13 to

## Appendix B (Continued)

$$h(r, \phi, t) = J_0 \left( z_{02} \frac{r}{r_o} \right) \cos(cz_{02}/r_o), \quad (\text{B14})$$

where  $z_{02}$  is 5.52008. Figure 52 presents the solution to Equation B14 for two distinct times,  $t = 0.0$  and 4.4 ms, for the following parameters:  $c = 1.45 \text{ m s}^{-1}$  ( $We = 60$ ) and  $r_o = 2.34 \text{ mm}$ . The wave velocity was approximated as the droplet impact velocity  $U_0$  (234). The solution  $h$  was also rescaled with  $h_{\max} = 3.0 \text{ mm}$ . There are two important features to note from this exercise. First, the oscillation behavior between the real case and that in Figure 52—while not being physically equivalent—show distinct similarities; therefore, we infer that it is a capillary wave with a relatively long wavelength—of the order of  $r_o$ —fast wave speed ( $\sim 1 \text{ m s}^{-1}$ ), and large amplitude ( $h_{\max} \sim 3 \text{ mm}$ ; please verify) that drives the formation of an air cavity. Why that particular frequency is relatively long-lived (*i.e.*, not damped) is the subject for another study; however, we refer the reader to this paper for an in-depth view of the subject (241). Second, the first visible penetrating hole has  $r_h \approx 0.4 \text{ mm}$ , and it is instructive to compare this length scale with that of the wavelength of the vibrating circular membrane. The characteristic natural frequency of the vibrating circular membrane ( $m = 0, n = 2$ ) is  $f = c(z_{02}/r_o)$ ; therefore, the wavelength is  $\lambda = z_{02}/r_o = 2.36 \text{ mm}$ . From this we see that the diameter of the air cavity ( $2r_h$ ) is of the order of half of the wavelength  $\lambda$ . If we compare the moment when an air cavity forms, depicted in Figure 51, with the wave equation solution when the centerline value is minimum, we see similarities. Obviously the solution does not capture physically what is happening in the drop (*i.e.*, negative values of  $h$ ); however, it does act as a decent guide to understanding how a capillary wave can drive the formation of an air cavity.

## Appendix B (Continued)

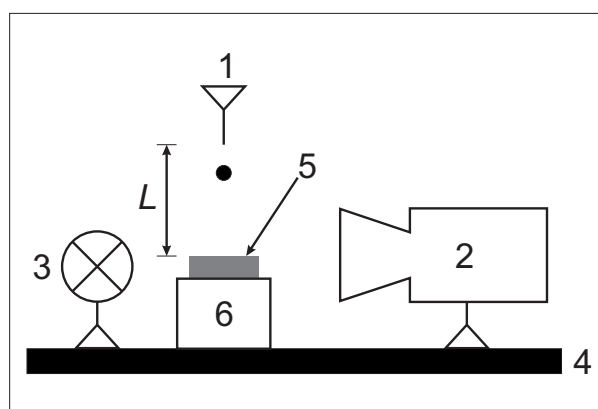


Figure B1. Schematic of the experimental setup. 1) drop generation; 2) high speed camera; 3) cold light source; 4) floating table; 5) sample; 6) platform.  $L$  represents the distance from tip of needle to surface of sample.

## Appendix B (Continued)

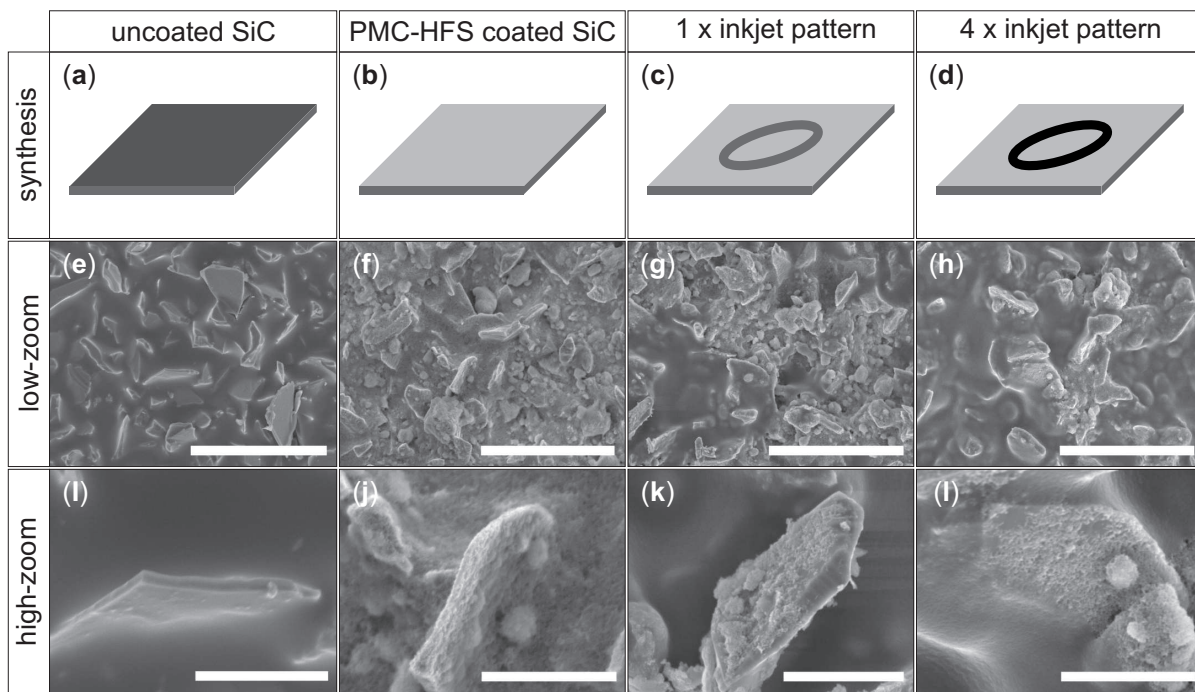


Figure B2. (a-d) Schematic demonstrating the wettability patterned coating synthesis process; SEM micrographs of the wettability patterned coating before and after each processing step at (e-h) low- and (i-l) high-magnifications. Scale bar in (e-h) equals 50  $\mu\text{m}$ ; Scale bar in (i-l) equals 10  $\mu\text{m}$ .

## Appendix B (Continued)

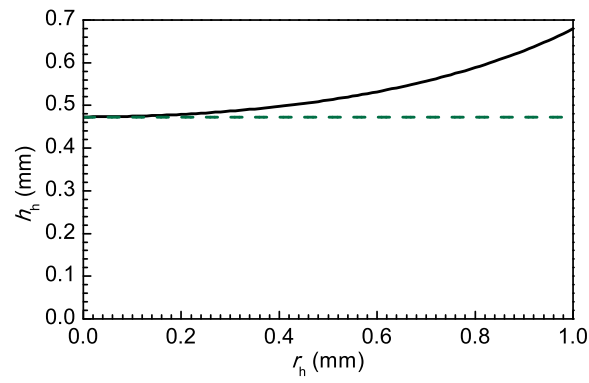


Figure B3. Plot of hole height ( $h_h$ ) vs. hole radius ( $r_h$ ) for two cases: 1) Accounting for the change in lens shape due to volume displacement as a result of hole formation (—); 2) no change in lens shape (---). The following parameters were used:  $D_0 = 2.1$  mm,  $r_0 = 2.5$

mm.

## Appendix B (Continued)

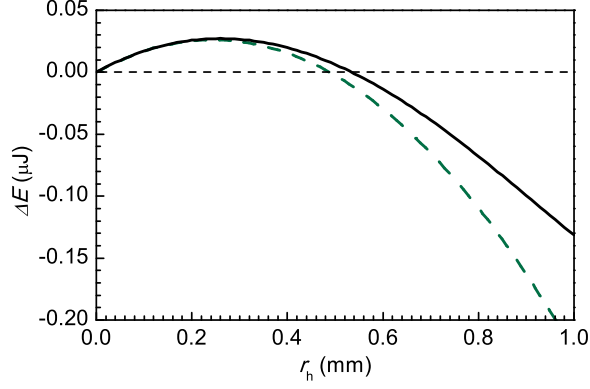


Figure B4. Plot of  $\Delta E$  vs.  $r_h$  for two cases: 1) Accounting for the change in lens shape due to volume displacement as a result of hole formation (—); 2) no change in lens shape (---). The following parameters were used:  $D_0 = 2.1$  mm,  $r_0 = 2.5$  mm.

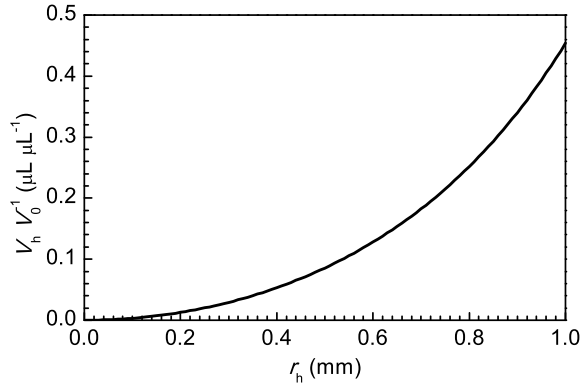


Figure B5. Plot of  $V_h V_0^{-1}$  vs.  $r_h$  accounting for the change in lens shape due to volume displacement as a result of hole formation (—). The following parameters were used:  $D_0 = 2.1$  mm,  $r_0 = 2.5$  mm.  $V_h V_0^{-1}$  is 9.3% at  $r_h = 0.52$  mm which is the critical hole radius.



## Appendix B (Continued)

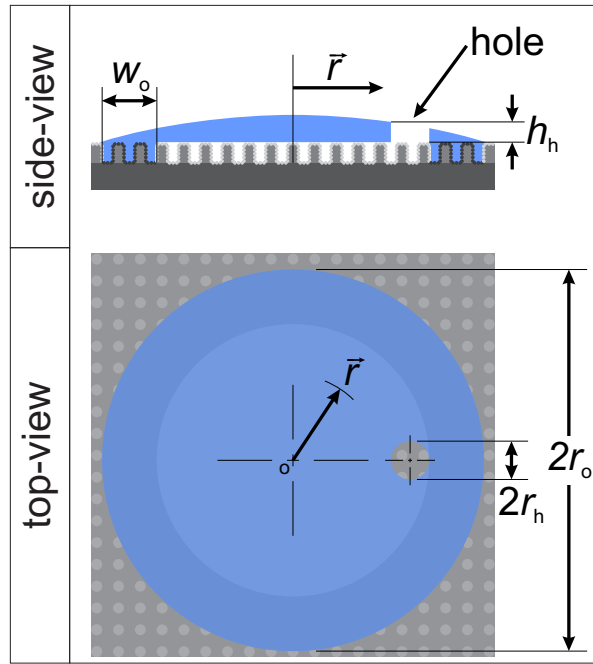


Figure B6. Schematic depicting a non-axisymmetric penetrating hole in a liquid lens on a single annulus wettability pattern with outer radius  $r_o$  and width  $w_o$ . The hole has a height  $h_h$  and a radius  $r_h$ , and its centerline is positioned at  $r = r_o - w_o - r_h$ .

## Appendix B (Continued)

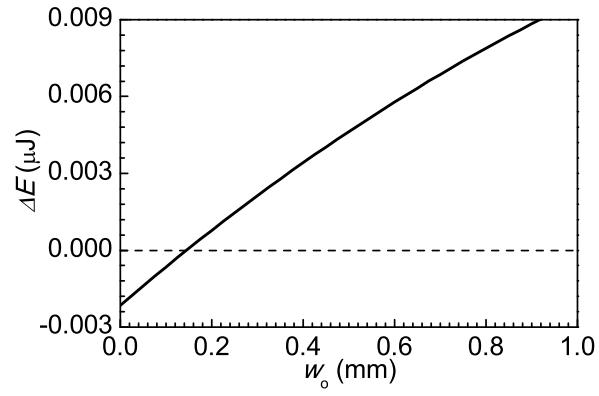


Figure B7. Plot of  $\Delta E$  (calculated from Equation B11) vs.  $w_o$  for the following conditions:

$D_0 = 2.1$  mm,  $r_o = 2.5$  mm,  $r_h = 0.05$  mm; no inner annulus is considered in this analysis.

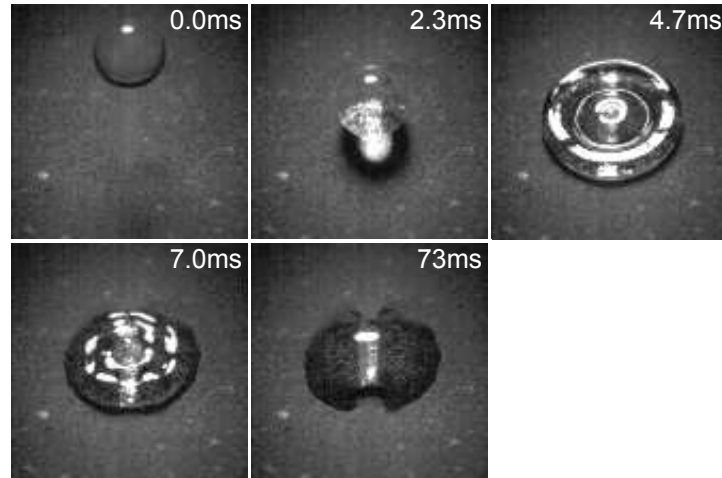


Figure B8. Drop impact ( $We = 30$ ) on a superhydrophobic line of width 0.5 mm.

## Appendix B (Continued)

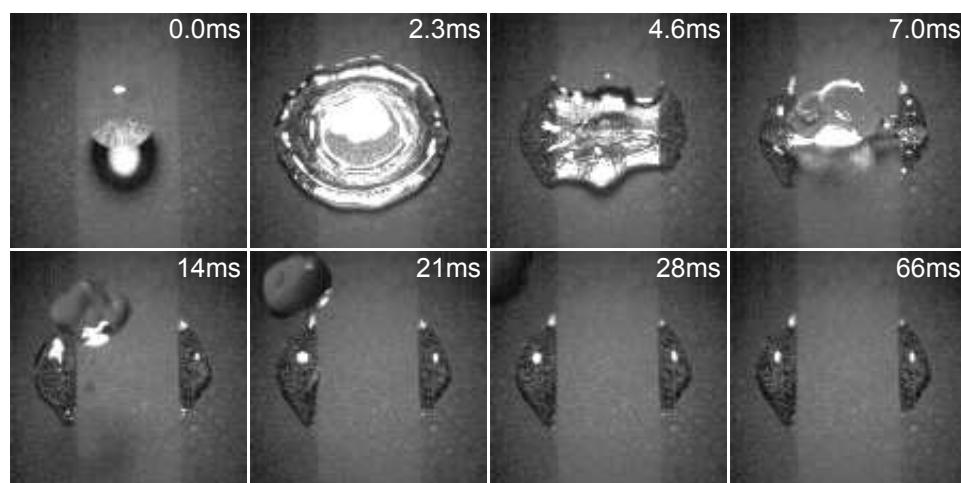


Figure B9. Drop impact ( $We = 60$ ) on a superhydrophobic line of width 3.0 mm.

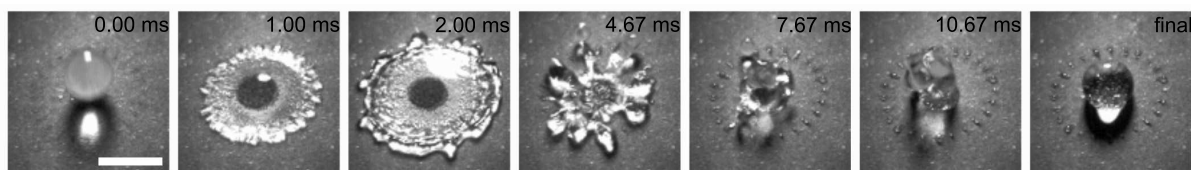


Figure B10. Droplet impact ( $We = 100$ ) on a wettability patterned surface designed to rapidly sample numerous small volumes of liquid.

## Appendix C

### COPYRIGHT, PERMISSIONS, & CO-AUTHORSHIP

#### C.1 Copyright

Chapter 2 is not subject to copyright from any publisher; however, it was submitted for a non-provisional patent application (83). It was submitted for peer review too (82).

Chapter 3 is subject to copyright. This chapter is reprinted from Composites Part A: Applied Science and Manufacturing, 42, Thomas M. Schutzius, Manish K. Tiwari, Ilker S. Bayer, and Constantine M. Megaridis, High Strain Sustaining, Nitrile Rubber Based, Large-Area, Superhydrophobic, Nanostructured Composite Coatings, 979–985, Copyright 2011, with permission from Elsevier (118). The permission to reprint (both print and electronically) was obtained on September 17, 2013 under license number 3231160887553 (see Figure B11).

Chapter 4 is subject to copyright. This chapter is reprinted (adapted) with permission from Industrial & Engineering Chemistry Research, 50, Thomas M. Schutzius, Ilker S. Bayer, Manish K. Tiwari, and Constantine M. Megaridis, 11117–11123, Copyright 2011, American Chemical Society (87). The permission to reprint (both print and electronically) was obtained on September 17, 2013 for a one-time use in the author's thesis (see Figure B12).

Chapter 5 is subject to copyright. This chapter was published in T. M. Schutzius, M. Elsharkawy, M. K. Tiwari and C. M. Megaridis, Lab Chip, 2012, 12, 5237 DOI: 10.1039/C2LC40849J, and was reproduced by permission of The Royal Society of Chemistry (46). Permission to re-

## Appendix C (Continued)

produce the whole article in a third party publication was allowed only in the case of a thesis or dissertation (see Figure B13).

Chapter 6 is subject to copyright. This chapter and its associated appendix (Appendix A) were published in T. M. Schutzius, I. S. Bayer, G. M. Jursich, A. Das and C. M. Megaridis, *Nanoscale*, 2012, 4, 5378 DOI: 10.1039/C2NR30979C and were reproduced by permission of The Royal Society of Chemistry (48). Permission to reproduce the whole article in a third party publication was allowed only in the case of a thesis or dissertation (see Figure B14).

Chapter 7 is not subject to copyright. It is currently being planned for submission to peer review. The journal is to be determined.

### **C.2 Permission & Co-authorship**

Since a majority of the content in this thesis is drawn from publications that have co-authors, the purpose of this section is to outline the extent of contribution from the student. It also acts to show that each of the co-authors approves of co-authored content being included in this thesis.

## Appendix C (Continued)

9/16/13

Rightslink Printable License

### ELSEVIER LICENSE TERMS AND CONDITIONS

Sep 17, 2013

This is a License Agreement between Thomas M. Schutzius ("You") and Elsevier ("Elsevier") provided by Copyright Clearance Center ("CCC"). The license consists of your order details, the terms and conditions provided by Elsevier, and the payment terms and conditions.

All payments must be made in full to CCC. For payment instructions, please see information listed at the bottom of this form.

Supplier	Elsevier Limited The Boulevard, Langford Lane Kidlington, Oxford, OX5 1GB, UK
Registered Company Number	1982084
Customer name	Thomas M. Schutzius
Customer address	The University of Illinois at Chicago CHICAGO, IL 60607
License number	3231160887553
License date	Sep 17, 2013
Licensed content publisher	Elsevier
Licensed content publication	Composites Part A: Applied Science and Manufacturing
Licensed content title	High strain sustaining, nitrile rubber based, large-area, superhydrophobic, nanostructured composite coatings
Licensed content author	Thomas M. Schutzius, Manish K. Tiwari, Ilker S. Bayer, Constantine M. Megaridis
Licensed content date	August 2011
Licensed content volume number	42
Licensed content issue number	8
Number of pages	7
Start Page	979
End Page	985
Type of Use	reuse in a thesis/dissertation
Intended publisher of new work	other
Portion	full article
Format	both print and electronic
Are you the author of this	Yes



<https://s100.copyright.com/AppDispatchServlet>

1/5


Figure B11. Copy of the license allowing republication of copyright material for Chapter 3.

## Appendix C (Continued)

9/16/13 RightsLink® by Copyright Clearance Center

[Home](#)
[Create Account](#)
[Help](#)



**Title:** Novel Fluoropolymer Blends for the Fabrication of Sprayable Multifunctional Superhydrophobic Nanostructured Composites

**Author:** Thomas M. Schutzius, Ilker S. Bayer, Manish K. Tiwari, and Constantine M. Megaridis

**Publication:** Industrial & Engineering Chemistry Research

**Publisher:** American Chemical Society

**Date:** Oct 1, 2011

Copyright © 2011, American Chemical Society

User ID

Password

☐ Enable Auto Login

[LOGIN](#)

[Forgot Password/User ID?](#)

If you're a copyright.com user, you can login to RightsLink using your copyright.com credentials. Already a RightsLink user or want to learn more?

PERMISSION/ LICENSE IS GRANTED FOR YOUR ORDER AT NO CHARGE

This type of permission/license, instead of the standard Terms & Conditions, is sent to you because no fee is being charged for your order. Please note the following:

- Permission is granted for your request in both print and electronic formats, and translations.
- If figures and/or tables were requested, they may be adapted or used in part.
- Please print this page for your records and send a copy of it to your publisher/graduate school.
- Appropriate credit for the requested material should be given as follows: "Reprinted (adapted) with permission from (COMPLETE REFERENCE CITATION). Copyright (YEAR) American Chemical Society." Insert appropriate information in place of the capitalized words.
- One-time permission is granted only for the use specified in your request. No additional uses are granted (such as derivative works or other editions). For any other uses, please submit a new request.

[BACK](#)
[CLOSE WINDOW](#)

Copyright © 2013 Copyright Clearance Center, Inc. All Rights Reserved. [Privacy statement](#). Comments? We would like to hear from you. E-mail us at [customercare@copyright.com](mailto:customercare@copyright.com).

<https://s100.copyright.com/AppDispatch5.en?let>

Figure B12. Copy of the license allowing republication of copyright material for Chapter 4.

## Appendix C (Continued)

00713
Request Permission

**Surface tension confined (STC) tracks for capillary-driven transport of low surface tension liquids**

T. M. Schutzu, M. Elsharkawy, M. K. Tiwari and C. M. Megaridis, Lab Chip, 2012, 12, 5237  
DOI: 10.1039/C2LC40849J

If you are not the author of this article and you wish to reproduce material from it in a third party non-RSC publication you must [formally request permission](#) using Rightslink. Go to our [instructions for using Rightslink page](#) for details.

Authors contributing to RSC publications (journal articles, books or book chapters) do not need to formally request permission to reproduce material contained in this article provided that the correct acknowledgement is given with the reproduced material.

Reproduced material should be attributed as follows:

- For reproduction of material from NJC:  
Reproduced from Ref. XX with permission from the Centre National de la Recherche Scientifique (CNRS) and The Royal Society of Chemistry.
- For reproduction of material from PCCP:  
Reproduced from Ref. XX with permission from the PCCP Owner Societies.
- For reproduction of material from PPS:  
Reproduced from Ref. XX with permission from the European Society for Photobiology, the European Photochemistry Association, and The Royal Society of Chemistry.
- For reproduction of material from all other RSC journals and books:  
Reproduced from Ref. XX with permission from The Royal Society of Chemistry.

If the material has been adapted instead of reproduced from the original RSC publication "Reproduced from" can be substituted with "Adapted from".

In all cases the Ref. XX is the XXth reference in the list of references.

If you are the author of this article you do not need to formally request permission to reproduce figures, diagrams etc. contained in this article in third party publications or in a thesis or dissertation provided that the correct acknowledgement is given with the reproduced material.

Reproduced material should be attributed as follows:

- For reproduction of material from NJC:  
[Original citation] - Reproduced by permission of The Royal Society of Chemistry (RSC) on behalf of the Centre National de la Recherche Scientifique (CNRS) and the RSC

00713
Request Permission

- For reproduction of material from PCCP:  
[Original citation] - Reproduced by permission of the PCCP Owner Societies
- For reproduction of material from PPS:  
[Original citation] - Reproduced by permission of The Royal Society of Chemistry (RSC) on behalf of the European Society for Photobiology, the European Photochemistry Association, and RSC
- For reproduction of material from all other RSC journals:  
[Original citation] - Reproduced by permission of The Royal Society of Chemistry

If you are the author of this article you still need to obtain permission to reproduce the whole article in a third party publication with the exception of reproduction of the whole article in a thesis or dissertation.

Information about reproducing material from RSC articles with different licences is available on our [Permission Request page](#).

[pubs.rsc.org/doi/10.1039/C2LC40849J](https://pubs.rsc.org/doi/10.1039/C2LC40849J)

1/2

[pubs.rsc.org/doi/10.1039/C2LC40849J](https://pubs.rsc.org/doi/10.1039/C2LC40849J)

2/2

Figure B13. Copy of the license allowing republication of copyright material for Chapter 5.



## Appendix C (Continued)

05/11/13
Request Permission

**Superhydrophobic–superhydrophilic binary micropatterns by localized thermal treatment of polyhedral oligomeric silsesquioxane (POSS)–silica films**

T. M. Schuttkie, I. S. Bayer, G. M. Jursich, A. Das and C. M. Megerle, *Nanoscale*, 2012, 4, 5378  
DOI: 10.1039/C2NR30979C

If you are not the author of this article and you wish to reproduce material from it in a third party non-RSC publication you must [formally request permission](#) using Rightel ink. Go to our [instructions for using Rightel link](#) page for details.

Authors contributing to RSC publications (journal articles, books or book chapters) do not need to formally request permission to reproduce material contained in this article provided that the correct acknowledgement is given with the reproduced material.

Reproduced material should be attributed as follows:

- For reproduction of material from NJC:  
Reproduced from Ref. XX with permission from the Centre National de la Recherche Scientifique (CNRS) and The Royal Society of Chemistry.
- For reproduction of material from PCCP:  
Reproduced from Ref. XX with permission from the PCCP Owner Societies.
- For reproduction of material from PPS:  
Reproduced from Ref. XX with permission from the European Society for Photobiology, the European Photochemistry Association and The Royal Society of Chemistry.
- For reproduction of material from all other RSC journals and books:  
Reproduced from Ref. XX with permission from The Royal Society of Chemistry.

If the material has been adapted instead of reproduced from the original RSC publication "Reproduced from" can be substituted with "Adapted from".

In all cases the Ref. XX is the XXth reference in the list of references.

If you are the author of this article you do not need to formally request permission to reproduce figures, diagrams etc. contained in this article in third party publications or in a thesis or dissertation provided that the correct acknowledgement is given with the reproduced material.

Reproduced material should be attributed as follows:

- For reproduction of material from NJC:  
[Original citation] – Reproduced by permission of The Royal Society of Chemistry (RSC) on behalf of the

05/11/13
Request Permission

Centre National de la Recherche Scientifique (CNRS) and the RSC

- For reproduction of material from PCCP:  
[Original citation] – Reproduced by permission of the PCCP Owner Societies
- For reproduction of material from PPS:  
[Original citation] – Reproduced by permission of The Royal Society of Chemistry (RSC) on behalf of the European Society for Photobiology, the European Photochemistry Association and RSC
- For reproduction of material from all other RSC journals:  
[Original citation] – Reproduced by permission of The Royal Society of Chemistry

If you are the author of this article you still need to obtain permission to reproduce the whole article in a third party publication with the exception of reproduction of the whole article in a thesis or dissertation.

Information about reproducing material from RSC articles with different licences is available on our [Permission Request page](#).

pubs.rsc.org/doi/10.1039/C2NR30979C 1/2

pubs.rsc.org/doi/10.1039/C2NR30979C 2/2

Figure B14. Copy of the license allowing republication of copyright material for Chapter 6.

## Appendix C (Continued)



Mechanical and Industrial Engineering (M/C 251)  
2039 Engineering Research Facility  
842 W. Taylor St., Chicago, IL 60607-7022

Declaration of Co-authorship

Information on PhD student:				
Name of PhD student	Thomas M. Schutzius			
E-mail	tom.schutzius@gmail.com			
Date of birth	Blue Island, IL			
Work place	The University of Illinois at Chicago			
Principal supervisor	Constantine M. Megaridis			

Title of PhD thesis <sup>†</sup> :	
Large-area Coating and Patterning of Functional Nanocomposites: Design, Synthesis and Characterization	

This declaration concerns the following article:	
High Strain Sustaining, Nitrile Rubber Based, Large-Area, Superhydrophobic, Nanostructured Composite Coatings	

The PhD student's contribution to the article: <i>(please use the scale (A,B,C) below as benchmark*)</i>	(A,B,C)
1. Formulation/identification of the scientific problem that from theoretical questions need to be clarified. This includes a condensation of the problem to specific scientific questions that is judged to be answerable by experiments	B
2. Planning of the experiments and methodology design, including selection of methods and method development	A
3. Involvement in the experimental work	A
4. Presentation, interpretation and discussion in a journal article format of obtained data	A

*Benchmark scale of the PhD student's contribution to the article		
A. refers to:	Has predominantly executed the work independently	67-100 %
B. refers to:	Has contributed considerably to the co-operation	34-66 %
C. refers to:	Has contributed to the co-operation	0-33 %

Signature of the co-authors:				
Date:	Title:	Name:	Approval:**	Signature:
9/21/13	Dr.	Manish K. Tiwari	<input checked="" type="checkbox"/>	Manish K. Tiwari
9/21/13	Dr.	Ilker S. Bayer	<input checked="" type="checkbox"/>	
10/7/13	Prof.	Constantine M. Megaridis	<input checked="" type="checkbox"/>	Constantine M. Megaridis
			<input type="checkbox"/>	

\*\*Do the co-authors approve of this article being used in the thesis entitled<sup>†</sup> here (e.g., Yes=☒, No=☐)?

Signature of the PhD student and the principal supervisor:	
Date: 9/21/13 PhD student: Thomas Schutzius	Date: Oct 7, 2013 Principal supervisor: Constantine M. Megaridis

Figure B15. Copy of the declaration of co-authorship allowing republication of co-authored material for Chapter 3.

## Appendix C (Continued)



Mechanical and Industrial Engineering (M/C 251)  
2039 Engineering Research Facility  
842 W. Taylor St., Chicago, IL 60607-7022

Declaration of Co-authorship

Information on PhD student:				
Name of PhD student	Thomas M. Schutzzius			
E-mail	tom.schutzzius@gmail.com			
Date of birth	Blue Island, IL			
Work place	The University of Illinois at Chicago			
Principal supervisor	Constantine M. Megaridis			

Title of PhD thesis <sup>†</sup> :	
Large-area Coating and Patterning of Functional Nanocomposites: Design, Synthesis and Characterization	

This declaration concerns the following article:	
Novel Fluoropolymer Blends for the Fabrication of Sprayable Multifunctional Superhydrophobic Nanostructured Composites	

The PhD student's contribution to the article: <i>(please use the scale (A,B,C) below as benchmark*)</i>	(A,B,C)
1. Formulation/identification of the scientific problem that from theoretical questions need to be clarified. This includes a condensation of the problem to specific scientific questions that is judged to be answerable by experiments	B
2. Planning of the experiments and methodology design, including selection of methods and method development	A
3. Involvement in the experimental work	A
4. Presentation, interpretation and discussion in a journal article format of obtained data	A

*Benchmark scale of the PhD student's contribution to the article		
A. refers to:	Has predominantly executed the work independently	67-100 %
B. refers to:	Has contributed considerably to the co-operation	34-66 %
C. refers to:	Has contributed to the co-operation	0-33 %

Signature of the co-authors:				
Date:	Title:	Name:	Approval:**	Signature:
9/21/13	Dr.	Ilker S. Bayer	<input checked="" type="checkbox"/>	
9/21/13	Dr.	Manish K. Tiwari	<input checked="" type="checkbox"/>	Manish K. Tiwari
10/7/13	Prof.	Constantine M. Megaridis	<input checked="" type="checkbox"/>	Constantine M. Megaridis
			<input type="checkbox"/>	

\*\*Do the co-authors approve of this article being used in the thesis entitled<sup>†</sup> here (e.g., Yes=☒, No=☐)?

Signature of the PhD student and the principal supervisor:	
Date: 9/21/13 PhD student: Thomas Schutzzius	Date: Oct 7, 2013 Principal supervisor: Constantine M. Megaridis

Figure B16. Copy of the declaration of co-authorship allowing republication of co-authored material for Chapter 4.

## Appendix C (Continued)



Mechanical and Industrial Engineering (M/C 251)  
2039 Engineering Research Facility  
842 W. Taylor St., Chicago, IL 60607-7022

Declaration of Co-authorship

Information on PhD student:				
Name of PhD student	Thomas M. Schutzius			
E-mail	tom.schutzius@gmail.com			
Date of birth	Blue Island, IL			
Work place	The University of Illinois at Chicago			
Principal supervisor	Constantine M. Megaridis			

Title of PhD thesis <sup>†</sup> :	
Large-area Coating and Patterning of Functional Nanocomposites: Design, Synthesis and Characterization	

This declaration concerns the following article:	
Surface Tension Confined (STC) Tracks For Capillary-Driven Transport of Low Surface Tension Liquids	

The PhD student's contribution to the article: (please use the scale (A,B,C) below as benchmark*)	(A,B,C)
1. Formulation/identification of the scientific problem that from theoretical questions need to be clarified. This includes a condensation of the problem to specific scientific questions that is judged to be answerable by experiments	B
2. Planning of the experiments and methodology design, including selection of methods and method development	A
3. Involvement in the experimental work	B
4. Presentation, interpretation and discussion in a journal article format of obtained data	A

*Benchmark scale of the PhD student's contribution to the article		
A. refers to:	Has predominantly executed the work independently	67-100 %
B. refers to:	Has contributed considerably to the co-operation	34-66 %
C. refers to:	Has contributed to the co-operation	0-33 %

Signature of the co-authors:				
Date:	Title:	Name:	Approval:**	Signature:
10/02/13	Mr.	Mohamed Elsharkawy	<input checked="" type="checkbox"/>	Mohamed Elsharkawy
9/21/13	Dr.	Manish K. Tiwari	<input checked="" type="checkbox"/>	Manish K. Tiwari
10/7/13	Prof.	Constantine M. Megaridis	<input checked="" type="checkbox"/>	Constantine M. Megaridis
			<input type="checkbox"/>	

\*\*Do the co-authors approve of this article being used in the thesis entitled<sup>†</sup> here (e.g., Yes=☒, No=☐)?

Signature of the PhD student and the principal supervisor:	
Date: 9/21/13 PhD student: Thomas Schutzius	Date: Oct 7, 2013 Principal supervisor: Constantine M. Megaridis

Figure B17. Copy of the declaration of co-authorship allowing republication of co-authored material for Chapter 5.

## Appendix C (Continued)



Mechanical and Industrial Engineering (M/C 251)  
2039 Engineering Research Facility  
842 W. Taylor St., Chicago, IL 60607-7022

Declaration of Co-authorship

Information on PhD student:				
Name of PhD student	Thomas M. Schutzius			
E-mail	tom.schutzius@gmail.com			
Date of birth	Blue Island, IL			
Work place	The University of Illinois at Chicago			
Principal supervisor	Constantine M. Megaridis			

Title of PhD thesis <sup>†</sup> :	
Large-area Coating and Patterning of Functional Nanocomposites: Design, Synthesis and Characterization	

This declaration concerns the following article:	
Superhydrophobic-Superhydrophilic Binary Micropatterns by Localized Thermal Treatment of Polyhedral Oligomeric Silsesquioxane (POSS)-Silica Films	

The PhD student's contribution to the article: <i>(please use the scale (A,B,C) below as benchmark*)</i>	(A,B,C)
1. Formulation/identification of the scientific problem that from theoretical questions need to be clarified. This includes a condensation of the problem to specific scientific questions that is judged to be answerable by experiments	B
2. Planning of the experiments and methodology design, including selection of methods and method development	A
3. Involvement in the experimental work	A
4. Presentation, interpretation and discussion in a journal article format of obtained data	A

*Benchmark scale of the PhD student's contribution to the article		
A. refers to:	Has predominantly executed the work independently	67-100 %
B. refers to:	Has contributed considerably to the co-operation	34-66 %
C. refers to:	Has contributed to the co-operation	0-33 %

Signature of the co-authors:				
Date:	Title:	Name:	Approval:**	Signature:
10/03/13	Dr.	Ilker S. Bayer	<input checked="" type="checkbox"/>	
9/23/13	Dr.	Gregory M. Jursich	<input checked="" type="checkbox"/>	Greg Jursich <small>Digitally signed by Greg Jursich (DN: cn=Greg Jursich, o=UIC, ou=UIC, email=jursich@uic.edu, c=US) Date: 2013.09.23 15:04:51 -0400</small>
9/21/13	Dr.	Arindam Das	<input checked="" type="checkbox"/>	Arindam Das <small>Digitally signed by Arindam Das (DN: cn=Arindam Das, o=UIC, ou=UIC, email=arindamdas@uic.edu, c=US) Date: 2013.09.21 14:46:21 -0400</small>
10/7/13	Prof.	Constantine M. Megaridis	<input checked="" type="checkbox"/>	Constantine M. Megaridis <small>Digitally signed by Constantine M. Megaridis (DN: cn=Constantine M. Megaridis, o=UIC, ou=UIC, email=cmegaridis@uic.edu, c=US) Date: 2013.10.07 10:00:00 -0400</small>
**Do the co-authors approve of this article being used in the thesis entitled <sup>†</sup> here (e.g., Yes= <input checked="" type="checkbox"/> , No= <input type="checkbox"/> )?				

Signature of the PhD student and the principal supervisor:	
Date: 9/21/13 PhD student: Thomas Schutzius <small>Digitally signed by Thomas Schutzius (DN: cn=Thomas Schutzius, o=UIC, ou=UIC, email=schutzius@uic.edu, c=US) Date: 2013.09.21 14:46:21 -0400</small>	Date: Oct 7, 2013 Principal supervisor: Constantine M. Megaridis <small>Digitally signed by Constantine M. Megaridis (DN: cn=Constantine M. Megaridis, o=UIC, ou=UIC, email=cmegaridis@uic.edu, c=US) Date: 2013.10.07 10:00:00 -0400</small>

Figure B18. Copy of the declaration of co-authorship allowing republication of co-authored material for Chapter 6.

## Appendix C (Continued)



Mechanical and Industrial Engineering (M/C 251)  
2039 Engineering Research Facility  
842 W. Taylor St., Chicago, IL 60607-7022

Declaration of Co-authorship

Information on PhD student:				
Name of PhD student	Thomas M. Schutzzius			
E-mail	tom.schutzzius@gmail.com			
Date of birth	Blue Island, IL			
Work place	The University of Illinois at Chicago			
Principal supervisor	Constantine M. Megaridis			

Title of PhD thesis <sup>†</sup> :	
Large-area Coating and Patterning of Functional Nanocomposites: Design, Synthesis and Characterization	

This declaration concerns the following article:	
Shaping and Mobilizing Liquid $\mu$ -Volumes With Wettability Engineered Surfaces	

The PhD student's contribution to the article: <i>(please use the scale (A,B,C) below as benchmark*)</i>	(A,B,C)
1. Formulation/identification of the scientific problem that from theoretical questions need to be clarified. This includes a condensation of the problem to specific scientific questions that is judged to be answerable by experiments	B
2. Planning of the experiments and methodology design, including selection of methods and method development	B
3. Involvement in the experimental work	C
4. Presentation, interpretation and discussion in a journal article format of obtained data	A

*Benchmark scale of the PhD student's contribution to the article		
A. refers to:	Has predominantly executed the work independently	67-100 %
B. refers to:	Has contributed considerably to the co-operation	34-66 %
C. refers to:	Has contributed to the co-operation	0-33 %

Signature of the co-authors:				
Date:	Title:	Name:	Approval:**	Signature:
9/22/13	Mr.	Gustav Graeber	<input checked="" type="checkbox"/>	Gustav Graeber <small>Digitally signed by Gustav Graeber DN: cn=Gustav Graeber, o=The Chicago Center for Nanotechnology, ou=UIC, email=gustav.graeb@uic.edu, c=US</small>
9/22/13	Mr.	James Oreluk	<input checked="" type="checkbox"/>	James Oreluk <small>Digitally signed by James Oreluk DN: cn=James Oreluk, o=The Chicago Center for Nanotechnology, ou=UIC, email=james.oreluk@uic.edu, c=US</small>
10/7/13	Prof.	Constantine M. Megaridis	<input checked="" type="checkbox"/>	Constantine M. Megaridis <small>Digitally signed by Constantine M. Megaridis DN: cn=Constantine M. Megaridis, o=The Chicago Center for Nanotechnology, ou=UIC, email=cmegaridis@uic.edu, c=US</small>
			<input type="checkbox"/>	

\*\*Do the co-authors approve of this article being used in the thesis entitled<sup>†</sup> here (e.g., Yes=☒, No=☐)?

Signature of the PhD student and the principal supervisor:	
Date: 9/21/13 PhD student: Thomas Schutzzius <small>Digitally signed by Thomas Schutzzius DN: cn=Thomas Schutzzius, o=The Chicago Center for Nanotechnology, ou=UIC, email=tom.schutzzius@gmail.com, c=US</small>	Date: Oct 7, 2013 Principal supervisor: Constantine M. Megaridis <small>Digitally signed by Constantine M. Megaridis DN: cn=Constantine M. Megaridis, o=The Chicago Center for Nanotechnology, ou=UIC, email=cmegaridis@uic.edu, c=US</small>

Figure B19. Copy of the declaration of co-authorship allowing republication of co-authored material for Chapter 7.

## CITED LITERATURE

1. Daniel, M. C. and Astruc, D.: Gold nanoparticles: Assembly, supramolecular chemistry, quantum-size-related properties, and applications toward biology, catalysis, and nanotechnology. Chemical Reviews, 104(1):293–346, 2004.
2. Helcher, H. H.: Aurum potabile, oder Gold-Tinctur. Breslau and Leipzig, Johann Herbord Kloss, 1718.
3. Faraday, M.: The bakerian lecture: Experimental relations of gold (and other metals) to light. Philosophical Transactions of the Royal Society of London, 147:145–181, 1857.
4. Zsigmondy, R. A.: Properties of colloids. Nobel Lecture, 1926.
5. Röntgen, W. C.: On a new kind of rays. Science, 3(59):227–231, 1896.
6. von Laue, M.: Concerning the detection of x-ray interferences. Nobel Lecture, 1915.
7. Bragg, W. H. and Bragg, W. L.: The structure of the diamond. Nature, 91(2283):557, 1913.
8. Debye, P. and Scherrer, P.: Interferenzen an regellos orientierten teilchen im röntgenlicht. I. Nachrichten von der Gesellschaft der Wissenschaften zu Göttingen, Mathematisch-Physikalische Klasse, 1916:1–15, 1916.
9. Debye, P.: Methods to determine the electrical and geometrical structure of molecules. Nobel Lecture, 1936.
10. Franklin, B., Brownrigg, W., and Farish, M.: Of the stilling of waves by means of oil. extracted from sundry letters between Benjamin Franklin, LL. D. F. R. S. William Brownrigg, M. D. F. R. S. and the Reverend Mr. Farish. Philosophical Transactions, 64:445–460, 1774.
11. Wyckoff, A. B.: The use of oil in storms at sea. Proceedings of the American Philosophical Society, 23:383–388, 1886.

12. Rayleigh, L.: Investigations in capillarity:—The size of drops.—The liberation of gas from supersaturated solutions.—Colliding jets.—The tension of contaminated water-surfaces. The London, Edinburgh, and Dublin Philosophical Magazine and Journal of Science, 48(293):321–337, 1899.
13. Langmuir, I.: Surface chemistry. Nobel Lecture, 1932.
14. Feynman, R. P.: There's plenty of room at the bottom. Engineering and Science, 23(5):22–36, 1960.
15. Drexler, K. E.: Molecular engineering: An approach to the development of general capabilities for molecular manipulation. Proceedings of the National Academy of Sciences of the United States of America: Physical Sciences, 78(9):5275–5278, 1981.
16. Binnig, G. and Rohrer, H.: Scanning tunneling microscope, 1982. US Patent 4,343,993.
17. eds. T. Kondow and F. Mafuné Progress In Experimental And Theoretical Studies Of Clusters. New Jersey, World Scientific Publishing, 2003.
18. Halperin, W. P.: Quantum size effects in metal particles. Reviews of Modern Physics, 58(3):533–606, 1986.
19. Kroto, H. W., Heath, J. R., O'Brien, S. C., Curl, R. F., and Smalley, R. E.: C<sub>60</sub>: Buckminsterfullerene. Nature, 318(6042):162–163, 1985.
20. Monthieux, M. and Kuznetsov, V. L.: Who should be given the credit for the discovery of carbon nanotubes? Carbon, 44(9):1621–1623, 2006.
21. Iijima, S.: Helical microtubules of graphitic carbon. Nature, 354(6348):56–58, 1991.
22. Iijima, S. and Ichihashi, T.: Single-shell carbon nanotubes of 1-nm diameter. Nature, 363(6430):603–605, 1993.
23. Bethune, D. S., Kiang, C. H., Vries, M. S. D., Gorman, G., Savoy, R., Vazquez, J., and Beyers, R.: Cobalt-catalysed growth of carbon nanotubes with single-atomic-layer walls. Nature, 363:605–607, 1993.
24. Bethune, D. S., Beyers, R. B., and Kiang, C.-H.: Carbon fibers and method for their production, 1995. US Patent 5,424,054.



25. Sandler, J. K. W., Kirk, J. E., Kinloch, I. A., Shaffer, M. S. P., and Windle, A. H.: Ultra-low electrical percolation threshold in carbon-nanotube-epoxy composites. Polymer, 44(19):5893–5899, 2003.
26. Ringsdorf, H., Schlarb, B., and Venzmer, J.: Molecular architecture and function of polymeric oriented systems - models for the study of organization, surface recognition, and dynamics of biomembranes. Angewandte Chemie International Edition, 27(1):113–158, 1988.
27. Shimomura, M. and Sawadaishi, T.: Bottom-up strategy of materials fabrication: a new trend in nanotechnology of soft materials. Current Opinion In Colloid & Interface Science, 6(1):11–16, 2001.
28. Seeman, N. C. and Belcher, A. M.: Emulating biology: Building nanostructures from the bottom up. Proceedings of the National Academy of Sciences of the United States of America, 99:6451–6455, 2002.
29. Xia, Y. and Whitesides, G. M.: Soft lithography. Angewandte Chemie International Edition, 37(5):551–575, 1998.
30. Xia, Y. and Whitesides, G. M.: Soft lithography. Annual Review of Materials Science, 28:153–184, 1998.
31. eds. P. M. Ajayan, L. S. Schadler, and P. V. Braun Nanocomposite Science and Technology. Wiley-VCH, 2003.
32. Mayer, G. and Sarikaya, M.: Rigid biological composite materials: Structural examples for biomimetic design. Experimental Mechanics, 42(4):395–403, 2002.
33. Chan, C. M., Wu, J. S., Li, J. X., and Cheung, Y. K.: Polypropylene/calcium carbonate nanocomposites. Polymer, 43(10):2981–2992, 2002.
34. Lin, A. and Meyers, M. A.: Growth and structure in abalone shell. Materials Science & Engineering A: Structural Materials: Properties, Microstructure and Processing, 390(1-2):27–41, 2005.
35. He, F., Lau, S., Chan, H. L., and Fan, J.: High dielectric permittivity and low percolation threshold in nanocomposites based on poly(vinylidene fluoride) and exfoliated graphite nanoplates. Advanced Materials, 21(6):710–715, 2009.

36. Das, A., Schutzius, T. M., Megaridis, C. M., Subhechha, S., Wang, T., and Liu, L.: Quasi-optical terahertz polarizers enabled by inkjet printing of carbon nanocomposites. Applied Physics Letters, 101(24):243108, 2012.
37. Xia, Y. N., Zhao, X. M., and Whitesides, G. M.: Pattern transfer: Self-assembled monolayers as ultrathin resists. Microelectronic Engineering, 32(1-4):255–268, 1996.
38. Betz, A. R., Xu, J., Qiu, H. H., and Attinger, D.: Do surfaces with mixed hydrophilic and hydrophobic areas enhance pool boiling? Applied Physics Letters, 97(14):141909, 2010.
39. Kobaku, S. P. R., Kota, A. K., Lee, D. H., Mabry, J. M., and Tuteja, A.: Patterned superomniphobic-superomniphilic surfaces: templates for site-selective self-assembly. Angewandte Chemie International Edition, 51(40):10109–13, 2012.
40. Start, P. R. and Mauritz, K. A.: Surlyn/silicate nanocomposite materials via a polymer in situ sol-gel process: Morphology. Journal of Polymer Science Part B: Polymer Physics, 41(13):1563–1571, 2003.
41. Lee, D. S.: Golf ball having hydrophilic and hydrophobic portions, 2012. US Patent Application 13/338,129.
42. Parker, A. R. and Lawrence, C. R.: Water capture by a desert beetle. Nature, 414:33–34, 2001.
43. Zhai, L., Berg, M. C., Cebeci, F. C., Kim, Y., Milwid, J. M., Rubner, M. F., and Cohen, R. E.: Patterned superhydrophobic surfaces: Toward a synthetic mimic of the namib desert beetle. Nano Letters, 6(6):1213–1217, 2006.
44. Barona, D. and Amirfazli, A.: Producing a superhydrophobic paper and altering its repellency through ink-jet printing. Lab On A Chip, 11(5):936–940, 2011.
45. Chitnis, G., Ding, Z., Chang, C.-L., Savran, C. A., and Ziaie, B.: Laser-treated hydrophobic paper: An inexpensive microfluidic platform. Lab On A Chip, 11(6):1161–1165, 2011.
46. Schutzius, T. M., Elsharkawy, M., Tiwari, M. K., and Megaridis, C. M.: Surface tension confined (STC) tracks for capillary-driven transport of low surface tension liquids. Lab On A Chip, 12(24):5237–5242, 2012.

47. Varanasi, K. K., Hsu, M., Bhate, N., Yang, W. S., and Deng, T.: Spatial control in the heterogeneous nucleation of water. Applied Physics Letters, 95(9):094101, 2009.
48. Schutzius, T. M., Bayer, I. S., Jursich, G. M., Das, A., and Megaridis, C. M.: Superhydrophobic-superhydrophilic binary micropatterns by localized thermal treatment of polyhedral oligomeric silsesquioxane (POSS)-silica films. Nanoscale, 4:5378–5385, 2012.
49. Michel, T., Mock, U., Roisman, I. V., Ruhe, J., and Tropea, C.: The hydrodynamics of drop impact onto chemically structured surfaces. Journal of Physics: Condensed Matter, 17(9):S607–S622, 2005.
50. Mock, U., Michel, T., Tropea, C., Roisman, I., and Ruhe, J.: Drop impact on chemically structured arrays. Journal of Physics: Condensed Matter, 17(9):S595–S605, 2005.
51. Meyers, M. A., Chen, P.-Y., Lin, A. Y.-M., and Seki, Y.: Biological materials: Structure and mechanical properties. Progress In Materials Science, 53(1):1–206, 2008.
52. Tekin, E., Smith, P. J., Hoeppener, S., van den Berg, A. M. J., Susa, A. S., Rogach, A. L., Feldmann, J., and Schubert, U. S.: Inkjet printing of luminescent CdTe nanocrystal-polymer composites. Advanced Functional Materials, 17(1):23–28, 2007.
53. Schirmer, N. C., Strohle, S., Tiwari, M. K., and Poulikakos, D.: On the principles of printing sub-micrometer 3D structures from dielectric-liquid-based colloids. Advanced Functional Materials, 21(2):388–395, 2011.
54. Schirmer, N. C., Hesselbarth, J., Strohle, S., Burg, B. R., Tiwari, M. K., and Poulikakos, D.: Millimeter-wave on-chip solenoid inductor by on-demand three-dimensional printing of colloidal nanoparticles. Applied Physics Letters, 97(24):243109, 2010.
55. Galliker, P., Schneider, J., Eghlidi, H., Kress, S., Sandoghdar, V., and Poulikakos, D.: Direct printing of nanostructures by electrostatic autofocussing of ink nanodroplets. Nature Communications, 3:890, 2012.
56. Kumar, K., Duan, H., Hegde, R. S., Koh, S. C. W., Wei, J. N., and Yang, J. K. W.: Printing colour at the optical diffraction limit. Nature Nanotechnology, 7(9):557–561, 2012.

57. Bellan, L. M., Cross, J. D., Strychalski, E. A., Moran-Mirabal, J., and Craighead, H. G.: Individually resolved DNA molecules stretched and embedded in electrospun polymer nanofibers. Nano Letters, 6(11):2526–2530, 2006.
58. de Gennes, P., Brochard-Wyart, F., and Quéré, D.: Capillarity and wetting phenomena: Drops, bubbles, pearls, waves. Springer Verlag, 2004.
59. Young, T.: An essay on the cohesion of fluids. Philosophical Transactions of the Royal Society of London, 95:65–87, 1805.
60. Duineveld, P. C.: The stability of ink-jet printed lines of liquid with zero receding contact angle on a homogeneous substrate. Journal of Fluid Mechanics, 477:175–200, 2003.
61. Stringer, J. and Derby, B.: Formation and stability of lines produced by inkjet printing. Langmuir, 26:10365–10372, 2010.
62. Derby, B.: Inkjet printing of functional and structural materials: Fluid property requirements, feature stability, and resolution. Annual Review of Materials Research, 40:395–414, 2010.
63. Dockendorf, C. P. R., Choi, T. Y., Poulikakos, D., and Stemmer, A.: Size reduction of nanoparticle ink patterns by fluid-assisted dewetting. Applied Physics Letters, 88(13):131903, 2006.
64. Quéré, D.: Fluid coating on a fiber. Annual Review of Fluid Mechanics, 31:347–384, 1999.
65. Sen, A. K.: Coated Textiles: Principles and Applications. Boca Raton, FL, Taylor & Francis Group, 2nd edition, 2008.
66. Hermans, T. M., Frauenrath, H., and Stellacci, F.: Droplets out of equilibrium. Science, 341:243, 2013.
67. Timonen, J. V. I., Latikka, M., Leibler, L., Ras, R. H. A., and Ikkala, O.: Switchable static and dynamic self-assembly of magnetic droplets on superhydrophobic surfaces. Science, 341(6143):253–257, 2013.
68. de Gennes, P. G.: Wetting: Statics and dynamics. Reviews of Modern Physics, 57(3):827–863, 1985.

69. Wenzel, R. N.: Resistance of solid surfaces to wetting by water. Industrial & Engineering Chemistry, 28(8):988–994, 1936.
70. Cassie, A. and Baxter, S.: Wettability of porous surfaces. Transactions of the Faraday Society, 40:546–551, 1944.
71. Bico, J., Thiele, U., and Quéré, D.: Wetting of textured surfaces. Colloids and Surfaces A: Physicochemical and Engineering Aspects, 206(1-3):41–46, 2002.
72. Marmur, A.: Wetting on hydrophobic rough surfaces: To be heterogeneous or not to be? Langmuir, 19(20):8343–8348, 2003.
73. Quéré, D.: Surface chemistry: Fakir droplets. Nature Materials, 1(1):14–15, 2002.
74. Feng, L., Zhang, Y., Xi, J., Zhu, Y., Wang, N., Xia, F., and Jiang, L.: Petal effect: A superhydrophobic state with high adhesive force. Langmuir, 24(8):4114–4119, 2008.
75. Furmidge, C. G. L.: Studies at phase interfaces. I. The sliding of liquid drops on solid surfaces and a theory for spray retention. Journal of Colloid Science, 17(4):309–324, 1962.
76. Extrand, C. W. and Gent, A. N.: Retention of liquid-drops by solid-surfaces. Journal of Colloid and Interface Science, 138(2):431–442, 1990.
77. Tuteja, A., Choi, W., Ma, M. L., Mabry, J. M., Mazzella, S. A., Rutledge, G. C., McKinley, G. H., and Cohen, R. E.: Designing superoleophobic surfaces. Science, 318:1618–1622, 2007.
78. Tuteja, A., Choi, W., McKinley, G. H., Cohen, R. E., and Rubner, M. F.: Design parameters for superhydrophobicity and superoleophobicity. MRS Bulletin, 33(8):752–758, 2008.
79. Lafuma, A. and Quéré, D.: Slippery pre-suffused surfaces. Europhysics Letters, 96(5):56001, 2011.
80. Wong, T.-S., Kang, S. H., Tang, S. K. Y., Smythe, E. J., Hatton, B. D., Grinthal, A., and Aizenberg, J.: Bioinspired self-repairing slippery surfaces with pressure-stable omniphobicity. Nature, 477(7365):443–447, 2011.

81. Anand, S., Paxson, A. T., Dhiman, R., Smith, J. D., and Varanasi, K. K.: Enhanced condensation on lubricant-impregnated nanotextured surfaces. ACS Nano, 6(11):10122–10129, 2012.
82. Schutzius, T. M., Bayer, I. S., Qin, J., Waldroup, D., and Megaridis, C. M.: Water-based, non-fluorinated dispersions for environmentally benign, large-area superhydrophobic coatings. Submitted to ACS Applied Materials & Interfaces, 2013.
83. Megaridis, C. M., Schutzius, T. M., Bayer, I. S., Qin, J., and Waldroup, D. E.: Non-fluorinated water-based superhydrophobic compositions, 2013. US Non-provisional Patent Application 13/873,663.
84. Bayer, I. S., Brown, A., Steele, A., and Loth, E.: Transforming anaerobic adhesives into highly durable and abrasion resistant superhydrophobic organoclay nanocomposite films: A new hybrid spray adhesive for tough superhydrophobicity. Applied Physics Express, 2(12):125003, 2009.
85. Bayer, I. S., Steele, A., Martorana, P., Loth, E., Robinson, S. J., and Stevenson, D.: Bi-olubricant induced phase inversion and superhydrophobicity in rubber-toughened biopolymer/organoclay nanocomposites. Applied Physics Letters, 95(6):063702, 2009.
86. Bayer, I. S., Steele, A., Martorana, P. J., and Loth, E.: Fabrication of superhydrophobic polyurethane/organoclay nano-structured composites from cyclomethicone-in-water emulsions. Applied Surface Science, 257:823–826, 2010.
87. Schutzius, T. M., Bayer, I. S., Tiwari, M. K., and Megaridis, C. M.: Novel fluoropolymer blends for the fabrication of sprayable multifunctional superhydrophobic nanostructured composites. Industrial & Engineering Chemistry Research, 50(19):11117–11123, 2011.
88. Das, A., Schutzius, T. M., Bayer, I. S., and Megaridis, C. M.: Superoleophobic and conductive carbon nanofiber/fluoropolymer composite films. Carbon, 50(3):1346–1354, 2012.
89. Das, A., Hayvacı, H. T., Tiwari, M. K., Bayer, I. S., Erricolo, D., and Megaridis, C. M.: Superhydrophobic and conductive carbon nanofiber/PTFE composite coatings for EMI shielding. Journal of Colloid and Interface Science, 353(1):311–315, 2011.

90. Das, A., Megaridis, C. M., Liu, L., Wang, T., and Biswas, A.: Design and synthesis of superhydrophobic carbon nanofiber composite coatings for terahertz frequency shielding and attenuation. Applied Physics Letters, 98(17):174101, 2011.
91. Martin, J. W., Mabury, S. A., Solomon, K. R., and Muir, D. C. G.: Dietary accumulation of perfluorinated acids in juvenile rainbow trout (*Oncorhynchus mykiss*). Environmental Toxicology and Chemistry, 22(1):189–195, 2003.
92. Martin, J. W., Mabury, S. A., Solomon, K. R., and Muir, D. C. G.: Bioconcentration and tissue distribution of perfluorinated acids in rainbow trout (*Oncorhynchus mykiss*). Environmental Toxicology and Chemistry, 22(1):196–204, 2003.
93. U.S. Environmental Protection Agency: Preliminary risk assessment of the developmental toxicity associated with exposure to perfluorooctanoic acid and its salts. Technical report, Office of Pollution Prevention and Toxics, Risk Assessment Division, 2003.
94. Martin, J. W., Whittle, D. M., Muir, D. C. G., and Mabury, S. A.: Perfluoroalkyl contaminants in a food web from Lake Ontario. Environmental Science & Technology, 38(20):5379–5385, 2004.
95. Meyer, M. F., McConnell, R. L., and Joyner, F. B.: Water-dispersible polyolefin compositions useful as hot melt adhesives, 1975. US Patent 3,919,176.
96. Lang, F. J., Clough, P. H., Dyer, T. J., Goulet, M. T., Liu, K.-C., Lostocco, M. R., Nickel, D. J., Rekoske, M. J., Runge, T. M., Seabaugh, M. L., Timm, J. J., and Zwick, K. J.: Tissue products containing non-fibrous polymeric surface structures and a topically-applied softening composition, 2009. US Patent 7,588,662.
97. Lin, J. J., Chu, C. C., Chiang, M. L., and Tsai, W. C.: Manipulating assemblies of high-aspect-ratio clays and fatty amine salts to form surfaces exhibiting a lotus effect. Advanced Materials, 18(24):3248–3252, 2006.
98. Megaridis, C. M., Schutzius, T. M., Bayer, I. S., and Qin, J.: Superhydrophobic compositions, 2013. US Patent Application 13/193,145.
99. Jeon, I.-Y., Shin, Y.-R., Sohn, G.-J., Choi, H.-J., Bae, S.-Y., Mahmood, J., Jung, S.-M., Seo, J.-M., Kim, M.-J., Chang, D. W., et al.: Edge-carboxylated graphene nanosheets via ball milling. Proceedings of the National Academy of Sciences, 109(15):5588–5593, 2012.

100. Bayer, I. S., Caramia, V., Fragouli, D., Spano, F., Cingolani, R., and Athanassiou, A.: Electrically conductive and high temperature resistant superhydrophobic composite films from colloidal graphite. Journal of Materials Chemistry, 22(5):2057–2062, 2012.
101. Lin, Y., Ehlert, G. J., Bukowsky, C., and Sodano, H. A.: Superhydrophobic functionalized graphene aerogels. ACS Applied Materials & Interfaces, 3(7):2200–2203, 2011.
102. Zhang, L., Zha, D.-A., Du, T., Mei, S., Shi, Z., and Jin, Z.: Formation of superhydrophobic microspheres of poly(vinylidene fluoride- hexafluoropropylene)/graphene composite via gelation. Langmuir, 27(14):8943–8949, 2011.
103. Choi, B. G. and Park, H. S.: Superhydrophobic graphene/naion nanohybrid films with hierarchical roughness. The Journal of Physical Chemistry C, 116(5):3207–3211, 2012.
104. Lin, Z., Liu, Y., and Wong, C.-P.: Facile fabrication of superhydrophobic octadecylamine-functionalized graphite oxide film. Langmuir, 26(20):16110–16114, 2010.
105. Rafiee, J., Rafiee, M., Yu, Z., and Koratkar, N.: Superhydrophobic to superhydrophilic wetting control in graphene films. Advanced Materials, 22(19):2151–2154, 2010.
106. Nishino, T., Meguro, M., Nakamae, K., Matsushita, M., and Ueda, Y.: The lowest surface free energy based on -CF<sub>3</sub> alignment. Langmuir, 15(13):4321–4323, 1999.
107. Holtzinger, C., Niparte, B., Wächter, S., Berthomé, G., Riassetto, D., and Langlet, M.: Superhydrophobic TiO<sub>2</sub> coatings formed through a non-fluorinated wet chemistry route. Surface Science, DOI: 10.1016/j.susc.2013.07.002, 2013.
108. Schmidt, D. L., Coburn, C. E., Dekoven, B. M., Potter, G. E., Meyers, G. F., and Fischer, D. A.: Water-based nonstick hydrophobic coatings. Nature, 368(6466):39–41, 1994.
109. Smitha, V. S., Jyothi, C. K., Pillai, S., Warriar, K. G., et al.: Novel multifunctional titania–silica–lanthanum phosphate nanocomposite coatings through an all aqueous sol–gel process. Dalton Transactions, 42:4602–4612, 2013.
110. Li, D., Müller, M., Gilje, S., Kaner, R., and Wallace, G.: Processable aqueous dispersions of graphene nanosheets. Nature Nanotechnology, 3(2):101–105, 2008.



111. Stankovich, S., Piner, R. D., Chen, X. Q., Wu, N. Q., Nguyen, S. T., and Ruoff, R. S.: Stable aqueous dispersions of graphitic nanoplatelets via the reduction of exfoliated graphite oxide in the presence of poly(sodium 4-styrenesulfonate). Journal of Materials Chemistry, 16(2):155–158, 2006.
112. Campos, R., Guenther, A. J., Meuler, A. J., Tuteja, A., Cohen, R. E., McKinley, G. H., Haddad, T. S., and Mabry, J. M.: Superoleophobic surfaces through control of sprayed-on stochastic topography. Langmuir, 28(25):9834–9841, 2012.
113. Johnson, R. and Dettre, R. H.: Contact angle hysteresis. In Contact Angle, Wettability, and Adhesion, volume 43 of Advances in Chemistry, pages 112–135. 1964.
114. Manoudis, P., Karapanagiotis, I., Tsakalof, A., Zuburtikudis, I., and Panayiotou, C.: Superhydrophobic composite films produced on various substrates. Langmuir, 24(19):11225–11232, 2008.
115. Bayer, I. S., Tiwari, M. K., and Megaridis, C. M.: Biocompatible poly(vinylidene fluoride)/cyanoacrylate composite coatings with tunable hydrophobicity and bonding strength. Applied Physics Letters, 93(17):173902, 2008.
116. Steele, A., Bayer, I., and Loth, E.: Inherently superoleophobic nanocomposite coatings by spray atomization. Nano Letters, 9(1):501–505, 2009.
117. Tiwari, M. K., Bayer, I. S., Jursich, G. M., Schutzius, T. M., and Megaridis, C. M.: Highly liquid-repellent, large-area, nanostructured poly (vinylidene fluoride)/poly (ethyl 2-cyanoacrylate) composite coatings: Particle filler effects. ACS Applied Materials & Interfaces, 2(4):1114–1119, 2010.
118. Schutzius, T. M., Tiwari, M. K., Bayer, I. S., and Megaridis, C. M.: High strain sustaining, nitrile rubber based, large-area, superhydrophobic, nanostructured composite coatings. Composites Part A: Applied Science and Manufacturing, 42(8):979 – 985, 2011.
119. Rodgers, B. and Waddell, W. H.: Rubber Compounding, volume 11 of Encyclopedia of Polymer Science and Technology. Hoboken, NJ, John Wiley & Sons, 3rd edition, 2004.
120. Hamed, G. R.: Engineering with Rubber: How to design Rubber Components. Cincinnati, OH, Hanser Gardner, 2nd edition, 2001.

121. ed. R. C. Klingender Handbook of Specialty Elastomers. Boca Raton, FL, Taylor & Francis, 2008.
122. Han, M., Kim, H., and Kim, E.: Nanocomposites prepared from acrylonitrile butadiene rubber and organically modified montmorillonite with vinyl groups. Nanotechnology, 17:403–409, 2006.
123. Kim, J. T., Lee, D. Y., Oh, T. S., and Lee, D. H.: Characteristics of nitrile-butadiene rubber layered silicate nanocomposites with silane coupling agent. Journal of Applied Polymer Science, 89(10):2633–2640, 2003.
124. Nah, C., Ryu, H. J., Han, S. H., Rhee, J. M., and Lee, M. H.: Fracture behaviour of acrylonitrile-butadiene rubber/clay nanocomposite. Polymer International, 50(11):1265–1268, 2001.
125. Nah, C., Ryu, H. J., Kim, W. D., and Chang, Y. W.: Preparation and properties of acrylonitrile-butadiene copolymer hybrid nanocomposites with organoclays. Polymer International, 52(8):1359–1364, 2003.
126. Sadhu, S. and Bhowmick, A. K.: Preparation and properties of nanocomposites based on acrylonitrile-butadiene rubber, styrene-butadiene rubber, and polybutadiene rubber. Journal of Polymer Science Part B: Polymer Physics, 42(9):1573–1585, 2004.
127. Gao, L. and McCarthy, T.: The lotus effect explained: two reasons why two length scales of topography are important. Langmuir, 22(7):2966–2967, 2006.
128. Quéré, D.: Non-sticking drops. Reports On Progress In Physics, 68(11):2495–2532, 2005.
129. Ma, M. L. and Hill, R. M.: Superhydrophobic surfaces. Current Opinion In Colloid & Interface Science, 11(4):193–202, 2006.
130. Bayer, I. S., Steele, A., Martorana, P. J., Loth, E., and Miller, L.: Superhydrophobic cellulose-based bionanocomposite films from pickering emulsions. Applied Physics Letters, 94(16):163902, 2009.
131. Furstner, R., Barthlott, W., Neinhuis, C., and Walzel, P.: Wetting and self-cleaning properties of artificial superhydrophobic surfaces. Langmuir, 21(3):956–961, 2005.
132. Gao, L. and McCarthy, T.: Artificial lotus leaf prepared using a 1945 patent and a commercial textile. Langmuir, 22(14):5998–6000, 2006.

133. Kim, S. H.: Fabrication of superhydrophobic surfaces. Journal of Adhesion Science and Technology, 22(3-4):235–250, 2008.
134. Zhang, J., Lu, X., Huang, W., and Han, Y.: Reversible superhydrophobicity to superhydrophilicity transition by extending and unloading an elastic polyamide film. Macromolecular Rapid Communications, 26(6):477–480, 2005.
135. Choi, W., Tuteja, A., Chhatre, S., Mabry, J. M., Cohen, R. E., and McKinley, G. H.: Fabrics with tunable oleophobicity. Advanced Materials, 21(21):2190–2195, 2009.
136. Bormashenko, E., Goldshtein, V., Barayev, R., Stein, T., Whyman, G., Pogreb, R., Barkay, Z., and Aurbach, D.: Robust method of manufacturing rubber waste-based water repellent surfaces. Polymers for Advanced Technologies, 20(7):650–653, 2009.
137. Bahnert, T., Textor, T., Opwis, K., and Schollmeyer, E.: Recent approaches to highly hydrophobic textile surfaces. Journal of Adhesion Science and Technology, 22:285–309, 2008.
138. Gowri, S., Almeida, L., Amorim, T., Carneiro, N., Pedro Souto, A., and Fátima Esteves, M.: Polymer nanocomposites for multifunctional finishing of textiles: A review. Textile Research Journal, 80(13):1290–1306, 2010.
139. Coulson, S. R., Woodward, I. S., Badyal, J. P. S., Brewer, S. A., and Willis, C.: Plasma-chemical functionalization of solid surfaces with low surface energy perfluorocarbon chains. Langmuir, 16(15):6287–6293, 2000.
140. Coulson, S. R., Woodward, I. S., Badyal, J. P. S., Brewer, S. A., and Willis, C.: Ultralow surface energy plasma polymer films. Chemistry of Materials, 12(7):2031–2038, 2000.
141. Brewer, S. and Willis, C.: Structure and oil repellency: Textiles with liquid repellency to hexane. Applied Surface Science, 254(20):6450–6454, 2008.
142. Hoefnagels, H., Wu, D., and Ming, W.: Biomimetic superhydrophobic and highly oleophobic cotton textiles. Langmuir, 23(26):13158–13163, 2007.
143. Leng, B., Shao, Z., and Ming, W.: Superoleophobic cotton textiles. Langmuir, 25(4):2456–2460, 2009.

144. Nosonovsky, M.: On the range of applicability of the Wenzel and Cassie equations. Langmuir, 23(19):9919–9920, 2007.
145. Pak, B. and Cho, Y.: Hydrodynamic and heat transfer study of dispersed fluids with submicron metallic oxide particles. Experimental Heat Transfer, 11(2):151–170, 1998.
146. Wang, X., Xu, X., and Choi, S.: Thermal conductivity of nanoparticle-fluid mixture. Journal of Thermophysics and Heat Transfer, 13(4):474–480, 1999.
147. Nguyen, C., Desgranges, F., Roy, G., Galanis, N., Mare, T., Boucher, S., and Angue Mintsu, H.: Temperature and particle-size dependent viscosity data for water-based nanofluids-hysteresis phenomenon. International Journal of Heat and Fluid Flow, 28(6):1492–1506, 2007.
148. Jia-Fei, Z., Zhong-Yang, L., Ming-Jiang, N., and Ke-Fa, C.: Dependence of nanofluid viscosity on particle size and pH value. Chinese Physics Letters, 26(6):066202, 2009.
149. Hwang, Y., Lee, J., Jeong, Y., Cheong, S., Ahn, Y., and Kim, S.: Production and dispersion stability of nanoparticles in nanofluids. Powder Technology, 186(2):145–153, 2008.
150. Prasher, R., Song, D., Wang, J., and Phelan, P.: Measurements of nanofluid viscosity and its implications for thermal applications. Applied Physics Letters, 89(13):133108, 2006.
151. Michielsen, S. and Lee, H.: Design of a superhydrophobic surface using woven structures. Langmuir, 23(11):6004–6010, 2007.
152. Gross, D. and Seelig, T.: Fracture Mechanics: With an Introduction to Micromechanics. Mechanical Engineering Series. New York, NY, Springer, 2006.
153. Kramer, E.: Microscopic and molecular fundamentals of crazing, volume 52-53 of Advances in Polymer Science. New York, NY, Springer, 1983.
154. Liu, Y., He, J., Yu, J., and Zeng, H.: Controlling numbers and sizes of beads in electrospun nanofibers. Polymer International, 57(4):632–636, 2008.

155. Reneker, D. H. and Yarin, A. L.: Electrospinning jets and polymer nanofibers. Polymer, 49:2387–2425, 2008.
156. Hayakawa, Y., Terasawa, N., Hayashi, E., and Abe, T.: Synthesis of novel polymethacrylates bearing cyclic perfluoroalkyl groups. Polymer, 39(17):4151–4154, 1998.
157. Park, I. J., Lee, S.-B., and Choi, C. K.: Surface properties of the fluorine-containing graft copolymer of poly((perfluoroalkyl)ethyl methacrylate)-g-poly(methyl methacrylate). Macromolecules, 31(21):7555–7558, 1998.
158. Thomas, R. R., Anton, D. R., Graham, W. F., Darmon, M. J., Sauer, B. B., Stika, K. M., and Swartzfager, D. G.: Preparation and surface properties of acrylic polymers containing fluorinated monomers. Macromolecules, 30(10):2883–2890, 1997.
159. Ma, M., Mao, Y., Gupta, M., Gleason, K. K., and Rutledge, G. C.: Superhydrophobic fabrics produced by electrospinning and chemical vapor deposition. Macromolecules, 38(23):9742–9748, 2005.
160. U.S. Environmental Protection Agency: Perfluorooctyl sulfonates; proposed significant new use rule. Federal Register, 65:62319–62333, 2001.
161. Manda, C. and Roy, S. K.: Industrial Polymers, Specialty Polymers, and Their Applications, volume 73 of Plastics Engineering. Boca Raton, FL, Taylor & Francis, 2009.
162. Braga, F. J. C., Rogero, S. O., Couto, A. A., Marques, R. F. C., Ribeiro, A. A., and Campos, J. S. C.: Characterization of PVDF/HAP composites for medical applications. Materials Research, 10:247–251, 2007.
163. Bottino, A., Capannelli, G., Munari, S., and Turturro, A.: Solubility parameters of poly(vinylidene fluoride). Journal of Polymer Science Part B: Polymer Physics, 26(4):785–794, 1988.
164. Yeow, M., Liu, Y., and Li, K.: Isothermal phase diagrams and phase-inversion behavior of poly (vinylidene fluoride)/solvents/additives/water systems. Journal of Applied Polymer Science, 90(8):2150–2155, 2003.
165. Cheng, L.: Effect of temperature on the formation of microporous PVDF membranes by precipitation from 1-octanol/DMF/PVDF and water/DMF/PVDF systems. Macromolecules, 32(20):6668–6674, 1999.

166. Ho, S. and Soo, Y.: Phase behaviour of polymer/solvent/non-solvent systems. Polymer, 36(19):3711–3717, 1995.
167. Cheng, L., Young, T., Fang, L., and Gau, J.: Formation of particulate microporous poly (vinylidene fluoride) membranes by isothermal immersion precipitation from the 1-octanol/dimethylformamide/poly (vinylidene fluoride) system. Polymer, 40(9):2395–2403, 1999.
168. Young, T., Cheng, L., Lin, D., Fane, L., and Chuang, W.: Mechanisms of PVDF membrane formation by immersion-precipitation in soft (1-octanol) and harsh (water) nonsolvents. Polymer, 40(19):5315–5323, 1999.
169. Hong, P. and Chou, C.: Phase separation and gelation behaviors in poly (vinylidene fluoride)/tetra (ethylene glycol) dimethyl ether solutions. Polymer, 41(23):8311–8320, 2000.
170. Jian, K. and Pintauro, P.: Integral asymmetric poly (vinylidene fluoride) (PVDF) pervaporation membranes. Journal of Membrane Science, 85(3):301–309, 1993.
171. Jian, K., Pintauro, P., and Ponangi, R.: Separation of dilute organic/water mixtures with asymmetric poly (vinylidene fluoride) membranes. Journal of Membrane Science, 117(1-2):117–133, 1996.
172. Jian, K. and Pintauro, P.: Asymmetric PVDF hollow-fiber membranes for organic/water pervaporation separations. Journal of Membrane Science, 135(1):41–53, 1997.
173. Dillon, D., Tenneti, K., Li, C., Ko, F., Sics, I., and Hsiao, B.: On the structure and morphology of polyvinylidene fluoride-nanoclay nanocomposites. Polymer, 47(5):1678–1688, 2006.
174. Peng, Q., Cong, P., Liu, X., Liu, T., Huang, S., and Li, T.: The preparation of PVDF/clay nanocomposites and the investigation of their tribological properties. Wear, 266(7-8):713–720, 2009.
175. Pramoda, K., Mohamed, A., Phang, I., and Liu, T.: Crystal transformation and thermo-mechanical properties of poly (vinylidene fluoride)/clay nanocomposites. Polymer International, 54(1):226–232, 2005.

176. Priya, L. and Jog, J.: Poly(vinylidene fluoride)/clay nanocomposites prepared by melt intercalation: Crystallization and dynamic mechanical behavior studies. Journal of Polymer Science Part B: Polymer Physics, 40(15):1682–1689, 2002.
177. Shah, D., Maiti, P., Gunn, E., Schmidt, D., Jiang, D., Batt, C., and Giannelis, E.: Dramatic enhancements in toughness of polyvinylidene fluoride nanocomposites via nanoclay-directed crystal structure and morphology. Advanced Materials, 16(14):1173–1177, 2004.
178. Shah, D., Maiti, P., Jiang, D., Batt, C., and Giannelis, E.: Effect of nanoparticle mobility on toughness of polymer nanocomposites. Advanced Materials, 17(5):525–528, 2005.
179. Song, Y., Zhao, Z., Yu, W., Li, B., and Chen, X.: Morphological structures of poly(vinylidene fluoride)/montmorillonite nanocomposites. Science in China Series B: Chemistry, 50(6):790–796, 2007.
180. Wu, T., Xie, T., and Yang, G.: Characterization of poly(vinylidene fluoride)/Na<sup>+</sup>-MMT composites: An investigation into the  $\beta$ -crystalline nucleation effect of Na<sup>+</sup>-MMT. Journal of Polymer Science Part B: Polymer Physics, 47(9):903–911, 2009.
181. Tiwari, M. K., Bayer, I. S., Jursich, G. M., Schutzius, T. M., and Megaridis, C. M.: Poly(vinylidene fluoride) and poly(ethyl 2-cyanoacrylate) blends through controlled polymerization of ethyl 2-cyanoacrylates. Macromolecular Materials and Engineering, 294(11):775–780, 2009.
182. Lam, P., Wynne, K. J., and Wnek, G. E.: Surface-tension-confined microfluidics. Langmuir, 18(3):948–951, 2002.
183. Lee, J.-T., George, M. C., Moore, J. S., and Braun, P. V.: Multiphoton writing of three-dimensional fluidic channels within a porous matrix. Journal of the American Chemical Society, 131(32):11294–11295, 2009.
184. Han, Y. H., Levkin, P., Abarientos, I., Liu, H. W., Svec, F., and Frechet, J. M. J.: Monolithic superhydrophobic polymer layer with photopatterned virtual channel for the separation of peptides using two-dimensional thin layer chromatography-desorption electrospray ionization mass spectrometry. Analytical Chemistry, 82(6):2520–2528, 2010.

185. Zahner, D., Abagat, J., Svec, F., Frechet, J. M. J., and Levkin, P. A.: A facile approach to superhydrophilic-superhydrophobic patterns in porous polymer films. Advanced Materials, 23(27):3030–3034, 2011.
186. Zimmermann, J., Rabe, M., Artus, G. R. J., and Seeger, S.: Patterned superfunctional surfaces based on a silicone nanofilament coating. Soft Matter, 4:450–452, 2008.
187. Chang, B., Sariola, V., Aura, S., Ras, R. H. A., Klöpper, M., Lipsanen, H., and Zhou, Q.: Capillary-driven self-assembly of microchips on oleophilic/oleophobic patterned surface using adhesive droplet in ambient air. Applied Physics Letters, 99(3):034104, 2011.
188. Chu, K.-H., Xiao, R., and Wang, E. N.: Uni-directional liquid spreading on asymmetric nanostructured surfaces. Nature Materials, 9(5):413–417, 2010.
189. Mertaniemi, H., Jokinen, V., Sainiemi, L., Franssila, S., Marmur, A., Ikkala, O., and Ras, R. H. A.: Superhydrophobic tracks for low-friction, guided transport of water droplets. Advanced Materials, 23(26):2911–2914, 2011.
190. Xing, S., Harake, R. S., and Pan, T.: Droplet-driven transports on superhydrophobic-patterned surface microfluidics. Lab On A Chip, 11(21):3642–3648, 2011.
191. Balu, B., Berry, A. D., Hess, D. W., and Breedveld, V.: Patterning of superhydrophobic paper to control the mobility of micro-liter drops for two-dimensional lab-on-paper applications. Lab On A Chip, 9(21):3066–3075, 2009.
192. Fox, H. W. and Zisman, W. A.: The spreading of liquids on low-energy surfaces. III. Hydrocarbon surfaces. Journal of Colloid Science, 7(4):428–442, 1952.
193. Zisman, W. A.: Relation of the equilibrium contact angle to liquid and solid constitution. Advances in Chemistry Series, 43(1):1–51, 1964.
194. Washburn, E. W.: The dynamics of capillary flow. The Physical Review, 17(3):273–283, 1921.
195. Squires, T. M. and Quake, S. R.: Microfluidics: Fluid physics at the nanoliter scale. Reviews of Modern Physics, 77(3):977–1026, 2005.



196. Kamusewitz, H., Possart, W., and Paul, D.: The relation between Young's equilibrium contact angle and the hysteresis on rough paraffin wax surfaces. Colloids and Surfaces A: Physicochemical and Engineering Aspects, 156(1-3):271–279, 1999.
197. Li, G. Z., Wang, L. C., Ni, H. L., and Pittman, C. U.: Polyhedral oligomeric silsesquioxane (POSS) polymers and copolymers: A review. Journal of Inorganic and Organometallic Polymers, 11(3):123–154, 2001.
198. Ro, H. W. and Soles, C. L.: Silsesquioxanes in nanoscale patterning applications. Materials Today, 14(1-2):20–33, 2011.
199. Albrecht, M. G. and Blanchette, C.: Materials issues with thin film hydrogen silsesquioxane low k dielectrics. Journal of the Electrochemical Society, 145(11):4019–4025, 1998.
200. Loboda, M. J., Grove, C. M., and Schneider, R. F.: Properties of a-SiOx: H thin films deposited from hydrogen silsesquioxane resins. Journal of the Electrochemical Society, 145(8):2861–2866, 1998.
201. Siew, Y. K., Sarkar, G., Hu, X., Hui, J., See, A., and Chua, C. T.: Thermal curing of hydrogen silsesquioxane. Journal of the Electrochemical Society, 147(1):335–339, 2000.
202. Wang, C. Y., Shen, Z. X., and Zheng, J. Z.: Thermal cure study of a low-k methyl silsesquioxane for intermetal dielectric application by FT-IR spectroscopy. Applied Spectroscopy, 54(2):209–213, 2000.
203. Lee, L. H., Chen, W. C., and Liu, W. C.: Structural control of oligomeric methyl silsesquioxane precursors and their thin-film properties. Journal of Polymer Science Part A: Polymer Chemistry, 40(10):1560–1571, 2002.
204. Yang, C. C. and Chen, W. C.: The structures and properties of hydrogen silsesquioxane (HSQ) films produced by thermal curing. Journal of Materials Chemistry, 12(4):1138–1141, 2002.
205. Laine, R. M., Rahn, J. A., Youngdahl, K. A., Babonneau, F., Hoppe, M. L., Zhang, Z. F., and Harrod, J. F.: Synthesis and high-temperature chemistry of methyl-silsesquioxane polymers produced by titanium-catalyzed redistribution of methyl-hydridooligosiloxanes and methylpolysiloxanes. Chemistry of Materials, 2(4):464–472, 1990.

206. Baney, R. H., Itoh, M., Sakakibara, A., and Suzuki, T.: Silsesquioxanes. Chemical Reviews, 95(5):1409–1430, 1995.
207. Rochow, E. G.: An Introduction to the Chemistry of the Silicones. New York, NY, John Wiley & Sons, 1946.
208. Zhou, W. J., Yang, H., Guo, X. Z., and Lu, J. J.: Thermal degradation behaviors of some branched and linear polysiloxanes. Polymer Degradation and Stability, 91(7):1471–1475, 2006.
209. Branson, E. D., Shah, P. B., Singh, S., and Brinker, C. J.: Preparation of hydrophobic coatings, 2009. US Patent 7,485,343.
210. Garrod, R. P., Harris, L. G., Schofield, W. C. E., McGettrick, J., Ward, L. J., Teare, D. O. H., and Badyal, J. P. S.: Mimicking a stenocara beetle's back for microcondensation using plasmachemical patterned superhydrophobic-superhydrophilic surfaces. Langmuir, 23(2):689–693, 2007.
211. Jokinen, V., Sainiemi, L., and Franssila, S.: Complex droplets on chemically modified silicon nanograss. Advanced Materials, 20(18):3453–3456, 2008.
212. Tadanaga, K., Morinaga, J., Matsuda, A., and Minami, T.: Superhydrophobic-superhydrophilic micropatterning on flowerlike alumina coating film by the sol-gel method. Chemistry of Materials, 12(3):590–592, 2000.
213. Pastine, S. J., Okawa, D., Kessler, B., Rolandi, M., Llorente, M., Zettl, A., and Frechet, J. M. J.: A facile and patternable method for the surface modification of carbon nanotube forests using perfluoroarylazides. Journal of the American Chemical Society, 130(13):4238–4239, 2008.
214. Zhang, X., Kono, H., Liu, Z., Nishimoto, S., Tryk, D. A., Murakami, T., Sakai, H., Abe, M., and Fujishima, A.: A transparent and photo-patternable superhydrophobic film. Chemical Communications, pages 4949–4951, 2007.
215. von Allmen, M.: Laser-Beam Interactions with Materials, volume 2. Berlin, Springer-Verlag, 1987.
216. Allcock, G., Dyer, P. E., Elliner, G., and Snelling, H. V.: Experimental observations and analysis of CO<sub>2</sub> laser-induced microcracking of glass. Journal of Applied Physics, 78(12):7295–7303, 1995.

217. Illyefalvi-Vitéz, Z.: Laser processing for microelectronics packaging applications. Microelectronics Reliability, 41(4):563–570, 2001.
218. Hurwitz, F. I., Heimann, P., Farmer, S. C., and Hembree, D. M.: Characterization of the pyrolytic conversion of polysilsesquioxanes to silicon oxycarbides. Journal of Materials Science, 28:6622–6630, 1993.
219. Drelich, J., Chibowski, E., Meng, D. D., and Terpilowski, K.: Hydrophilic and superhydrophilic surfaces and materials. Soft Matter, 7(21):9804–9828, 2011.
220. Xue, Z., Liu, M., and Jiang, L.: Recent developments in polymeric superoleophobic surfaces. Journal Of Polymer Science: Part B: Polymer Physics, 50(17):1209–1224, 2012.
221. Betz, A. R., Jenkins, J., Kim, C.-J. C., and Attinger, D.: Boiling heat transfer on superhydrophilic, superhydrophobic, and superbiphilic surfaces. International Journal of Heat and Mass Transfer, 57:733–741, 2013.
222. Mishchenko, L., Aizenberg, J., and Hatton, B. D.: Spatial control of condensation and freezing on superhydrophobic surfaces with hydrophilic patches. Advanced Functional Materials, DOI: 10.1002/adfm.201300418, 2013.
223. Ueda, E. and Levkin, P. A.: Emerging applications of superhydrophilic-superhydrophobic micropatterns. Advanced Materials, 25(9):1234–1247, 2013.
224. Kim, S., Moon, M.-W., and Kim, H.-Y.: Drop impact on super-wettability-contrast annular patterns. Journal of Fluid Mechanics, 730:328–342, 2013.
225. Courbin, L., Bird, J. C., Belmonte, A., and Stone, H. A.: “black hole” nucleation in a splash of milk. Physics of Fluids, 20:091106, 2008.
226. Taylor, G. I.: On making holes in fluid. Journal of Fluid Mechanics, 58:625–639, 1973.
227. Bormashenko, E. and Bormashenko, Y.: Non-stick droplet surgery with a superhydrophobic scalpel. Langmuir, 27(7):3266–3270, 2011.
228. Deng, T., Varanasi, K. K., Hsu, M., Bhate, N., Keimel, C., Stein, J., and Blohm, M.: Nonwetting of impinging droplets on textured surfaces. Applied Physics Letters, 94(13):133109, 2009.

229. Clanet, C., Beguin, C., Richard, D., and Quere, D.: Maximal deformation of an impacting drop. Journal of Fluid Mechanics, 517:199–208, 2004.
230. Taylor, G.: The dynamics of thin sheets of fluid. III. Disintegration of fluid sheets. Proceedings of the Royal Society of London. Series A. Mathematical and Physical Sciences, 253(1274):313–321, 1959.
231. Culick, F. E. C.: Comments on a ruptured soap film. Journal of Applied Physics, 31(6):1128–1129, 1960.
232. Gao, L. and McCarthy, T.: How Wenzel and Cassie were wrong. Langmuir, 23(7):3762–3765, 2007.
233. Gao, L. and McCarthy, T. J.: An attempt to correct the faulty intuition perpetuated by the Wenzel and Cassie “laws”. Langmuir, 25(13):7249–7255, 2009.
234. Renardy, Y., Popinet, S., Duchemin, L., Renardy, M., Zaleski, S., Josserand, C., Drumright-Clarke, M. A., Richard, D., Clanet, C., and Quéré, D.: Pyramidal and toroidal water drops after impact on a solid surface. Journal of Fluid Mechanics, 484:69–83, 2003.
235. Bartolo, D., Josserand, C., and Bonn, D.: Singular jets and bubbles in drop impact. Physical Review Letters, 96(12):124501, 2006.
236. Malouin, B. A., Koratkar, N. A., Hirs, A. H., and Wang, Z.: Directed rebounding of droplets by microscale surface roughness gradients. Applied Physics Letters, 96(23):234103, 2010.
237. Bayer, I. and Megaridis, C.: Contact angle dynamics in droplets impacting on flat surfaces with different wetting characteristics. Journal of Fluid Mechanics, 558:415–449, 2006.
238. Khoo, H. S. and Tseng, F.-G.: Spontaneous high-speed transport of subnanoliter water droplet on gradient nanotextured surfaces. Applied Physics Letters, 95(6):063108, 2009.
239. White, F. M.: Fluid Mechanics. New York, NY, McGraw-Hill, 7 edition, 2011.
240. Haberman, R.: Applied Partial Differential Equations with Fourier Series and Boundary Value Problems. New Jersey, Pearson, 4 edition, 2004.

241. Yarin, A. L. and Weiss, D. A.: Impact of drops on solid-surfaces: Self-similar capillary waves, and splashing as a new-type of kinematic discontinuity. Journal of Fluid Mechanics, 283:141–173, 1995.

## VITA

### NAME

Thomas M. Schutzius

### EDUCATION

B.S., Mechanical Engineering, University of Illinois at Chicago, 2008

Ph.D., Mechanical Engineering, University of Illinois at Chicago, Expected 2013

### TEACHING EXPERIENCE

Teaching Assistant (TA), Intermediate Thermodynamics (ME 325), University of Illinois at Chicago, Fall 2009

Teaching Assistant (TA), Experimental Methods in Mechanical Engineering (ME 341), University of Illinois at Chicago, Spring 2010

### HONORS

Eidgenössische Technische Hochschule (ETH) Fellowship 2013–2015

UIC Dean's Scholar Award 2013–2014

UIC Excellence in Undergraduate Mentoring Award, 2013

Faydor Litvin Graduate Award, 2012–2013

Valerie J. Kennedy Scholarship, 2008

Aileen S. Andrew Award, 2006

### PROFESSIONAL MEMBERSHIP

Member, American Society of Mechanical Engineers (2011–present)

Member, Materials Research Society (2012–present)

Member, American Physical Society (2011–present)

Senior Adviser, Pi Tau Sigma – Alpha Sigma (2006–present)

Member, Tau Beta Pi – IL Zeta (2006–present)

## PUBLICATIONS

M. K. Tiwari, I. S. Bayer, G. M. Jursich, T. M. Schutzius, C. M. Megaridis, “Poly(vinylidene fluoride) and Poly(ethyl 2-cyanoacrylate) Blends through Controlled Polymerization of Ethyl 2-Cyanoacrylates,” *Macromolecular Materials and Engineering*, 2009, 294, 775–780

M. K. Tiwari, I. S. Bayer, G. M. Jursich, T. M. Schutzius, C. M. Megaridis, “Highly Liquid-Repellent, Large-Area, Nanostructured Poly(vinylidene fluoride) / Poly(ethyl 2-cyanoacrylate) Composite Coatings: Particle Filler Effects,” *ACS Applied Materials & Interfaces*, 2010, 2, 1114–1119

T. M. Schutzius, M. K. Tiwari, I. S. Bayer, C. M. Megaridis, “High Strain Sustaining, Nitrile Rubber Based, Large-Area, Superhydrophobic, Nanostructured Composite Coatings,” *Composites Part A: Applied Science and Manufacturing*, 2011, 42, 979–985

T. M. Schutzius, I. S. Bayer, M. K. Tiwari, C. M. Megaridis, “Novel Fluoropolymer Blends for the Fabrication of Sprayable Multifunctional Superhydrophobic Nanostructured Composites,” *Industrial & Engineering Chemistry Research*, 2011, 50, 11117–11123

A. Das., T. M. Schutzius, I. S. Bayer, C. M. Megaridis, “Superoleophobic and Conductive Carbon Nanofiber/Fluoropolymer Composite Films,” *Carbon*, 2012, 50, 1346–1354

T. M. Schutzius, I. S. Bayer, G. M. Jursich, A. Das, C. M. Megaridis, “Superhydrophobic-Superhydrophilic Binary Micropatterns by Localized Thermal Treatment of Polyhedral Oligomeric Silsesquioxane (POSS)-Silica Films,” *Nanoscale*, 2012, 4, 5378–5385

T. M. Schutzius, M. Elsharkawy, M. K. Tiwari, C. M. Megaridis, “Surface Tension Confined (STC) Tracks for Capillary-Driven Transport of Low Surface Tension Liquids,” *Lab on a Chip*, 2012, 12, 5237–5242

A. Das., T. M. Schutzius, C. M. Megaridis, S. Subhechha, T. Wang, L. Liu, “Quasi-optical Terahertz Polarizers Enabled by Inkjet Printing of Carbon Nanocomposites,” *Applied Physics Letters*, 2012, 101, 243108

J. E. Mates, T. M. Schutzius, I. S. Bayer, J. Qin, D. E. Waldrup, C. M. Megaridis, “Water-Based Superhydrophobic Coatings for Nonwoven and cellulosic substrates,” *Submitted for publication in Industrial & Engineering Chemistry Research*.

T. M. Schutzius, J. Qin, D. Waldrup, C. M. Megaridis, “Water-based, Non-fluorinated Dispersions for Environmentally Benign, Large-area Superhydrophobic Coatings,” *Submitted for publication in ACS Applied Materials & Interfaces*.

T. M. Schutzius, G. Graeber, J. Oreluk, C. M. Megaridis, “Shaping and Mobi-



lizing Liquid  $\mu$ -Volumes With Wettability Engineered Surfaces,” *In preparation for Lab on a Chip*.

M. Elsharkawy, T. M. Schutzius, C. M. Megaridis. “Inkjet patterned superhydrophobic paper for open-air surface microfluidic devices.” *In preparation for Lab on a Chip*.

P. R. Jones, E. R. Cruz-Chu, K. Rykaczewski, K. Nandy, T. M. Schutzius, X. Hao, K. K. Varanasi, C. M. Megaridis, J. H. Walther, P. Koumoutsakos, H. D. Espinosa, N. A. Patankar. Practically dry under water. *In preparation for Nature Communications*.

D. Attinger, C. Frankiewicz, A. R. Betz, T. M. Schutzius, R. Ganguly, C.-J. Kim, C. M. Megaridis, “Wettability Engineering to Control Phase Change Heat Transfer” *Review paper in preparation*.

## PATENTS & DISCLOSURES

C. M. Megaridis, T. Schutzius, I. S. Bayer., J. Qin, D. E. Waldrup. *Non-Fluorinated Water-Based Superhydrophobic Compositions*. US Non-provisional Patent Application 13/873,663 (filed on 4-30-2013).

J. Qin, D. E. Waldrup, C. M. Megaridis, T. Schutzius, I. S. Bayer. *Non-Fluorinated Water-Based Superhydrophobic Surfaces*. US Non-provisional Patent Application 13/873,614 (filed on 4-30-2013).

C. M. Megaridis, T. Schutzius, I. S. Bayer. *Superhydrophobic/Superhydrophilic Binary Micropatterns by Localized Thermal Treatment of Polyhedral Oligomeric*

*Silsesquioxane (POSS)-Silica Films.* US Non-provisional Patent Application 61/671,456 (filed on 7-13-2012).

C. M. Megaridis, T. M. Schutzius, I. S. Bayer, J. Qin. *Superhydrophobic Compositions.* US Publication Number 20,130,030,098 A1. US Non-provisional Patent Application 13/193,145 (filed on 7-28-2011).

J. Qin, D. E. Walldrop, C. M. Megaridis, T. M. Schutzius, I. S. Bayer. *Superhydrophobic Surfaces.* US Publication Number 20,130,029,551 A1. US Non-provisional Patent Application 13/193,065 (filed on 7-28-2011).

C. M. Megaridis, T. Schutzius, A. Das. *Elastomeric (Stretchable) Electrically-Conducting Composite Coatings.* Invention Disclosure DE153 (filed on 5-31-2011).

T. M. Schutzius, M. K. Tiwari, C. M. Megaridis. *High Strain Sustaining Nitrile Rubber-based Superhydrophobic Composite Coatings Applied by Spray.* US Provisional Patent Application 61/288,749 (filed on 12-21-09).

## CONFERENCES

T. M. Schutzius, I. S. Bayer, A. Das, C. Megaridis. Large-Area Wettability  $\mu$ -Patterning for Boiling Heat Transfer Enhancement In: *International Workshop on Micro and Nano Structures for Phase Change Heat Transfer*, April 22-23, 2013, MIT Endicott House, Dedham, MA.

T. Schutzius, I. Bayer, G. Jursich, A. Das, C. Megaridis. Superhydrophobic - Superhydrophilic Binary Micropatterned Coatings by Localized Thermal Treat-

ment of Methylsilsesquioxane - Silica Films. In: *2012 Materials Research Society Fall Meeting*, November 25–30, 2012.

D. Attinger, A. R. Betz, T. M. Schutzius, J. Jenkins, C.-J. Kim, C. M. Megaridis. Biphilicity and Superbiphilicity for Wettability Control of Multiphase Heat Transfer. In: *65th Annual Meeting of the APS Division of Fluid Dynamics*, 57(17). 2012.

C. Megaridis, T. Schutzius, M. Elsharkawy, M. Tiwari. Pumpless Transport of Low Surface Tension Liquids in Surface Tension Confined (STC) Tracks. In: *65th Annual Meeting of the APS Division of Fluid Dynamics*, 57(17). 2012.

T. M. Schutzius, M. K. Tiwari, I. S. Bayer, C.M. Megaridis. High Strain Sustaining, Nitrile Rubber Based, Large-Area, Superhydrophobic, Nanostructured Composite Coatings. In: *2011 ASME Applied Mechanics and Materials Conference*, May 30–June 1, 2011.

C. Megaridis, T. Schutzius, A. Das, M. Tiwari, I. Bayer. Multifunctional Superhydrophobic Coatings for Large Area Applications. In: *62nd Annual Meeting of the APS Division of Fluid Dynamics*, 54(19). 2009.